THÈSE

En vue de l'obtention du

DOCTORAT DE L'UNIVERSITÉ DE TOULOUSE

Délivré par :

Institut National Polytechnique de Toulouse (Toulouse INP)

Discipline ou spécialité :

Energétique et Transferts

Présentée et soutenue par :

M. FABIEN DUPUY

le mardi 30 juin 2020

Titre :

Reduced Order Models and Large Eddy Simulation for Combustion Instabilities in aeronautical Gas Turbines

---

Ecole doctorale :

Mécanique, Energétique, Génie civil, Procédés (MEGeP)

Unité de recherche :

Centre Européen de Recherche et Formation Avancées en Calcul Scientifique (CERFACS)

Directeur(s) de Thèse :

M. THIERRY POINSOT

M. LAURENT GICQUEL

Rapporteurs :

Mme FRANÇOISE BAILLOT, UNIVERSITE DE ROUEN

M. SÉBASTIEN DUCRUIX, CENTRALESUPELEC GIF SUR YVETTE

Membre(s) du jury :

M. ERIC SERRE, CNRS MARSEILLE, Président

M. FLORENT LACOMBE, , Invité

M. FRANCK NICOUD, UNIVERSITE DE MONTPELLIER, Membre

M. LAURENT GICQUEL, CERFACS, Membre

M. THIERRY POINSOT, CNRS TOULOUSE, Membre

M. THIERRY SCHULLER, ECOLE CENTRALE PARIS, Membre

Abstract

Increasingly stringent regulations as well as environmental concerns have lead gas turbine powered engine manufacturers to develop the current generation of combustors, which feature lower than ever fuel consumption and pollutant emissions. However, modern combustor designs have been shown to be prone to combustion instabilities, where the coupling between acoustics of the combustor and the flame results in large pressure oscillations and vibrations within the combustion chamber. These instabilities can cause structural damages to the engine or even lead to its destruction. At the same time, considerable developments have been achieved in the numerical simulation domain, and Computational Fluid Dynamics (CFD) has proven capable of capturing unsteady flame dynamics and combustion instabilities for aforementioned engines. Still, even with the current large and fast increasing computing capabilities, time remains the key constraint for these high fidelity yet computationally intensive calculations. Typically, covering the entire range of operating conditions for an industrial engine is still out of reach. In that respect, low order models exist and can be efficient at predicting the occurrence of combustion instabilities, provided an adequate modeling of the flame/acoustics interaction as appearing in the system is available. This essential piece of information is usually recast as the so called Flame Transfer Function (FTF) relating heat release rate fluctuations to velocity fluctuations at a given point. One way to obtain this transfer function is to rely on analytical models, but few exist for turbulent swirling flames. Another way consists in performing costly experiments or numerical simulations, negating the requested fast prediction capabilities.

This thesis therefore aims at providing fast, yet reliable methods to allow for low order combustion instabilities modeling. In that context, understanding the underlying mechanisms of swirling flame acoustic response is also targeted. To address this issue, a novel hybrid approach is first proposed based on a reduced set of high fidelity simulations that can be used to determine input parameters of an analytical model used to express the FTF of premixed swirling flames. The analytical model builds on previous works starting with a level-set description of the flame front dynamics while also accounting for the acoustic-vorticity conversion through a swirler. The analysis shows that three parameters characterize the response of a laminar V-shaped flame. These can be obtained from a reacting simulation mean flow. Three other parameters characterizing the swirl fluctuation amplitude and an induced delay between acoustic and vorticity perturbations are furthermore needed and can be obtained in different ways. Combining these features yields the FTF of a swirled premixed V-flame. For such a model, validation is obtained using reacting stationary and pulsed numerical simulations of a laboratory scale premixed swirl stabilized flame. To this end, a robust methodology is

defined for the parameters extraction, and it is shown that good agreement with reference data from experiments is obtained for the predicted flame response. The model is also shown to be able to handle various perturbation amplitudes. At last, 3D high fidelity simulations of an industrial gas turbine powered by a swirled spray flame are performed to determine whether a combustion instability observed in experiments can be predicted using numerical analysis. To do so, a series of forced simulations is carried out in en effort to highlight the importance of the two-phase flow flame response evaluation. In that case, sensitivity to reference velocity perturbation probing positions as well as the amplitude and location of the acoustic perturbation source are investigated. The analytical FTF model derived in the context of a laboratory premixed swirled burner is furthermore gauged in this complex case. Results show that the unstable mode is predicted by the acoustic analysis, but that the flame model proposed needs further improvements to extend its applicability range and thus provide data relevant to actual aero-engines.

Résumé

Des réglementations de plus en plus strictes et un intérêt environnemental grandissant ont poussé les constructeurs de moteurs aéronautiques à développer la génération actuelle de chambres de combustion, affichant des consommations et émissions de polluants plus basses que jamais. Cependant, les phases de conception de chambres modernes ont clairement mis en évidence que celles-ci sont plus susceptibles de développer des instabilités de combustion, où le couplage entre l'acoustique de la chambre et la flamme suscite de larges oscillations de pression ainsi que des vibrations de la structure. Ces instabilités peuvent endommager le moteur, et potentiellement entraîner sa destruction. Dans le même temps, de considérables avancées ont eu lieu dans le domaine de la simulation numérique, et la Mécanique des Fluides Numérique (MFN) a démontré sa capacité à reproduire la dynamique de flammes instationnaires et les instabilités de combustion observées dans les moteurs. Pourtant, même avec le matériel informatique moderne, le temps de calcul reste la contrainte clé de ces simulations haute-fidélité, qui demeurent très coûteuses. Typiquement, couvrir la totalité du domaine de fonctionnement pour un moteur industriel est encore hors de portée. Des modèles dits bas-ordre existent également, et prédire efficacement les instabilités de combustion par leur intermédiaire est envisageable à la condition d'une modélisation appropriée de l'interaction entre l'acoustique et la flamme. La méthode de modélisation la plus commune de cet élément critique est la fonction de transfert de flamme (FTF) qui lie les fluctuations de taux de dégagement de chaleur aux fluctuations de vitesse en un point donné. Cette fonction de transfert peut être obtenue à partir de modèles analytiques, mais très peu existent pour des flammes swirlées turbulentes. Une autre approche consiste à réaliser des mesures expérimentales ou des simulations haute fidélité coûteuses, réduisant à néant la capacité de prédiction rapide recherchée avec les méthodes bas-ordre.

Cette thèse vise donc à développer des outils bas ordre à la fois rapides et fiables pour la modélisation des instabilités de combustion, ainsi qu'à améliorer la compréhension des mécanismes inhérents à la réponse acoustique d'une flamme swirlée. A cet effet, une approche hybride nouvelle est proposée, où un nombre réduit de simulations haute fidélité peut être utilisé pour déterminer les paramètres d'entrée d'un modèle analytique représentatif de la fonction de transfert d'une flamme swirlée prémélangée. Le modèle analytique s'appuie sur des travaux antérieurs traitant la flamme comme une interface perturbée, et prend en compte la conversion acoustique-vorticité à travers un swirler. L'analyse montre que trois paramètres caractérisent la réponse d'une flamme en "V" laminaire, et qu'ils peuvent être obtenus à partir du champ moyen d'une simulation réactive, tandis que trois autres paramètres caractérisent l'amplitude des fluctuations de swirl et le délai entre les perturbations acoustiques et de vorticité qui

se propagent dans l'injecteur. La combinaison de ces phénomènes permet de reproduire la FTF d'une flamme de prémélange en V swirlée. La validité du modèle est mise à l'épreuve en déterminant les divers paramètres nécessaires associés à partir de simulations numériques réactives stationnaires et pulsées d'une flamme prémélangée swirlée académique. A cette occasion, une méthodologie robuste de détermination de ces paramètres est définie, et un bon accord avec les données expérimentales de référence est obtenu pour la réponse acoustique de la flamme. Il est également démontré que le modèle peut prendre en compte diverses amplitudes de perturbation. Enfin, des simulations haute-fidélité 3D d'une turbine à gaz industrielle alimentée par un combustible liquide sont réalisées afin de déterminer s'il est possible de prédire numériquement un mode d'instabilité de combustion observé lors des essais. Pour cela, un ensemble de simulations forcées est mené à bien afin de souligner l'importance de l'acquisition de la réponse de la flamme diphasique, en comparant les positions de référence utilisées pour mesurer les vitesses fluctuantes ainsi que l'amplitude et l'origine de la perturbation acoustique. L'applicabilité du modèle analytique à ce cas complexe est aussi étudiée. Les résultats montrent que l'analyse acoustique proposée prédit bien la présence d'un mode instable, mais que le modèle bas ordre nécessite davantage de développements pour étendre son domaine de validité présumé.

Acknowledgements

Voilà donc la derniére partie à rédiger de ce manuscrit. Si j'avais su dans quoi je m'embarquais il y a trois ans de cela je pense que j'aurais pu prendre peur... mais nous y voilà, et après tout il y a quand même plus de positif que du reste.

Je souhaite remercier en premier lieu les rapporteurs de mon manuscrit, Françoise Baillot et Sébastien Ducruix, qui ont accepté de relire mon manuscrit, évaluer mon travail, ainsi que pour leurs remarques éclairées. Je remercie également Eric Serre pour avoir évalué ma soutenance et avoir contribué avec les rapporteurs aux discussions qui ont suivi.

Je remercie ensuite Thierry Poinsot, Laurent Gicquel, mes encadrants de thèse, sans qui ce travail n'aurait jamais vu le jour. Merci de m'avoir donné la possibilité de découvrir la recherche dans un contexte particulier (au bon sens du terme !) comme celui du Cerfacs, et pour vos conseils toujours opportuns. Je me dois également de remercier Franck Nicoud, qui vise bien souvent très juste quand il s'agit de trouver la prochaine piste à explorer, et Thierry Schuller qui a bien voulu m'accorder de son temps à plusieurs reprises pour des discussions toujours intéressantes sur des développements analytiques, alors qu'il n'en avait pas du tout l'obligation. Côté Safran je remercie Florent et Yoann qui ont bien voulu suivre mes travaux, m'ont acueilli chaleureusement lors de mes séjours à Villaroche, et m'ont facilité la compréhension des problématiques industrielles.

Nous avons la chance au Cerfacs d'avoir une équipe administrative pour nous éviter des maux de tête et nous permettre de nous dédier entièrement à nos travaux. Aussi, un grand merci à Marie, Nicole, Chantal, Michèle, Jade, et toute l'administration. Dans le même ordre d'idée je remercie également tous les membres de l'équipe CSG, qui nous aident avec les pépins informatiques (et ils furent légion !) et sont toujours disponibles quand on leur demande un peu de leur temps. Je remercie les séniors CFD actuels et passés qui ont répondu à mes questions souvent naïves au début de la thèse : Michaël, Corentin, Gab, Eléonore, Antoine, et d'autres encore. Merci également à Maxence Brebion pour son aide en début de thèse et à Marco Gatti que

je dois bien évidemment remercier puisque la quasi-totalité des résultats expérimentaux utilisés dans ma thèse sont issus de ses travaux.

Il est maintenant temps de remercier ceux que j'ai côtoyés le plus souvent au Cerfacs, les doctorants et post-doctorants qui se succèdent et font vivre ce labo. J'ai une pensée pour le Big 4: on aura passés de sacrés moments, sérieux ou non. Charlélie, on est arrivé le même jour, on a partagé ce famoso bureau, et nos sujets se sont beaucoup entre-coupés notamment au début. Je suis sûr que tu feras un super chercheur mais il faudrait songer à traiter plus respectueusement ton clavier ! Queguy, le musclé, le poulet-riz-vore, le "grot" gradient du Cerfacs, merci pour tous ces moments... je t'échange 3 scripts Antares contre 1 million d'heures Occigen, ok ? Pacaud, où l'homme de gauche qui s'habille à droite, j'espère bien le lire un jour ce bouquin ! Il paraît que ça ne parle même pas d'explosion alors... Merci à Maël, Quentin, Paul, Soizic, Simon, Varun, et tous ceux que j'ai pu connaître au Cerfacs et plus en dehors: dans Toulouse, au tennis, à vélo, à la salle de sport, autour d'un banquet ou d'un melon... Je ne citerais certainement pas tout le monde, mais merci à tous les autres : Omar, Félix, Lulu, O'malé, Bastien, Maxime, Abhijeet, la "italian team" (Davide, Ermanno, Walter, qui a été flashée à plus de 75 dB dans les couloirs...), et tant d'autres qui n'ont pas été cités.

En dehors du laboratoire je remercie les mineurs Yvan, Séb, Alex, Bastien, avec qui j'ai passé de bons moments à Toulouse, Carcassonne, Porto, et à Hambourg (comment ça pas Hambourg ?).

Pour finir un immense merci à ma famille qui m'a accompagné dans les bons comme dans les mauvais moments, et il y en a eu. A mes parents, que je tente de vous expliquer ce que je fais exactement avec mes "flammes qui font du bruit dans le moteur" ou que je me fasse recadrer "parce que je travaille trop", vous avez toujours été là quand j'en avais besoin, et pour cela merci. Lucas, Corentin, les frangins, à vous aussi un grand merci pour tous vos mots d'encouragement, notamment sur la fin.

Contents

1 Introduction **1**

1.1 Context : Aeronautical gas turbines 1

1.2 Combustion instabilities 7

1.3 Prediction of combustion instabilities 10

1.4 Modelling the flame in acoustic calculations 22

1.5 Swirling flame transfer functions 25

1.6 Thesis objectives and outline 27

2 Premixed swirling V-shaped flames acoustic response modeling **29**

2.1 FTF of laminar V-shaped premixed flames 29

2.2 Dynamics of forced swirling flames 40

2.3 Modelling of premixed swirling FTF 45

3 Large Eddy Simulation of a turbulent swirling premixed flame: the NoiseDyn burner **51**

3.1 Objectives 51

3.2 Experimental set-up 52

3.3 Numerical modelling 56

3.4 Validation and flame dynamics 63

3.5 SFTF model application 80

3.6 Improving the SFTF model: extension to other geometries and forcing amplitudes 93

3.7 Concluding remarks 108

4 Thermoacoustic study of an industrial engine **111**

4.1 Objectives 111

4.2 Description of the industrial combustor 112

4.3 Numerical setup 114

4.4 Determination of the real engine FTF 119

4.5 Applicability of the SFTF model to a real combustor 145

4.6 Thermoacoustic stability analysis using a Helmholtz solver 151

4.7 Conclusions 161

5 General conclusions **165**

Bibliography **169**

Appendices **191**

A Navier-Stokes equations for reacting flows **193**

B NoiseDyn configuration mesh convergence study **195**

C Study of the Noisedyn aerodynamically swirled stabilized flame **199**

D Extended SFTF model sensitivity analysis **207**

E Helmholtz computations of the SAFRAN combustor with a null acoustic pressure outlet boundary condition **213**

F Acoustic equivalence of reference points in Helmholtz computations **215**

Chapter 1

Introduction

Contents

1.1 Context : Aeronautical gas turbines 1
1.1.1 Present and upcoming challenges for civil aviation 1
1.1.2 Emission mitigation technologies for aeronautical turbines . . 3
1.2 Combustion instabilities 7
1.3 Prediction of combustion instabilities 10
1.3.1 General overview 10
1.3.2 High fidelity simulations 12
1.3.3 Linearized Navier-Stokes/Euler equations 15
1.3.4 Helmholtz solvers 17
1.3.5 Low order models 19
1.4 Modelling the flame in acoustic calculations 22
1.4.1 Flame transfer functions 22
1.4.2 Extensions of the FTF formalism 24
1.5 Swirling flame transfer functions 25
1.6 Thesis objectives and outline 27

1.1 Context : Aeronautical gas turbines

1.1.1 Present and upcoming challenges for civil aviation

It is now common knowledge that transportation is one of the most important sources of both energy consumption and pollutant emissions. Figures from 2015 indicate that transport was the second most energy consuming sector with 31% of the global consumption, Fig. 1.1. In addition, this sector has been undergoing a continuous growth that is not likely to stop over the next few decades. Among all transportation means, the part associated to commercial aviation has tremendously developed, Fig. 1.2, as a result of both globalization and technical improvements, making air travel accessible for an unprecedented fraction of the world population.

This global increase of air traffic does however not come without issues. Indeed, the vast majority if not the totality of the air fleet uses kerosene or other fossil fuel derivatives as its main source of power. Indeed, only few prototypes of electric airplanes have emerged since the beginning of the millennium, although historic actors of the

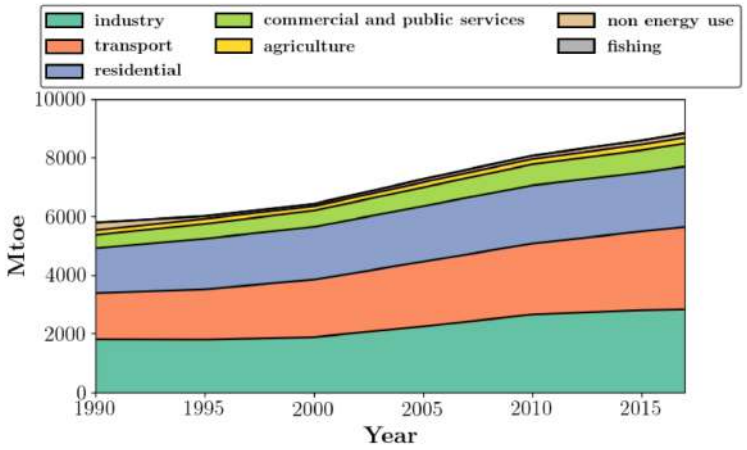


Figure 1.1: World total energy consumption by sector (Million Tons of Oil Equivalent, Mtoe) from 1990 to 2015. Adapted from Internal Energy Agency data [1].

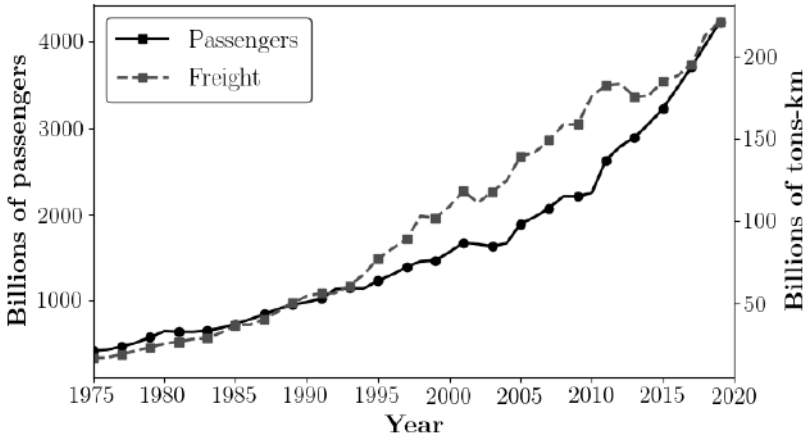


Figure 1.2: Air traffic evolution from 1975 to 2019. Source: ICAO estimates, indicators IS.AIR.PSGR and IS.AIR.GOOD.MT.K1 from the World Bank database.

industry such as Airbus, Boeing or Safran have announced programs related to the topic. High or medium capacity airplanes running solely on electricity, hydrogen, or other renewable sources of energy are however still a dream, especially with current technologies. At the same time, environmental as well as public healthcare concerns have been raised regarding the role of civil aviation as a source of pollutant emissions, but also greenhouse gas emissions (even though it represents merely 2% of the global production according to the Air Transport Action Group). Figure 1.3 discloses typical emission figures for a jet aircraft equipped with two engines for a 150 passengers one-hour flight. Combined to a thriving market, emissions of all sorts (chemicals, noise, *etc*) are only expected to increase in the future if nothing is done. For this reason, incrementally strict

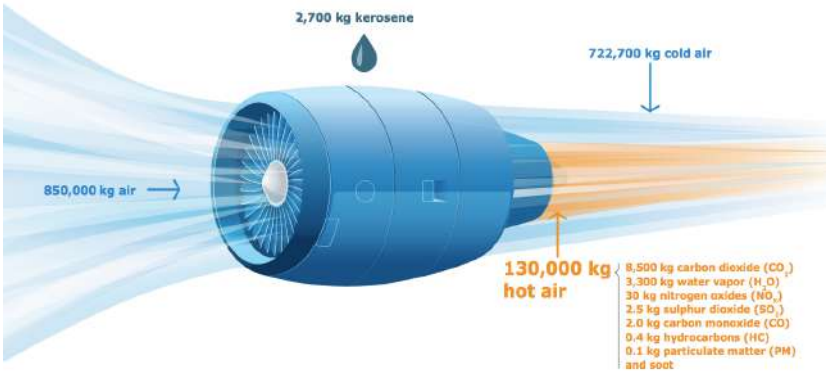


Figure 1.3: Typical consumption and emission figures for a jet aircraft equipped with two engines during a one-hour flight and with 150 passengers. Extracted from the European Aviation Environmental Report 2019.

objectives and regulations have been enforced. At the European level, the Advisory Council for Aeronautics Research (ACARE) set the following objectives for 2020:

- Fuel consumption and CO_2 emissions should be reduced by 50%,
- Nitrogen oxides NO_x emissions should be reduced by 80%,
- Global perceived noise should be reduced by 50%,

2005 being the reference year. Ambitious plans have also been set by the International Civil Aviation Organisation (ICAO) for 2050 compared to 2000:

- CO_2 emissions should be reduced by 75%,
- NO_x emissions should be reduced by 90%,
- Global perceived noise should be reduced by 65%,
- Emission-free taxiing phases.

The engine is evidently one of the most important source of cited emissions. To overcome future challenges, major progress will therefore undoubtedly have to be accomplished through modifications of the current propulsion system and the associated technologies. Aircraft engine manufacturers are hence at the forefront to tackle these issues.

1.1.2 Emission mitigation technologies for aeronautical turbines

International organizations and engine manufacturers have determined three main areas of improvement regarding civil aviation emissions:

- Operational improvements: more efficient procedures and weight reduction measures,

- Incremental improvements: developing and enhancing current technologies,
- Breakthrough innovations: proposing disruptive concepts that will change the industry.

Operational improvements are already being put in place or at least being investigated by airline companies. On the ground, pre-conditioned air and fixed electrical ground power could eliminate the need for embarked auxiliary power units. During departure and arrival, smarter scheduling or continuous descents (instead of successive steps) are considered, and measures are taken to reduce weight while cruising.

On the other end of the spectrum, breakthrough innovations are longer-term solutions that require substantial research and development efforts. Completely new aircraft fuselages are investigated but the most probable improvements are expected to come from the power source. The use of bio-fuels for future low carbon transportation is still in its infancy and will require structures to be adapted anyhow. Low carbon fuels such as cryogenic methane and hydrogen could provide a viable replacement to kerosene since their energy density per unit mass is important, Fig. 1.4, but their use requires major modifications of the aircraft structure. The most notable ones are linked to the

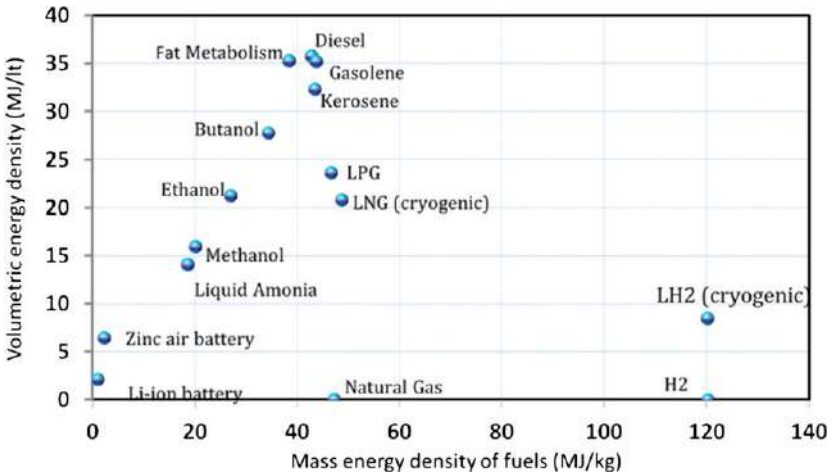


Figure 1.4: Energy density for various energy sources, reproduced from [2].

high pressure and low temperature storage tanks they require: these need to be strong enough, yet light enough. The energetic density of electric batteries, while tripled in the last two decades, is still one to two orders of magnitude lower than the one of kerosene, Fig. 1.4. Thus, their use is for now restricted to light on the ground operations or for a very minor portion of propulsion through micro-hybridation. Note also that in parallel to the above-mentioned possibilities, new combustion technologies are being investigated, among which constant volume combustion [3] and rotating detonation engines [4] are the most promising ones.

Finally, incremental evolution is the current concern for aircraft engine manufacturers that try to improve efficiency by building up on current technologies. Nowadays, most civil aircraft use double-flux gas turbines where the air entering the upfront fan is split into two separate fluxes, Fig. 1.5. In an effort to optimize the thermodynamic cycle, the primary air flux pressure is increased by going through low and high-pressure compressor stages. The compressed air then enters the combustion chamber where it mixes with the injected kerosene and burns, producing hot gases with a lower density and a higher velocity. The majority of the generated kinetic energy is transferred to turbines stages, before the flux exits the engine through a nozzle. The turbine in turn drives the compressor and upfront fan, increasing the momentum of the secondary flux. With this design, the major part of the engine thrust is produced by this secondary flux being ejected at a higher velocity compared to its original intake state.

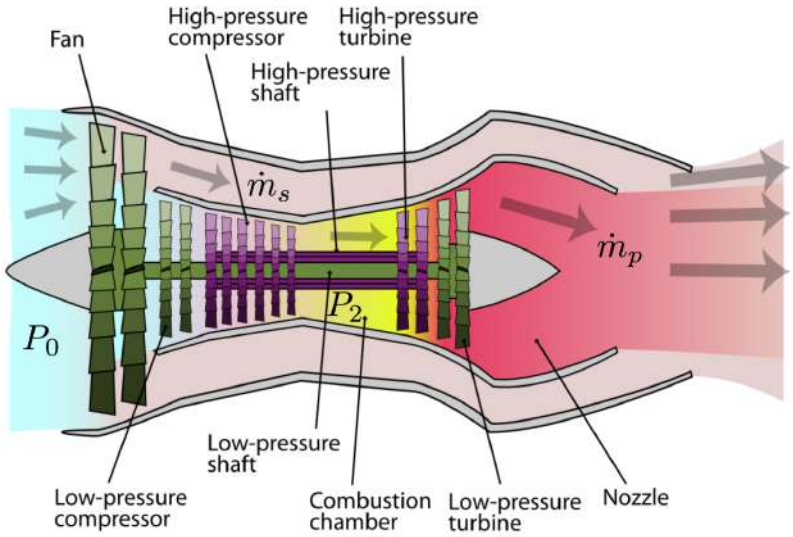


Figure 1.5: Schematic representation of a low bypass double flux gas turbine engine.

Regarding the engine, incremental improvements can be decomposed into improvements of the propulsive efficiency and of the engine core efficiency. Propulsive efficiency is to first order controlled by the ByPass Ratio (BPR) relating the secondary flux mass flow rate $\dot{m}_s$ to the primary flux mass flow rate $\dot{m}_p$, Fig. 1.5. For the same thrust level, increased BPR allows for lower fuel consumption and hence, reduced pollutant emissions. For example the CFM LEAP engine operates with a 11:1 BPR compared to a 6:1 ratio for the best previous generation model (CFM 56). Increasing the BPR can however become detrimental as it requires larger and heavier engine casings producing more drag. Regarding the engine core efficiency, *i.e.* the primary flux, it is governed by the Overall Pressure Ratio (OPR) between the intake air pressure P_0 and the pressure at the compressor exit P_2, just before the combustion chamber. Increasing the OPR im-

proves the overall engine efficiency by increasing the total useful work produced by the turbine thanks to a standard Brayton cycle. Although these new architectures decrease CO_2 emission levels, the method also comes with its drawbacks: increasing the combustion chamber pressure leads to higher temperature gas products which favour the creation of nitrogen oxides NO_x. Figure 1.6 shows that there is an optimum combustion temperature when considering carbon monoxide CO produced for high temperatures or when the combustion process is incomplete.

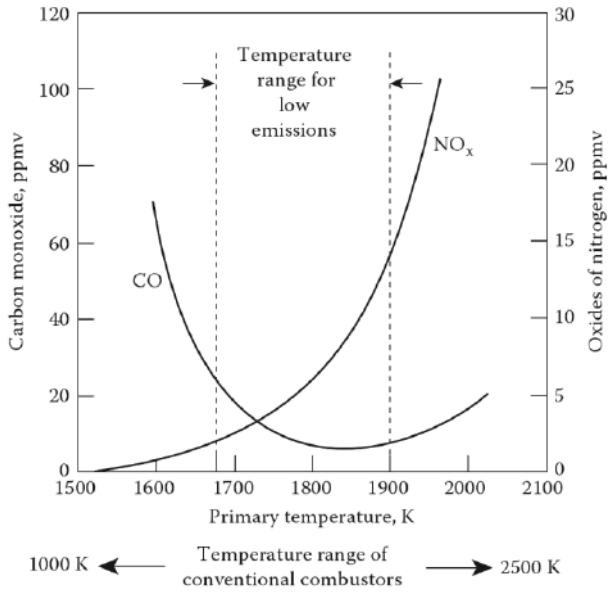


Figure 1.6: CO and NO_x production evolution with combustion zone temperature, reproduced from [5].

With such observations in mind, and recalling that turbine blades cannot withstand very high temperatures, solutions have been developed to decrease the overall combustor temperature while maintaining an efficient combustion process. Among these technologies, one can cite Lean Direct Injection (LDI) [6], Lean Premixed Pre-vaporized (LPP) [7], Rich-Quench-Lean combustors (RQL) [8], Multipoint Injection Systems (MIS) [9], other examples being described in [10, 11]. Most of these technological solutions rely on the use of lean (or low equivalence ratio) mixtures to reduce the final chamber temperature while ensuring a good combustion efficiency. As a consequence, the technology is pushed close to the lean blow out limit at which point the flame simply extinguishes. Operating close to this limit makes the combustor prone to the development of non desired oscillations known as combustion or thermoacoustic instabilities [12].

1.2 Combustion instabilities

In gas turbines, complex technological systems like multi-perforated liners and dilution holes are combined with a precise control of the fuel injection to ensure that the high power flame remains in its intended place and delivers the required power for all flight regimes. The flame itself is a source of strong heat release, creating high density gradients across the flame front. If the heat release rate fluctuates over time, the flame will act as a source of sound through time evolving density variations [13]. The generated acoustic waves will then propagate in the combustion chamber, potentially reflecting on the enclosing walls, inlets, or outlets, and impacting again the flame surface, thereby generating additional heat release rate fluctuations. When this interaction is constructive, acoustics and combustion get strongly coupled and the cycle enters a feedback loop where the burner operates on a non-desired oscillating state called combustion or thermoacoustic instability. A simple schematic representation of this feedback loop is presented in Fig. 1.7.

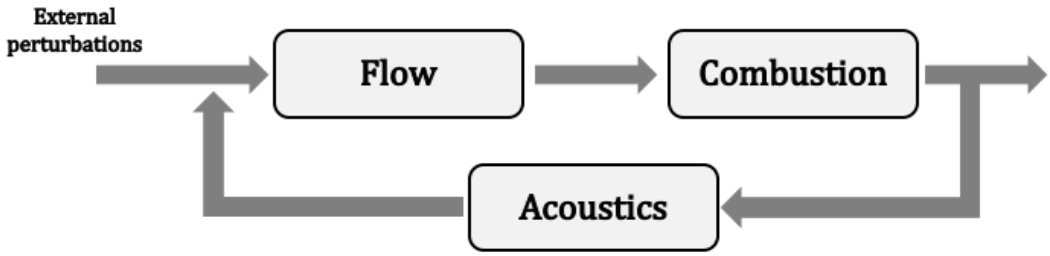


Figure 1.7: Schematic diagram of a combustion instability with acoustic coupling feedback.

Combustion instabilities have been known for more than a century and the pioneering works of Rijke [14] and Rayleigh [15] on the sound produced by flames enclosed in ducts. Lord Rayleigh proposed a first qualitative criterion for combustion instabilities, stating that a resonant coupling occurs when pressure and heat release rate oscillations are in phase. This criterion can be expressed as:

$$\int_{V_c} \int_0^{\tau} p' q' dt dV > 0 \tag{1.1}$$

where p' and q' are pressure and volumetric heat release rate perturbations, V_c is the combustor volume and τ the oscillation period respectively. Thus, coupling should occur only when the flame response provides energy back to the acoustic field. When considering losses at boundaries due to non-ideal reflections for the acoustic energy balance, the criterion becomes [13]:

$$\frac{\gamma - 1}{\gamma p} \int_{V_c} \int_0^{\tau} p' q' dt dV - \int_{A_c} \int_0^{\tau} p' \mathbf{u}' dt dA_c > 0 \tag{1.2}$$

with A_c the combustor surface, $\mathbf{u}'$ the acoustic velocity and γ the gas heat capacity ratio. A more detailed analysis taking into account entropy fluctuations can also be considered and is available in [16].

Pressure fluctuations generate unsteady heat release through three distinct mechanims [17]:

- Direct flame surface variations: acoustic pressure fluctuations are always related to velocity fluctuations that locally modify the flame surface and hence heat release.
- Indirect flame surface variations: variations of strain rate caused for instance by flame-vortex interactions issued from the response of the injector to the modulated acoustic field.
- Equivalence ratio: when fuel and oxidizer lines are separated (non-premixed combustion) or for multipoint injection systems, different feeding line responses lead to fluctuations of equivalence ratio and thus heat release variations.

For high power flames, unsteady movements of the flame and density variations in the fresh gases also become important factors. It is worth noting that when triggered, a thermoacoustic limit cycle usually appears after going through a specific transient.

A typical combustion instability cycle can be decomposed into three parts, Fig. 1.8. In a first phase, called the linear regime and corresponding to the first oscillation cy-

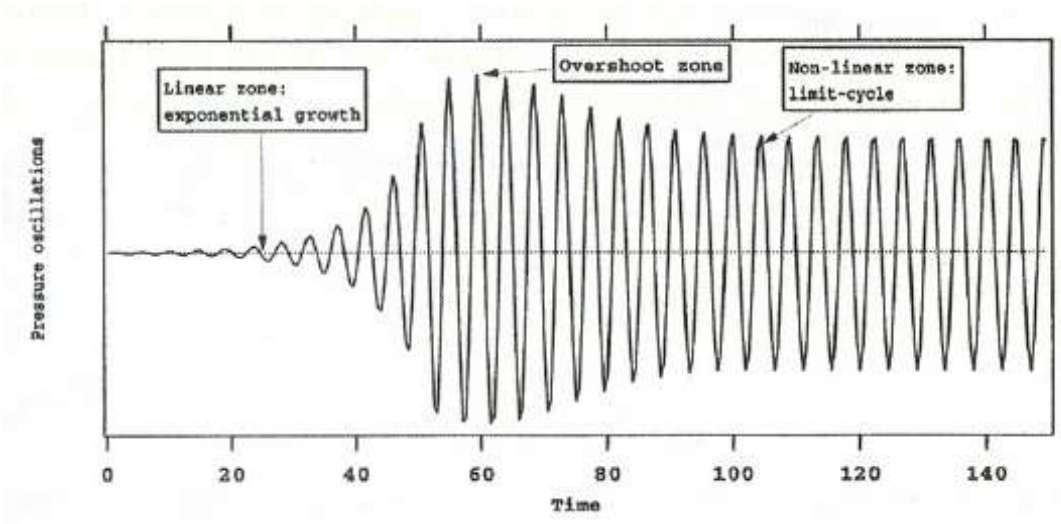


Figure 1.8: Pressure signal growth during a combustion instability, extracted from [13].

cles, heat release and acoustic fluctuations are proportional and grow in time with an exponential rate. In a second phase, called the nonlinear transition, saturation and acoustic dissipation due to viscous effects gradually counterbalance the acoustic energy generated by the flame. This leads to an overshoot of both pressure and heat release

followed by a decrease of the oscillation amplitude. In a final phase, corresponding to a limit cycle, the instability growth rate and the global damping rate cancel each other so that the oscillation amplitude remains constant.

A combustion instability is thus characterized by its frequency f, its growth rate corresponding to the exponential phase of Fig. 1.8, and its spatial shape. It is often chosen to describe the instability using a complex valued frequency, in which case the imaginary part corresponds to the growth rate. In this work, the $e^{-i\omega t}$ time convention is chosen, so that positive growth rates, $\Im(\omega) > 0$, are associated to exponential growth of the instability (unstable thermoacoustic mode), while negative ones, $\Im(\omega) < 0$, correspond to an exponential decay (stable thermoacoustic mode).

A first consequence of combustion instabilities is the generation of high amplitude pressure oscillations. In the context of industrial gas turbines, these oscillations jeopardize the engine structural integrity as it is not designed to endure such sustained abnormal mechanical stress. Other consequences are linked to the flame response to the acoustic excitation that may trigger extinction, blow-off, flash-back or large heat fluxes at walls. These non desired processes can indeed damage the engine or even lead to its complete destruction in worst cases, Fig. 1.9. Major thermoacoustic instabilities



(a) **(b)** **(c)**

Figure 1.9: Multipoint swirled injector before (a) and after (b) a combustion instability melted the chamber multi-perforated backplane. Extracted from [18]. (c) Rocket engine from the 1957 US rocket program destroyed after a combustion instability [12].

issues were first observed in liquid rocket engines [19, 20, 21] but more recent developments have seen the rise of this same phenomena in aircraft engines, especially for LPP systems [12, 22, 23].

Avoiding these instabilities is therefore a major concern for engine manufacturers which have to validate the combustor stability for a wide range of operating conditions. Minor modifications of the injection system are sometimes sufficient to supress the instability [24] and passive systems such as Helmholtz resonators [25] or multi-perforated inlets [26] can be used to introduce acoustic damping, although limited to a narrow

frequency range. In the case of annular combustors, the apparition of instabilities can also be prevented by introducing several types of burners in a symmetry breaking attempt [27, 28]. Another solution consists in tuning fuel and air injection laws to avoid combustion instabilities during transient regimes. Active control, although difficult, has also been investigated [29] but is rarely used in industrial systems due to the extra cost of not only the system itself but also its certification for the whole operating range. The reader is referred to the literature for further details regarding fundamental aspects of thermoacoustic instabilities [21, 30], or for the current status for real engines [12].

Ultimately, each of the mitigation technologies previously mentioned needs to be validated. In the previous decades, this has mainly been achieved thanks to experimental testing, which can be both arduous and expensive. Alternatives (or complementary validations) to assess the stability of a specific combustor during its design process make use of numerical methods and tools as detailed hereafter.

1.3 Prediction of combustion instabilities

1.3.1 General overview

As for every crucial issue observed in industry, the prediction of combustion instabilities is a very active research field involving laboratories [30] as well as multiple actors linked to the industry [12]. Historically, gas turbine engines were designed through incremental evolutions of previous designs. The full characterization of a combustion chamber stability was achieved with experimental validation campaigns which required to build engine prototypes for almost every new design. Significant advancements have since been made in both computational power/resources and numerical methods over the last three decades. As a result, predicting combustion instabilities using numerical simulations is now not only possible but also accurate and a potential cost-effective solution that can complement experiments in the context of design.

When it comes to numerical approaches, one may distinguish two categories of tools: high fidelity Computational Fluid Dynamics (CFD) based simulations with a complete description of the flow and acoustics [31], generating a large amount of data and requiring considerable computational resources; and reduced order tools devised for fast and cheap predictions [32, 33, 34]. The first category necessitates accurate chemistry models and high order numerical schemes but yields a complete description of the instability and all flow variables. In particular, it provides the structure and evolution of the instability at any location, contrary to the limited set of probes used during engine test sessions. In contrast, cheap numerical tools retain only the core acoustics description, sometimes mean flow description [35, 36], and further rely on models to achieve fast predictions [37]. Such methods are well adapted in the context

of engine design where numerous modifications have to be tested: burner position, chamber length, fuel mass flow rate, *etc.* They also allow for sensitivity analyses where the impact of the modification of a baseline parameter can be gauged [38]. Figure 1.10 presents a visualization of the full spectrum of numerical tools accessible today for the modelling and prediction of combustion instabilities. Modelling strategies range from

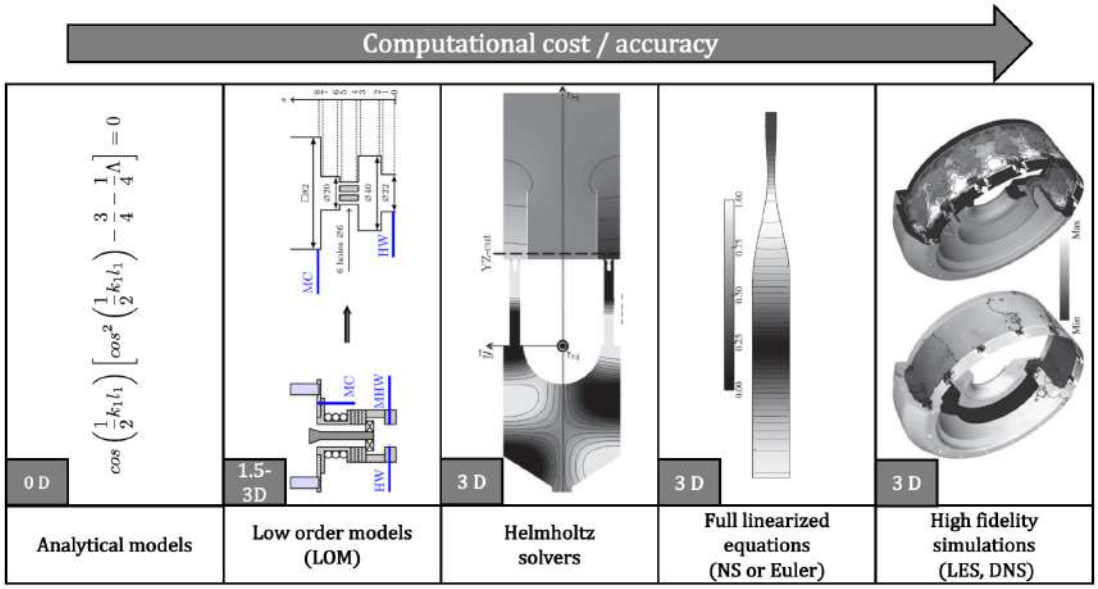


Figure 1.10: List of numerical methods for the prediction of thermoacoustic instabilities, with increasing accuracy and computational cost. Illustrations extracted from (left to right): [32], [39], [34], [40], [41].

analytical models providing a very simplified description of the flame and acoustics, to high fidelity simulations such as Large Eddy Simulations (LES) or Direct Numerical Simulation (DNS). The computational time needed and resulting accuracy are of course extremely different, and the proper tool must be chosen for the appropriate situation.

Addressing combustion instability predictions using reduced order tools can either be done in the time domain or in the frequency domain, both approaches having advantages and drawbacks. Time domain simulations follow the evolution of oscillations over time and cover the full development of the instability presented in Fig. 1.8. They are therefore easier to comprehend for the "non-initiated" and describe the full instability development from triggering to the limit cycle (provided the adequate modelling). Yet, they do not provide a straightforward understanding for cases where several modes appear at the same time, and one dominates the others [42]. Moreover, most flame representations and acoustic boundary conditions are usually derived in the frequency domain [43]. Frequency domain simulations assume all fluctuations to be periodic and provide information regarding all modes of the system at once: mode shapes, frequencies, growth rate, stability, *etc.* Finally, it should be emphasized that such simulations

are limited to the linear regime in the majority of cases, although successfull attempts to retrieve the full instability cycle exist [44, 45, 46].

1.3.2 High fidelity simulations

High fidelity numerical flow simulations constitute the most accurate description of the interaction between acoustics and flames. They rely on the full set of Navier-Stokes equations: mass, momentum and energy, which are provided in Appendix A. Nonlinear terms in the equations prevent their analytical resolution so far, hence three distinct strategies have emerged to solve them numerically:

- **Direct Numerical Simulation (DNS)**: All turbulent scales from the integral length scale l_t to the Kolmogorov scale l_κ are resolved [47, 48]. Results are therefore accurate, but achieving such a fine description requires a very fine spatial discretization. In a typical combustor, the smallest scales are of the order of few dozen microns while the total volume of one combustion chamber sector of an aero-jet engine is of the order of 10^{-6} m^{-3}. Resolving even a single sector of an annular gas turbine would hence necessitate an extremely large number of cells ($\approx 10^{14}$) which simply cannot be done even with the current most powerful supercomputer.

- **Large Eddy Simulations (LES)**: Turbulent scales are resolved up to a cut-off length scale k_Δ while the smallest eddies are modelled. In practice the filter size Δ is often equal to the grid cell size Δ_x, which bounds the quality of the LES to the mesh resolution. LES has become a valuable and usable tool for turbulent flow and combustion studies [49, 50]. With a very fine discretization, DNS is obtained, in all other cases, it constitutes a trade-off between accuracy and computational time and models need to be used for turbulent fluxes as well as for the flame description.

- **Reynolds Averaged Navier Stokes (RANS)**: Only the Reynolds or Favre averaged balance equations are solved [13, 48]. The averaged equations require closure rules for turbulent fluxes and combustion processes. RANS was historically the first developed approach as explicitly computing a turbulent flow with the available computational resources was simply impossible at the time. It only provides averaged quantities and is hence of limited interest for the study of unsteady phenomena such as combustion instabilities.

Choosing the adequate CFD approach is therefore crucial, especially in an industrial context. By construction, RANS simulations cannot capture transient and dynamics features of a flow and are not adapted to the prediction of combustion instabilities,

although some studies have been performed using the Unsteady RANS (URANS) formalism [51]. DNS has been applied with some success on academic cases but is still out of reach for complex industrial configurations and is mainly used in laminar flow configurations to decipher physical mechanisms (see for example [52, 53]). On the other hand, LES has proven its capabilities for the prediction of thermoacoustic instabilities for both academic configurations [54, 55, 56, 57, 58] and industrial gas turbines [12, 59], including full annular combustors [41]. It furthermore provides a direct insight on the interactions between the flame and acoustics and is not limited to instability predictions. In the context of thermoacoustics, LES has also been used to study the influence of fuel mixing [60], heat transfer [61, 62] and many other aspects. For these reasons, high fidelity simulations described in the remaining of this manuscript will only refer to LES.

Mathematical derivation of the governing equations usually relies on decomposing a variable X into a mean part $\overline{X}$ and a turbulent fluctuating part X', $X = \overline{X} + X'$ as typically done for the RANS approach. Similarly, LES decomposes any variable X into a filtered part and an unfiltered one that needs to be modelled. Figure 1.11 presents typical temporal signals of any variable X with DNS, LES and RANS approaches while Fig. 1.12 summarizes the corresponding resolved and modelled turbulent scales. Note

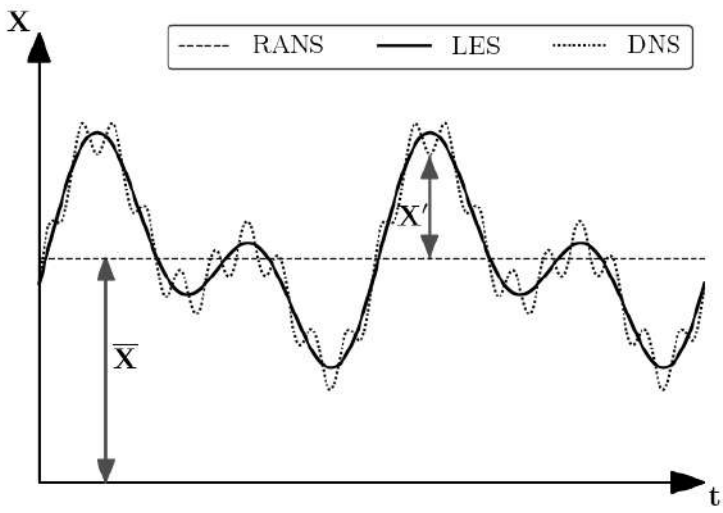


Figure 1.11: Time evolution of variable $\mathbf{X} = \overline{\mathbf{X}} + \mathbf{X}'$ with DNS, RANS, or LES formulations.

that the LES filtering procedure can be performed either in spectral or in physical space. If performed in space, the filtered quantity $\overline{X}$ results from a convolution of the function $X(x)$ with the LES filter kernel F_Δ:

$$\overline{X}(x) = \int X(y) F_\Delta(x - y) dy, \tag{1.3}$$

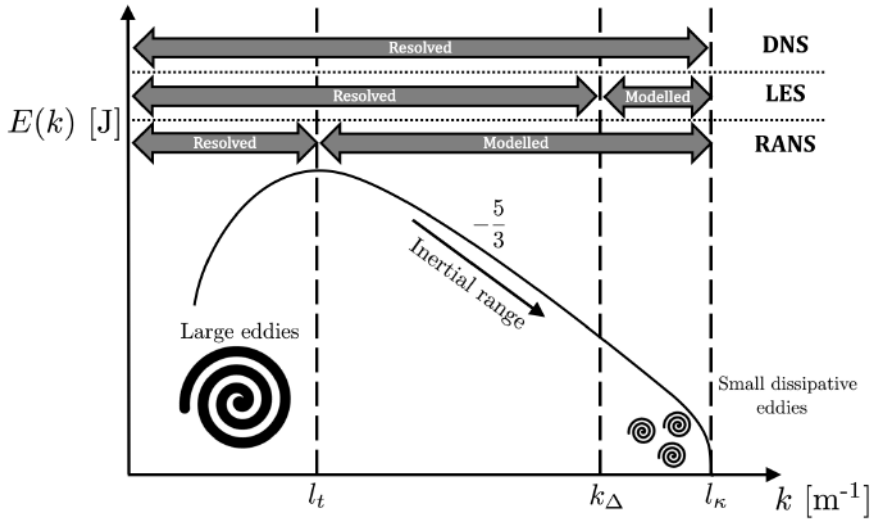


Figure 1.12: Turbulence energy spectrum as a function of the wave number k, with indications corresponding to the resolved and modelled ranges for DNS, RANS and LES. k_Δ is the LES cut-off wave number.

where Δ is the filter width, often chosen as the cell size in practical computations. For variable density flows, mass weighted Favre filtering is usually preferred [13]. The filtered quantity $\tilde{X}$ is then defined by;

$$\overline{\rho}\tilde{X}(x) = \int \rho(y)X(y)F_\Delta(x-y)dy \tag{1.4}$$

Such low-pass filtering results in smoother temporal signals, but also introduces additional difficulties compared to a simple time average as done for RANS. Indeed, contrary to RANS, the filtered value of a LES perturbation is not exactly null: $\tilde{X}' \neq 0$ for arbitraty filter kernels. Single and double filtering are also not equivalent: $\tilde{X} \neq \tilde{\tilde{X}}$. Arguably, the biggest issue lies in the fact that the filtering operator F_Δ and derivative operators do not commute. Nonetheless, LES codes rely on filtered equations and usually assume the commutativity of operators. Implications are investigated by Ghosal and Moin in [63], but in the general case, the corresponding uncertainties are dominated by the uncertainty of models used for the unfiltered quantities [13]. Applied to the Navier-Stokes equations, the filtering procedure yields:

- Filtered mass conservation

$$\frac{\partial\overline{\rho}}{\partial t} + \frac{\partial}{\partial x_j}\left(\overline{\rho}\widetilde{u}_j\right) = 0, \tag{1.5}$$

  where ρ is the mixture density and u_j is the j$^{\text{th}}$ velocity component.

- Filtered species conservation

$$\frac{\partial\overline{\rho}\tilde{Y}_k}{\partial t} + \frac{\partial\overline{\rho}\widetilde{Y}_k\tilde{u}_j}{\partial x_j} = -\frac{\partial}{\partial x_j}\left(\overline{J}_{j,k} + \overline{J}^t_{j,k}\right) + \overline{\dot{\omega}}_k, \quad \text{for } k = 1, n_{spec}, \tag{1.6}$$

where Y_k is the mass fraction for species k, $J_{j,k}$ is the species diffusive flux and $\dot{\omega}_k$ is the chemical source term for species k. The superscript $^{\mathrm{t}}$ indicates the matrix transpose.

- Filtered momentum conservation

$$\frac{\partial \overline{\rho}\widetilde{u}_i}{\partial t} + \frac{\partial \overline{\rho}\widetilde{u}_j\tilde{u}_i}{\partial x_j} = -\frac{\partial}{\partial x_j}\left(\overline{P}\delta_{ij} - \overline{\tau}_{ij} - \overline{\tau}^t_{ij}\right), \quad \text{for } i = 1,2,3, \tag{1.7}$$

where P is the pressure tensor, and τ_{ij} is the viscous stress tensor.

- Filtered energy conservation

$$\frac{\partial \overline{\rho}\widetilde{E}}{\partial t} + \frac{\partial}{\partial x_j}\left(\overline{\rho}\widetilde{E}\widetilde{u}_j\right) = -\frac{\partial}{\partial x_j}\left(\overline{u_i\left(P\delta_{ij} - \tau_{ij}\right)} + \overline{q}_j + \overline{q}^t_j\right) + \overline{\dot{\omega}}_T, \tag{1.8}$$

where E it the total non chemical energy, q_j is the energy flux and $\dot{\omega}_T$ is the volumetric heat release rate.

This set of equations presents several unclosed quantities that need to be modelled: Reynolds subgrid stresses ($\widetilde{u_iu_j} - \tilde{u}_i\tilde{u}_j$), subgrid scalar fluxes $\left(\widetilde{u_iY_k} - \tilde{u}_i\tilde{Y}_k\right)$, subgrid enthalpy fluxes $\left(\widetilde{u_ih_s} - \tilde{u}_i\tilde{h}_s\right)$ with h_s the sensible enthalpy. A wide variety of closure models is available in the literature. These are not detailed here for the sake of brevity but details can be found in [48] for turbulent stresses closures and in [13] for chemical reaction rate modelling. Note also that in the context of combustion instabilities, recent studies have shown that the acoustic response of a flame can be affected by the modelling choice for the subgrid stresses [34], underlining the difficulty of the present modelling context.

Although overall reliable in their reproduction of flame dynamics from flame/acoustics interactions (see however [64]), LES remain quite computationally intensive for practical application during design stages where a large number of potential designs and operating points has to be tested. Consequently, a variety of faster and cheaper solutions has been developed by simplifying the flame/acoustics problem, as detailed below.

1.3.3 Linearized Navier-Stokes/Euler equations

A straightforward way to simplify the analysis is to decouple acoustics and the flame response, before linearizing the basic set of equations, whether it be Navier-Stokes or Euler equations. In this view, chemical processes are discarded and the flame is described as a volumetric thermal source term as will be discussed in Sec. 1.4. A direct consequence is that Eq. (1.6) for species conservation is discarded and a unique molecular weight and heat capacity are usually considered. All quantities are then

linearized around a mean state, with the additional assumption that perturbations are harmonic waves for which spatial and temporal variations are decoupled:

$$X(x,t) = \overline{X}(x) + \Re\left(\hat{X}(x)e^{-i\omega t}\right) \tag{1.9}$$

where $\Re$ designates the real part of a complex number, $i^2 = -1$ and $\hat{X}$ is a complex valued quantity corresponding to the Fourier component for an angular frequency $\omega = 2\pi f$. The mean value is here noted $\overline{X}$ for the sake of simplicity but should not be confused with LES filtered quantities defined in the previous section, that will not be further utilized in the following. The fluctuation amplitude is then assumed to be much smaller than the mean value, $|\hat{X}| \ll \overline{X}$. This notation simplifies the description of periodic acoustic waves and allows to differentiate the frequency $\Re(f)$ and growth rate $\Im(f)$ of an acoustic mode. It is recalled that with the time convention used in this work ($e^{-i\omega t}$), a positive growth rate is associated to linearly increasing fluctuations while negative ones indicate a progressive damping.

Linearizing the Navier-Stokes Equations (LNSE) and keeping only first order terms, one gets the new set of equations presented here in the frequency space:

- Linearized mass conservation

$$-i\omega\hat{\rho} + \frac{\partial}{\partial x_i}(\overline{u}_i\hat{\rho} + \overline{\rho}\hat{u}_i) = 0 \tag{1.10}$$

- Linearized momentum conservation

$$-i\omega\overline{\rho}\hat{u}_i + \frac{\partial}{\partial x_j}(\overline{\rho u}_j\hat{u}_i) + \frac{\partial \overline{u}_i}{\partial x_j}(\overline{\rho}\hat{u}_j + \overline{u}_j\hat{\rho}) = -\frac{\partial \hat{p}}{\partial x_i} + \frac{\partial \hat{\tau}_{ij}}{\partial x_j} \tag{1.11}$$

- Linearized energy conservation

  In that case, the conservation of entropy s is generally preferred and is formally equivalent [35]:

$$-i\omega\hat{s} + \overline{u}_i\frac{\partial \hat{s}}{\partial x_i} + \hat{u}_i\frac{\partial \overline{s}}{\partial x_i} = \frac{r}{\overline{p}}\left[\left(\hat{\dot{\omega}}_T - \frac{\hat{p}}{\overline{p}}\overline{\dot{\omega}}_T\right) + \left(\overline{\tau}_{ij}\left(\frac{\partial \hat{u}_i}{\partial x_j} - \frac{\hat{p}}{\overline{p}}\frac{\partial \overline{u}_i}{\partial x_j}\right)\right) + \hat{\tau}_{ij}\frac{\partial \overline{u}_i}{\partial x_j}\right] \tag{1.12}$$

  with r the specific gas constant. For an ideal gas, entropy fluctuations are related to pressure and density fluctuations by:

$$\hat{s} = \frac{r}{\gamma - 1}\frac{\hat{p}}{\overline{p}} + \frac{\gamma r}{\gamma - 1}\frac{\hat{\rho}}{\overline{\rho}} \tag{1.13}$$

  where γ is the heat capacity ratio.

For acoustics studies, viscous effects are usually neglected and linearized Euler Equations (LEE) are used instead of LNSE. The RHS of Eq 1.11 and 1.12 is in this case further simplified by discarding all terms related to the viscous stress tensor τ_{ij}.

Equations 1.10 to 1.13 are solved for fluctuations $\hat{p}$, $\hat{u}_i$, $\hat{\rho}$, $\hat{s}$ assuming the mean reference quantities to be known. These latter are typically determined from RANS or LES computations averaged over time. The resolution of such a problem is only possible when closed using an acoustic model for the fluctuating heat release source term $\hat{\dot{\omega}}_T$. Such models are discussed in Sec. 1.4. When these linearized equations are used (LNSE or LEE), the mean flow has to be provided as said previously, but the actual resolution of the linearized problem can be performed on much coarser grids than the ones typically used in CFD computations. Indeed, the limiting factor for meshing is not the characteristic length of the flow anymore, but rather the acoustic wavelength λ, which is generally much larger, or $M\lambda$ if entropic waves are considered, M being the Mach number of the flow. This allows a considerable reduction of the computational power needed, or equivalently, to obtain results much faster with the same computational power compared to LES.

By construction, LNSE and LEE describe the propagation of vorticity, acoustic and entropy waves by a turbulent mean flow. As such, conversion of acoustic waves into entropy waves (through a choked nozzle for instance [65]) is retrieved. LNSE also accounts for the conversion of acoustics into vorticity at sharp edges [66]. Note however that the simplification induced by the harmonic decomposition of Eq. (1.9) does not distinguish turbulent fluctuations from acoustic ones. In that respect, very few studies make use of a triple decomposition (mean, coherent, stochastic parts) as proposed in [67] to include this missing effect. These approaches are however limited to non reactive studies as of now [68, 69]. Despite this limitation, LNSE have been shown to provide satisfactory results for academic configurations such as a 2D tube with a flame [36] or a 3D swirled burner [70]. Blanchard *et al.* [71] were able to reproduce the FTF of a laminar flame with a LNSE solver with reasonable agreement compared to experiments. LEE applications to the prediction of combustion instabilities are scarce and mainly focus on theoretical issues such as the influence of the mean flow on stability and non-normal interactions [35, 72]. In addition, numerical stability constraints require the use of artificial viscosity [40] which severely limits the interest of the method. Consequently, to this day and to the author's knowledge, the use of linearized equations for industrial geometries has never been done.

1.3.4 Helmholtz solvers

In numerous combustion applications, the mean flow velocity $\overline{u}$ is low compared to the mean sound speed $\overline{c}$. Further simplification of the LEE can thus be achieved by assuming a null Mach number $M = \overline{u}/\overline{c} = 0$. In this specific limit, the classical linear acoustics equations in the frequency domain are obtained. These are:

- Zero Mach number linearized mass conservation

$$-i\omega\hat{\rho} + \hat{u}_i \frac{\partial \overline{\rho}}{\partial x_i} + \overline{\rho}\frac{\partial \hat{u}_i}{\partial x_i} = 0 \tag{1.14}$$

- Zero Mach number linearized momentum conservation

$$-i\omega\hat{u}_i = -\frac{1}{\overline{\rho}}\frac{\partial \hat{p}}{\partial x_i} \tag{1.15}$$

- Zero Mach number linearized energy conservation
  The mean entropy conservation simplifies to:

$$\frac{\partial \overline{s}}{\partial t} = \frac{r\overline{\dot{\omega}}_T}{\overline{p}} = 0 \tag{1.16}$$

  Inserting Eq. (1.16) into Eq. (1.12) yields:

$$-i\omega\hat{s} + \hat{u}_i \frac{\partial \overline{s}}{\partial x_i} = \frac{r\hat{\dot{\omega}}_T}{\overline{p}} \tag{1.17}$$

  Noting that the mean momentum conservation equation reads:

$$\overline{\rho}\frac{\partial \overline{u}_i}{\partial t} = -\frac{\partial \overline{p}}{\partial x_i} = 0, \tag{1.18}$$

  and reintroducing it in the differential formulation of entropy for an ideal gas:

$$ds = \frac{r}{\gamma - 1}\frac{dp}{p} - \frac{\gamma r}{\gamma - 1}\frac{d\rho}{\rho}, \tag{1.19}$$

  one gets:

$$\frac{\partial \overline{s}}{\partial x_i} = -\frac{\gamma r}{(\gamma - 1)\,\overline{\rho}}\frac{\partial \overline{\rho}}{\partial x_i}. \tag{1.20}$$

  Finally, combining Eq. (1.13), Eq. (1.17) and Eq. (1.20) gives the more traditional energy conservation for zero Mach number flows:

$$\hat{u}_i \frac{\partial \overline{\rho}}{\partial x_i} = -\hat{\dot{\omega}}_T \frac{\overline{\rho}\,(\gamma - 1)}{\gamma \overline{p}} - i\omega\left(\frac{\hat{p}}{\overline{c}^2} - \hat{\rho}\right). \tag{1.21}$$

Conservation equations of mass (Eq. (1.14)) and energy (Eq. (1.21)) can then be joined to yield:

$$-i\omega\frac{\hat{p}}{\gamma\overline{p}} + \frac{\partial \hat{u}_i}{\partial x_i} = \frac{\gamma - 1}{\gamma\overline{p}}\hat{\dot{\omega}}_T. \tag{1.22}$$

Finally, taking the time derivative of Eq. (1.22) and subtracting the spatial derivative of the momentum conservation equation, Eq. (1.15), provides the so-called Helmholtz equation for pressure:

$$\frac{\partial}{\partial x_i}\left(\frac{1}{\overline{\rho}}\frac{\partial \hat{p}}{\partial x_i}\right) + \omega^2\frac{\hat{p}}{\gamma\overline{p}} = i\omega\frac{\gamma - 1}{\gamma\overline{p}}\hat{\dot{\omega}}_T. \tag{1.23}$$

The Helmholtz equation is the equivalent of the classical wave equation in the frequency domain without mean flow. It describes the propagation of acoustic waves without mean flow effects and in the absence of viscous dissipation. Helmholtz solvers solve a discretized version of this equation on multi-dimensional grids. Just like for LNSE or LEE, coarser grids can be used compared to LES, with the additional advantage of a single equation to be solved instead of a set of coupled ones. Moreover, only fields of mean density $\overline{\rho}$ and heat capacity ratio γ (or equivalently for a perfect gas mixture the mean sound speed $\overline{c}$) are needed as input. Note however that when combustion is considered, an additional model for the unsteady heat release source term $\hat{\dot{\omega}}_T$ appearing in Eq. (1.23) is required.

The term on the RHS of Eq. (1.23) vanishes when no combustion is considered. In that case, and if only simple boundary conditions are used (zero acoustic pressure $\hat{p} = 0$ or normal velocity $\hat{u}$=0), discretizing Eq. (1.23) leads to a linear sparse eigenvalue problem. The resolution of such problems can be performed with known algorithms [73, 74, 75] that can be massively parallelized on multi-processor systems. When combustion is considered, or when more complex boundary conditions are used, the eigenproblem is not linear anymore with respect to frequency and needs to be solved using more advanced techniques. Using fixed point algorithms [43] is probably the most intuitive approach.

Helmholtz solvers have been successfully employed using a linear modelling of the acoustic flame response for the prediction of combustion instability on academic cases [43, 76, 77] as well as for complex industrial configurations [41]. Few works have even included a nonlinear description of the flame in an effort to reproduce limit cycle oscillation amplitudes [44, 45, 46].

These reduced order codes are also convenient for their robust handling of boundary conditions through the use of complex impedances, Z, defined by:

$$Z = \frac{\hat{p}}{\overline{\rho c}\hat{\mathbf{u}}.\mathbf{n}}, \tag{1.24}$$

where $\mathbf{n}$ is the boundary normal. These impedances can be used to reintroduce back some of the information lost when linearizing the equations. For example, the acoustic damping created by conversion into vorticity through perforated plates [78], or even mean flow effects due to the propagation of both acoustic and entropy waves [79, 80].

1.3.5 Low order models

Helmholtz solvers make use of finite elements or finite volumes method to solve a spatially discretized version of the acoustic problem. Computational costs associated to these computations can still be prohibitive for parametric design studies due to the large number of degrees of freedom considered. In an effort to circumvent this issue, numerous

groups have developed Low Order Models (LOM) to allow for very cheap combustion instability studies. LOM aim at providing a framework where a limited number of degrees of freedom is used, allowing to quickly perform geometrical or physical parameter modifications. They can also be used to gain insight on results obtained with LES or experiments. Successful applications of LOM include highly intensive Monte-Carlo computations for uncertainty quantifications [27, 81], sensitivity analyses [38], and shape optimization for passive control [82]. Thermoacoustic LOM can be organized in two main categories;

- **Acoustic networks**: geometries are split into a set of one-dimensional acoustic elements where mean properties (density, heat capacity ratio, sound speed, mean flow velocity) are constant. Here, the acoustic pressure fluctuation in the temporal domain is noted p'. In each element, the wave equation hence reads:

$$\left(\frac{\partial}{\partial t} + \overline{\mathbf{u}}.\frac{\partial}{\partial x}\right)^2 p' - \overline{c}^2 \frac{\partial^2 p'}{\partial x^2} = 0, \tag{1.25}$$

  the solution being the sum of two planar waves A^+ and A^- travelling in opposite directions with speeds $\overline{c} + \overline{u}$ and $\overline{c} - \overline{u}$ respectively. In the zero Mach number limit, acoustic pressure p' and velocity u' are then written as:

$$p'(x,t) = A^+(t - x/\overline{c}) + A^-(t - x/\overline{c}) \tag{1.26}$$

$$u'(x,t) = \frac{1}{\overline{\rho c}}\left[A^+(t - x/\overline{c}) - A^-(t - x/\overline{c})\right] \tag{1.27}$$

  Elements are then connected together using jump conditions for acoustic pressure and velocity [13] describing the mean field changes, section changes, or the presence of a flame (modelled as a velocity source term between two elements). Together with boundary conditions, the system of N_{eq} equations can be recast into matrix form. The eigenfrequencies are then determined by finding values of angular frequencies ω for which the corresponding determinant is nullified. Acoustic mode shapes are then retrieved by solving the linear system.

  Network methods have been successfully applied either in the frequency domain assuming a linear flame response [83, 84, 85] as well as in time with a nonlinear flame description [86, 87, 88], with few examples for a swirled combustor [89]. Some codes such as the Oscilos LOM from Imperical College London are even open source [90]. The one-dimensional approach has also been generalized to more complex geometries such as industrial annular combustors [83], or a plenum-burners-chamber complex system [85, 91]. By construction, acoustic networks are very fast but cannot describe acoustic modes involving three-dimensional features.

- **Galerkin based methods**: This type of method solves the wave equation with a source term in the temporal domain or in the frequency domain (just like Helmholtz solvers), here written under the zero Mach number assumption:

$$\nabla^2 p' - \frac{1}{\bar{c}^2}\frac{\partial^2 p'}{\partial t^2} = (\gamma - 1)\frac{\partial \dot{\omega}'_T}{\partial t}, \tag{1.28}$$

along with complex boundary conditions of the general form:

$$\nabla p'.\mathbf{n} = -f, \tag{1.29}$$

where f is any general function of time and space. This approach further relies on a modal expansion of the acoustic pressure and velocity fields on a family of known orthogonal acoustic modes $\Psi_k(x)$ solution of Eq. (1.28) with no RHS;

$$p'(x,t) = \sum_{k=1}^{N} \Gamma_k(t)\Psi_k(x), \tag{1.30}$$

where $\Gamma_k(t)$ are the complex valued and time dependent coefficients of the modal expansion. Classically these modes also verify Eq. (1.29) with $f = 0$ or $f = j\omega a$ with a a real number. Inserting Eq. (1.30) in Eq. (1.28) and Eq. (1.29) and integrating over the volume yields a system of second order differential equations not shown here for the sake of brevity but presented in [92] for instance. These allow the resolution of the problem. Once again, when a flame is considered in one of the sub-domains, an appropriate modelling is needed for the combustion source term $\dot{\omega}'_T$.

First examples of modal expansion in the field of thermoacoustics were dedicated to the study of combustion instabilities in liquid rocket engines [93, 94]. Further studies were then conducted on canonical configurations [95, 96], annular combustors [86, 97], and even chamber-plenum geometries [98, 99, 100]. Standard modal expansions make use of acoustic modes with rigid-wall (null normal velocity), which may require a large number of modes to converge when boundary conditions are not close to this state (opening to the atmosphere for example) [21]. Recent works [92] show that using overcomplete frames with appropriate numerical techniques may help circumventing this issue. Contrarily to acoustic networks, Galerkin methods are more general and can be used to describe complex 3D configurations. One drawback however lies in the fact that large modal bases may be necessary and have to be computed using Helmholtz solvers for instance for three-dimensional problems.

Note finally that Galerkin and acoustic network methods can be combined to retain the best of each strategy. In this view, simple one-dimensional acoustic propagation

can be modelled using Riemann invariants A^+ and A^- while modal expansion can be used in more complex geometries. Whenever applicable, each decomposition can be applied to the system sub-domain of interest, the total number of degrees of freedom being limited and the full three-dimensional description still being used only in key areas. This method was successfully employed in [101] to model an annular chamber with multiple burners that may not all be equivalent, or in [102, 103] where acoustics in a plenum and a combustion chamber are resolved using a Galerkin expansion while acoustic propagation in burners is assumed to be fully one-dimensional.

1.4 Modelling the flame in acoustic calculations

1.4.1 Flame transfer functions

In the remaining of the manuscript, the term "Reduced Order Model" (ROM) is used to qualify the concatenation of LNSE/LEE, Helmholtz solver and LOM approaches, signifying that such methods feature reduced orders of accuracy compared to LES. In LES, the heat release from the flame is determined thanks to models describing the chemical reactions taking place inside and outside the flame front. All ROM have in common that the fluctuating heat release source term $\dot{\omega}'_T$ (Eq. (1.28)) or equivalently in the frequency domain $\hat{\dot{\omega}}_T$ (Eq. (1.13) and (1.23)) is not resolved, but modelled. Heat release rate perturbations are the driving source of combustion instabilities and cannot simply be neglected. Modelling the flame as an acoustic element allows to completely discard the complexity of chemical kinetics while still considering unsteady effects. This step is essential to produce accurate and relevant predictions by use of ROM.

The classical modelling element employed to describe the flame response to perturbations is the Flame Transfer Function (FTF) which links incoming perturbations to resulting global heat release rate fluctuations $\hat{Q}$ defined as $\hat{Q} = \int_{V_f} \Lambda \hat{\dot{\omega}}_T dV$ where Λ is a multiplication factor depending on the exact equation to be solved. For a perturbation of a given quantity, noted hereafter a (velocity, pressure, equivalence ratio, *etc*), the transfer function is defined in the frequency domain as:

$$\mathcal{F}(\omega) = \frac{\hat{Q}}{\overline{Q}} . \frac{\overline{a}}{\hat{a}} \tag{1.31}$$

When it comes to thermoacoustic studies, the perturbing variables are generally the velocity u, or the equivalence ratio ϕ for non fully premixed flames. The most simple and widespread FTF model is the one proposed by Crocco [37], formally known as the '$n - \tau$' model. The idea of Crocco was simple: a velocity perturbation at a given location x_{ref} propagates at the sound speed c and takes a time τ (which also potentially accounts for a chemical time or a vortex formation time for instance) to reach the flame and burn, generating an unsteady heat release amplified by a factor n with respect to the

original velocity fluctuation amplitude, Fig. 1.13. The original model of Crocco assumed

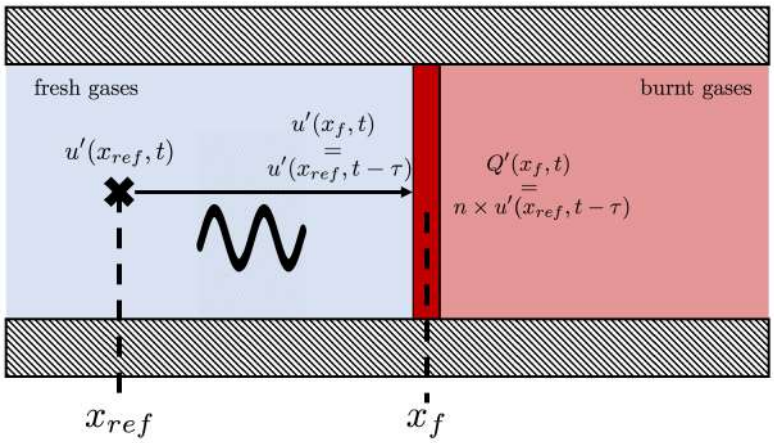


Figure 1.13: Schematic diagram of the Crocco n − τ model principle. The velocity perturbation at x_{ref} takes a time τ to reach the flame front at position x_f and burn with an amplification factor n.

a compact flame, that is a flame with geometrical extension L_f much smaller than the acoustic wavenumber $k = \omega/\overline{c}$ and a constant time delay across the whole frequency range. In the generalized version of the $n - \tau$ model, the FTF is often expressed in terms of a frequency dependent gain $G(\omega)$ and a phase $\varphi(\omega)$ (or time delay $\tau(\omega)$) [17]:

$$\mathcal{F}(\omega) = G(\omega)e^{i\varphi(\omega)} = G(\omega)e^{i\omega\tau(\omega)}. \tag{1.32}$$

A first option to determine the gain and phase of a FTF is to perform experimental studies. Examples can be found in the literature for laminar flames [104], laboratory scale swirling flames [105, 106, 107, 108], and more rarely for full annular combustors [100]. In real engines however, there is limited if no optical access, and sensors cannot be placed close to the high power flames.

As an alternative, numerical simulations can be used to predict the forced flame response, and thus FTF. Few examples rely on unsteady RANS simulations [109, 110], and the majority on LES [111, 112, 113, 114]. In some cases, a broadband forcing combined with system identification techniques [115] can be used to retrieve the FTF using a limited set of LES. In the general case however, and especially for turbulent flames in complex geometries as encountered in gas turbines, a significant number of single frequency forced simulations has to be performed if one wants to cover the frequency range of interest. As a direct consequence, performing high fidelity simulations to feed ROM essentially moves the numerical cost issue from one perspective to another.

Reducing the overhead cost associated to numerical simulations to predict combustion instabilities is the critical element for application to real engine design. Less

computationally intensive approaches have thus been explored, such as a level-set tracking of the flame front [71, 116, 117, 118]. Semi-analytical models can even be obtained when starting from a level-set description and adding a few simplifying assumptions. Such analytical models will be detailed in Chap. 2. These constitute the only substantial option that does not compromise the objective of fast computations required to enable parametric studies of engine thermoacoustic stability. Analytical FTF models are therefore the main object of interest in this manuscript.

1.4.2 Extensions of the FTF formalism

A FTF characterizes the flame frequency response to vanishingly small acoustic perturbations. This modelling allows to predict the linear stability of modes (see Fig. 1.8) but cannot capture the limit cycle appearing in the nonlinear regime. To circumvent this issue, the FTF method can be extended to the Flame Describing Function (FDF) formalism [119], which introduces the amplitude of the incoming perturbation as an additional parameter:

$$\mathcal{F}(\omega, |\hat{u}/\overline{u}|) = G(\omega, |\hat{u}/\overline{u}|) \exp\left(i\varphi(\omega, |\hat{u}/\overline{u}|)\right) \tag{1.33}$$

As a result, a FDF is essentially a collection of FTF obtained for different acoustic perturbation amplitudes. Coupled to Helmholtz computations, the FDF description was shown to retrieve experimentally observed limit cycle behaviours for fully premixed swirled flames [44], partially premixed swirled flames [120] and an annular combustor with multiple injectors[46].

Another acoustic model for flames, is the Flame Transfer Matrix (FTM). This approach assimilates the flame to a compact interface with jump conditions relating pressure and velocity on its upstream (noted $|_u$) and downstream (noted $|_d$) sides:

$$\begin{bmatrix} \hat{p}|_d \\ (\overline{\rho c}\hat{u})\,|_d \end{bmatrix} = \mathbb{T}_{flame} \begin{bmatrix} \hat{p}|_u \\ (\overline{\rho c}\hat{u})\,|_u \end{bmatrix} \tag{1.34}$$

with $\mathbb{T}$ the flame transfer matrix. As for the FTF, the FTM can be measured with experiments or numerical simulations [121]. It is especially well adapted to longitudinal configurations. Note that FTF and FTM methods are formally equivalent when the FTF reference location is chosen close enough to the flame [122]. See also [123] for an extension of these concepts to include the forcing level.

Finally, it is worth mentioning that with the rise of artificial intelligence/machine learning based modelling, a neural network representation of the flame acoustic response could be considered in a near future, as already done for the prediction of subgrid scale reaction rates for LES [124].

1.5 Swirling flame transfer functions

In industrial gas turbines, flames are highly turbulent and stabilized by a swirling flow. The injector imparts a rotating motion to the fresh gases so that combustion occurs around an inner hot gas recirculation zone that helps anchoring the flame in the vicinity of the injection feed. If the flame is confined, outer recirculation zones also appear on the outskirts of the flame branches, Fig. 1.14a. The swirl number S is generally used to characterize the rate of rotation of the flow and is defined as the ratio between the angular momentum flux G_θ and the axial momentum flux G_x projections along the axial direction. Neglecting the pressure term contribution, as often done in the literature, it reads [125, 126]:

$$S = \frac{G_\theta}{R_0 G_x} = \frac{1}{R_0} \frac{\int_0^{R_0} \rho u_x u_\theta r^2 dr}{\int_0^{R_0} \rho u_x^2 r dr}, \tag{1.35}$$

where u_x and u_θ are the axial and tangential velocities in cylindrical coordinates and R_0 is a characteristic dimension, usually the outer radius of the injection device. When the swirl number is increased, the increased tangential momentum flux produces a wider IRZ, Fig. 1.14b. The rotating motion is generally imposed either by forcing the flow

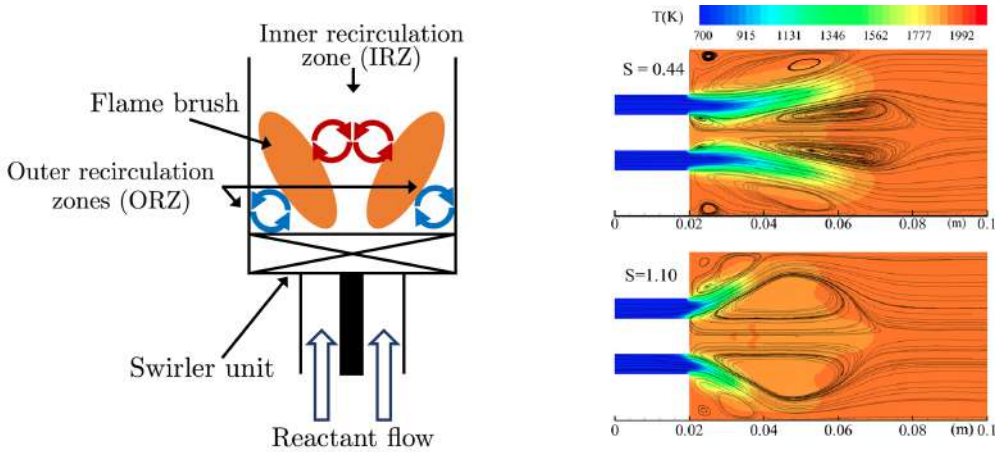
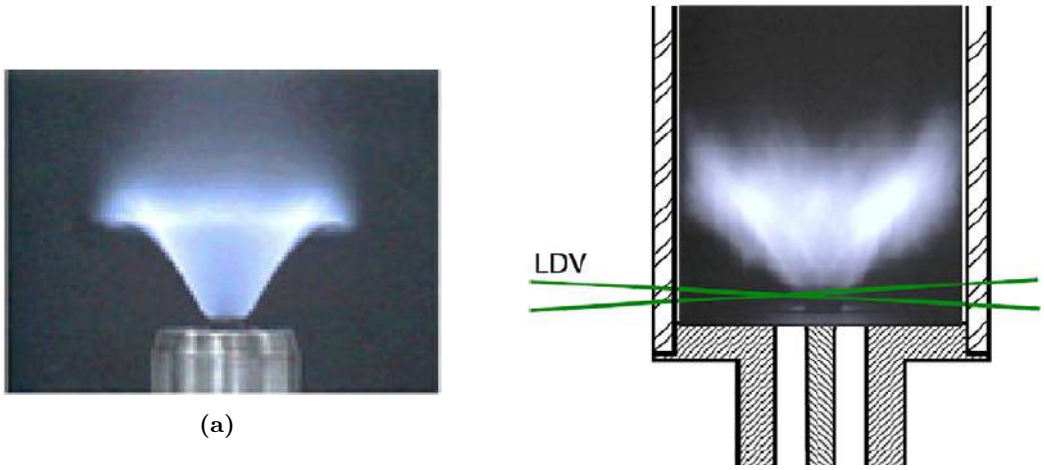


Figure 1.14: (a) Schematic representation of a swirling flame with inner and outer recirculation zones (b) LES mean temperature fields and streamline patterns for two different swirl numbers, reproduced from [125].

through tilted blades (axial swirler), or by changing its direction and guiding it through radial channels (radial swirler).

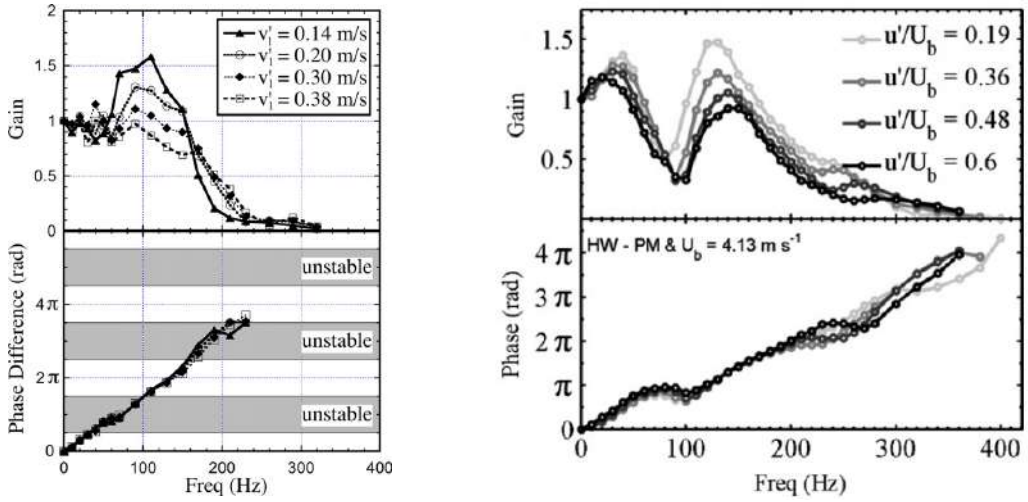
Examples of laminar and swirling V-shaped flames as visualized during experiments are presented in Fig. 1.15. The addition of swirl modifies the frequency dependency of the flame response to acoustics, as shown in Fig. 1.16 for inverted conical (or V-shaped) flames. The typical FDF gain of a laminar non-swirling V-shaped flame presents above



(a) (b)

Figure 1.15: (a) Typical laminar V-shaped flame, reproduced from [127] and (b) typical swirling V-shaped flame, reproduced from [128].

unity values for a large low frequency range and generally behaves as a low-pass filter for higher frequencies [127]. The corresponding FDF phase is linear. Contrarily, the FDF of a swirling flame anchored on a bluff-body (Fig. 1.16b) presents local minima in between maximum gains [89, 106]. In addition, the phase curves exhibit inflection points around frequencies corresponding to the local gain minima.



(a) (b)

Figure 1.16: (a) Experimental FDF of a fully premixed non-swirling laminar V-shaped flame, extracted from [127] and (b) experimental FDF of a fully premixed swirling flame, extracted from [89]. Both flames are anchored on a bluff-body.

Differences between the response of swirling and non-swirling flames stem from fundamental mechanisms associated to acoustics/vorticity conversion through swirlers

and flame/vortex interactions [51, 126, 129]. These aspects will be further discussed in Chap. 2. Lastly, note that the behaviour of both swirling/non-swirling flames is modified when increasing the acoustic perturbation amplitude, with a decrease of the global gain levels. Interestingly, phase curves remain unchanged with stronger forcing amplitudes.

FTF/FDF of swirling flames have been determined experimentally [105, 106, 107] as well as with numerical simulations [112, 113, 114, 130, 131]. While the effects of swirl are inherently accounted for in experiments or LES, they need special treatment to be accounted for in cheaper alternatives such as analytical formulations. This point is addressed in details in Chap. 2.

1.6 Thesis objectives and outline

Achieving accurate, yet fast combustor stability predictions constitutes the next step for numerical methods to be effectively used in a conception context for lean combustion technological solutions. In regard of existing modelling strategies, a stability mapping of a given engine can only be obtained using ROM. This means that accuracy will rely on the acoustic description of the flame, often chosen to be recast into a FTF or a FDF formalism. In any case, obtaining FTF/FDF data from experiments or costly CFD simulations does not cope with the fast prediction requirements and hence, there is an essential need for fast qualitative modelling.

In this context, this PhD thesis funded by Safran Aircraft Engines has the long-term objective of creating fast and reliable combustion instability predicting tools for the design of the next generation of low emission aeronautical gas turbines. This thesis therefore establishes a first step towards this goal and focuses on the derivation and application of semi-analytical FTF models based on a concise description of key mechanisms responsible for the flame response. In particular, the response of premixed V-shaped swirling flames is investigated both from a theoretical point of view and using numerical simulations. Accordingly, three main objectives are as follows:

- Propose analytical formulations for the FTF of swirling flames as encountered in real gas turbines. Although a few derivations exist for laminar flames, the case of turbulent swirling flames is still insufficiently documented.

- Assess the capabilities and range of application for the proposed models. These should ideally be robust and cover a range of injector/burner geometries. Other questions also need to be answered: can the model reproduce nonlinear features ? could it be extended to two-phase flow flames ?

- Confirm the ability of the acoustic modelling chain, with a FTF determined from forced LES coupled to Helmholtz computations, to predict combustion instabilities. To do so, the AVBP LES solver and the AVSP Helmholtz solver are used in a joint study.

The manuscript is organized as follows. Chapter 2 details the current state in regard to analytical FTF models for premixed flames, with emphasis on swirling flows. Building upon a previous work from Palies *et al.* [128], an analytical model for V-shaped premixed swirling flames is then proposed. This model, denoted as the SFTF model, depends on six parameters, three of which describe the laminar flame response, while the three remaining ones take into account the effect of swirl.

The proposed methodology is applied to a laboratory scale premixed swirl stabilized flame exhibiting features representative of real aero-engines in Chap. 3. The discussion then focuses on an efficient procedure to evaluate these parameters based on a reduced set of LES. For this case, cold and reactive flow LES are performed, and three distinct approaches of increasing complexity are presented for the determination of the SFTF model parameters. A first estimation of the flame acoustic response is obtained by evaluating parameters from a single unperturbed flame simulation. Flame dynamics and swirl related parameters are then determined from a series of robust treatments applied on pulsed simulation data to improve the model accuracy. Overall, a good qualitative agreement is obtained compared to reference data, and the modelling strategy is shown to naturally handle different perturbation levels. Thanks to the obtained database, the complex swirling flow and flame dynamics are investigated for frequencies corresponding to local minimum and maximum FTF gains (Fig. 1.16b).

Finally, LES and Helmholtz computations are performed on a real annular industrial combustor in Chap. 4 in order to determine its thermoacoustic stability. All aspects of the modelling chain detailed previously are investigated to determine the best strategies for a reliable FTF appraisal when carrying out LES. The applicability of the SFTF model is also gauged and indicates that further modelling is needed to handle features out of the scope of the initial model derivation. Despite this natural limit, the LES acquired FTF is used as an input to Helmholtz computations. An unstable mode at a frequency close to the one observed during engine test sessions is retrieved.

Chapter 2

Premixed swirling V-shaped flames acoustic response modeling

Contents

2.1 FTF of laminar V-shaped premixed flames 29
2.1.1 Early studies 29
2.1.2 G-equation description of flame wrinkling 31
2.1.3 G-equation based FTF models 34
2.1.4 About the time domain representation of FTF 39
2.2 Dynamics of forced swirling flames 40
2.2.1 Acoustic-vorticity conversion through a swirler 41
2.2.2 Swirl fluctuations impact on the flame response 43
2.3 Modelling of premixed swirling FTF 45
2.3.1 A baseline model for swirling flames FTF 45
2.3.2 The SFTF model 47

2.1 FTF of laminar V-shaped premixed flames

2.1.1 Early studies

The flame response to acoustic waves is often characterized by the FTF presented in Eq. (1.32). This "black-box" modelling does not a priori indicate what the phenomena responsible for the flame unsteady heat release fluctuations precisely are. Studies on laminar flames have demonstrated the FTF dependency on several aspects:

- burner/injector geometry [132],
- mean flow properties (mean velocity, mean density jump across the flame sheet for instance) [133],
- heat transfer [52],
- flame shape [134],
- acoustic modulation amplitude [134, 135],

to name the most obvious ones. In a turbulent flame, all these features can interact with each other, making the underlying physical mechanisms harder to identify. Despite this observation, first attempts to parametrize a FTF as a function of a small set of input parameters were historically derived for liquid-fueled rocket engines [37, 136], as there was an essential need to mitigate combustion instabilities observed in such devices at the time. The semi-empirical nature of the derived transfer functions and the large set of parameters used restrain their use to designs close to the one they were originally developed for. In particular, the accuracy of predicted FTF gain and phase is highly conditioned by the choice of quantities identified to be "representative of the system".

From then on, laminar flames have been a subject of choice for the understanding of flame/acoustics coupling in general and the derivation of analytical formulations for FTF. Theoretical attempts to derive non-empirical FTF gains and time delays are numerous for laminar conical flames [104, 137, 138]. The case of inverted conical flames, that will be denoted as V-shaped flames in the following, is slightly less documented. In [139], Marble and Candel study the unsteady behaviour of a V-shaped flame stabilized by a flame holder at the center of a long two-dimensional duct, and submitted to a uniform velocity perturbation, Fig. 2.1. Their analytical analysis considers both

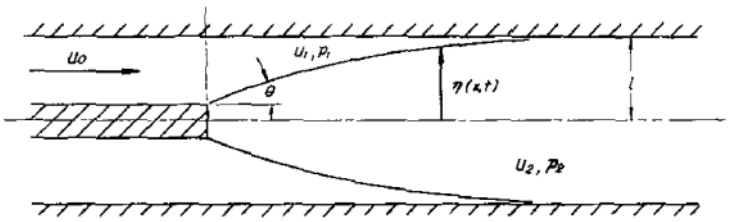
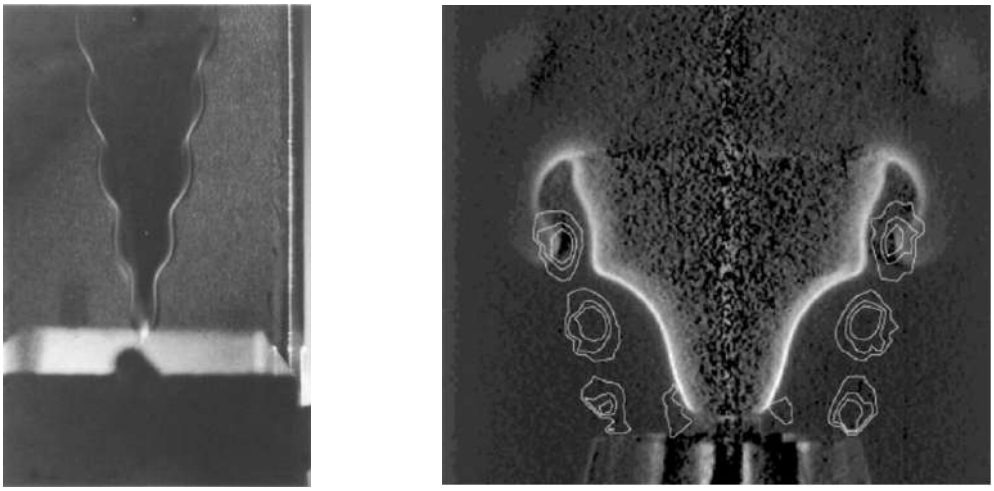


Figure 2.1: Geometry of the ducted V-shaped flame considered by Marble and Candel, reproduced from [139].

upstream and downstream acoustic waves, and the problem is treated using an integral technique for separated cold and hot sides with a matching condition at the thin flame front interface assumed to be infinitely thin. They conclude that very large responses of the flame are observed for particular frequencies corresponding to well-defined values of a dimensionless parameter $\omega L_f/\overline{v}$, L_f being the characteristic flame length. They attribute this preferential response to vorticity shed from the distorted flame inducing a convective wave propagating along the flame front. This convective wave was also observed when applying a low-frequency modulation to laboratory premixed flames, Fig. 2.2a. In the case of non-ducted flames, vorticity generation at the edges of the burner rim was also shown to perturb the flame surface, Fig. 2.2b. This work was then extended in [141] by considering an incompressible flow upstream of the flame.

Later, Bloxsidge *et al.* [142] conducted a series of experiments to study the same ducted flame response. The general trends observed in the experiments were used to



(a) (b)

Figure 2.2: (a) Tomographic cut of a premixed laminar V-shaped flame forced with amplitude $\hat{v}/\overline{v} = 9\%$ at f = 22.6 Hz, extracted from [140] (b) Instantaneous unsteady vorticity field and flame front location of a forced laminar premixed flame, $\hat{v}/\overline{v} = 8\%$, f = 150 Hz, from [127].

derive an empirical FTF model, which matched the experimental result for the few configurations considered. As noted by Dowling [135], in the low frequency range, the empirical FTF reduces to a simple low pass filter:

$$\mathcal{F}(\omega) = \frac{1}{1 + i\omega\tau_1} \tag{2.1}$$

where

$$\tau_1 = \frac{2\pi a}{\overline{v}} \tag{2.2}$$

with a the radius of the central bluff-body piece and $\overline{v}$ the mean velocity in the incoming flow at the gutter. Arguably, one drawback of such a model is the need for experiments to calibrate it outside of the low frequency range, with a priori no further indication that the resulting FTF could be transposed to different geometries.

2.1.2 G-equation description of flame wrinkling

Here we introduce the standard geometry for a premixed laminar V-shaped flame anchored on a central bluff-body piece. A complete schematic overview of the configuration is displayed in Fig. 2.3. The flame is assumed to be perfectly axisymmetric, anchored on a central bluff-body at radial position $x = a$ and extending to a radial position $x = b$ so that the mean flame radius is $R_f = b - a$. The half-flame opening angle with respect to the vertical axis y is noted α. A second reference coordinates frame is defined from the mean flame front position with axes X and Y. In this new frame, the projected velocity components are noted (U, V). Local flame wrinkling is assumed to

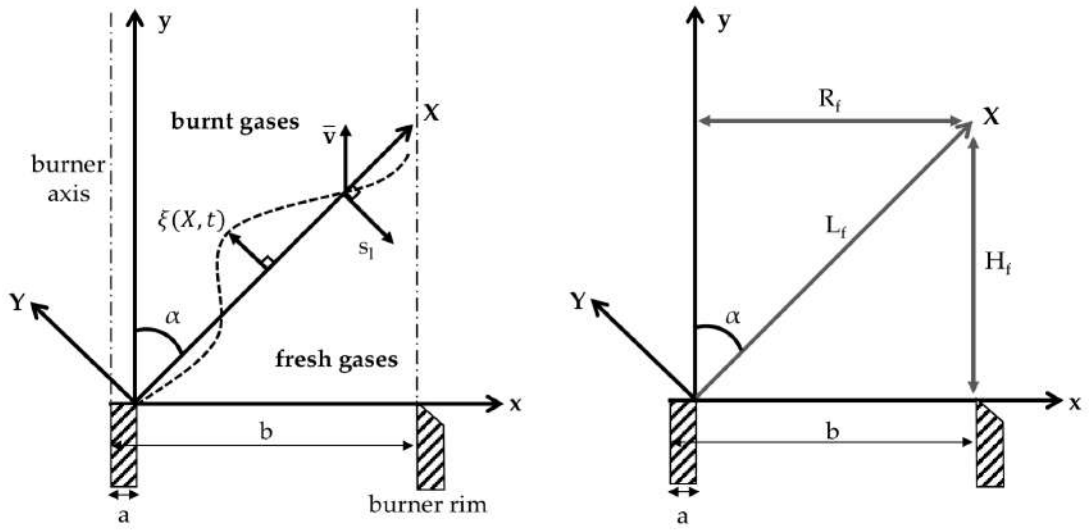


Figure 2.3: Schematic of the studied laminar premixed V-shaped flame configuration. Reference frame axes are noted x and y while a second frame directly linked to the steady flame has axes X and Y, see [143]. The steady flame is aligned on the X axis, is anchored on a rod at position a and extends to a radial abscissa x = b which may not be a wall. Definitions of the flame length $\mathbf{L_f}$, flame height $\mathbf{H_f}$ and flame radius $\mathbf{R_f}$ are provided on the right

occur around this mean position which does not change when acoustic forcing is applied, which translates for a premixed flame to only considering linear acoustics [144]. The unsteady displacement of the flame around its mean position is noted ξ, and can conveniently be parametrized in each of the reference frame to ease calculations (see [143]).

In the following, all theoretical derivations make use of a level-set description of the flame known as the G-equation to track the perturbed flame front surface. In this view, the flame front is represented as an infinitely thin interface separating fresh and burnt gases, with a scalar G so that $G(x,t) = 0$ effectively describes its position [145, 146]. The G-equation for a premixed laminar flame is here expressed as:

$$\frac{\partial G}{\partial t} + \mathbf{v}.\nabla G = S_d|\nabla G| \tag{2.3}$$

where S_d is the flame displacement speed that is asssumed to correspond to the laminar burning velocity S_l, and the velocity field $\mathbf{v}$ can be decomposed as the sum of a uniform mean axial component and acoustic perturbations:

$$\mathbf{v}(\mathbf{x},t) = u'(\mathbf{x},t)\mathbf{e_x} + (\overline{v} + v'(\mathbf{x},t))\mathbf{e_y}. \tag{2.4}$$

Equivalently, the velocity field in the frame attached to the steady flame front is:

$$\mathbf{V}(\mathbf{X},t) = \left[\overline{U} + U'(\mathbf{X},t)\right]\mathbf{e_X} + \left[\overline{V} + V'(\mathbf{X},t)\right]\mathbf{e_Y} \tag{2.5}$$

with $\overline{U} = \overline{v}\cos\alpha$ the mean flow velocity component tangential to the flame front, and $\overline{V} = \overline{v}\sin\alpha$ its normal counterpart. In the frame linked to the steady flame position, the unsteady flame displacement can easily be linked to the scalar G:

$$G = Y - \xi(X,t) \tag{2.6}$$

The constant flame speed assumption then allows to reduce Eq. (2.3) to a simple expression:

$$\frac{\partial \xi}{\partial t} + \overline{U}\frac{\partial \xi}{\partial X} = V'(X,t) \tag{2.7}$$

with $\xi(X,t) = \hat{\xi}(X)e^{-i\omega t}$ the harmonic flame front perturbation in the normal direction with respect to the steady flame front. The general solution of this equation can be found using the characteristics method, or can conveniently be expressed by a telegraph integral as proposed in [140]:

$$\xi(X,t) = \frac{1}{\overline{U}}\int_0^X V'\left(X', t - \frac{X-X'}{\overline{U}}\right)dX' + \xi\left(0, t - \frac{X}{\overline{U}}\right) \tag{2.8}$$

The first term on the RHS of Eq. (2.8) corresponds to a forcing term describing the convection of the perturbation at the mean tangential flow speed $\overline{U}$ along the flame front, while the second term describes the displacement at the base of the flame. Since in this work the flame is assumed to remain anchored on a bluff-body, this second term vanishes, and the equation is recast in the frequency domain:

$$\hat{\xi} = \frac{e^{i\frac{\omega}{\overline{U}}X}}{\overline{U}}\int_0^X \hat{V}(X')e^{-i\frac{\omega}{\overline{U}}X'}dX' \tag{2.9}$$

The unsteady flame displacement $\hat{\xi}$ constitutes the basis of all G-equation based analytical formulations for laminar premixed flames transfer functions. Indeed, under the flamelet assumption, the heat release rate per unit volume Q is expressed as:

$$Q = \rho S_l A_f Q_f \tag{2.10}$$

with A_f the specific flame flame surface area, ρ the unburnt mixture density and Q_f the heat of reaction per unit mass of reactant. Linearizing this equation for vanishingly small perturbations, one gets:

$$\frac{\hat{Q}}{\overline{Q}} = \frac{\hat{\rho}}{\overline{\rho}} + \frac{\hat{S}_l}{\overline{S}_l} + \frac{\hat{A}_f}{\overline{A}_f} + \frac{\hat{Q}_f}{\overline{Q}_f} \tag{2.11}$$

The first term on the RHS, $\hat{\rho}/\overline{\rho}$, takes small values for low acoustic perturbation amplitudes. The G-equation is derived here for a constant flame speed S_l so that the second term is not considered. Finally, for a fully premixed mixture, the term $\hat{Q}_f/\overline{Q}_f$ further vanishes. Hence, under these assumptions, fluctuations of heat release rate $\hat{Q}$

are directly tied to flame surface variations $\hat{A}_f$. The FTF from Eq. (1.31) is then recast as:

$$\mathcal{F}(\omega) = \frac{\hat{Q}}{\overline{Q}}\frac{\overline{v}}{\hat{v}} = \frac{\hat{A}_f}{\overline{A}_f}\frac{\overline{v}}{\hat{v}} \tag{2.12}$$

Therefore, obtaining an analytical FTF model is conditioned by the determination of the unsteady flame surface $\hat{A}_f$. For a V-shaped flame and noting $\hat{dl}$ the instantaneous flame element along the X axis, the instantaneous flame surface differential element is $d\hat{A}_f = 2\pi x d\hat{l} = 2\pi x d\hat{\xi}/\tan\alpha$. The total unsteady flame surface is retrieved by integration:

$$\hat{A}_f = \frac{2\pi}{\tan\alpha}\int_a^b x\frac{\partial\hat{\xi}}{\partial x}dx \tag{2.13}$$

Integrating Eq. (2.13) by part, and noting that the flame is anchored at position a, $\hat{\xi}(a) = 0$, it becomes:

$$\hat{A}_f = \frac{2\pi}{\tan\alpha}b\hat{\xi}(R) - \int_0^R \hat{\xi}(x')dx'. \tag{2.14}$$

The steady axisymmetric flame surface area $\overline{A}_f$ is given by:

$$\overline{A}_f = \pi\frac{b^2 - a^2}{\sin\alpha} \tag{2.15}$$

Ultimately, $\hat{A}_f$ and thus the analytical FTF can be fully characterized provided that an analytical expression is available for $\hat{\xi}$ as defined in Eq. (2.9). One must therefore provide an expression for the perturbed velocity field $(u'(\mathbf{x},t), v'(\mathbf{x},t))$, or equivalently in the steady flame reference frame, for $(U'(\mathbf{X},t), V'(\mathbf{X},t))$.

2.1.3 G-equation based FTF models

The vast majority of analytical FTF rely on the G-equation formalism presented in the previous paragraph. Fleifil *et al.* [147] were the first to introduce its use to describe the unsteady response of an elongated conical flame attached to walls in a duct. They considered a uniform harmonic velocity perturbation, $\hat{u} = 0$ and $\hat{v} = v_1$ as well as a radially non uniform one $\hat{v} = v_1(x)$. The same procedure was later adapted by Dowling *et al.* [148] to extend the modelling to an axisymmetric turbulent V-shaped flame stabilized on a centre-body. After some calculus and assuming a small uniform axial disturbance, the FTF is shown to depend on a single parameter ω_* defined by:

$$\omega_* = \frac{\omega(b-a)}{S_l\left(1 - S_l/\overline{v}\right)^{1/2}} \tag{2.16}$$

In the low frequency limit, the analytical FTF of Dowling *et al.* [148] resumes to a second order low pass filter:

$$\mathcal{F}(\omega_*) = \frac{1}{1 + i\omega_*\tau_{2*} + (i\omega_*)^2\tau_{2*}\tau_{3*}} \tag{2.17}$$

where

$$\tau_{2*} = \frac{(2b+a)}{3(b+a)} \tag{2.18}$$

$$\tau_{3*} = \tau_{2*}\frac{7b^2+4ab+a^2}{4(2b+a)^2} \tag{2.19}$$

with S_l the flame speed. Note that for small $\omega_*\tau_{2*}$, Eq. (2.17) reduces to the first order law of Eq. (2.1). With the notations of Fig. 2.3, and introducing the characteristic dimension $R = b - a$, Eq. (2.16) can be rewritten as:

$$\omega_* = \frac{\omega R}{S_l \cos\alpha} = \frac{\omega R}{\overline{v}\sin\alpha\cos\alpha} \tag{2.20}$$

Interestingly, the same parameter ω_* was also shown to control the response of laminar conical flames submitted to a uniform velocity modulation in [104], which suggests that this unique parameter describes the dynamics of both conical, and V-shaped flames [143]. The ratio ω_*/ω corresponds to a convection time at the mean flow velocity $\overline{U} = \overline{v}\cos\alpha$ along the steady front from the base of the flame ($x = a$) to the end of the flame branch ($x = b$), *i.e.* over the distance L_f, see Fig. 2.3. This simplified approach is shown to be in good agreement with experimental data in the original article. For large amplitude oscillations, propagation upstream of the flame holder and reattachment are observed in [148], but the characteristic wrinkling of flame branches shown in Fig. 2.2a is not retrieved. Moreover, the model is limited by construction to low frequencies and significant differences are observed between experiments and predictions when the reduced frequency ω_* is increased [104].

Baillot *et al.* [149, 150] conducted experiments on a laminar conical flame and identified that deformations of the flame front originate from two progressive waves. The first one corresponds to a convection in the axial direction and in the fresh reactants at a velocity $\overline{v}$. The second one characterizes the convection of disturbances along the flame front starting from the flame base at a velocity $\overline{v}\cos\alpha$. These observations indicate that a single parameter ω_* as obtained when considering a uniform harmonic velocity perturbation is not sufficient to describe the perturbed flame dynamics. To comply with these findings and overcome the limitations observed with a uniform velocity perturbation, Schuller *et al.* [143] chose to impose a convective velocity perturbation at the flame base:

$$u'(y,t) = 0 \tag{2.21}$$

$$v'(y,t) = v_1 \exp\left(iky - i\omega t\right) \tag{2.22}$$

with $k = \omega/\overline{v}$ the axial convective wavenumber and v_1 the amplitude of the velocity excitation. Substituting Eq. (2.22) in Eq. (2.9), yields the unsteady flame displacement:

$$\hat{\xi}(x) = \frac{v_1}{\overline{v}}\frac{R}{i\omega_*\cos\alpha}\frac{1}{1-\cos^2\alpha}\left[e^{i\omega_*\frac{x}{R}} - e^{i\omega_*\frac{x}{R}\cos^2\alpha}\right] \tag{2.23}$$

which can in turn be reintroduced in Eq. (2.14) first, before obtaining the analytical FTF for a V-shaped flame with Eq. (2.12). The final expression obtained in [143] is recalled here:

$$\begin{aligned}\mathcal{F}_v(\omega,\alpha,a,b) =& \frac{2}{\omega_*^2}\frac{1}{1-\cos^2\alpha}\frac{b-a}{b+a}\left[e^{i\omega_*}-1-\frac{e^{i\omega_*\cos^2\alpha}-1}{\cos^2\alpha}\right] \\ &+\frac{2i}{\omega_*}\frac{1}{1-\cos^2\alpha}\frac{b}{b+a}\left[e^{i\omega_*\cos^2\alpha}-e^{i\omega_*}\right]\end{aligned} \tag{2.24}$$

This time, the FTF is parametrized not only by the reduced pulsation ω_* but also by the half flame angle α, and by the characteristic radius $R = b - a$. In many configurations, but not always, flames are stabilized on a narrow bluff-body, so that $a \ll b$. In this case Eq. (2.24) reduces to:

$$\mathcal{F}_v(\omega_*,\alpha) = \frac{2}{\omega_*^2}\frac{1}{1-\cos^2\alpha}\left[e^{i\omega_*}-1-\frac{e^{i\omega_*\cos^2\alpha}-1}{\cos^2\ \alpha}\right]+\frac{2i}{\omega_*}\frac{1}{1-\cos^2\alpha}\left[e^{i\omega_*\cos^2\alpha}-e^{i\omega_*}\right] \tag{2.25}$$

The corresponding FTF gain and phase lag curves obtained in [143] are presented in Fig. 2.4b while Fig .2.4a displays the FTF obtained when considering a uniform velocity perturbation as done by Dowling *et al.* [148], Eq. (2.17). Both analytical FTF model

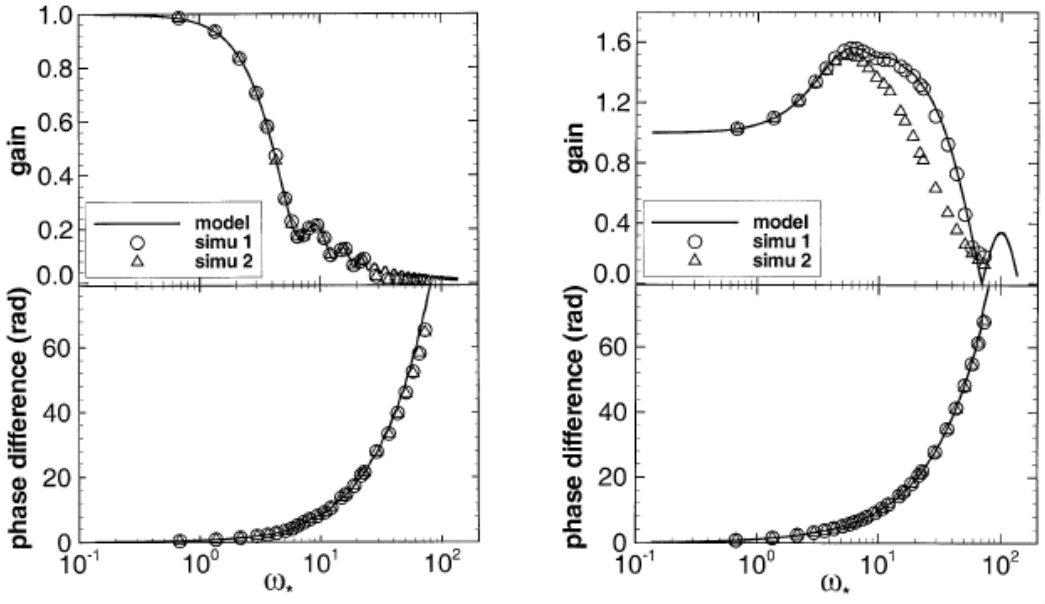


Figure 2.4: Comparison between analytical FTF and simulations results using a G-equation solver with two different perturbation levels $\hat{v}/\overline{v} = 0.02$ (circles) and $\hat{v}/\overline{v} = 0.1$ (triangles) using a uniform velocity perturbation (a) and a convective perturbation (b). Parameters are $S_l = 0.39$ m.s^{-1}, $\overline{v} = 1.30$ m.s^{-1}, a = 3 mm, b = 11 mm and $\alpha = 17°$. Reproduced from [143].

perfectly match numerical solutions of the G-equation for low amplitude modulations.

Uniform velocity fluctuations lead to a standard low-pass filter behaviour as expected from theory, and the flame response is shown to be insensitive to the amplitude of the fluctuation $\hat{v}/\overline{v}$ at the burner outlet. The FTF gain obtained with convective velocity perturbations exhibits a strong sensitivity when the fluctuation amplitude is increased, which is in line with experiments [134]. However, it features a gain overshoot that was not present when using a uniform perturbation. This overshoot is also observed when assessing FTF using experiments [127], proving that some additional information is gained with this more complete description. Note that some authors such as You *et al.* [151] also explored the influence of radial dependency of the mean velocity $\overline{v}$, and a description of the flame as a succession of constant angle portions in their attempt to propose a unified approach accounting for all possible sources of disturbances. These derivations yield limited improvements and are of limited practical use since they require a numerical integration of the unsteady flame displacement ξ, thus, they are not considered here.

The FTF of Eq. (2.25) was derived considering a uniform mean flow. As such, it solely depends on mean flow and geometrical quantities, which is not surprising in the context of laminar flame it was originally developed for but raises questions for turbulent flames where dynamics and flame sheet wrinkling due to local vorticity effects are likely to play an important role. As discussed by Preetham *et al.* in [152], a limitation of this model stems from the fact that the convective velocity behind Eq. (2.22) assumes that perturbations travel along the flame front at the mean flow velocity $\overline{U} = \overline{v}\cos\alpha$. In reality these perturbations (that we will assimilate to vortical perturbations to simplify the analysis) travel in the outer shear layer in the case of a V-shaped flame at a velocity U_{c-v} that can be very different from $\overline{v}$. For example, Durox *et al.* [127] measured the local velocity in the vicinity of the flame sheet to be half of the bulk velocity at the injector exit. The flame surface can be affected by large scale structures being shed from the burner rim which induce local vorticity and thus wrinkling, as illustrated in Fig. 2.5. In general, the total disturbance field can hence have both acoustic and vortical components, with relative magnitude determined by the injector shear layer dynamics. According to [152], it originates from two mechanisms: flow non-uniformities and boundary conditions at the flame root. The physical interpretation of these effects can be easily devised. Flow non uniformities result in fluctuating velocity gradients at the burner rim which periodically generate vorticity. This effect is further amplified in the case of swirling flames as will be discussed in Sec. 2.2. On the other hand, flow disturbances impacting the flame base will propagate along the whole flame branch. Preetham *et al.* [152] therefore introduced the true to mean velocity ratio $K = \overline{v}/U_{c-v}$,

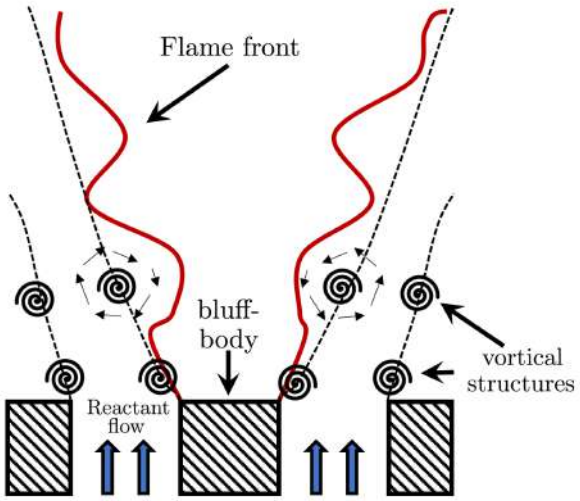
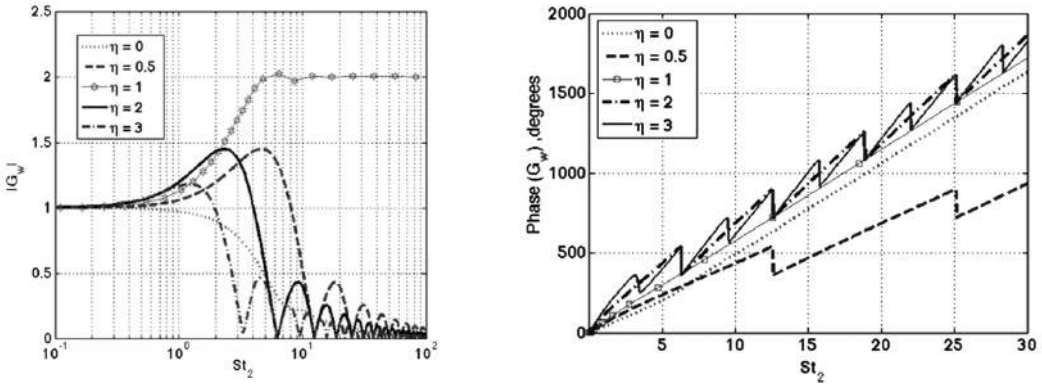


Figure 2.5: Schematic representation of a bluff-body anchored V-shaped flame wrinkled by vorticity disturbances generated at the injector exit edges when an acoustic modulation is applied.

which modifies Eq. (2.25) in a straightforward manner:

$$\mathcal{F}_v(\omega_*,\alpha)=\frac{2}{\omega_*^2}\frac{1}{1-K\cos^2\alpha}\left[e^{i\omega_*}-1-\frac{e^{i\omega_* K\cos^2\alpha}-1}{K\cos^2\ \alpha}\right]+\frac{2i}{\omega_*}\frac{1}{1-K\cos^2\alpha}\left[e^{i\omega_* K\cos^2\alpha}-e^{i\omega_*}\right] \tag{2.26}$$

K is merely a correction factor intended to describe the convection of disturbance waves at the actual velocity U_{c-v}. Choosing $K=1$ yields the FTF model obtained by Schuller *et al.* [143], Eq. (2.25). As shown in Fig. 2.6a, parameter K has a strong influence on both predicted FTF gain and phase lag. It directly controls the magnitude and frequency for which an above unity gain peak is observed, as well as the general slope of the phase curve. These drastic modifications with the chosen value for K underline



(a) **(b)**

Figure 2.6: FTF gain and phase from the model of Eq. (2.26) for various values of the correction factor K. $\eta = K\cos\alpha$ and $St_2 = \omega_*$, reproduced from [152].

the need for its precise identification.

A potential drawback for the FTF model of Eq. (2.26), especially for wide flame angles (when $\alpha \to \pi/2$), is that it may result in large gain values for high frequencies which are not observed in experiments for this type of flames [134]. In [116], PIV measurements are performed in the fresh gases and show that the velocity perturbation amplitude decreases with the axial distance to the burner exit plane, with a frequency dependent decay rate. The authors also point out that this feature is needed to retrieve the FTF obtained experimentally when using a model derived from a G-equation (see [116]). Birbaud *et al.* [153] performed further studies on the fresh reactant side and found velocity perturbations to have an exponential decay rate which increases with frequency. By construction, the FTF model $\mathcal{F}_v$ only considers one-dimensional propagation without any decay, which may be true in a narrow injection system but may not hold as the perturbation enters the larger combustion chamber enclosure. To take this feature into account, the spatial component $\hat{v}$ of the convective velocity $v' = \hat{v}e^{i\omega t}$ in Eq. (2.22) can again be modified following the formulation proposed in [154] for conical flames:

$$\hat{v} = v_1 \exp\left(i\frac{K\omega}{\overline{v}}y\right)\exp\left(-\beta\frac{K\omega}{\overline{v}}y\right) = v_1 \exp\left(i\frac{K(1+i\beta)\omega}{\overline{v}}y\right) \tag{2.27}$$

which effectively comes down to introducing a new complex velocity correction factor $K' = K(1+i\beta)$ instead of a real-valued quantity. In this case, the corresponding decay rate $-\beta K\omega/\overline{v}$ increases with frequency which complies with experimental findings. This means that Eq. (2.26) retains the same form, and in the latter, the parameter K is always assumed to be complex for conciseness purposes.

2.1.4 About the time domain representation of FTF

FTF correspond to a frequency domain description of the flame response and are often preferred to a time domain description since LOM such as Helmholtz solvers also use a frequency domain description of acoustics. Their time domain equivalent is the impulse response (IR), which can be obtained by performing an inverse Laplace transform of the FTF. Over the last decade, several advancements have been made in the thermoacoustic research community so that time domain simulations have gained in popularity. Notably, time domain simulations allow to retrieve limit cycle oscillations and can include damping/saturation effects. They can also be used to explain some of the features seen in analytical FTF gain and phase lag curves.

A study by Blumental *et al.* [155] investigated the impulse response of premixed laminar flames to velocity perturbations in the time domain and obtained analytical formulas for the corresponding FTF. In the particular case of a V-shaped flame, their time domain IR is formally equivalent to Eq. (2.26) of the previous section. Their work

provides additional valuable insights on phenomena observed in [104, 143, 152]. From the analytical impulse response, two time scales corresponding to (1) flame anchoring and restoration and (2) convective flame displacement due to forcing are identified. These time scales are said to correspond to the two non dimensional quantities already observed: ω_* and $\cos\alpha$. The relative importance and time delay difference between these two times scales is then used to explain physical phenomena such as low or high FTF gains for specific frequencies.

Figures 2.4b and 2.6a show that the modelled FTF gain features undulations for which a series of cutoff-frequencies corresponding to local gain minima are observed. Ducruix *et al.* [104] noted that the cut-off frequency of the FTF of a conical flame perturbed by a uniform velocity modulation corresponds exactly to $\omega_* = 2\pi$. This is attributed to the fact that for this value, the convective wavelength $\lambda_c = \overline{v}\cos\alpha/f$ is exactly equal to the flame length L_f so that positive and negative flame displacement cancel each other. Blumenthal *et al.* [155] argue that according to Eq. (2.14), this is not exactly true since a weighting term is present when integrating the flame displacement along the flame length. For a V-shaped flame, this weight is simply the radial coordinate x: the flame perimeter associated to higher radii is bigger, as such, its overall contribution is stronger. The authors show that from the impulse response perspective and in the limiting case of small flame angles α, ie when convective effects are prominent, the interval of strong flame response is defined by the difference of the two time scales identified. Cut-off frequencies then correspond to a situation where this zone of importance (higher radii: towards the end of flame branches) contains an integer number of periods, thus leading to cancellation. Hence, cut-off frequencies ω_{co}^j are defined by:

$$\omega_{co}^j = \frac{2\pi j}{\sin^2\alpha} \tag{2.28}$$

The reader is referred to [155] for further information. They also attribute the above unity gain observed for V-flames FTF gain (Fig. 2.4b) to the difference of time scales: when the length of the region of importance can fit exactly one half-period, the relative flame displacement and hence heat release is maximal.

Several further studies propose various extensions based on a more complete description of the flow field [156] or the use of distributed time delays instead of simple dirac functions for the IR [157]. These are not discussed here for the sake of brevity.

2.2 Dynamics of forced swirling flames

As first shown in Fig. 1.16, the frequency response of premixed swirled V-shaped flames differs from the one of non swirling V-shaped flames that were considered in the previous section. In this section, the specific dynamics of premixed swirling flames and the

associated processes responsible for unsteady heat release are discussed. Comprehensive reviews on the topic can be found in [11, 126, 158]. According to the literature, the FTF of swirling flames is influenced by two distinct mechanisms: flame tip roll-up and swirl number fluctuations [126]. Figure 2.8 presents a general overview of how incident acoustic waves finally lead to the two aforementioned processes. Flame tip roll-up is

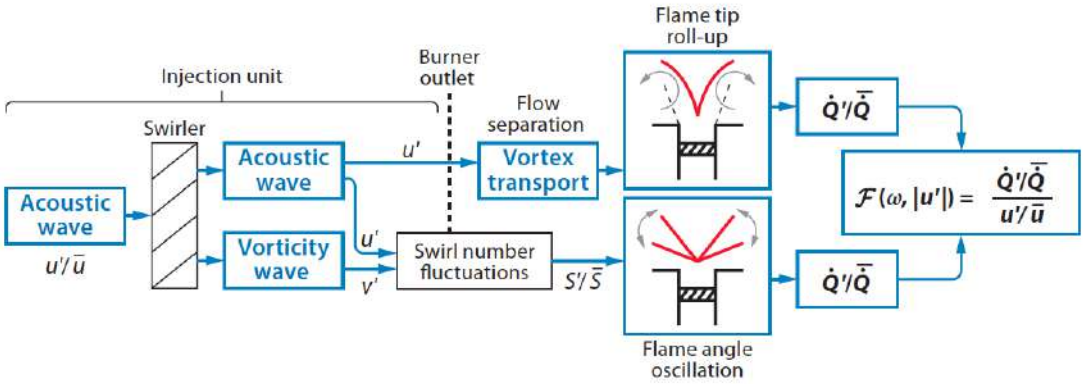


Figure 2.7: Block diagram representation of mechanisms generating heat release rate fluctuations in swirling flows. Reproduced from [126].

essentially the same process that was presented in the previous section for non-swirling flame and shown in Fig. 2.5. Vortical structures are created at the burner outlet under the influence of the acoustic modulation, travel in shear layers and roll up along the flame branches up to their tip. Swirl number fluctuations are however evidently specific to swirling flames. Interactions of the flame with hydrodynamic structures such as the Precessing Vortex Core (PVC) [159] are not considered in this work. The reader is referred to [160] for conditions leading to nonlinear interactions between PVC and acoustic disturbances.

2.2.1 Acoustic-vorticity conversion through a swirler

Before any further investigation is made on swirling flames, it is worth describing the interaction between an acoustic wave and a swirler unit. Such an interaction can be modelled by considering that the swirler acts as a blade row, and using an actuator disk theory [129]. The swirler is then simply viewed as a series of jump conditions relating upstream and downstream variables, as shown by Cumpsty and Marble in [161] for a finite Mach number flow. In most cases, this assumption is justified since the characteristic swirler length is much smaller than the acoustic wavelength considered: the swirler is a compact element.

When an acoustic modulation is imposed in the injection unit, the generated acoustic wave propagates and reaches the upstream side of the swirler. A fraction of the wave

is reflected, while another is transmitted. In the low Mach number limit, the one-dimensional velocity fluctuation upstream of the swirler thus reads:

$$v_1' = \frac{A}{\overline{\rho c}} \exp\left[i\omega\left(\frac{y}{\overline{c}} - t\right)\right] - \frac{AR_c}{\overline{\rho c}} \exp\left[i\omega\left(-\frac{y}{\overline{c}} - t\right)\right] \tag{2.29}$$

with A the amplitude of the incident wave, R_c the reflection coefficient and y the axial coordinate. On the downstream side, the acoustic wave is partially transmitted, yielding a velocity v_2', but an additional velocity component resulting from a vorticity wave generated at the swirler trailing edge also appears [106]:

$$v_2' = \frac{T_c A}{\overline{\rho c}} \exp\left[i\omega\left(\frac{y}{c} - t\right)\right] \tag{2.30}$$

$$u_\theta' = B \exp\left[i\omega\left(\frac{y}{\overline{v}_2} - t\right)\right], \tag{2.31}$$

with T_c the transmission coefficient and B the transverse velocity disturbance amplitude. A visualization of all generated disturbances and waves assuming a compact swirler following the actuator disk theory is available in Fig. 2.8. The theoretical work of Palies

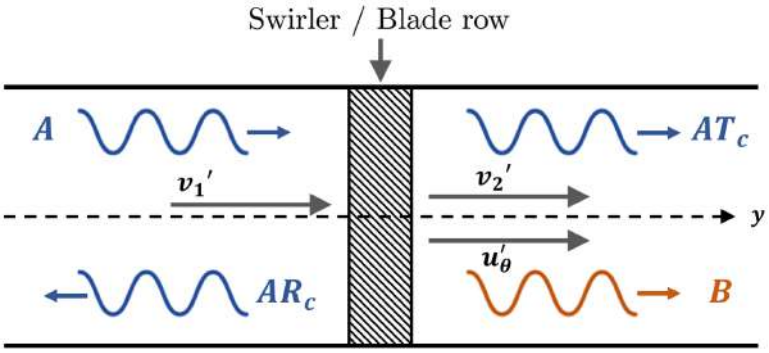


Figure 2.8: Representation of a swirler as a discontinuity between upstream and downstream flows. The acoustic wave v_1' impinges on the swirler and creates a transmitted acoustic wave v_2' as well as a vorticity wave represented by a transverse velocity fluctuation u_θ' convected by the flow. Adapted from [126].

et al. in [106] makes use of these low Mach jump conditions and show that further assuming the equality of mean pressure and density on the two sides of the swirler yields $R_c = 0$, $T_c = 1$: the acoustic waves are fully transmitted. Applying a Kutta condition at the trailing edge of the swirler, the amplitude B of the transverse velocity is shown to be:

$$u_\theta' = \frac{A}{\overline{\rho c}} \tan\theta_2 \exp\left[i\omega\left(\frac{x}{\overline{v}_2} - t\right)\right] \tag{2.32}$$

where θ_2 is the angle made by a swirler blade with respect to the axial direction. The linearized jump conditions assume that the vorticity wave generated across the swirler is

convected at the downstream mean flow velocity $\overline{v}_2$. Experimental studies yet show that this is not always the case [51, 162]. This point is further addressed in Sec. 3.5.1, but general conclusions discussed in the following apply nonetheless. This result indicates that in a swirling flow, axial acoustic and tangential convective perturbations have the same order of magnitude, and can thus both affect the flame response. This theoretical vorticity generation was then confirmed with unsteady RANS simulations in [51], DNS of a blade row submitted to an acoustic modulation [129] and experiments on a cylindrical channel equipped with an axial swirler [129].

2.2.2 Swirl fluctuations impact on the flame response

In the linear regime and in Fourier space, swirl number fluctuations $\hat{S}$ can be expressed as [129]:

$$\frac{\hat{S}}{\overline{S}} = \frac{\hat{u}_\theta}{\overline{u}_\theta} - \frac{\hat{v}}{\overline{v}} \tag{2.33}$$

Hence, axial and tangential velocity fluctuations generated across the swirler give rise to swirl number fluctuations. Since the first ones travel at the sound speed c while the other ones travel at a convection speed u_c close to the mean flow velocity, their relative phase is directly controlled by the distance between the swirler exit and the location where they impact the flame.

In this matter, Komarek *et al.* [51] designed an experiment where the axial position of a swirler located upstream of a combustion chamber could be varied. The objective of the experiment was to confirm that the phase difference (or equivalently time delay) between axial and tangential velocity had an impact on the FTF. Figure 2.9 discloses the results obtained in this study for three swirler axial positions. From this data, it is evident that the impact on the FTF is important. The swirling flame FTF is characterized by a series of local minimum and maximum gain values as already examined in Sec. 1.5. When the swirler to combustion chamber distance is increased, and thus the time delay for convective perturbations, the first local minimum frequency is shifted to lower frequencies. In the case where the swirler is located close to the combustion chamber with $\Delta_x = 30$ mm, this first FTF gain minimum is not visible for the considered frequency range but one can devise that it would be present at a higher frequency. A similar result is obtained in [106] by varying the bulk flow velocity.

A first interpretation of this effect was proposed in [106]. In this article, the high and low FTF gains observed in experiments are said to arise from constructive or destructive interferences of axial and tangential velocity perturbations giving rise to swirl fluctuations at the injector exit plane. The authors performed experiments on a laboratory scale swirl burner where a V-shaped flame is stabilized on a central bluff-body. They split the flame into an upper windows and a lower window to assess flame tip

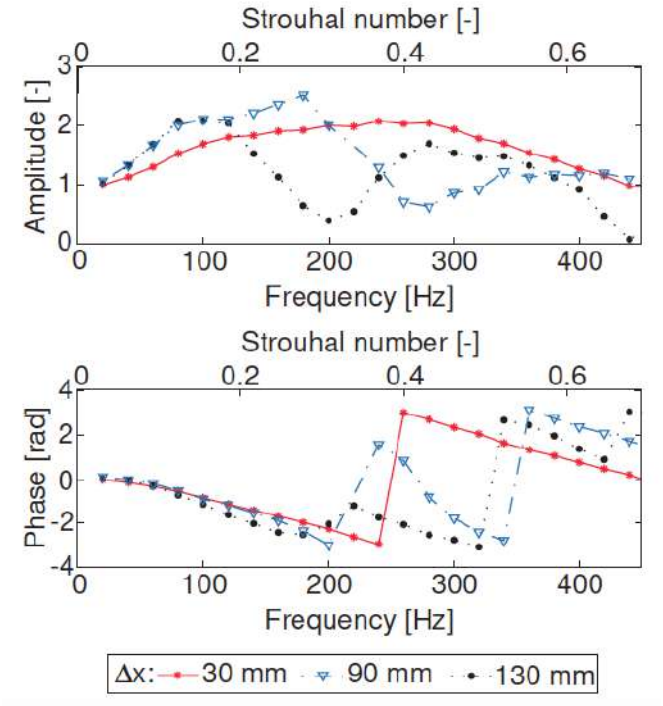


Figure 2.9: FTF gain and phase for various swirler exit to combustion chamber backplane distances Δx, reproduced from [51].

and flame base response respectively. Then, they examined their relative contribution to heat release rate fluctuations and phasing. They found heat release rate signals to be out of phase at the FTF minimum gain frequency. On the contrary, for a frequency corresponding to a local FTF gain maximum, the same signals were found to be nearly in phase. The authors followed up with a numerical analysis on a similar configuration in [163]. It was observed that when swirl number fluctuations were large, the flame response was weak. On the contrary, for low fluctuations, maximum heat release rate oscillations were seen. According to Palies *et al.* [163], this behaviour originates from the flame opening angle oscillations resulting from interaction with the local flow structure at the base of the flame. Indeed, flame angle oscillations lead in turn to more or less intense vorticity generation at the flame base that will roll-up along flame branches.

Bunce *et al.* [164] used the same two windows flame division procedure and performed a series of experiments on a similar configuration but did not retrieve a constructive interference between the upper and lower part of the flame at the FTF maximum gain frequency regardless of the considered windows. They however found that when applying forcing at frequencies corresponding to minimum local FTF gains, the mean flame position envelope at the flame base was rather large. This is indicative of swirl fluctuations. In contrast, at frequencies corresponding to local FTF gain maxima, the flame base fluctuations were very low, which could indicate an absence of swirl fluctuations at the flame base. Following the diagram of Fig. 2.8, this means that in this

case, only flame tip roll-up is responsible for the creation of unsteady flame surface and hence, heat release.

The observations made in [163] and [164] regarding the role of swirl fluctuations on preferential low or high FTF gains are investigated from a new perspective in Sec. 3.4.3.2.

2.3 Modelling of premixed swirling FTF

2.3.1 A baseline model for swirling flames FTF

To this point, only laminar V-shaped flames FTF have been developed, without any consideration regarding swirl or any azimuthal velocity component. The effect of flame tip roll-up can be accounted for through the mean velocity correction parameter K described in Sec. 2.1 and appearing in the expression of the laminar premixed V-shaped flame FTF $\mathcal{F}_v$ from Eq. (2.26). Yet, there is no indication on how to consider azimuthal velocity or swirl fluctuations which have been identified as a crucial element for the response of swirling flames.

Analytical expressions for the frequency response of perturbed swirling flames are much more scarce than for standard laminar flames. One particularly compelling work in this regard is the one of Palies *et al.* [128]. These authors start from the description of a turbulent flame using a G-equation. In this matter, the turbulent version of Eq. (2.3) is:

$$\frac{\partial G'}{\partial t} + \left(\overline{\mathbf{v}} + \overline{S}_t \mathbf{n}\right).\nabla G' = \left[\mathbf{v}'.\mathbf{n} - \frac{S'_t}{\overline{S}_t}\overline{\mathbf{v}}.\mathbf{n}\right] |\nabla \overline{G}| \tag{2.34}$$

This expression relates the perturbed flame motion to both axial flow velocity perturbations v' but also turbulent flame speed perturbations S'_t. The two types of perturbations act in a similar fashion. Accordingly, for linear acoustics, the heat release rate response can be linked to the standard laminar transfer function of a V-flame $\mathcal{F}_v$:

$$\frac{\hat{Q}}{\overline{Q}} = \mathcal{F}_v(\omega)\left[\frac{\hat{v}}{\overline{v}} - \frac{\hat{S}_t}{\overline{S}_t}\right] \tag{2.35}$$

In the remaining of this work, $\mathcal{F}_v$ is defined from the convectively perturbed analytical FTF of Eq. (2.26). The global flame transfer function of a swirling flame $\mathcal{F}_s$ is then defined by:

$$\mathcal{F}_s = \mathcal{F}_v\left[1 - \frac{\hat{S}_t/\overline{S}_t}{\hat{v}/\overline{v}}\right] \tag{2.36}$$

This expression is of no practical use unless an additional modeling for the turbulent flame speed ratio $\hat{S}_t/\overline{S}_t$ is proposed. Noting that the turbulent flame speed S_t is essentially a function of the swirl number [165], it is therefore legitimate to express this ratio as a modified version of Eq. (2.33) for linearized swirl fluctuations. Hence, turbulent

velocity fluctuations are assumed to be linked to the normalized velocity fluctuations in a linear fashion using two real valued model parameters χ and ζ so that [128]:

$$\frac{\hat{S}_t}{\overline{S}_t} = \chi \frac{\hat{u}_\theta}{\overline{u}_\theta} + \zeta \frac{\hat{v}}{\overline{v}} \tag{2.37}$$

At the burner outlet, the axial and azimuthal velocity disturbances are then assumed to be related by:

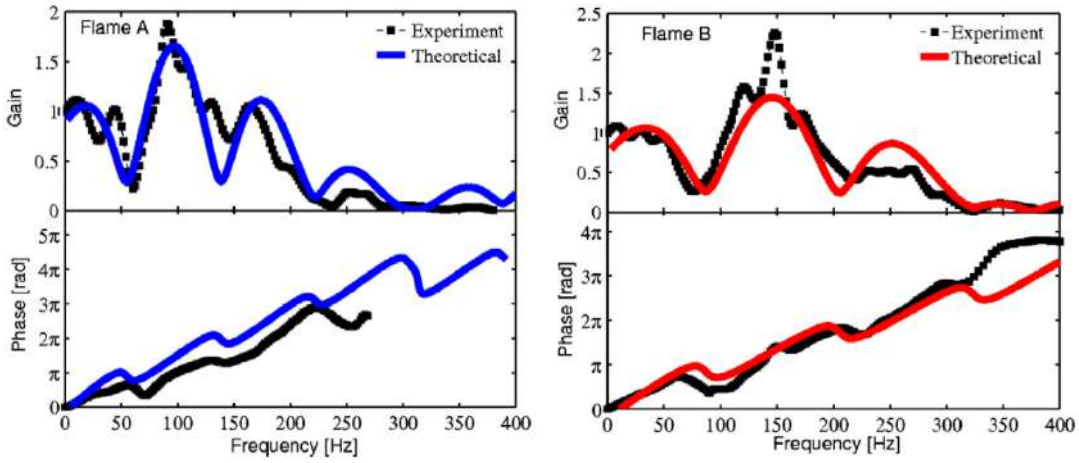
$$\frac{\hat{u}_\theta}{\overline{u}_\theta} = \frac{\hat{v}}{\overline{v}} e^{i\phi_{\hat{u}_\theta - \hat{v}}} \tag{2.38}$$

This means that the normalized velocity fluctuations are essentially the same, but with a phase shift $\phi_{\hat{u}_\theta - \hat{v}}$ between the axial and the azimuthal components. Reintroducing Eq. (2.37) and (2.38) in Eq. (2.36) finally yields the FTF for a swirling V-shaped flame:

$$\mathcal{F}_s = \mathcal{F}_v \left[1 - \left(\zeta + \chi e^{i\phi_{\hat{u}_\theta - \hat{v}}} \right) \right] \tag{2.39}$$

which depends on a set of six parameters: ω_*, α, K, χ, ζ and $\phi_{\hat{u}_\theta - \hat{v}}$. The three first parameters correspond to the modeling of the laminar premixed flame response while the three remaining ones aim at providing swirling flow features. Note that at this point, parameters χ and ζ defined in Eq. (2.37) and related to turbulent flame speed fluctuations are rather hard to interpret.

Palies *et al.* [128] assessed the validity of the model of Eq. (2.39) on a confined methane/air swirled V-shaped flame with a swirl number $S = 0.55$ and for two operating conditions corresponding to two imposed bulk velocity values in the injection unit: $U_b = 2.67$ m.s^{-1} and $U_b = 4.13$ m.s^{-1}. In their experiment, the flame was anchored on a 6 mm wide cylindrical rod. In Eq. (2.39), the laminar FTF $\mathcal{F}_v$ was chosen to be the convective model of Eq. (2.25), hence the flame was assumed to be anchored at the center of the rod and no correction factor K was applied. The phase $\phi_{\hat{u}_\theta - \hat{v}}$ between axial and tangential velocity perturbation was evaluated at the base of the flame for several forcing frequencies and a linear fit was determined. Parameters χ and ζ are set to $\chi = -0.4$ and $\zeta = 0.4$ according to a trial and error process. The comparison between the swirling FTF model and the experiment is shown in Fig. 2.10. For the two considered operating points, the experimental FTF gain exhibits the classical alternation of local minima and extrema observed for such swirling flames. The model is shown to qualitatively match experimental data and to reproduce the undulating behaviour of the FTF gain curve. In particular, local maximum and minimum gain values are reproduced at frequencies close to the ones observed in the experiment. The general behaviour of the FTF phase lag is also retrieved although some discrepancies are observed for the case with $U_b = 2.67$ m.s^{-1}. Note also that with the set of parameters used, the low frequency limit value of the FTF gain is lower than unity for both investigated cases. The swirled FTF model has later been used with some success in [166] to gain insight on the dynamics of stratified swirling flames.



(a) (b)

Figure 2.10: Comparisons of experimental and modelled FTF of Eq. (2.39) **for two V-shaped flames: (a) bulk velocity $U_b = 2.67$ m.s^{-1}, $\phi_{\hat{u}_\theta - \hat{v}} = 12 \times 10^{-3}\omega - 1$, (b) bulk velocity $U_b = 4.13$ m.s^{-1}, $\phi_{\hat{u}_\theta - \hat{v}} = 8.5 \times 10^{-3}\omega - 1.5$. In both cases $\phi_{\hat{u}_\theta - \hat{v}}$ is obtained from a linear fit of experimental data. Reproduced from [128].**

2.3.2 The SFTF model

In the original work of Palies *et al* [128], no additional constraint is present. One can however point out that according to theory, the FTF gain of a premixed flame submitted to flowrate disturbances in the zero frequency limit should always be unity [167]. Setting $\phi_{\hat{u}_\theta - \hat{v}} = \omega\tau$ where τ is a characteristic time delay between axial acoustic and tangential convective velocity perturbations imposes $\chi = -\zeta$. The other solution $\chi = 2 - \zeta$ is discarded as it yields non physical results. This simplistic assumption does however not hold when confronted to the experimental findings from [106] for instance. Indeed, in this work, the phase $\phi_{\hat{u}_\theta - \hat{v}}$ measured experimentally at the base of the flame is not null in the low frequency limit. In the present work, we introduce a more general framework by setting $\phi_{\hat{u}_\theta - \hat{v}} = \omega\tau + \phi_0$, and enforcing the low frequency limit unity gain, yielding:

$$\left|1 - \left(\zeta + \chi e^{i\phi_0}\right)\right| = 1 \tag{2.40}$$

where $|\cdot|$ stand for the modulus of a complex number. It results a second order equation relating χ and ζ:

$$\zeta^2 + 2\zeta\left(\chi\cos\phi_0 - 1\right) + \chi^2 - 2\chi\cos\phi_0 = 0 \tag{2.41}$$

Assuming χ and ϕ_0 to be known, solutions of this equation are:

$$\zeta_1 = 1 - \chi\cos\phi_0 + \left(1 - \chi^2\sin^2\phi_0\right)^{1/2} \tag{2.42}$$

$$\zeta_2 = 1 - \chi\cos\phi_0 - \left(1 - \chi^2\sin^2\phi_0\right)^{1/2} \tag{2.43}$$

Then, assuming $|\chi| \leq 1$, which is the case for values used in [106], ζ_1 and ζ_2 take real values. Since both a new model parameter ϕ_0 and the supplementary constraint of Eq. (2.40) are introduced at the same time, the total number of degrees of freedom remains unchanged. Without any data to compare the model results, and depending on parameters values, it is difficult to choose between one root or another. As previously mentioned, experiments for V-shaped flames FTF have shown that such flames exhibit an increase in gain in the low frequency limit [134]. Starting from Eq. (2.39) and inserting Eq. (2.42) or (2.43), one can show after some calculus that to first order, the low frequency derivative for the swirled FTF gain reads:

$$\lim_{\omega \to 0} \frac{\partial |\mathcal{F}_s|}{\partial \omega} = \tau \sin \phi_0 \left[\chi^2 \cos \phi_0 \pm \chi \left(1 - \chi^2 \sin^2 \phi_0\right)^{\frac{1}{2}} \right] \tag{2.44}$$

Therefore, the value ensuring a positive derivative of the FTF gain in the low frequency limit is chosen depending on values for χ, τ and ϕ_0.

Equation (2.39) along with Eq. (2.42) or (2.43) constitute the parametrization of a V-shaped premixed Swirling Flame Transfer Function that will be referred to as the SFTF model throughout the remaining of this manuscript. This model relies on a set of six independent parameters, three of which describe the premixed flame response (ω_*, α and K) while the three remaining ones account for the effect of the swirling motion (χ, τ, and ϕ_0). The SFTF model is a combination of several previous works, namely:

- an analytical expression for the FTF of a V-shaped laminar flame $\mathcal{F}_v$ from [143], recalled in Eq. (2.25),
- the introduction of a correction factor for the speed of disturbances acting on the flame from [152], $K = \overline{v}/U_{v-v}$, yielding the new analytical FTF of Eq. (2.26),
- the addition of a spatial decay for velocity disturbances amplitudes inspired by [154], by adding a complex component to parameter K, Eq. (2.27),
- the concept of swirling flame FTF [128], with the baseline expression for a swirling V-shaped flame FTF $\mathcal{F}_s$ recalled in Eq. (2.39).

To the author's knowledge, such works have never been combined in an effort to yield a complete description of a swirling flame FTF. The main novelty of this work in regard to FTF modelling alone resides in the addition of the unity FTF gain condition along with the extra modelling parameter ϕ_0.

Palies *et al.* [128] used a series of experimental measurements to characterize input parameters for their analytical model. In this work, it is proposed to make use of high fidelity numerical simulations instead of experiments, with the expectation of discerning the best strategies to extract model parameters. Among said parameters, ω_*, α and

K are related to the steady flame and thus do not require flow forcing techniques to be assessed, thus a single LES should be sufficient. Other parameters however are linked to the forced swirled flame dynamics and should be determined with forced flow simulations. At this point, the exact number of simulations necessary to capture the swirling flame FTF is unknown.

While the SFTF model is limited to premixed V-shaped flames, it could handle various flow injection conditions and fuels through parameters ω_* and α while various swirler designs would affect parameters τ, ϕ_0 and χ. Although the SFTF model was derived from linear acoustics theory, it will be shown in Chap. 3 that probing the decay rate of velocity disturbances $\beta = \Im(K)/\Re(K)$ with LES for various forcing amplitudes can provide a good estimation of some nonlinear effects.

Chapter 3

Large Eddy Simulation of a turbulent swirling premixed flame: the NoiseDyn burner

Contents

3.1 Objectives . . . 51
3.2 Experimental set-up . . . 52
3.3 Numerical modelling . . . 56
3.3.1 Numerical setup . . . 56
3.3.2 Meshing strategy . . . 59
3.4 Validation and flame dynamics . . . 63
3.4.1 Non-reacting flow . . . 63
3.4.2 Stable reacting flow . . . 65
3.4.3 Acoustically pulsed flows . . . 70
3.5 SFTF model application . . . 80
3.5.1 Model parameters from stationary data . . . 80
3.5.2 Model parameters from pulsed LES . . . 85
3.5.3 SFTF methodology summary . . . 91
3.6 Improving the SFTF model: extension to other geometries and forcing amplitudes . . . 93
3.6.1 Effect of the perturbation amplitude on the FTF . . . 93
3.6.2 Impact of minor geometrical modifications on the FTF . . . 98
3.6.3 Sensitivity of the SFTF model . . . 106
3.7 Concluding remarks . . . 108

3.1 Objectives

This chapter is dedicated to the study of a turbulent premixed swirling flame in a laboratory scale single injection burner. FTF modeling strategies for this type of flame were described in Chap. 2. The objective here is to define a robust methodology for the determination of SFTF model parameters presented in Sec. 2.3, and to assess the model ability to correctly capture the acoustic flame response in terms of both gain and

phase. Besides, high fidelity simulations are performed to analyse the root mechanisms responsible for changes in the flame acoustic response when a swirling motion is imposed. The selected configuration includes some of industrial engines most prominent features with a turbulent swirling flow and a confined flame operating with a lean mixture. At the same time, its geometry is easy to model and allows for a much simpler identification of flame dynamic features than in complex industrial configurations.

The experimental rig and the associated numerical setup are first presented in Sec. 3.2 and 3.3, and the numerical pipeline is validated against experimental data for cold and reacting flows in Sec. 3.4. Based on acoustically forced simulation data, the crucial role of preferential vortical structures formation at the injector edge is identified as the driving mechanism for the swirling flame response in Sec. 3.4.3. SFTF model parameters are then extracted from simulation data and results are compared to reference experimental data for the considered operating point in Sec. 3.5. It is shown that an increasing agreement is obtained when enhancing the amount and accuracy of LES input data used for the analytical model. Finally, to further validate the model application range, additional studies are performed in Sec. 3.6, with various acoustic perturbation amplitudes and a modified configuration where the injector has been shortened.

3.2 Experimental set-up

The experimental configuration studied in this work is a variation of the NoiseDyn setup originally designed for project ANR-14-CE35-0025-01. It is highly modular and has been used for the study of laminar conical flames [168], swirling flame dynamics and acoustic response [39, 108, 169], as well as for combustion noise [170, 171]. Numerous details regarding the burner itself and the experimental setup can be found in the PhD thesis manuscripts of R. Gaudron [172] and M. Gatti [162] from EM2C laboratory, Université Paris Saclay. The rig is composed of an injection system, a swirler unit and a combustion chamber ending with a short exhaust tube. The main component of this configuration is schematically presented in Fig. 3.1. A view of the real burner and fluid volume used for CFD computations is also available in Fig. 3.2

Gaseous methane and air supplied mass flow rates are controlled by a mass flow controller and mixed at ambient temperature $T_0 = 293$ K and pressure $P_0 = 1$ atm in a mixing box upstream of the burner. In all studied configurations, the injected air and methane mass flow rates are $\dot{m}_{air} = 2.28 \times 10^{-3}$ kg.s^{-1} and $\dot{m}_{CH_4} = 1.10 \times 10^{-4}$ kg.s^{-1} respectively, yielding a flame thermal Power $P_{th} = 5.44$ kW. The premixed mixture with equivalence ratio $\phi = 0.82$ is injected through the bottom of the device from two diametrically opposed injection channels and enters a cylindrical section of 65 mm

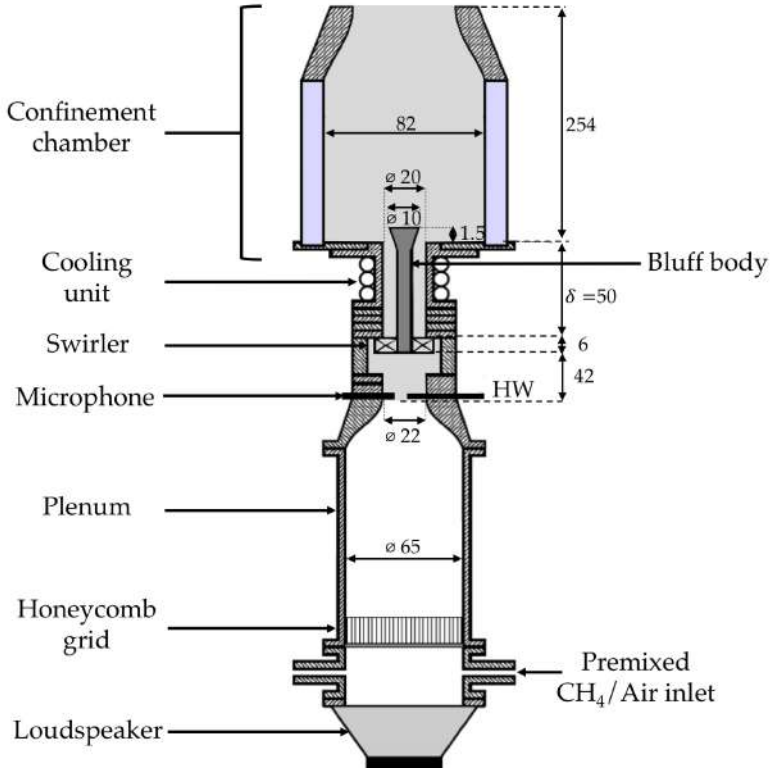


Figure 3.1: Sketch of the NoiseDyn burner from EM2C laboratory, dimensions in mm. δ is the distance between the combustion chamber backplane and the top of the swirler channels exit. Only the shaded domain is resolved in the LES, starting 8 mm under the hot wire position (HW).

diameter. It then passes through a multi-perforated grid and a honeycomb layer to homogenize the flow and break large turbulent eddies before reaching a convergent section ending with a $D_{in} = 22$ mm diameter. This section is equipped with a hot wire anemometer probe used to inquire the local velocity in the central region of the obtained top hat velocity profile with bulk velocity $U_b = 5.44$ m.s^{-1}. The bulk temperature of the flow in that section is equal to 293 K. The flow is then guided through a radial swirler using six cylindrical injection channels of diameter $d_{Sw} = 6$ mm forming a 33° angle with respect to the radial direction, Fig. 3.3, creating a strong rotating motion with a swirl number $S = 0.8$ measured at the burner outlet. The mixture leaves the swirler through a 22 mm wide section which length δ_1 can be adjusted from 1 to 16 mm with 5 mm increments, Fig. 3.4, and then through a smaller tube with outer radius $R_0 = 10$ mm. The total distance between the swirler channels exit and the combustion chamber backplane is $\delta = 50$ mm when all incremental pieces are used. The flame can be stabilized either using a bluff-body as shown in Fig. 3.4a, or fully aerodynamically as in Fig. 3.4b. In the first case, the injector includes a stainless steel rod of diameter $d_{rod} = 6$ mm topped by a 10 mm high truncated cone ending with a circular section of diameter $D_C = 10$ mm. The cone itself is protruding with an adjustable distance δ_2 in

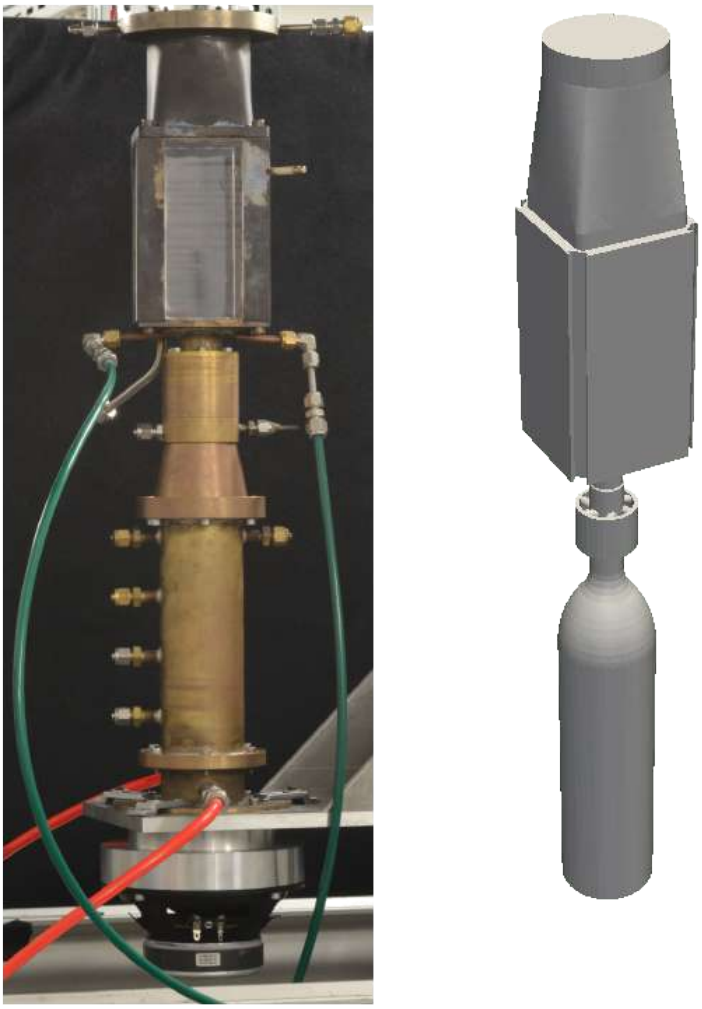


Figure 3.2: Front view of the Noisedyn burner (left) and associated 3D fluid volume used for CFD computations (right).



Figure 3.3: Top view sketch of the swirler used in this work (left), real swirler geometry (middle) and 3D rendering of the swirler as used in numerical simulations (right).

the chamber. In the absence of bluff-body, the main injector diameter is dropped down to 12 mm to favour the flame anchoring, with a 15° opening angle at the injector exit

edges. Regardless of the injector geometry, a water cooling loop is used to maintain the injector temperature as close to ambient values as possible. The combustion chamber

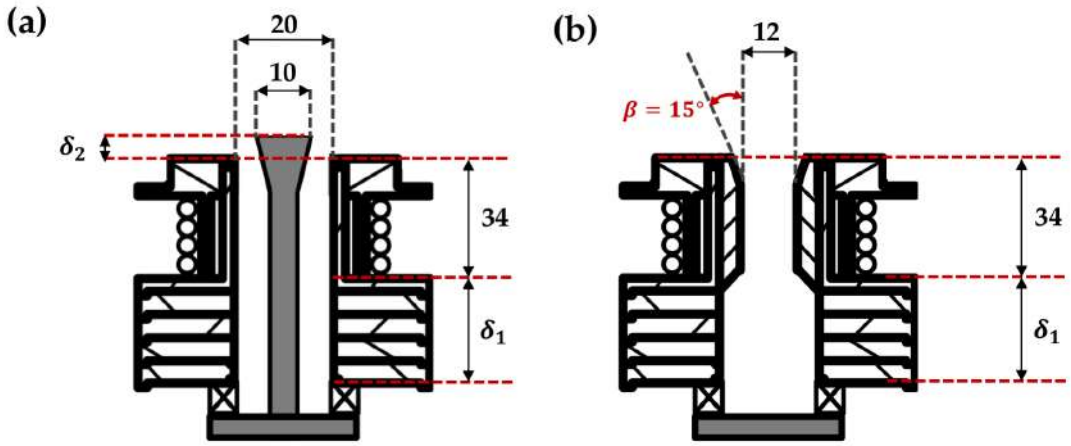


Figure 3.4: View and details of the injector for (a) the bluff-body stabilized flame, (b) the aerodynamically stabilized flame. Dimensions are in mm.

is 150 mm long and has a square cross-section of $L_{ch} = 82$ mm width. The enclosure is made of four 8 mm thick quartz windows which are kept in position using stainless steel rods at each corner, providing a tight seal for the flow and allowing a direct visualization of the flame, see Fig. 3.1 and 3.2. A convergent exhaust unit gradually changes the section from a square to a circle in order to guide the high temperature burnt gases to the outlet opened to the atmosphere.

The baseline configuration studied in this work corresponds to the injector shown in Fig. 3.4a and features a V-shaped flame anchored few millimeters above the bluff-body protruding $\delta_2 = 1.5$ mm in the chamber. The distance δ_1 can be tweaked by adding or removing a set of three 5 mm thick spacers, in the present case $\delta_1 = 16$ mm. This academic burner is not as complex as injectors used in real engines, yet it includes some of their most prominent features such as a turbulent swirling flow and a confined flame operating at lean premixed conditions. This academic configuration allows for an easier interpretation of LES results and for a better understanding of flame dynamics.

A wide selection of diagnostics has been employed by Gatti *et al.* [162, 169], providing a considerable results database for the present study. Among those, let us cite :

- A constant temperature anemometer Hot Wire (HW) to acquire reference velocity data for FTF, see HW in Fig. 3.1.

- A photomultiplier equipped with an OH^* filter to record the flame light emission and evaluate the global heat release.

- An intensified CCD camera with an UV objective and an OH^* filter used for flame imaging.
- Particle Image Velocimetry (PIV) to characterize the axial, radial and azimuthal velocity components in different planes within the combustor under both unperturbed and acoustically forced conditions.
- Laser Doppler Velocimetry (LDV) to characterize the unforced axial, radial and azimuthal velocity components near the injector exit.
- K-type thermocouples in the burnt gases close to the combustor backplane (TC1) and along the chamber wall for temperature measurements (TC2 and TC3), Fig. 3.5.
- A microphone in front of the hot wire to acquire pressure data and determine the acoustic impedance at this position.

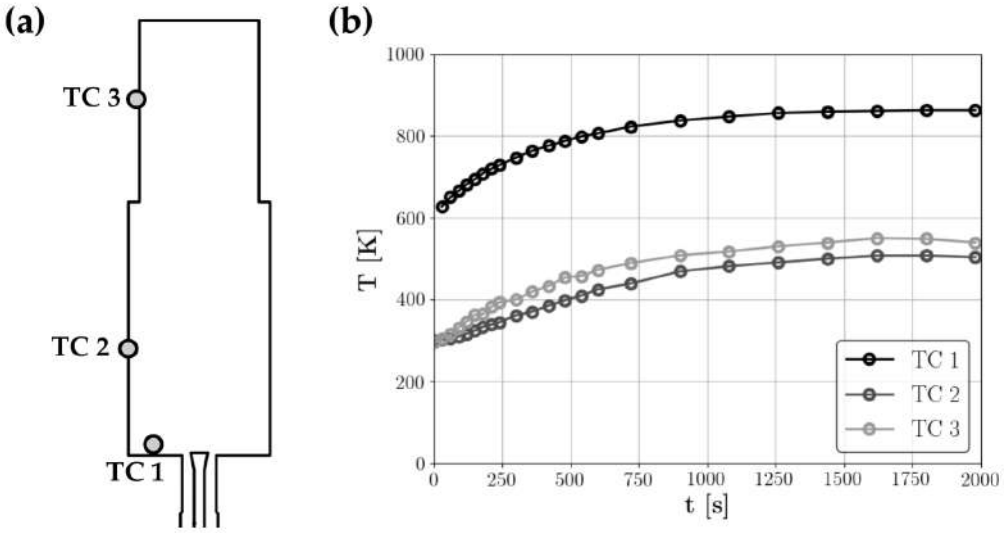


Figure 3.5: (a) Position of K-type thermocouples for temperature measurements and (b) temporal evolution of temperature for the three probing locations, from [162].

3.3 Numerical modelling

3.3.1 Numerical setup

In order to save computational time, the domain is restricted to the shaded area in Fig. 3.1 and covers a region starting 8 mm upstream of the hot wire position all the way to the exit of the exhaust tube. Minor geometric modifications of the fluid volume were made in order to ease the meshing process :

- The swirler fixation bolt which comprises numerous small sharp edges has its edges smoothened.
- The convergent exhaust area transition from a squared to a circle cross section is simplified.
- The quartz windows mounting brackets are removed.

The final geometry used throughout this chapter is shown under various viewpoints in Fig. 3.6.

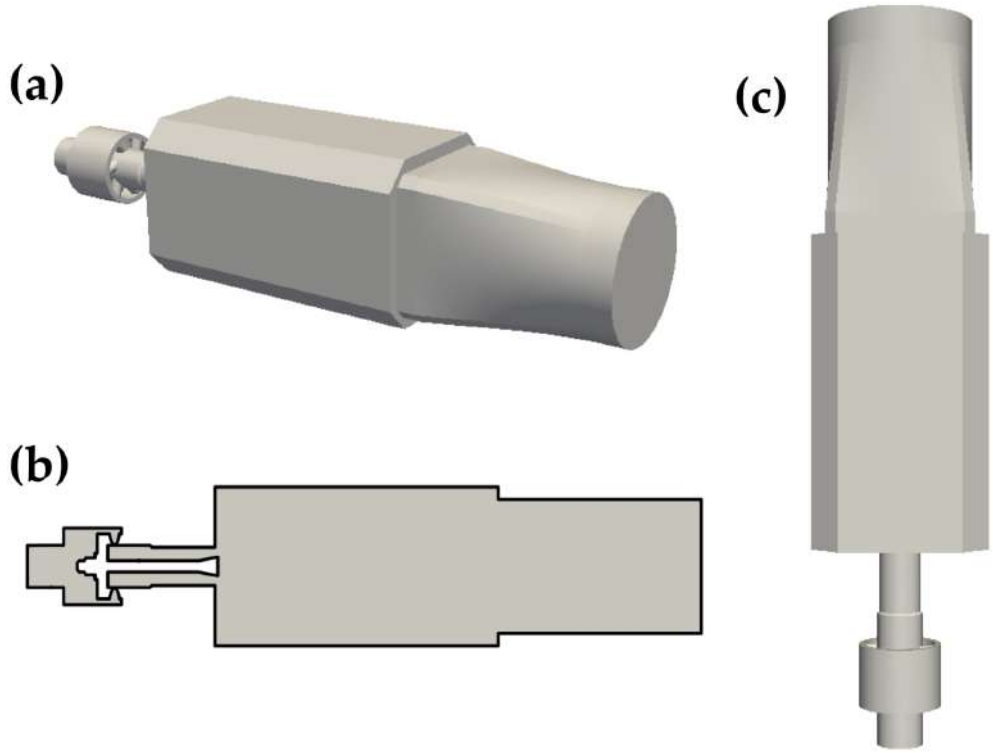


Figure 3.6: (a) Side, view of the fluid volume used for LES, (b) cut on a transverse plane of the fluid volume and (c) front view of the LES domain.

LES of the NoiseDyn configuration were performed using the AVBP solver developed by CERFACS (*www.cerfacs.fr/avbp7x*) [173], which solves the three-dimensional filtered compressible multi-species Navier-Stokes equations on unstructured grids. For all simulations, the TTGC centered spatial scheme [174] was used, featuring a third order accuracy in both space and time. Navier Stokes Characteristic Boundary Conditions (NSCBC) [175] were used for both inlet and outlet boundary conditions, ensuring a proper treatment of waves. For cold flow simulations, all other boundary conditions were set to adiabatic no slip walls. For reacting simulations, boundaries above the injection unit were changed to heat losing walls for which a reference temperature and thermal resistance were prescribed. Doing so, the heat flux at walls naturally adapts

according to the local flow temperature. Regarding reference temperature, data after thermalization was used, corresponding to the steady state shown in Fig. 3.5. Hence, the exhaust tube walls and main chamber walls are set to heat losing boundaries with an outside temperature of 863 K and 540 K respectively. Since the thermocouple TC1 exact position in the burnt gases recirculation zone was not known precisely, a hyperbolic tangent profile varying from 300 K in the central watercooled region to 700 K near the chamber walls was prescribed. Thermal conductivities for quartz glass $\lambda_{quartz} = 1.4$ W.m^{-1}.K^{-1} and stainless steel $\lambda_{steel} = 26$ W.m^{-1}.K^{-1} were used.

Considering the bluff-body tip mean diameter $D_{cm} = 8$ mm, the injector diameter $D_0 = 20$ mm(Fig. 3.7), and using mass conservation to evaluate the bulk velocity on an equivalent section $U_{b1} = 7.7$ m.s^{-1}, the mean Reynolds number around the bluff-body top portion is $Re = U_{b1}\left(D_{cm} - D_0\right)/\nu = 5.7 \times 10^3$. The Sieder and Tate empirical correlation [176] is used to evaluate the Nusselt number along the injector. Assuming a Prandtl number $Pr = 0.7$ and considering the bluff-body tip length $L_c = 10$ mm, one gets $Nu = 0.027 Re^{0.8} Pr^{1/3} = 24.14$. Then, the convection coefficient of the bluff-body tip h_{bb} is evaluated as $h_{bb} = Nu\lambda_{air}/L_c = 56.1$ W.m^{-2}.K^{-1}. A spatial dependant unitary heat resistance R_{bb} was derived for the tip of the bluff body from the steel fin theory :

$$R_{bb}(x) = \frac{\sinh(mL_c)}{\lambda_{steel} m \cosh\left(m[x - x_0]\right)} \tag{3.1}$$

where x_0 is the abscissa of the bluff body conical section base and $m = 2\left(h_{bb}/\lambda_{steel} D_{cm}\right)^{1/2} = 32.85$ m^{-1} is the steel fin parameter. The heat resistance is minimal at the top of the bluff-body, $R_{bb} = \tanh(mL_c)/(\lambda_{steel} m)$, and should allow the flame to stabilize few millimeters above the bluff body as observed in experiments.

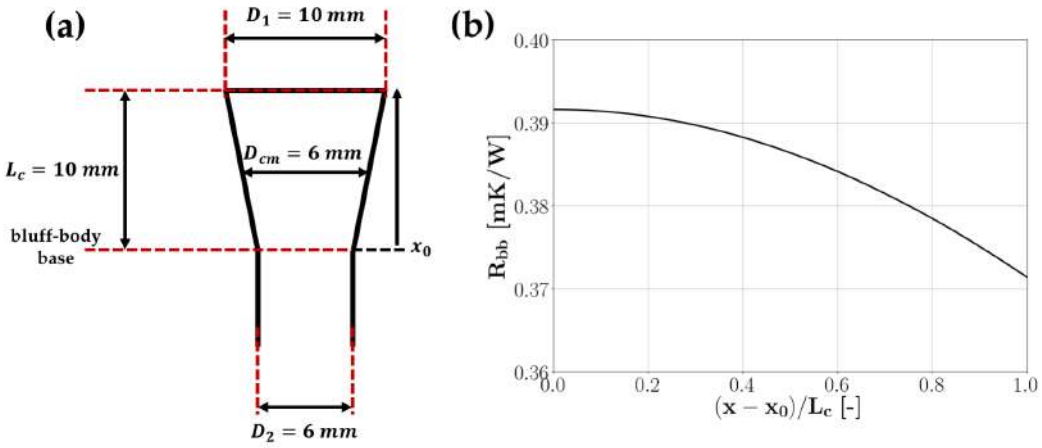


Figure 3.7: (a) Schematic view of the bluff body main dimensions and (b) associated heat resistance.

In the absence of acoustic modulation, a top hat velocity profile with bulk velocity $U_b = 5.44$ m.s^{-1} was imposed at the inlet, and in all cases the outlet pressure was set

to $P_{out} = 1$ atm. The SIGMA model [177] was used to handle subgrid stresses. For reacting cases, the flame/turbulence interaction was handled using the Dynamically Thickened Flame Model (DTFLES [178]) and a two-step BFER chemistry [179] validated for atmospheric conditions. The thickening relied on the constant version of the Charlette efficiency model [180] with an efficiency constant $\mathcal{E} = 0.5$, and used a laminar flame thickness $\delta_f = 4.14 \times 10^{-3}$ m and a laminar flame speed $s_l = 0.284$ m.s^{-1} obtained with one-dimensional premixed flames simulations.

3.3.2 Meshing strategy

For meshing, the mesh adaptation strategy proposed by Daviller *et al.* in [181] was employed to ensure a correct representation of the pressure drop across the swirler and injection channels. It has already been employed with success in [182]. To proceed, a baseline tetrahedra unstructured mesh $M1$ was first created, with refined regions around the swirler, the injection system and the supposed flame zone. The time averaged viscous dissipation defined by:

$$\overline{\Phi} = \overline{(\mu + \mu_t)\left(\frac{\partial u_i}{\partial x_j} + \frac{\partial u_j}{\partial x_i}\right)^2} \tag{3.2}$$

where μ and μ_t are the laminar and turbulent dynamic viscosities respectively was then extracted from the associated LES predictions. A rough analysis of Eq. (3.2) shows that large values of $\overline{\Phi}$ identify regions where the turbulent viscosity is high, or where velocity gradients are important, which typically correspond to zones that are not resolved enough. This quantity is then normalized following :

$$\tilde{\Phi} = 1 - \frac{\overline{\Phi} - \min(\overline{\Phi})}{\max(\overline{\Phi}) - \min(\overline{\Phi})} \tag{3.3}$$

and used as a metric for an automatic refinement process using an implementation of the MMG3D remeshing software [183, 184]. Regions where the metric is unity remain unchanged while regions where it falls below unity are refined accordingly. For instance a region where the metric equals 0.5 should be refined so that its characteristic dimension is half of the original one. It results a mesh $M2$, where the swirler vanes and exit have been refined compared to $M1$. The automatic refinement process is iterated once again with a geometrical constraint on $\tilde{\Phi}$ to only flag the injection and flame regions, yielding mesh $M3$. The metric field and changes between meshes $M2$ to $M3$ can be seen in Fig. 3.8. The non-dimensional metric flags critical flow areas that one may have suspected to need refinement: the injector edges where flow separation occurs, and more generally high velocity gradient zones. As a result, the nodal volume, and thus the local characteristic cell size Δ_x of this regions decreases after the remeshing process. The resulting characteristic dimensions for meshes $M1$, $M2$ and $M3$ are summarized

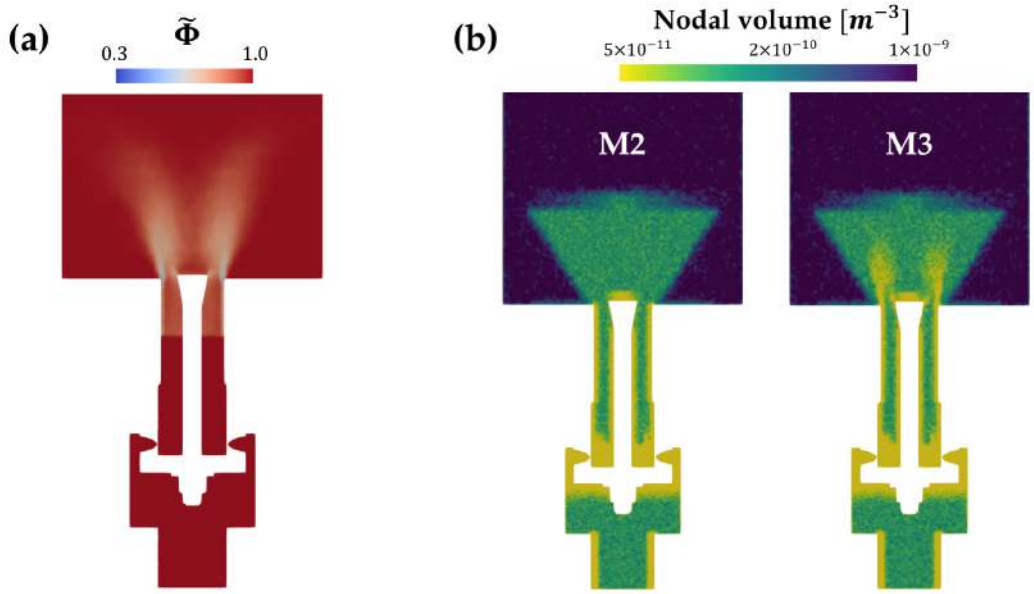
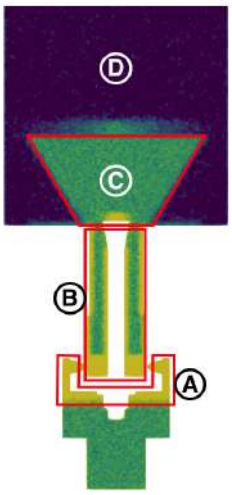


Figure 3.8: (a) Cut view of the metric field used for the second iteration of the automatic refinement process. (b) Nodal volume for the original mesh M2 and after refinement M3.

in Tab. 3.9b for the different mesh zones. One observes that the transition from $M1$ to $M2$ mainly affected the swirler region (zone A), while the transition from $M2$ to $M3$ affected the injector and flame region (zone B and C). Zone D corresponding to the downstream region is of no particular interest for the present study and remains unaffected, with a progressive coarsening towards the outlet. Note that a fourth mesh



(a)

Mesh id.	M1	M2	M3	M4
N_{cells} (Millions)	15.5	16.2	19.1	55.8
Δ_x (A) (mm)	0.31	0.25	0.25	0.16
Δ_x (B) (mm)	0.38	0.33	0.29	0.2
Δ_x (C) (mm)	0.52	0.50	0.48	0.26
Δ_x (D) (mm)	1.0	1.0	1.0	1.0

(b)

Figure 3.9: Cut of mesh M1 with main topologic regions, and associated characteristic cell sizes in each zone for all meshes.

$M4$ was also created in order to assess mesh invariance for reactive simulations. For

that purpose, characteristic cell sizes in zones A, B and C have been divided by two compared to mesh $M1$. This means that while the characteristic cell size in each zone has been lowered compared to $M3$, the latter may still feature a higher local refinement in regions of interest. As a result and despite an increase in the computing power needed to achieve the same physical time, only minor differences were observed between mesh $M3$ and $M4$. The reader is referred to appendix B for further details. As a consequence and unless told so, all results presented in the following are obtained with simulations based on mesh $M3$.

This refinement methodology not only allows the mesh to reach acceptable values of normalized wall distance y^+, but also greatly improves pressure loss predictions across the swirler. As a result a 2% error on the swirler pressure loss is obtained with $M3$ when compared to experiments, Tab. 3.1.

Case	$\mathbf{\Delta P}$ **[Pa]**	$\frac{\mathbf{\Delta P - \Delta P_{exp.}}}{\mathbf{\Delta P_{exp.}}}$ **[%]**	$\mathbf{y^+}$
M1	465.0	38.8	16
M2	364.0	8.7	10
M3	341.3	1.9	7
Exp.	335.0	NA	NA

Table 3.1: Mean pressure loss obtained with meshes M1, M2, M3, and in experiments. The average y+ data for injector walls is also disclosed.

This is of particular importance in the context of combustion instabilities where pressure losses are known to play a role in the damping rate of incoming acoustic perturbations [185, 186]. The most known examples are multi-perforated plates used to create a cold air flow to isolate the combustion chamber casing from the high temperature combustion gas [59]. The acoustic velocity is converted into vortical structures through the apertures, that are carried away along the plate and induce both pressures losses and acoustic damping [187, 188]. The same phenomena is observed for swirl injectors [129, 186]. Figure 3.10 shows the mean pressure along the rig and confirms that most of the pressure drop occurs through the swirler passage vanes.

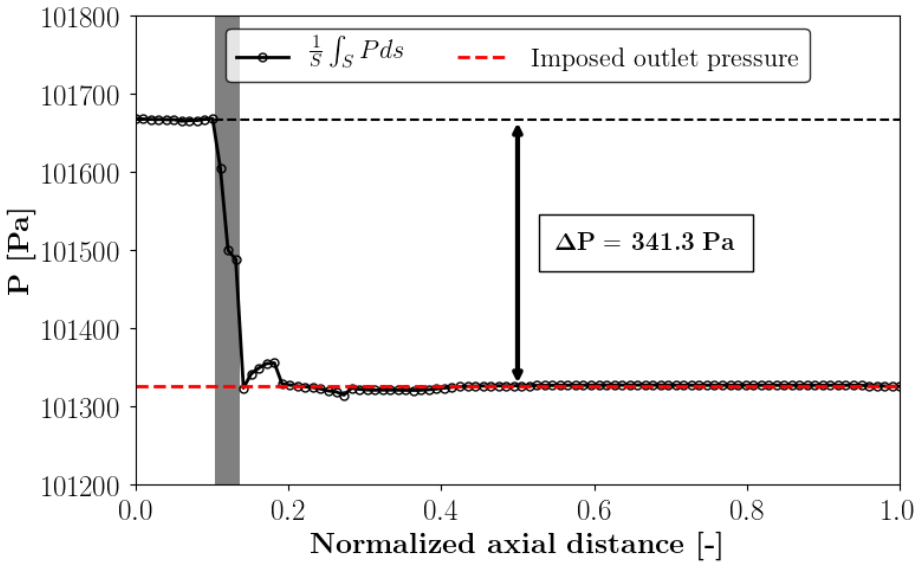


Figure 3.10: Integrated pressure along the vertical axis of the configuration. The swirler area is grayed out. The pressure drop ΔP is defined as the difference between the hot wire and outlet integrated pressures.

3.4 Validation and flame dynamics

3.4.1 Non-reacting flow

In the following, LES results based on mesh $M3$ are first compared to experimental data in non reacting conditions to assess the reliability of the numerical setup without any combustion. As already shown in the last section, pressure losses across the swirler are in very good agreement with experiments. Fig. 3.11 shows the mean field velocity components obtained after 137 ms of stationary simulation, which corresponds to approximately 8.6 inlet to injector backplane flow through times. Note that data is furthermore averaged in the azimuthal direction since the injector diameter to chamber width ratio is low, resulting in a quasi axisymmetric flow. The classic Inner (IRZ) and Outer (ORZ) Recirculation Zones observed for swirling flows are retrieved, and are identified with the axial velocity isocontour $u_x = 0$. The IRZ starts with an elongated shape after the bluff-body tip, only widens downstream of the injection and expands close to the quartz enclosure before closing itself at about one third of the exhaust tube due to the converging flow. LDV measurements available from experiments over

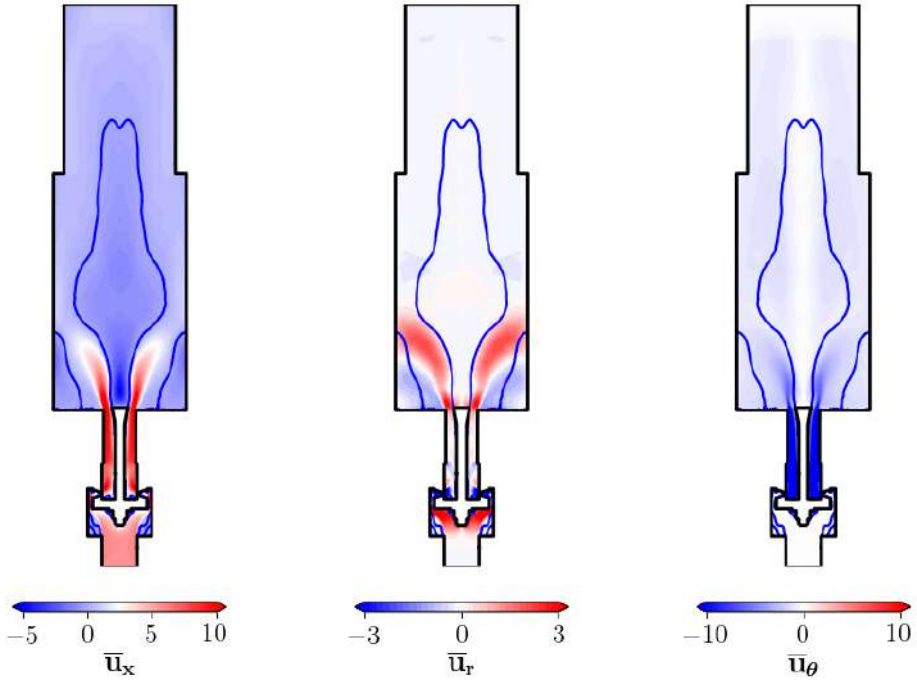


Figure 3.11: View of mean cylindrical velocity components on a transverse cut. Results have been temporally averaged over 137 ms and in the azimuthal direction. Recirculation zones are identified with the isocontour u_x=0 m.s^{-1} (plain blue line).

a line located 3 mm above the chamber backplane are used to gauge the numerical prediction. It is worth noting that measurements were obtained without the enclosing

chamber walls, while simulations are always fully enclosed. A slight overestimation of

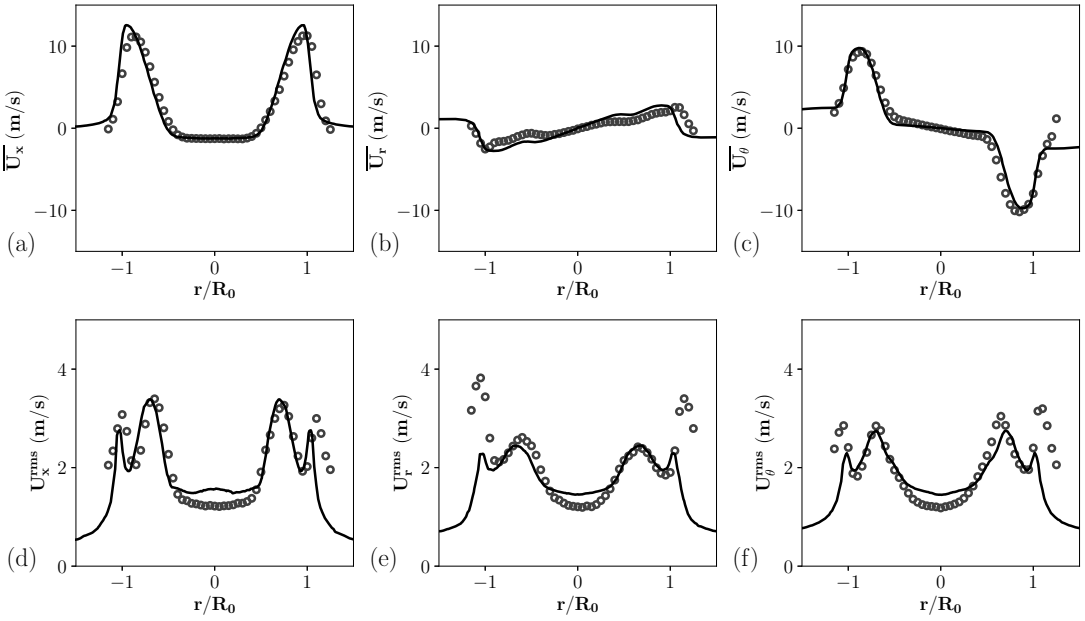


Figure 3.12: Comparison of velocity fields under cold flow conditions measured with LDV (o) and obtained in LES (—), 3 mm above the chamber back plane. (a), (b) and (c) : mean values, (d), (e) and (f) : RMS values of axial (left), radial (middle), and azimuthal (right) velocity components. The axial distance is normalized by the injector radius $R_0 = 10$ mm.

the axial velocity peaks is present, as well as minor discrepancies when $x/R_0 > 1$ for radial and azimuthal velocities, $R_0 = 10$ mm being the injector radius. RMS velocity components, Fig. 3.12d-f, are also in good agreement in the central region where the first series of peak is captured by LES. Again, discrepancies are visible in the outer shear layer ($x/R_0 > 1$) where only the RMS of axial velocity is observed to properly match the experiment. The estimated swirl number from LDV measurements is $S = 0.8$ while the LES yields $S = 0.73$ using the definition of Eq. (1.35). All these minor differences can be attributed to the unconfined experimental measurements versus confined simulations. Another possible explanation lies in the fact that LDV measurements are known to introduce a small bias for turbulent flows [189], and the discrepancies observed here are localized in the outer shear layer of the turbulent swirled jet.

Cold flow PIV data is also available on a vertical plane starting 2 mm above the bluff body tip, that is 3.5 mm above the combustion chamber backplane. Comparisons with simulation results, Fig. 3.13, show again good agreement for both mean and RMS velocity profiles. Additional verifications on several axial locations not shown here for the sake of brevity confirm that the overall excellent agreement still holds when moving away from the chamber backplane. The LES capability to accurately represent the

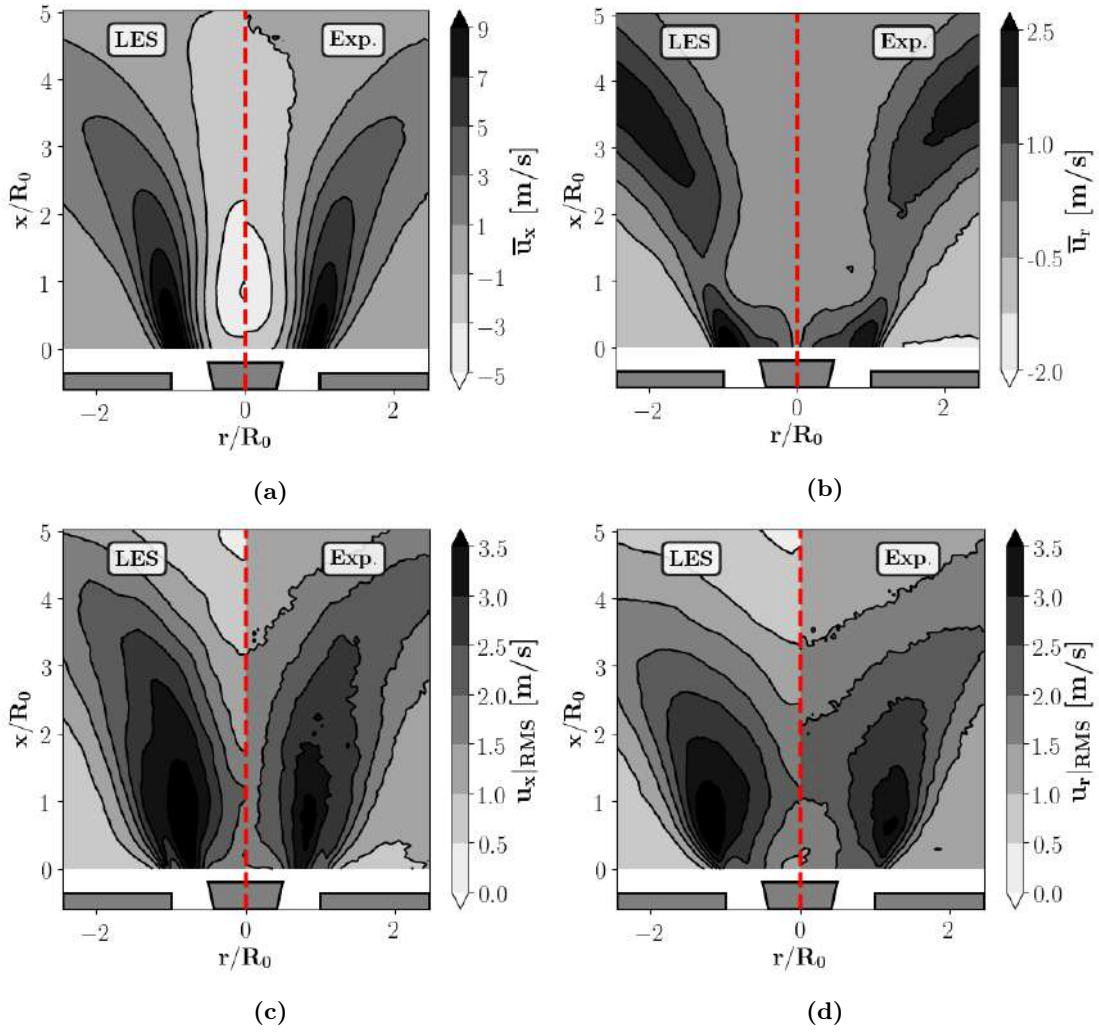


Figure 3.13: Comparison of non reactive flow mean axial (a), mean radial (b), RMS axial (c) and RMS radial (d) velocity profiles for LES (left) and PIV (right) on a vertical plane.

swirling flow is thus proven for the non reactive setting, allowing to proceed to the reacting conditions with confidence.

3.4.2 Stable reacting flow

The stable flame is studied before applying any acoustic forcing in order to validate the adopted modelling strategy. In the analytical FTF framework introduced in Sec. 2.3, flame characteristic dimensions are directly used to evaluate parameters ω_* and α of the SFTF model. An accurate prediction of the steady-state flame location and anchoring is hence mandatory.

Downstream of the injector, the flow structure is of course modified by the presence of the flame in comparison to cold flow conditions, Fig. 3.14. The expansion of the burnt gas increases the flow velocity near the flame, pushing the flow outer recirculation zones

downwards while the inner recirculation zone expands in the radial direction. As a result, the flow angle at the injector exit increases

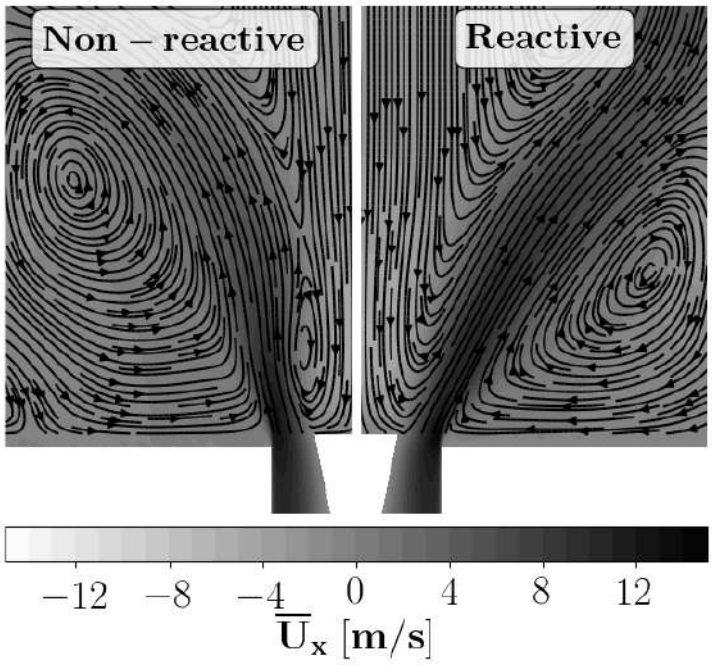


Figure 3.14: Non-reactive (left) and reactive (right) axial velocity pseudo-streamlines on a transverse cut plane.

The flame shape is inspected using the normalized mean heat release rate $\overline{Q}$ from the LES and compared to an Abel transform of OH^* signals issued by a photomultiplier in Fig. 3.15. This chemical radical has been widely used as a marker of the volumetric heat release rate for premixed flames [190]. In the steady state reacting regime, LES as well as experimental observations indicate that the flame has a classical V shape and is stabilized few millimeters above the bluff-body tip. The flame opening angle and main dimensions are reproduced, though a minor difference in flame height can be observed. This could influence the evaluation of the convection time ω_*/ω used for the SFTF model. This difference may possibly be explained by the limited thermal data available for the LES to match experiments, as well as by the fact that two different quantities of interest are used for comparisons (OH^* and Q). Indeed, in experiments the flame exhibits a larger lift-off distance than in LES, which may imply that the bluff-body tip temperature is lower than the value estimated from simulations. The high velocity swirling flow near the injector exit plane issues a turbulent flame as can be observed on a transverse cut plane for four different times in Fig. 3.16. The V-shaped structure can be decomposed into two main central branches and two lesser outer secondary branches that can either extend or almost disappear over time, leading to an intermittent release of hot gases pockets as seen on the top-left image of Fig. 3.16.

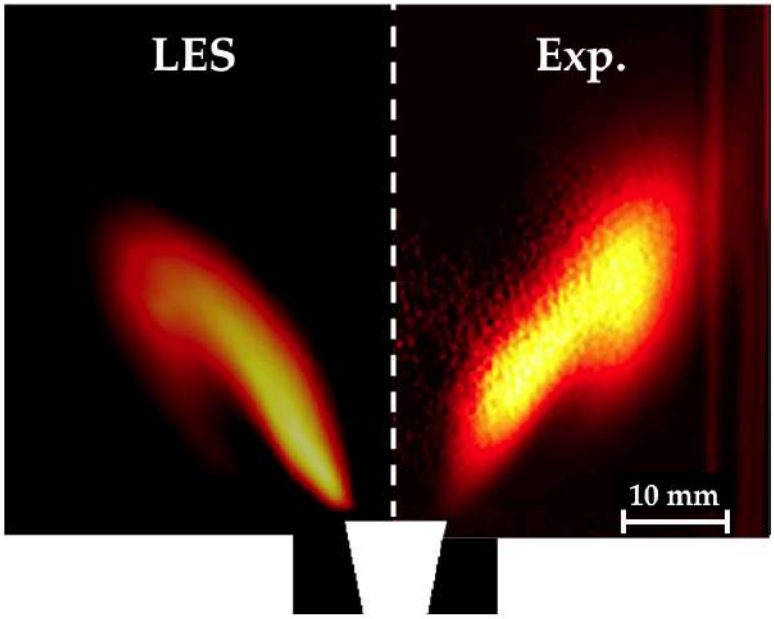


Figure 3.15: Comparison of steady flame shapes. On the left, LES volumetric heat release rate averaged over 80 ms (5 flow-through times). On the right, Abel transform of OH^* signals from the CCD camera with a narrowband filter centered around 310 nm averaged over 100 samples.

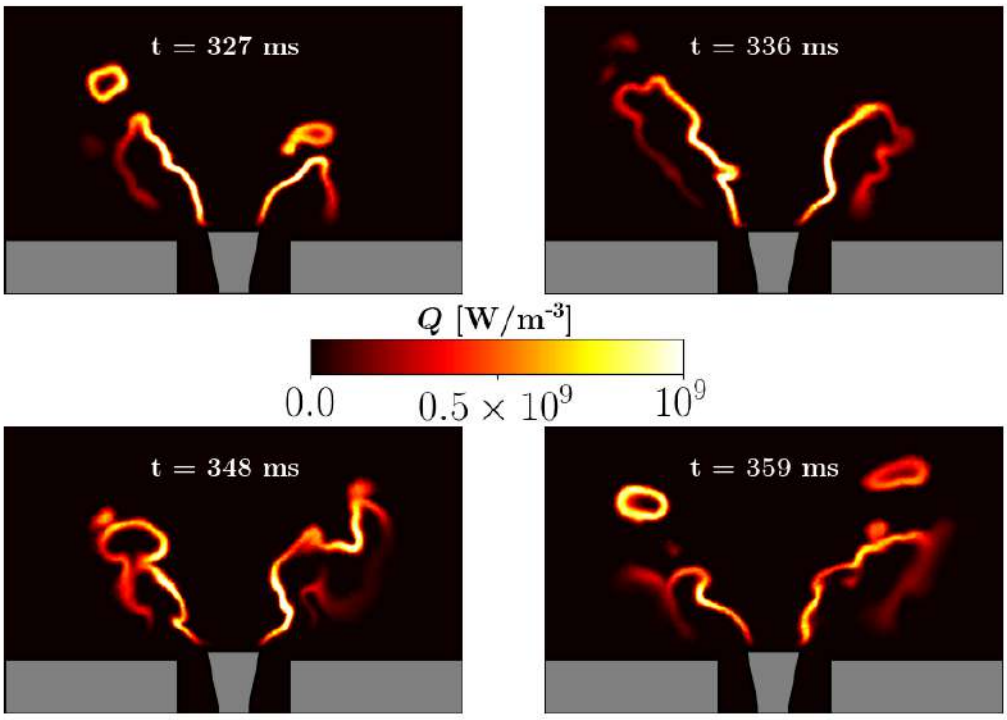


Figure 3.16: Visualization of the instantaneous volumetric heat release rate Q on a transverse cut for four distinct instants as obtained from reacting LES.

A validation study of the reactive LES is carried out by making use of PIV reference data obtained from experiments on an axial plane starting 3.5 mm above the bluff-body tip (5 mm above the combustion chamber backplane). In this case, PIV data was extracted in presence of the flame and with the quartz/metal enclosure. Fig. 3.17 shows a qualitative comparison between PIV and numerical results while Fig. 3.18 compares axial and radial velocities for various axial positions. Mean velocity profiles are in

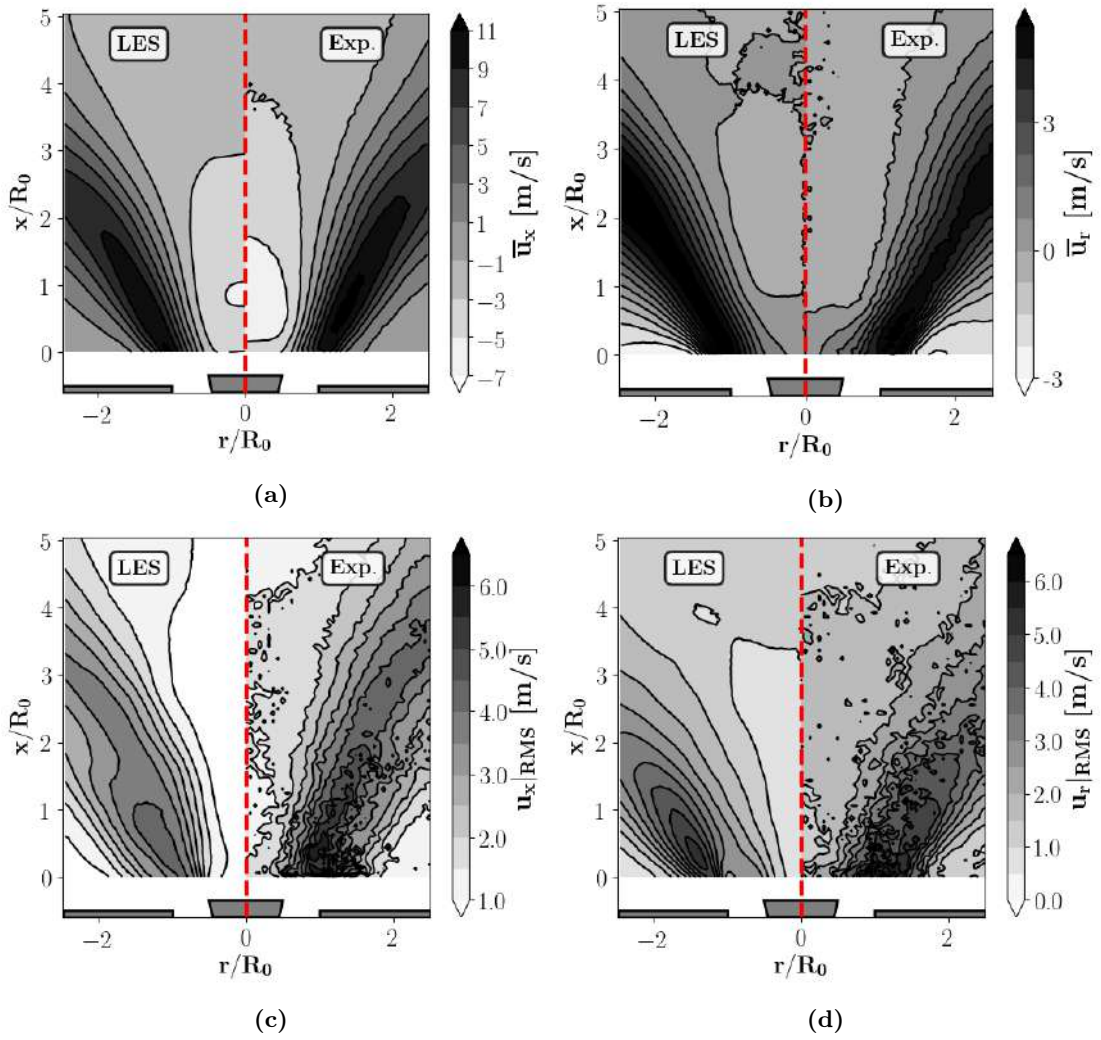


Figure 3.17: Comparison of reactive flow mean axial (a), mean radial (b), RMS axial (c) and RMS radial (d) velocity profiles for LES (left) and PIV (right) on a vertical plane.

excellent agreement with the experiment for all axial positions. For RMS velocities, a good agreement is observed. The simulation misses some of the fluctuations in the lower part of the IRZ ($x/R = 0$ to $x/R = 0.8$) but catches the correct local peak values. Overall, LES is able to capture the stable flame reactive flow features with good accuracy, allowing to move on with confidence to acoustically pulsed simulations

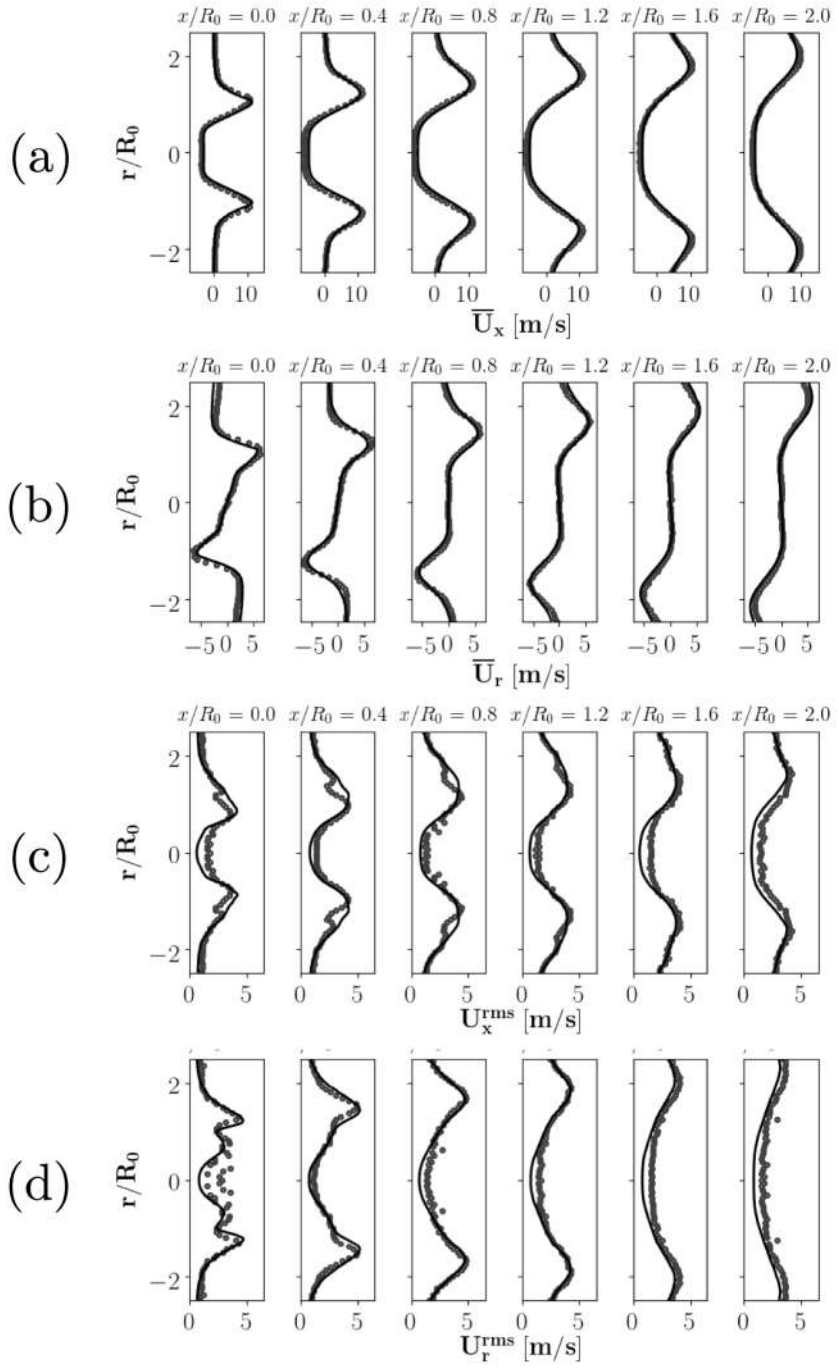


Figure 3.18: Comparison of reactive flow mean axial (a), mean radial (b), RMS axial (c) and RMS radial (d) velocity profiles for various axial locations. Exp. in grey dots(o) and LES in solid black line — . $x/R_0 = 0$ corresponds to the bottom of PIV data, that is 5 mm above the combustion chamber back plane.

3.4.3 Acoustically pulsed flows

3.4.3.1 Forced flame response

Building up on both stable reacting and non reacting cases, CFD simulations are now submitted to a uniform acoustic modulation at the inlet of the domain. In experiments, this is achieved by replacing the bottom part of the injection device by a loudspeaker and manually adjusting the feeding signal frequency content and amplitude. For LES, the inlet boundary condition is modified by adding a 30% RMS amplitude uniform velocity modulation, corresponding to 2.3 m.s^{-1} variations at the HW location, Fig. 3.1, with a unique frequency in the range 80-200 Hz. NSCBC relaxation coefficients are set low enough so that the target mass flow rate does not drift and spurious acoustic reflections are avoided [191]. Doing so, the amplitude of pressure fluctuations obtained at the HW position in the simulations cannot be perfectly controlled. As a result, these are slightly overestimated compared to experimental levels observed from the microphone in front of the HW. This aspect should however have a limited influence for the present study. Before any actual analysis of the forced dynamics, it is interesting to note that the acoustic time delay τ_{IN-SW} between the reference section (Hot wire position) and the injector exit is negligible, $\tau_{IN-SW} = 0.10$ ms. This represents only 2% of the lowest pulsation period investigated corresponding to $f = 200$ Hz. Reactive forced simulations are carried out for a set of eight frequencies between 80 and 200 Hz. For a given frequency f, the corresponding period will be denoted as $\tau_f = 1/f$ in the remaining of the manuscript.

For each forcing frequency, the flame is forced for a minimum of seven clean periods, *ie* seven periods after the initial transient necessary to establish the forced flow, Fig. 3.19. Global heat release signals are obtained by integrating the volumetric heat

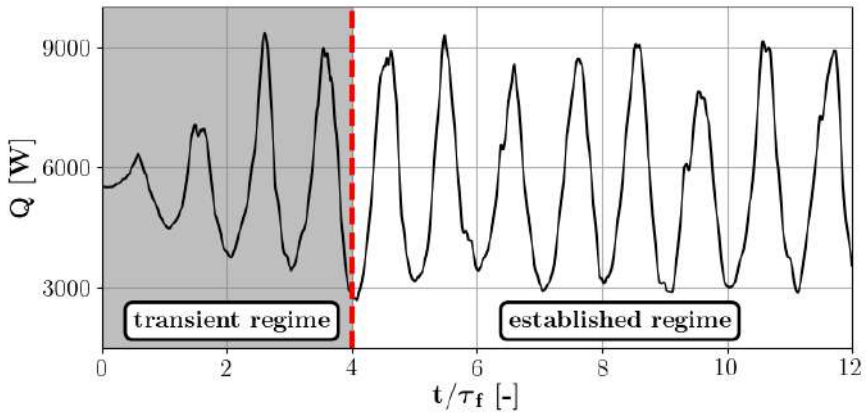


Figure 3.19: Global heat release rate temporal signal as obtained with LES with a forcing amplitude $\hat{u}_{ref}/\overline{u}_{ref}$ = 30% at f = 180 Hz. The grayed out zone corresponding to a transient regime is discarded for FTF measurements. $\tau_f = 1/f$ is the forcing period.

release rate over the complete fluid volume for each time step. In all cases, the reference velocity denoted as u_{ref} corresponds to the axial velocity u_x probed at the hot wire position, right in the center of the circular cross-section. The mean velocity for this centerline position is $\overline{u}_{ref} = 5.44$ m.s^{-1}. The flame response is evaluated by means of a Fourier analysis of the global heat release rate Q integrated over the domain, and of the velocity reference signal. The gain n_{FTF} and phase ϕ_{FTF} of the FTF at the forcing frequency are computed as :

$$n_{FTF} = \left| \frac{\hat{Q}}{\overline{Q}} . \frac{\overline{u}_{ref}}{\hat{u}_{ref}} \right|, \tag{3.4}$$

$$\phi_{FTF} = \arg\left(\hat{Q}\right) - \arg\left(\hat{u}_{ref}\right), \tag{3.5}$$

with $\overline{Q} = P_{th} = 5.44$ kW. Examples of velocity and heat release signals used are available in Fig. 3.20 for $f = 120$ Hz and $f = 180$ Hz. Heat release signals are marked by the

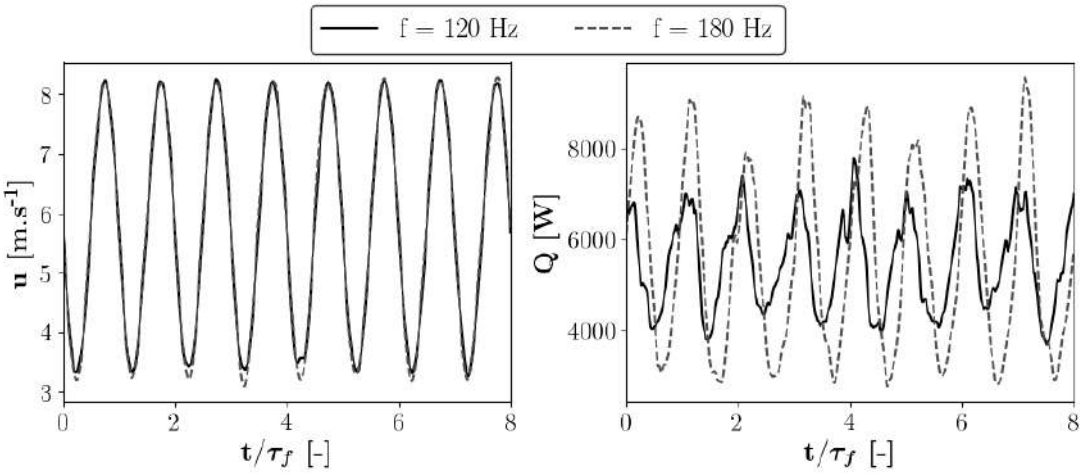


Figure 3.20: Reference velocity (axial velocity at the hot wire position, left) and heat release (right) signals for f = 120 Hz and f = 180 Hz. The flame power is $P_{th} = 5.44$ kW.

forcing frequency and are not perfect sine waves since the swirling flame is turbulent. One can immediately see that for the same excitation amplitude, the flame response in terms of heat release is stronger for $f = 180$ Hz, which will translate into a higher gain for this particular frequency. The flame response time delay varies with frequency, thus heat release signals for the two frequencies are in phase quadrature. Global simulation results are compared to experimental data in terms of FTF gain and phase in Fig. 3.21. A very good agreement is obtained for both FTF gain and phase for the eight tested frequencies. In particular, the characteristic high and low gain regions of a swirled V-shaped flame anchored on a bluff-body are well retrieved. The phase shift around $f_1 = 120$ Hz is also captured, though a minor difference between the LES at $f = 80$ Hz and the reference data is seen.

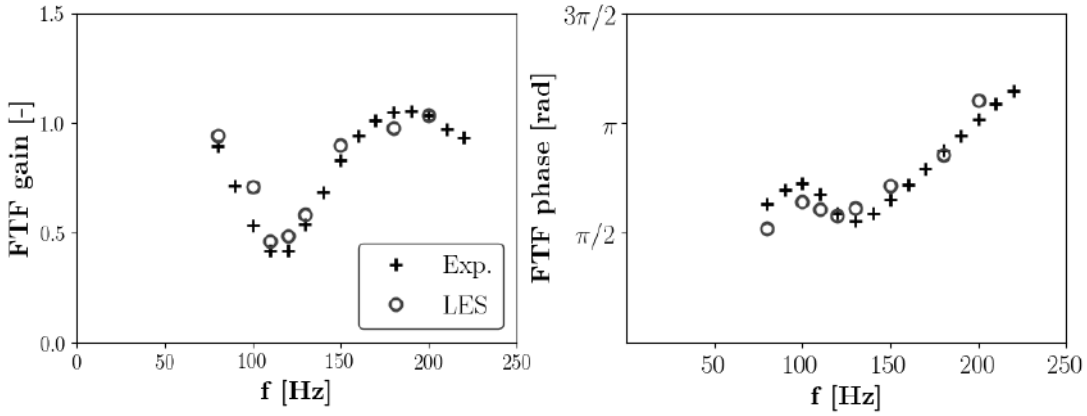


Figure 3.21: Flame transfer function of the NoiseDyn burner: gain (left) and phase (right). Single frequency pulsed LES data (grey circles) is compared to experimental measurements (black crosses). Bulk velocity $\overline{u}_{ref}$ = 5.44 m.s^{-1}, $\hat{u}_{ref}/\overline{u}_{ref}$ = 30%.

From these data it is confirmed that contrarily to conical laminar flames, the FTF gain of such flames is not quasi monotonous [143]. One may now explore the physical mechanisms responsible for the low FTF gain at $f_1 = 120$ Hz and the high gain for $f_2 = 180$ Hz. In configurations like the one studied here, vortices are shed from the edge of the injector exit and travel along the shear layer, affecting the velocity field near the flame and its response to acoustic modulation. As already mentioned in Sec. 2.2.2, and according to Palies *et al.* [106], the difference between low and high gains regions of the FTF can be explained by different flame dynamics behaviours :

- in the high gain regions, the flame base angle remains unaffected so that vortices have more time to travel along the flame,
- in the low gain regions, the flame base angle exhibits variations so that vortices are quickly "destroyed" by the flame flapping movements

These authors performed experiments [106] as well as numerical simulations [163] to specifically address this issue and showed that low swirl number fluctuations were associated to high gains while high fluctuations coincided with low gains. In this latter case, the flame base angle was modified, enhancing or preventing the development of vortices that would interact with the flame downstream. One major difference with the current setup however is that the forced flame entered the injector for some forcing frequencies, which is never the case in the present study. Bunce *et al.* [164] hinted that the presence of local FTF gain extrema was the result of an interaction between the flame and a Kelvin-Helmoltz instability in the mixing layer of their partially premixed configuration. Since the case studied here is fully premixed, one cannot use this argument. In recent works, Gatti *et al.* [162, 169] showed that preferential vortex shedding for certain

frequencies occurs even in the absence of a flame for high swirl levels, possibly pointing out that the flame is not the only or even the main driver of the preferential acoustic response. Based on this new finding, an extended analysis at two forcing frequencies f_1 Hz and f_2 Hz is carried out thanks to the current predictions to confirm or invalidate the reported statements.

In terms of flame dynamics and as reported experimentally, the flame response is different between f_1 and f_2 as shown by phase averaged images in Fig. 3.22 and 3.23, where five phases covering a complete forcing cycle are used. The phase φ is defined from the velocity signal at the hot wire position (see Fig. 3.1): $\varphi = 0$ correspond to null acoustic velocity while $\varphi = \pi/2$ corresponds to a maximum. Experimental phase

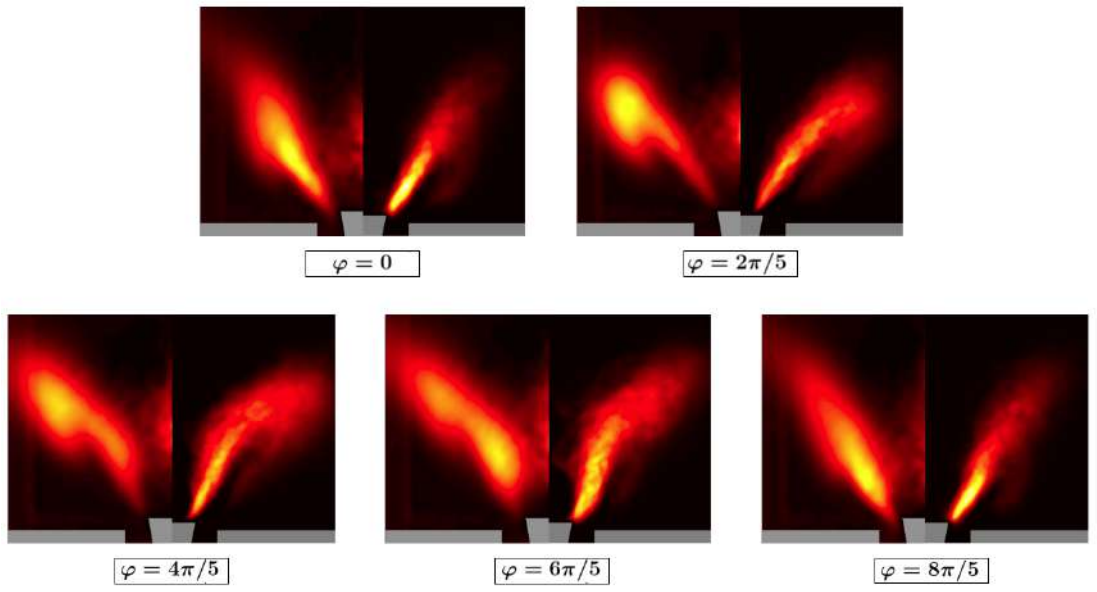


Figure 3.22: Abel transform of phase averaged OH* chemiluminescence pictures from experiments (left parts) and phase averaged field of normalized heat release rate from LES (right parts) for a forcing frequency f = 120 Hz.

averaged images (left part of each picture) have been built using 100 snapshots with a 40 μs exposure time while LES phase averaged images (right part) have been built using the azimuthally averaged heat release rate with ten phases over twelve periods, and normalized using the common maximum value for the two frequencies. Note that the experimental configuration used to obtain these images is slightly different from the one studied in this section, with a bluff-body tip protruding 1 mm higher in the chamber. Still, almost no difference was observed for the final measured FTF and conclusions should hold at least from a qualitative point of view. The flame motion itself does not differ for the two forcing frequencies, but it is more pronounced for f_2 corresponding to a high FTF gain. During the first phase of the forcing cycle ($\varphi = 0$ and $\varphi = 2\pi/5$) the flame branch is elongated and the most energetic zone is displaced from the flame base

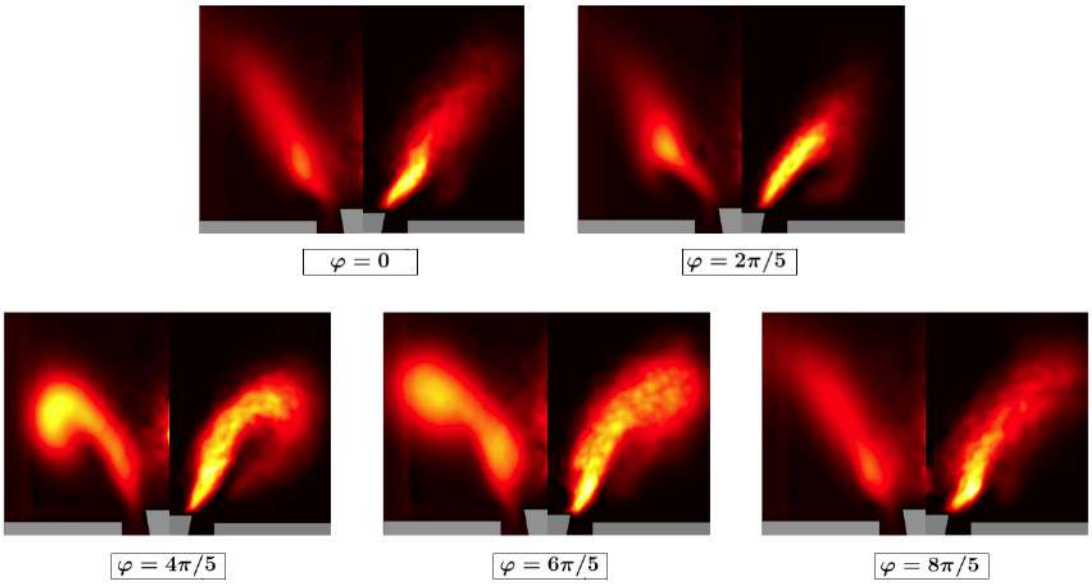


Figure 3.23: Abel transform of phase averaged OH* chemiluminescence pictures from experiments (left parts) and phase averaged field of normalized heat release rate from LES (right parts) for a forcing frequency f = 180 Hz.

to a higher axial location. In a second step ($\varphi = 4\pi/5$ and $\varphi = 6\pi/5$), the tip of the flame rolls up on itself, thus increasing the reacting surface, while the base of the flame is pushed further downstream. In the final step ($\varphi = 8\pi/5$), the flame progressively goes back to its original anchoring position as large pockets of burnt gases have detached from the flame extremities. For f_2, one observes a stronger rolling motion of the main flame branch for this frequency compared to f_1. Also, relative levels of heat release rate indicate that the flame releases more heat at f_2: in agreement with the higher FTF gain. Coming back to the original statement of Palies *et al.* [106], while experiments may show slightly larger flame base angle variations for f_1, LES does not exhibit a significant difference between f_1 and f_2. Still, LES obtained FTF gain and phase for these two frequencies match the reference, which tends to indicate that the flame base angle variation is not the main driver of the preferential acoustic response, at least for the present configuration, which is different from the one of Palies *et al.* [106].

3.4.3.2 Preferential frequency response of the swirling injector

Further investigation is carried out regarding the roll-up motion of the forced flame tips, by taking a deeper look at the shape of the inner recirculation zones and the paths followed by vortical structures shed from the injector exit rim. Figures 3.24 and 3.25 present such an evolution of vortical structures for f_1 and f_2 respectively. On these figures, the inner recirculation zone is identified by the isocontour $u_x = 0$ m.s^{-1} and further emphasized by the isocontour $u_x = -2.5$ m.s^{-1}. For visualization purposes, a

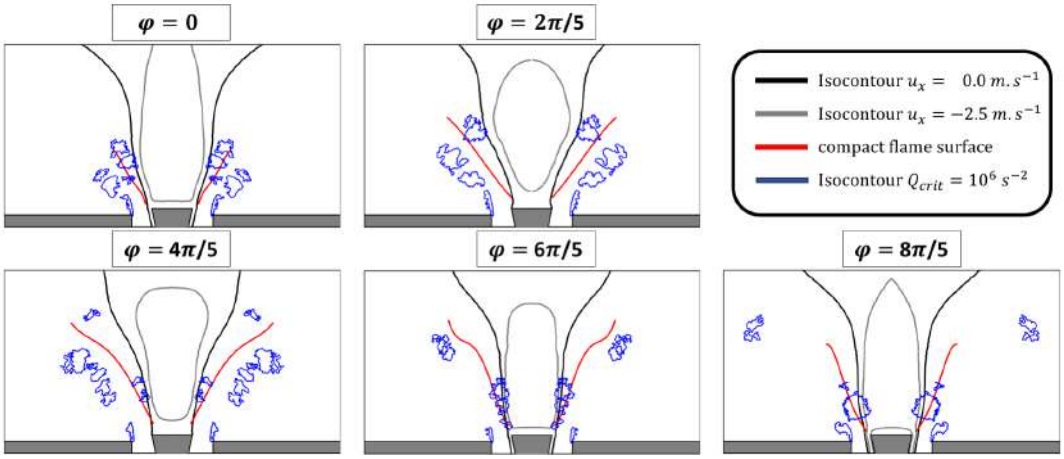


Figure 3.24: Azimuthally and phased averaged fields for f = 120 Hz, the phase reference is at the hot wire. The inner recirculation zone is marked with the black line. The plain red line illustrates the flame position if it was assumed to be infinitely thin. Vortices shed from the injector lip and bluff body edges are visualized with a Q-criterion isocontour (blue lines).

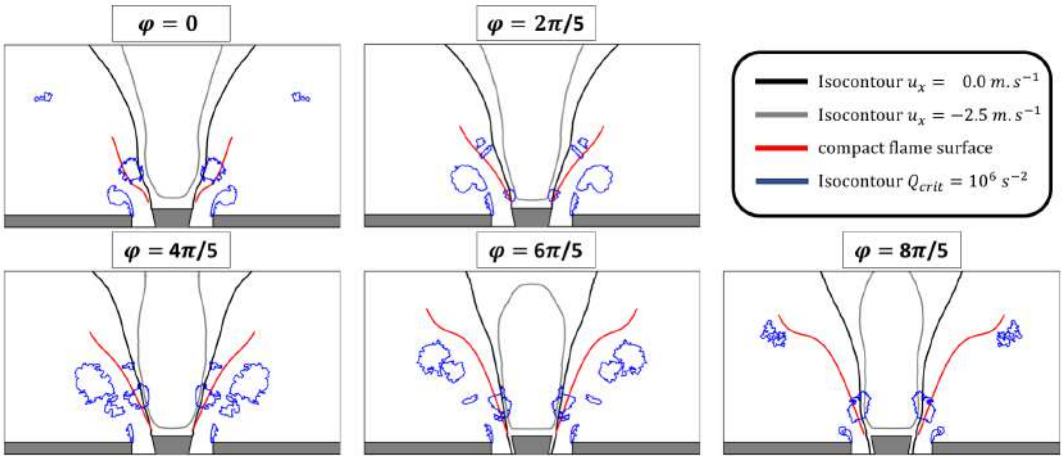


Figure 3.25: Azimuthally and phased averaged fields for sf = 180 Hz, the phase reference is at the hot wire. The inner recirculation zone is marked with the black line. The plain red line illustrates the flame position if it was assumed to be infinitely thin. Vortices shed from the injector lip and bluff body edges are visualized with an isocontour of the Q-criterion (blue lines).

red line representing the potential compact flame surface is shown. It was obtained by taking the maximum heat release rate for a collection of axial positions x_i only if it was superior to half of the maximum value. Note that this criterion is purely qualitative as it does not allow to precisely recover the flame roll-up motion at the tip. It is however sufficient for comprehension purposes. Shed vortices are then tracked using a Q-criterion [192] isocontour with an adequate threshold value $Q_{crit} = 10^6$ s^{-2}. The first noticeable effect of forcing is that the inner recirculation zone undergoes different variations during an oscillation cycle depending on the forcing frequency. For $f_1 = 120$ Hz, the isocontour

$u_x = 0$ m.s^{-1} indicates that the upper half of the IRZ withstands important width variations during a cycle, while for $f_2 = 180$ Hz it is essentially elongated in the axial direction. Considering the isocontour $u_x = -2.5$ m.s^{-1} further reveals that the IRZ core region is always shorter for f_1 compared to f_2. The origin of these motions is directly linked to velocity profiles at the injectors exit plane shown in Fig. 3.26. For both frequencies, the maximum velocity is observed near the outer wall of the injection channel, at $r/R_0 = 0.95$. At this specific radial position, the axial velocity amplitude over an oscillation cycle is $\Delta u_{max} = 6.3$ m.s^{-1} for $f = 120$ Hz, but reaches $\Delta u_{max} = 8.5$ m.s^{-1} for $f = 180$ Hz. For the latter frequency, higher temporal variations of the maximum axial velocity may indicate that strong vortical structures are generated by the stronger shear stress at the injector exit rim, and are able to travel in the outer shear layer, as observed in Fig 3.25. These structures then distort the flame sheet and stretch the IRZ in the axial direction.

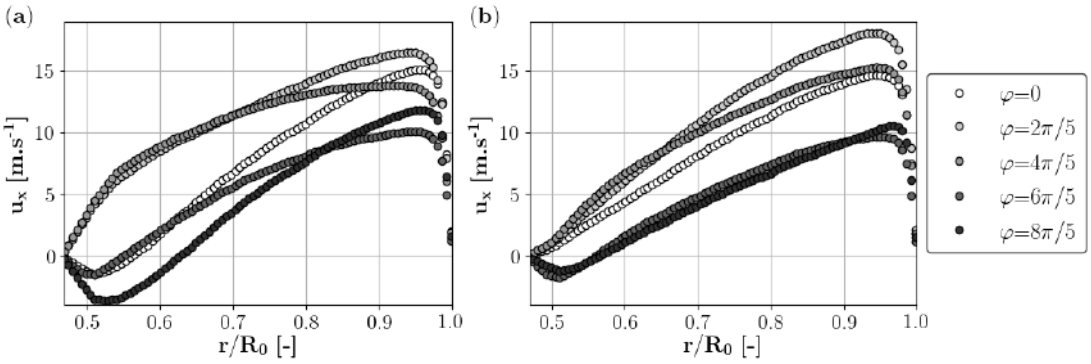


Figure 3.26: Axial velocity profiles at the injector exit plane for different phases of the forcing cycle for (a) f = 120 Hz and (b) f = 180 Hz .

To validate this assumption, a supplementary study is carried out using integrated data at the injector exit plane. The evolution of the fluctuating swirl number is computed from velocity profiles for both frequencies, with results shown in Fig. 3.27. It is recalled that $\varphi = 0$ corresponds to $\hat{u}_x = 0$ m.s^{-1} at the hot wire position. For $f = 120$ Hz, fluctuations have a sine profile while for $f = 180$ Hz the profile is not symmetric and shows a lower first local extremum but then a higher one for the second local extremum. The amplitude from a positive to a negative peak value is the same for both frequencies. An analysis of swirl number fluctuations is therefore not sufficient to draw conclusions on the occurrence of low or high FTF gain. The swirl number is defined as the ratio of the axial momentum flux G_x and the angular momentum flux G_θ, Eq. 1.35. It is therefore also worth analysing these momentum flux, Fig.3.28 and 3.29. In addition to the total fluxes on the surface, and noting r_i, r_o the inner and outer radii of the injection channel, the distinction is made between the contribution of the inner region noted "in" and corresponding to $r_i \leq r \leq (r_i + r_o)/2$, and the outer

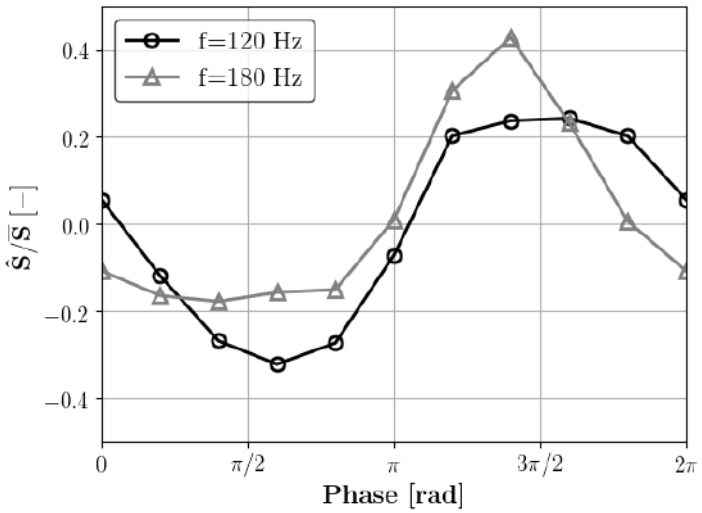
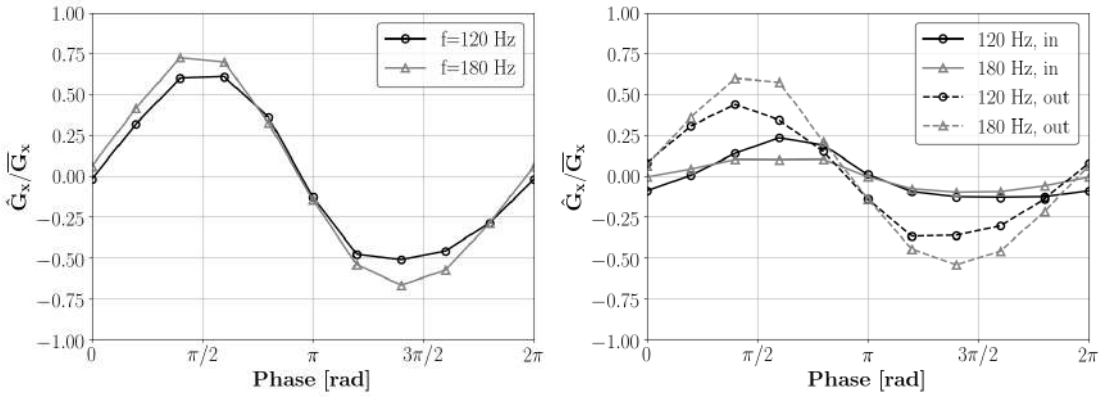


Figure 3.27: Swirl fluctuations at the injector exit during a forcing cycle for f = 120 Hz and f = 180 Hz.

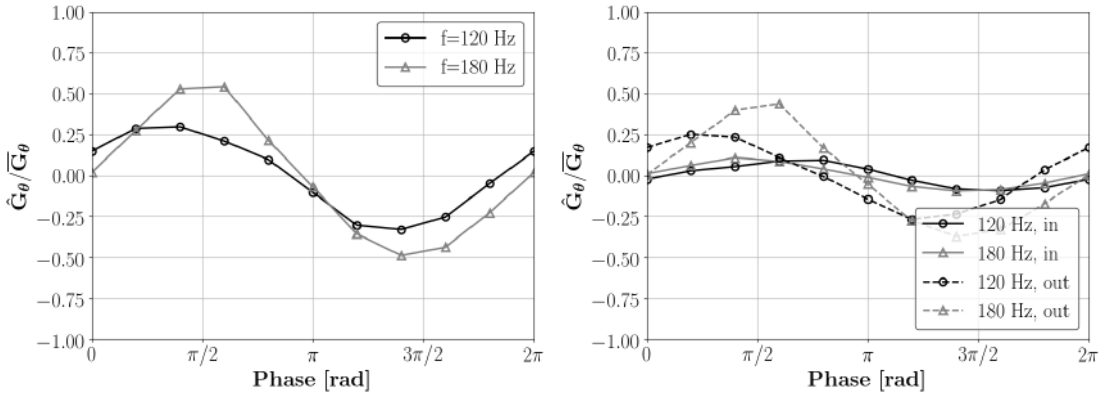
region noted "*out*" for which $(r_i + r_o)/2 \leq r \leq r_o$. LES results show that the total axial momentum flux is similar and in phase for both frequencies. However, the balance between inner and outer injector regions contributions differs significantly depending on the forcing frequency. The outer region contribution is higher for $f = 180$ Hz than for $f = 120$ Hz. Regarding the angular momentum, the total flux is higher for $f = 180$ Hz than for $f = 120$ Hz, and the contribution of the inner injector zone is low. Total and outer regions G_θ signals are thus similar. Note that this time, a $\pi/5$ phase is observed between angular momentum fluxes signals at $f = 120$ Hz and $f = 180$ Hz. From these observations, one can state that both axial and angular momentum fluxes are stronger for $f = 180$ Hz in the region of interest, that is the outer portion of the injector section. Consequently, the circulation strength of vortices generated at the outer rim of the injector exit is higher, wich corroborates LES observations of Fig. 3.24 and 3.25.

A particular attention is drawn to the instant where detachment occurs. The latter is identified as the instant for which the ratio of the vortex "tail" width W_Q to axial length L_Q is minimum, provided that the circulation computed inside the Q_{crit} contour is at least half of its maximum value during a cycle, see Fig. 3.30. From Fig. 3.24 one finds that a vortex is shed from the injector lip for phase $\varphi = 8\pi/5$ for frequency $f = 120$ Hz, and from 3.25 that this vortex shedding is delayed to $\varphi = 0$ for frequency $f = 180$ Hz. Making the link with data of Fig. 3.28 and 3.29, in the first case the vortex detaches from the wall when fluctuations of both axial and angular momentum flux are high. The high rotation rate forces the IRZ to move downwards and opens up the flame base angle. The vortex created is quickly torn apart and is not able to effectively modify the flame surface. In contrast, for $f = 180$ Hz, an annular vortex ring is shed later in the oscillation cycle, when momentum flux fluctuations are minimal. Consequently, the



(a) (b)

Figure 3.28: Axial momentum flux fluctuations at the injector exit for f = 120 Hz and f = 180 Hz. (a) total flux (b) flux in the central region (noted *in*, $r_i \leq r \leq (r_i + r_o)/2$) and in the near wall region (noted *out*, $(r_i + r_o)/2 \leq r \leq r_o$).



(a) (b)

Figure 3.29: Angular momentum flux fluctuations at the injector exit for f = 120 Hz and f = 180 Hz. (a) total flux (b) flux in the central region (noted *in*, $r_i \leq r \leq (r_i + r_o)/2$) and in the near wall region (noted *out*, $(r_i + r_o)/2 \leq r \leq r_o$).

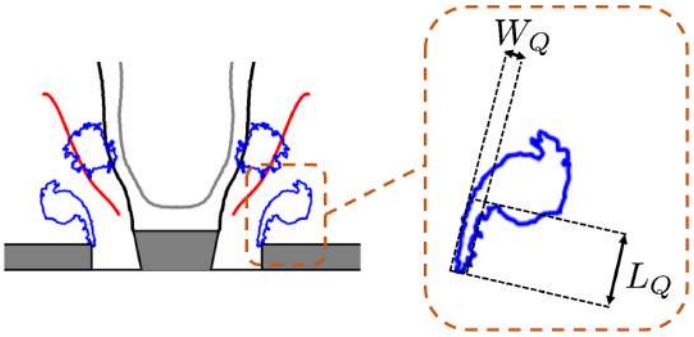


Figure 3.30: Schematic representation of the vortex dimensions used to identify the shedding instant.

IRZ has time to move upwards again and the flame base angle is smaller than in the

$f = 120$ Hz case. The vortical structure is thus not only strong, but also able to roll up along the flame front and thus, generate unsteady heat release by wrinkling the flame surface. This behaviour was already observed in [163] where the preferential dissipation of vortical structures was attributed to the flame: supposedly, vortices are dissipated when the flame opening angle is large. In the present study as well as in [162], it is shown that this phenomena does not depend on the flame as the same conclusions can be drawn from a non-reacting study. Figure. 3.31 discloses vortices as identified from a binarization procedure under non-reacting conditions: a vorticity threshold is chosen, the Q-criterion is then multiplied by 1 if the local vorticity is above the chosen value, or 0 else, yielding a new binarized field Q_{bin}. The observation is once again made that for f_1,

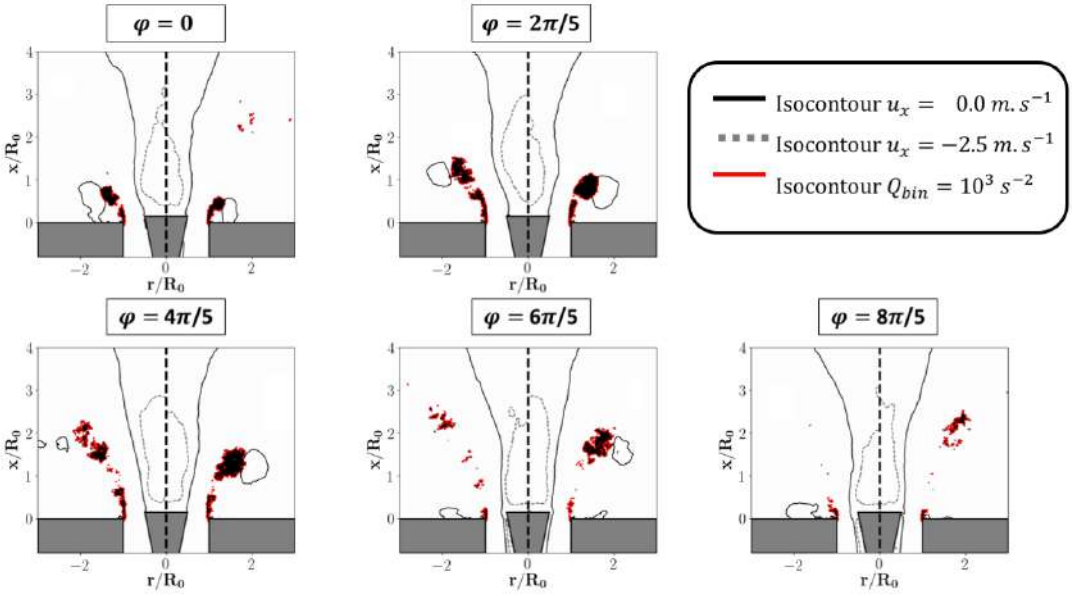


Figure 3.31: Phase averaged images of binarized Q-criterion Q_{bin} for f = 120 Hz (left) and f = 180 Hz (right), non-reacting LES.

vortical structures are created at the injector exit edges but are quickly torn apart into smaller ones during the cycle. On the contrary, large vortices are formed at $f_2 = 180$ Hz and are able to travel a non-negligible distance along the shear layer before being broken down. This confirms that the swirling flow induces a mechanism enhancing the generation vortices at certain frequencies, that will in turn be able to perturb positively or negatively the flame surface and hence the associated unsteady heat release. This mechanism is directly controlled by the response of the injector, Fig. 3.26, as annular vortices are shed at different instants in the forcing cycle depending on the momentum fluxes balance at the injector lip. In the present case, not only are generated vortices weaker for $f = 120$ Hz, but also since the shedding process occurs at an instant where the angular momentum is large, the IRZ is pushed downwards and breaks the annular

structure. For $f = 180$ Hz, vortices are both stronger and released when the fluctuating angular momentum flux is low.

It is concluded that the preferential vortex roll-up cannot be explained solely by global quantities such as swirl fluctuations and should instead be determined from an analysis of the unsteady rotating flowfield at the injector exit edge. This frequency dependent response of the injector will in turn affect the premixed flame acoustic response as shown in the FTF gain curve of Fig. 3.21.

3.5 SFTF model application

3.5.1 Model parameters from stationary data

In a first attempt to characterize the FTF of a V-shaped swirled flame, parameters of the SFTF model detailed in Sec. 2.3.2 are determined from a single simulation corresponding to the stationary flame situation. Although it would be unlikely for the SFTF model to already be able to accurately represent the FTF without any forced flame dynamics data, characterizing the role of each of the model parameter and how it contributes to a good estimation is important.

LES results are used to probe geometrical quantities of interest needed to determine the reduced frequency $\omega_* = \omega L_f^2/(\overline{u}_x H_f)$ from Eq. (2.20) as well as the half flame angle α. Note that in this expression, the flame displacement speed is not used because it is difficult to determine for a swirling flame. It has been replaced by quantities that are easier to determine from experiments or numerical simulations namely H_f and L_f defined in Fig. 3.32. A wide variety of flame dimension definitions is available in the literature, the most common ones rely on isolevels of a variable representative of the flame front (typically the heat release rate or a progress variable computed from temperature or species mass fractions) in the case of numerical simulations. In this document, dimensions are defined from the location of the center of mass of the volumetric heat release rate Q field obtained from time and azimuthally averaged solutions [193]. This robust definition does not leave any place for an arbitrary choice and can be easily applied to various flame shapes. Given N, the number of nodes in the solution, the centroid coordinates (x_c, y_c) of the heat release rate distribution in a vertical plane are given by:

$$x_C = \frac{\sum_{k=1}^{N} Q_k \; x_k \; y_k}{\sum_{k=1}^{N} y_k \; Q_k} \quad \text{and} \quad y_C = \frac{\sum_{k=1}^{N} Q_k \; y_k \; y_k}{\sum_{k=1}^{N} y_k \; Q_k} \tag{3.6}$$

Coordinates for the flame anchoring point are much less sensitive to its definition. It is here defined as the lowest point in the axial direction where Q is at least superior to 1% of its maximum value. Figure 3.32 shows the position of the retrieved centroid

of heat release rate distribution and the associated flame dimensions. Even though the flame features secondary branches, its most energetic region is located in the center of the main branch. For the specific configuration of this section, one gets : $R_f/R_0 = 1.0$,

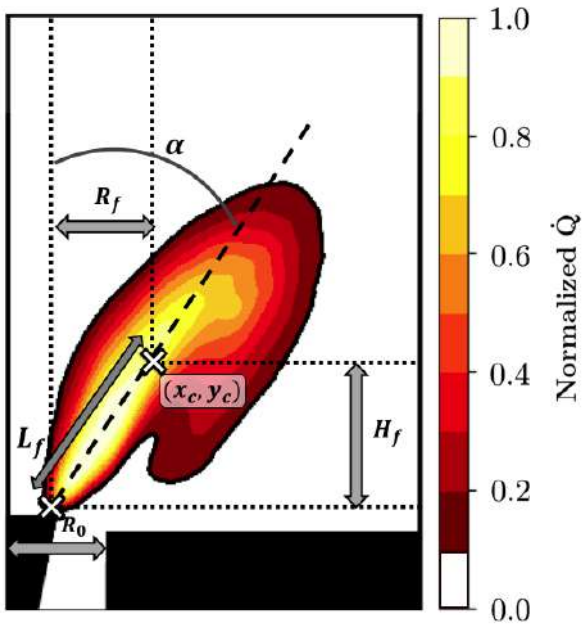


Figure 3.32: Schematic of the flame and associated quantities of interest : α, $\mathbf{L_f}$, $\mathbf{H_f}$, $\mathbf{R_f}$, $\mathbf{R_0}$. The position of the Q center of mass $(\mathbf{x_c}, \mathbf{y_c})$ is shown.

$L_f/R_0 = 1.75$, $H_f/R_0 = 1.44$ and $\alpha = 34.8°$. The mean axial velocity at the injector exit plane $U_0 = 8.78$ m.s^{-1} is measured from the stationary unperturbed LES to complete the analysis, yielding $\omega_*/\omega = 2.43$ ms.

The next critical step in the SFTF construction is to determine the axial convection velocity U_{c-v} of vortical structures along the outer shear layer of the swirling jet exhausting the injector. For V-shaped flames like the present one, these structures are responsible for large surface area perturbations and thus, in the case of a premixed flame, for the major part of the unsteady heat release [127, 144]. One possibility to assess the real speed of these disturbances is to use a tracking algorithm [194]. While theoretically appealing, this method has some limitations in a turbulent LES framework and requires acoustically pulsed simulations. Another possibility arising for highly swirling flows is to use properties coming from solid mechanics theory. For solid bodies, the norm of the second principal invariant of the deviatoric stress tensor is used as a measure of shear. In the present case, swirl is strong enough (and possibly the injection tube narrow enough) so that the angular momentum flux prevails, resulting in a fully developed turbulent pipe flow in solid body rotation. A similar criterion [195] resembling the classical λ_2 criterion for vortex identification is therefore used, that is the second invariant I_2 of the

strain rate tensor $\mathcal{S}$, which is in practice computed as:

$$I_2 = \frac{1}{2}\left(\mathcal{S}_{ii}\mathcal{S}_{jj} - \mathcal{S}_{ij}\mathcal{S}_{ji}\right) \tag{3.7}$$

Negative values of I_2 indicate high shear regions. Applied to the mean steady reacting field issued by LES, maximum negative values of I_2 identify a collection of abscissa starting from the injector exit up to the distance H_f associated to the height of the centroid of heat release rate distribution. This yields a curve assigned as the outer shear layer trajectory shown in Fig. 3.33. Note that other criteria could be used to identify the shear layer, such as the norm of the strain rate tensor, removing the potential high swirl limitation of the method. The I_2 criterion was however shown to be particularly robust for the high swirling flows studied. Along this path, the local axial velocity at a given x abscissa is retrieved and thereafter noted $u_l(x)$. The axial velocity component

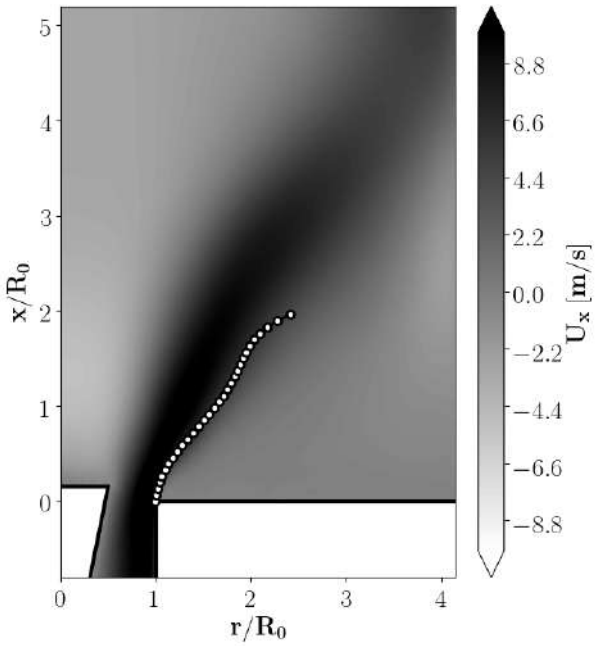


Figure 3.33: Identification of the outer shear layer using the I_2 criterion for the reactive case. Each white dot represent the local maximum at a given height x/R_0.

of vortical structures U_{c-v} is then evaluated by averaging the axial velocity along the shear layer path over the distance H_f, that is :

$$U_{c-v} = \frac{1}{H_f}\int_0^{H_f} u_l(x)dx \tag{3.8}$$

where H_f is the flame height (Fig. 3.32). Using the available average LES fields yields $U_{c-v} = 6.46$ m.s^{-1}. The real part of the correction factor K for the SFTF model therefore equals $K = U_0/U_{c-v} = 1.36$.

In the absence of pulsed LES data, one can estimate the time delay τ between axial and azimuthal velocity perturbations at the burner outlet by assuming that acoustic perturbations travel at the sound speed c while azimuthal perturbations are convected at the local flow speed u_c over the distance $\delta = 50$ mm between the swirler vanes exit where acoustic/vorticity conversion occurs [129] and the injector exit plane (see Fig. 3.1):

$$\tau = \delta \left(\frac{1}{u_c} - \frac{1}{c} \right) \tag{3.9}$$

As a first approximation, the phase ϕ_0 in the zero frequency limit is simply nullified. By doing so, the low frequency gain limit condition from Eq. (2.40) reduces to $\chi = -\zeta$ and the FTF phase is evidently forced to a null value in the zero frequency limit. The choice of the convective velocity u_c is still subject to discussions in the community. It has been observed experimentally [196] and while trying to reproduce FTF from models [51] that the actual value may be 40 to 50% larger than the bulk velocity in the injection device. The issue was discussed by Gatti in [162], where cold flow simulations were used to determine the value of u_c compared to mean and maximum velocities along the injection device for the same variation of the NoiseDyn configuration. Results showed that for the studied frequencies, the mean value of u_c along the injector was somewhere in between the maximum and the mean velocities, and closer to the bulk velocity at the base of the flame. Recently, Albayrak *et al.* [197] have proposed an analytical expression for this quantity in the low axial wavenumber limit based on a modal decomposition of the linearized Euler equations which resumes to:

$$u_c = U_0 \left(1 + 2\kappa/\lambda_0\right), \tag{3.10}$$

where κ is the circulation strength of the swirling flow and λ_0 is the first eigenvalue of a characteristic equation:

$$J_1(Ar_o)Y_1(Ar_i) - J_1(Ar_i)Y_1(Ar_o) = 0, \tag{3.11}$$

where r_i and r_o are the inner and outer radii of the cylindrical channel, and J_1, Y_1, are Bessel functions of the first and second kind respectively. Applied to the current configuration, the above expression yields $u_c = 1.55U_0$ with $\kappa = 1145$ s^{-1} and $\lambda_0 = 470$, resulting in a time delay $\tau = 3.51$ ms which does not comply with the time delay found in the LES as will be presented in Sec. 3.5.2. For this reason, it was chosen to use $u_c = U_0$, yielding $\tau = 5.55$ m.s^{-1}. No information is yet available for the determination of the swirl fluctuation intensity parameter χ. A value comparable to those found in [128, 166] is used: $\chi = -0.33$ for this preliminary study.

Parameters obtained from the single stationary LES are summarized in Tab. 3.2. To the exception of χ, all SFTF parameters have been roughly estimated from a stationary

Table 3.2: SFTF parameters as determined from a single reacting stationary LES (SFTF1)

Case	ω_*/ω[ms]	α [deg.]	K	χ	τ[ms]	ϕ_0 [rad]
SFTF1	2.43	34.8	1.36	−0.33	5.55	0.0

reactive simulation without any acoustic modulation. From the set of estimated parameters, one can obtain a first estimation of the flame acoustic response, that is denoted as SFTF1 and is shown in Fig. 3.34 . With only a single stationary flame simulation,

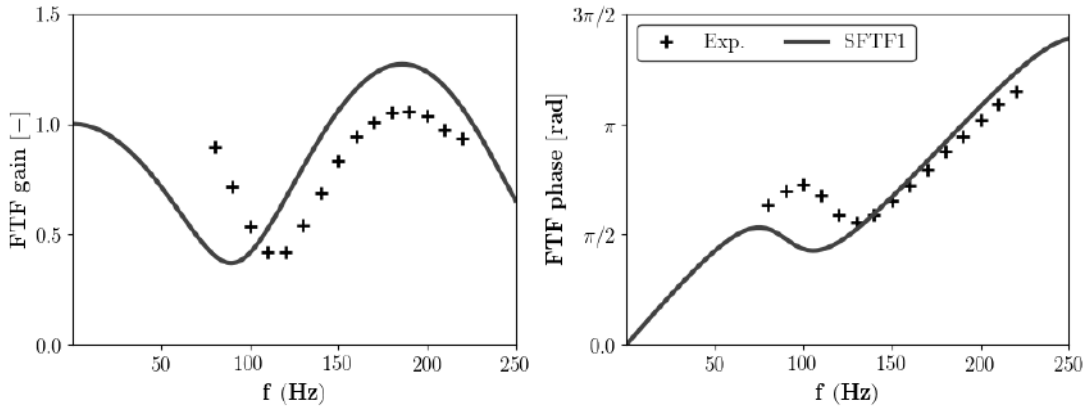


Figure 3.34: SFTF1 model results with parameters estimated from a single stationary unperturbed LES : $\omega_*/\omega = 2.43$ ms, $\alpha = 34.8°$, K = 1.36, $\chi = -0.33$, $\tau = 5.55$ ms, $\phi_0 = 0$ rad.

the model is able to depict the FTF gain and phase tendencies over the frequency range of interest. In particular, correct phase tendencies are already retrieved without the introduction of unsteady perturbations, and values match the experiment for $f \geq 150$ Hz. The frequency of the first local FTF gain minimum is however not retrieved using SFTF1, which also shows in the phase curve where the phase shift region is not well predicted. The position of this first minimum is fully controlled by parameters τ and ϕ_0 used to represent the phase shift $\phi_{\hat{u}_\theta - \hat{u}_x}$ introduced in Eq. (2.38). Consequently, the mismatch between the current SFTF model results and experiments can be explained by either one of these parameters (or even both at the same time). The missing piece of the puzzle may lie in the fact that only global quantities have been considered: nullifying ϕ_0 is equivalent to considering uniform velocity profiles at the injector exit, which is not the case as shown in Fig. 3.26. The gain around $f = 180$ Hz is also overestimated by the model, which was expected since no spatial decay of acoustic perturbations is accounted for at this point.

3.5.2 Model parameters from pulsed LES

3.5.2.1 Enhancing the model using reactive forced simulations

Building upon results obtained with SFTF1, this section aims at proving that a few additional simulations are sufficient to improve the accuracy of model predictions. By doing so, one avoids performing numerous single frequency forced simulations [114, 131] or the need for other identification techniques [112, 115] that can show their limit for highly turbulent flows. Acoustically pulsed simulations are used to obtain parameters ϕ_0, χ and β since they are related to dynamic features: the phase lag between acoustic and convective perturbations, the amplitude of swirl fluctuations and axial velocity disturbances decay.

It was shown in the previous section that a rough estimation of the phase $\phi_{\hat{u}_\theta - \hat{u}_x}$ is not sufficient to capture the frequency of the change in the FTF phase slope. As an alternative, this phase can be determined from a set of pulsed flow simulations. Such a study would of course defeat the initial purpose of using an analytical model which should avoid running several costly computations, but the study is performed as another validation step here. The phase between Fourier coefficients of axial and azimuthal unsteady velocity signals integrated on the injector exit plane is computed for the eight frequencies that have been simulated; as presented in Fig. 3.35, a linear fit can properly represent the data. The time delay $\tau = 5.54$ ms and phase at the

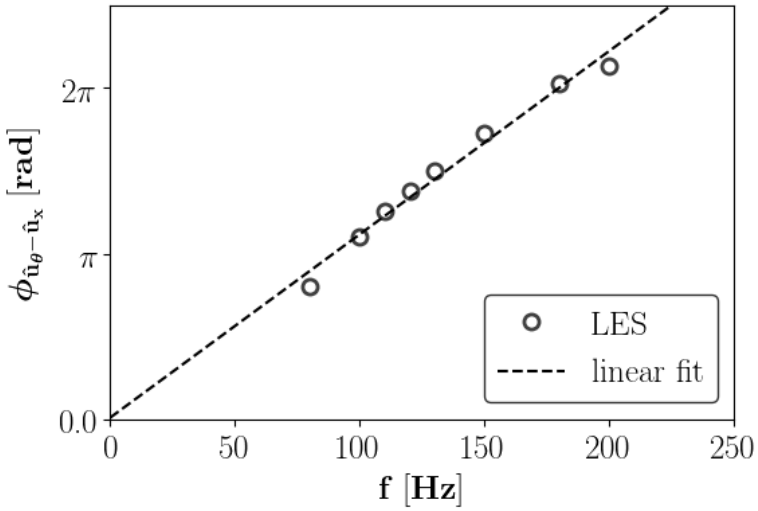


Figure 3.35: Phase between axial acoustic ($\hat{u}_x$) and azimuthal convective ($\hat{u}_\theta$) velocity perturbations at the injector exit plane from surface averaged data for different pulsed LES frequencies.

low frequency limit $\phi_0 = 0.03$ corresponding to the linear regression law are very close to those obtained using the simple one-dimensional propagation model from Eq. (3.9) leading to $\tau = 5.55$ ms.

This result may however not be satisfactory since the first local FTF gain minimum lies around $f = 120$ Hz and the maximum gain deviation is attained when swirl fluctuations are maximum, that is for $\phi_{\hat{u}_\theta - \hat{u}_x} = \pi$ according to the swirl number definition. In that case, using Eq. (3.9) shows that a value close to $\tau = \pi/\omega = 1/(2f) = 4.17$ ms would be expected. In [128], $\phi_{\hat{u}_\theta - \hat{u}_x}$ was evaluated experimentally at the base of the flame for different bulk velocities, reporting values of -1 and -1.5 rad for ϕ_0 with forcing frequencies going as low as 30 Hz. It is then important to notice that velocity profiles plotted in Fig. 3.26 are not flat at the injector outlet, and that considering only bulk quantities may not be satisfactory. Indeed, swirl fluctuations should be considered where they preponderantly affect the flame. In the particular case of the NoiseDyn confined swirled V-flame, this region is the edge of the injector wall where large vortical structures are created, travel along the shear layer and perturb the flame surface. Accordingly, one can see ϕ_0 as a phase lag between the bulk oscillation signals and signals obtained at a particular radial location close to the wall, here chosen as a point 0.5 mm away from the injector wall on the injector exit plane, see Fig. 3.36 and 3.37. A maxi-

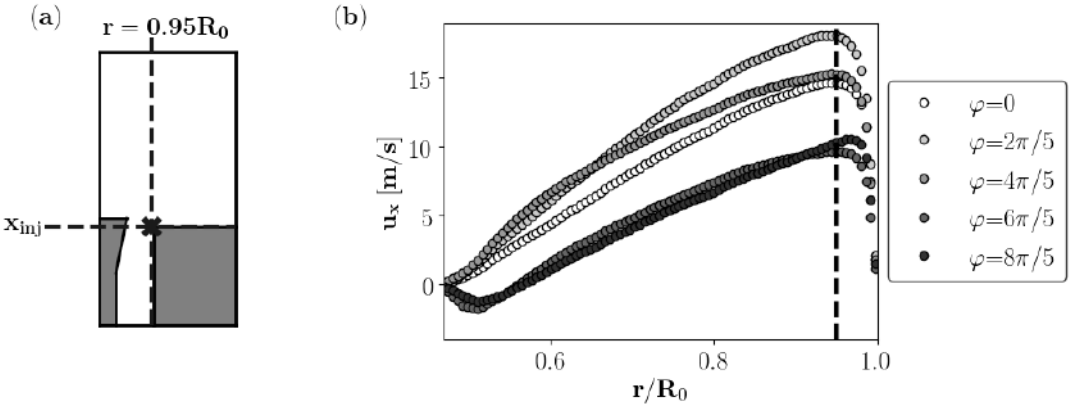


Figure 3.36: (a) Sketch of the burner with the position of the integration surface height marked as x_{inj} and the probe near the outer wall represented by a black cross, located 0.5 mm away from the wall. (b) Axial velocity profiles at axial position x_{inj} for different phases of the forcing cycle ($\varphi = \pi/2$ corresponds to a maximum velocity at the hot wire position) for f = 180 Hz.

mum deviation of less than 10% in ϕ_0 is obtained when the probe position changes by 0.3 mm. Larger deviations are seen when using locations closer to the wall, depending on the local mesh size. The phase ϕ_0 is hence evaluated as:

$$\phi_0 = \phi_{\hat{u}_\theta - \hat{u}_x}(x_{inj}, 0.95R_0) - \frac{1}{S_e}\int_{S_e} \phi_{\hat{u}_\theta - \hat{u}_x}(x_{inj}, r) dS_e \tag{3.12}$$

Or equivalently:

$$\phi_0 = \phi_{\hat{u}_\theta - \hat{u}_x}(x_{inj}, 0.95R_0) - \omega\tau \tag{3.13}$$

where S_e designates the cross section area at the burner outlet with axial position x_{inj}. Using data from forced LES, one gets the results of Tab. 3.3 which tend to validate the assumption that ϕ_0 is almost frequency independent in the studied pulsation range. This

Table 3.3: Phase ϕ_0 as obtained from LES data for different frequencies using Eq. (3.12).

f [Hz]	100	120	150	180
ϕ_0 [rad]	-0.832	-0.905	-0.887	-0.874

means that this quantity can be obtained using only a single pulsed simulation. Signals used to obtain these values are shown in Fig. 3.37, with ϕ_0 computed as $\phi_0 = \phi_p - \phi_b$ using the figure notations.

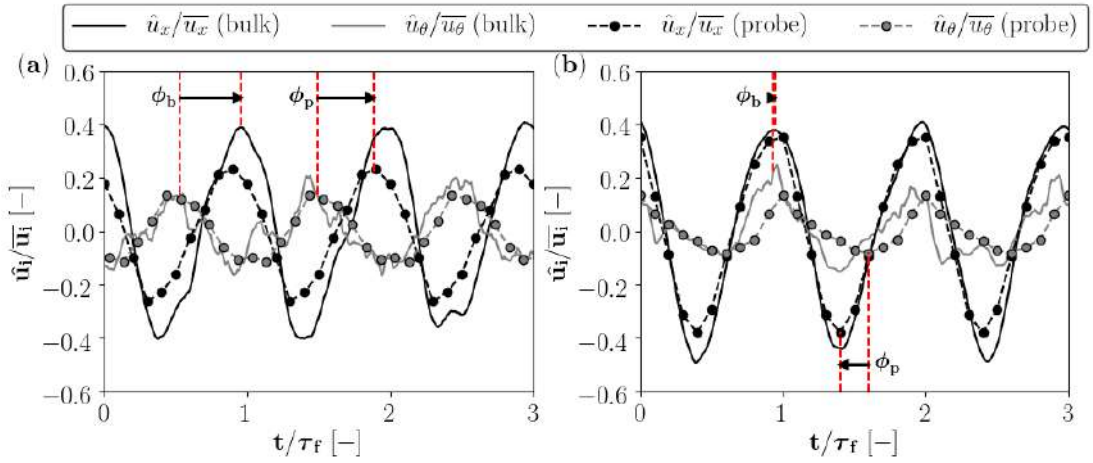


Figure 3.37: Normalized axial and tangential velocity signals on the injector exit plane (bulk, solid line) and on a probe 0.5 mm away from the outer injector wall (dashed line with markers) for (a) f = 120 Hz and (b) f = 180 Hz. These signals correspond to $\phi_0 = -0.905$ rad and $\phi_0 = -0.874$ rad respectively, with $\phi_0 = \phi_p - \phi_b$.

In the present case, it is observed that $\hat{u}_x$ and $\hat{u}_\theta$ signals measured for the probe at the injector exit rim ($r/R_0 = 0.95$) are in phase opposition at the minimum FTF gain frequency. The same behaviour is observed with a shorter injector as will be shown in Sec. 3.6.2. It is therefore argued that injecting $\phi_{\hat{u}_\theta - \hat{u}_x} = \pi$ in Eq. (3.13) [128] yields an evaluation of the frequency f_1 corresponding to the FTF minimum gain:

$$f_1 = \frac{1}{2\tau} - \frac{\phi_0}{2\pi\tau} \tag{3.14}$$

This criteria should be verified on other configurations in future studies. For $f = 120$ Hz and $f = 180$ Hz respectively, Eq. (3.14) yields $f_1 = 115$ Hz and $f_1 = 116$ Hz, which agrees well with the frequency range 110 Hz $\leq f_1 \leq$ 120 Hz obtained in the experiment, Fig. 3.21.

Pulsed reactive LES are in turn used to evaluate the swirl intensity parameter χ introduced to characterize swirl fluctuations amplitude in Eq. (2.37). Although its effect on the model is quite straightforward, it is still unclear how to directly measure it using either experiments or LES. In previous works in the literature, it was always optimized on a case by case basis to fit the experimental data, which does not comply with the goal of this study where experimental data may not exist at all. To remedy this situation, and since at least one acoustically forced reacting LES has to be performed to retrieve other model parameters dealing with the system dynamics, it is proposed to perform a pointwise optimization on both the FTF gain and phase at a particular frequency to determine a suitable value for χ. Best agreement can only be achieved when using frequencies corresponding to local extrema of the FTF gain. Since the first local gain minimum frequency is fully characterized by τ and ϕ_0 obtained from the previous steps, one can perform a forced LES at this particular frequency and use the obtained value of gain and phase as a target for optimization. The outcome of the pulsed LES at $f = 120$ Hz is used to determine the best value for the SFTF model to match the FTF gain and phase as obtained from LES at this particular frequency. The value $\chi = -0.368$ is obtained as the optimal one.

With the addition of ϕ_0 and the optimization process on χ, the SFTF model reaches a higher level of complexity, here denoted as SFTF2, with parameters summarized in Tab. 3.4. Corresponding results in terms of FTF gain and phase are shown in Fig. 3.38.

Table 3.4: SFTF parameters as determined from: a single reacting stationary LES + 1 pulsed LES to determine the FTF gain minimum frequency f = 120 Hz + 1 reacting pulsed LES at f = 120 Hz (SFTF2)

Case	ω_*/ω [ms]	α [deg.]	K	χ	τ [ms]	ϕ_0[rad]
SFTF2	2.43	34.8	1.36	-0.368	5.55	-0.905

As expected, introducing the appropriate value for $\phi_{\hat{u}_\theta - \hat{u}_x}$ allows the SFTF model to match the frequency f_1 for which the FTF gain reaches a minimal value and the FTF phase slope changes. The optimization technique for χ, while not ideal, is fully automated and only requires a single pulsed LES at frequency f_1. If unknown, this frequency can be determined by gauging ϕ_0 from a pulsed simulation at any frequency and using Eq. (3.14). Results show that this optimized value allows the first low FTF gain region to be matched, which constitutes an improvement over SFTF1. This is however not fully satisfactory yet since the gain for frequency higher than 160 Hz is overpredicted with the current state of the model. The FTF phase is very well reproduced at this point, and one may argue that most of the time (intrinsic thermoacoustic modes [198] are not considered in the present study), the phase is the dominating factor governing the stability of acoustic modes as obtained from reduced order models.

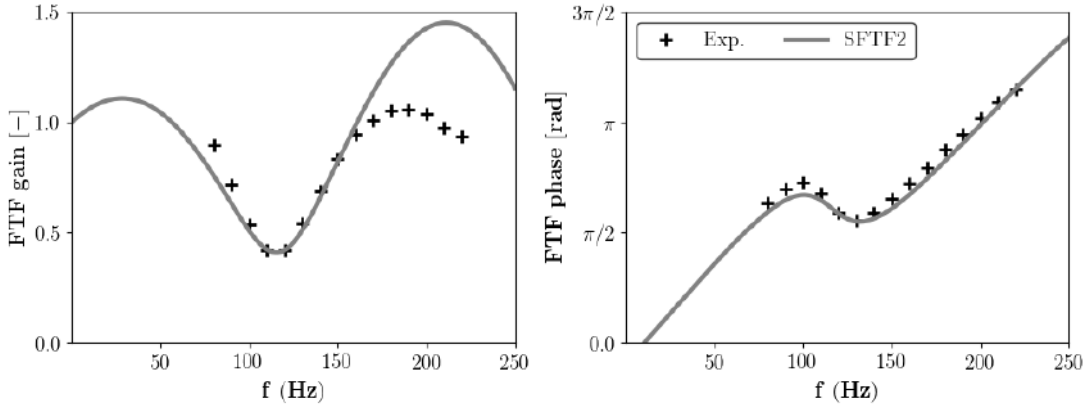


Figure 3.38: SFTF2 model results with parameters : $\omega_*/\omega = 2.43$ ms, $\alpha = 34.8°$, K = 1.36, $\chi = -0.368$, $\tau = 5.55$ ms, $\phi_0 = -0.905$ rad.

3.5.2.2 Accounting for the acoustic spatial decay

Finally, the spatial decay rate of the axial velocity perturbation amplitude β introduced in Eq. (2.27) can be evaluated by means of a single pulsed cold flow simulation. In the present case, it is evaluated for the same forcing amplitude $\hat{u}_{ref}/\overline{u}_{ref} = 30\%$ as in the reactive case presented in the previous section. It is recalled that this decay can be embedded in the correction factor K, so that $\beta = \Im(K)/\Re(K) = U_{c-v}/U_0 \times \Im(K)$. The FTF model derivation was done assuming a clear separation between fresh and hot gases, which is obviously not the case for a confined swirl burner where outer recirculation zones contain hot gases. For this reason cold flow simulations were preferred to determine β. Once again, focus is made on frequencies $f_1 = 120$ Hz and $f_2 = 180$ Hz corresponding to the identified local minimum and maximum amplitudes of the FTF gain. Velocity disturbances amplitudes are probed on a vertical line at $r/R_0 = 0.75$ which corresponds to the central line between the injector outer wall and the conical bluff body top as shown in Fig. 3.39a. Figure 3.39b shows that LES predicts a decrease of the amplitude as expected from experiments. Post-processing the LES data leads to $\beta = 0.184$ for $f = 120$ Hz and 0.188 for $f = 180$ Hz. These specific values were obtained following Eq. (2.27) by fitting an exponential function of the form $Ae^{-\gamma x}$ so that $\beta = \gamma \frac{U_{c-v}}{\omega}$ where $U_{c-v}|_{cold} = 3.83$ m.s^{-1} comes from the technique described in section (3.5) for the unperturbed cold LES fields. Embedding the decay rate in the SFTF model should allow for better gain prediction at relatively high frequencies. In the following it is chosen to proceed with the value obtained for $f = 120$ Hz as this particular frequency was already used for reacting conditions. The optimization procedure for χ is iterated once again with the new value of K featuring an imaginary component $U_0\beta/U_{c-v}$. The obtained optimal value is of course not the same with the spatial decay component addition, $\chi = -0.336$.

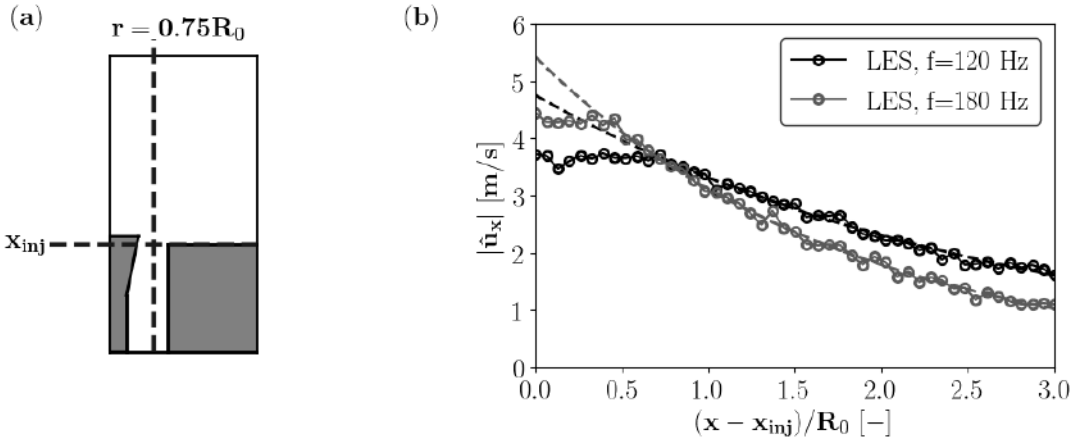


Figure 3.39: (a) Schematic of the central line located at $r/R_0 = 0.75$ used for the amplitude decay evaluation. (b) Acoustic velocity amplitudes on the same line, starting from the injector exit plane. Dotted lines show the best fit for each frequency in the form $Ae^{-\gamma x}$.

This new methodology requiring an additional non-reactive pulsed simulation for the decay rate determination is here denoted as SFTF3, with parameters summarized in Tab. 3.5. Corresponding results in terms of FTF gain and phase are shown in

Table 3.5: SFTF parameters as determined from : a single reacting stationary LES + 2 non-reacting/reacting pulsed LES at f = 120 Hz (SFTF3)

Case	ω_*/ω [ms]	α[deg.]	K	χ	τ [ms]	ϕ_0[rad]
SFTF3	2.43	34.8	$1.36 + 0.25i$	-0.336	5.55	-0.905

Fig. 3.40. By stepping up to SFTF3 with a total of four necessary simulations, the

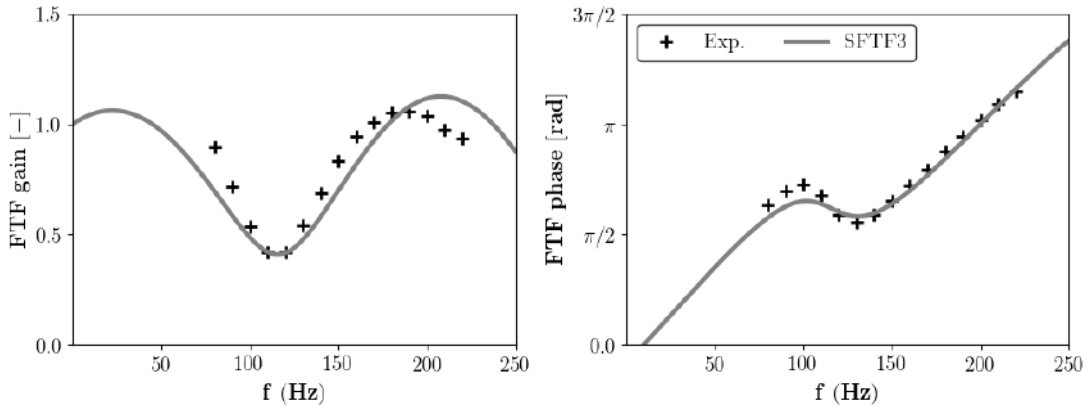


Figure 3.40: SFTF3 model results with parameters : $\omega_*/\omega = 2.43$ ms, $\alpha = 34.8°$, $K = 1.36 + 0.25i$, $\chi = -0.336$, $\tau = 5.55$ ms, $\phi_0 = -0.905$ rad.

FTF gain for frequencies $f \geq 160$ Hz matches reference data due to the fact that the spatial/high frequency acoustic velocity perturbation decay is taken into account. The phase curve in Fig. 3.40 is only marginally modified compared to results from

SFTF2 shown in Fig. 3.38, and remains in very good agreement with the experiments. A possible limitation of the current model lies in the low frequency limit where no experimental data is available for this particular configuration and set of operating conditions. For slightly different operating conditions the FTF gain was observed to reach values around 1.5 around 50 Hz. By imposing the unity gain limit for the SFTF model (see Eq.(2.40)), the evolution of the gain in the low frequencies as obtained from the SFTF model is constrained. For this reason, Fig. 3.40 shows different trends for low frequencies for the model and the reference data.

3.5.3 SFTF methodology summary

It was demonstrated that the SFTF strategy constitutes a modular semi-analytical FTF model for a premixed swirled V-flame, featuring different accuracy levels depending on the number of simulations the user can afford. In any case, it remains less computationally intensive than performing several single frequency forced simulations as usually needed to reconstruct the whole FTF. A methodology to assess model parameters has been proposed, based on robust criteria that can be easily transposed to other swirler/injector geometries. In this view, the final SFTF model can reach three accuracy levels SFTF1, SFTF2, SFTF3, depending on the way parameters are assessed and on the available computational resources. The design of these models can be abstracted as follows :

- A first LES of the stationary flame is performed. Geometric quantities are extracted and parameters ω_*/ω, α, K and τ are appraised. The first accuracy level SFTF1 is reached.

- A pulsed LES is performed over a few periods to evaluate the phase lag $\phi_{\hat{u}_\theta - u_x}$ between azimuthal and axial velocity disturbances at the injector exit rim, where large vortical structures are created. Alternately, this phase lag can be computed by adding a constant phase ϕ_0 to the phase lag of bulk signals. The frequency of the first local gain minimum f_1 is then assessed from Eq. (3.14).

- Another pulsed LES is performed at frequency f_1, the FTF gain and phase are evaluated at this particular frequency.

- The swirl amplitude parameter χ is obtained from a pointwise optimization process using LES estimated FTF gain and phase at f_1. The second accuracy level SFTF2 is reached.

- An additional cold pulsed LES at any frequency is performed and the velocity disturbances decay rate β is assessed. The final fidelity level SFTF3 is attained

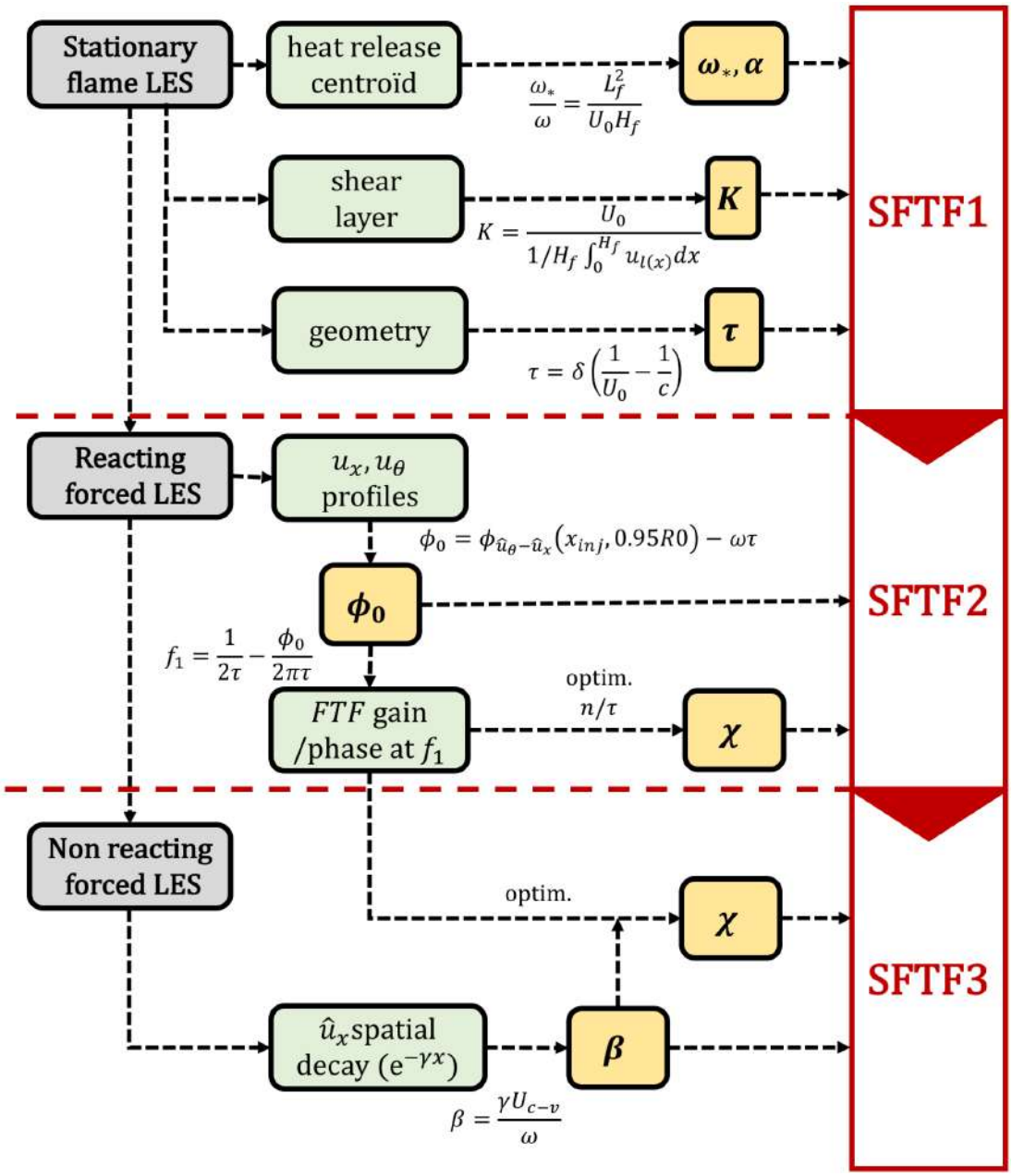


Figure 3.41: Schematic diagram representation of the SFTF methodology. Parameter estimations methods are recalled for the three increasing levels of complexity SFTF1, SFTF2 and SFTF3.

The diagram presented in Fig.3.41 summarizes this procedure. Applied to the current variation of the NoiseDyn burner, the methodology is shown to provide increasing accuracy levels in regard of the reference FTF gain and phase data, that are summarized in Tab. 3.6. The equivalent computational cost in terms of numbers of Single Frequency Forcing (SFF) reacting LES is also disclosed for comparison purposes. The computational advantage of the SFTF methodology is evident.

In particular the FTF phase curve is already quite well predicted with SFTF2, which

Table 3.6: Overview of the FTF reproduction accuracy using an increasingly complex evaluation of SFTF model parameters. The equivalent number of Single Frequency Forced (SFF) LES is also presented for comparison purposes.

Case	nb. of LES	SFF LES equivalence	agreement on gain	agreement on phase
(a) SFTF1	1 stationary	0.5	moderate	moderate
(b) SFTF2	1 stationary +2 reacting pulsed	2.5	moderate	good
(c) SFTF3	1 stationary +2 reacting pulsed + 1 non reacting pulsed	3.3	good	good

merely relies on three numerical simulations. Depending on the available computational resources, one can choose whether a single simulation is sufficient (SFTF1), or if accuracy is sought, if it is preferable to run additional forced simulations to obtain a better representation of the FTF gain and phase (SFTF2 and SFTF3). Assessing the spatial decay rates of velocity disturbances, SFTF3, yields a complete description of the flame acoustic response at the cost of an additional non reactive pulsed simulation at any frequency.

3.6 Improving the SFTF model: extension to other geometries and forcing amplitudes

3.6.1 Effect of the perturbation amplitude on the FTF

All analyses of the previous section have been made for a fixed RMS perturbation level $\hat{u}/\overline{u} = 30\%$. It is well known that in the linear regime, that is for acoustic perturbations of small amplitude, the acoustic response of flames remains the same, while for larger amplitudes, nonlinear phenomena modify the response. The flame describing function formalism [119] aims at introducing back the role of the forcing amplitude in the acoustic response modelling. Various forcing levels have been studied experimentally by M. Gatti [162] for the present version of the NoiseDyn configuration, yielding the FDF curves of Fig. 3.42. Note that the higher the forcing level is, the harder it gets to obtain experimental measurements of the FTF as the flame undergoes large vertical motions and may enter the injector. Another limitation is that the loudspeaker installed in the bottom of the test-rig could only reach the desired pulsation levels over a limited frequency ranges that narrows as the velocity level increases. For these reasons, data are quite scarce for RMS forcing levels $\hat{u}/\overline{u} = 55\%$ and $\hat{u}/\overline{u} = 72\%$. The first peak in the FTF gain decreases with increasing forcing amplitude and is heavily affected by

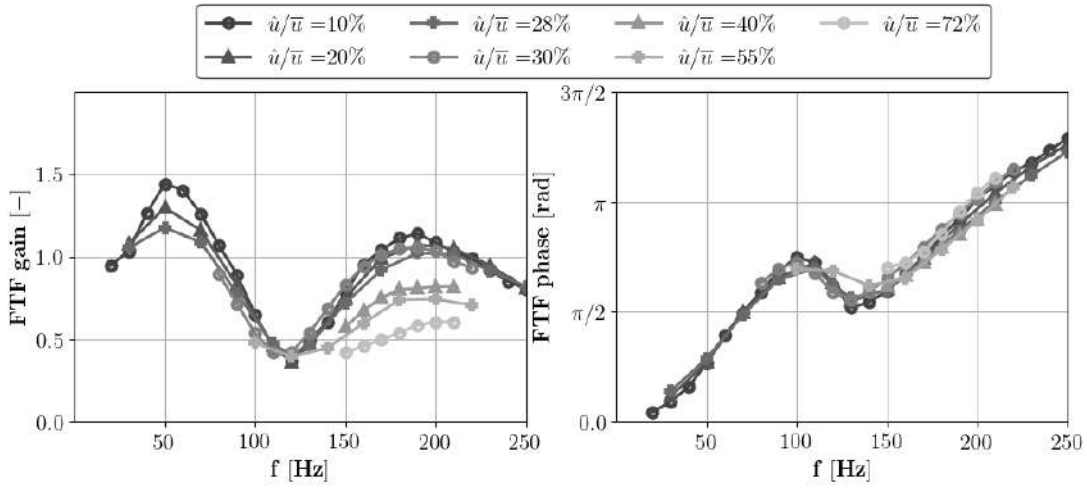


Figure 3.42: Flame describing function of the NoiseDyn burner as obtained from experiments for various forcing levels (RMS). Reproduced from [162].

nonlinear phenomena as expected for this low frequency range. In contrast, the second peak around $f = 180$ Hz remains almost unchanged for RMS amplitudes $\hat{u}/\overline{u}$ up to 28%. For higher forcing amplitudes, the gain for frequencies $f \geq 120$ Hz regularly decreases. The local gain extrema for $f_1 = 120$ Hz is not affected by the forcing level. Phase curves for all studied forcing levels are superimposed, confirming that the time delay τ and phase ϕ_0 are not affected by the modulation amplitude. Hence, in regard of the SFTF model, the two remaining parameters which could potentially represent the frequency dependency of the FTF curve depending on amplitude are β and χ. On one hand, the SFTF model itself derived in Sec. 2.3 is only valid for small perturbation amplitudes and should therefore not be suitable for higher forcing levels where nonlinear interactions affect the FTF. On the other hand, model parameters are determined from LES which solve the full Navier-Stokes equations and are intrinsically nonlinear. The question arises to know whether the semi-analytical model is able to handle different forcing amplitudes and if so, to which extent.

Three forcing levels are chosen with RMS amplitude levels $\hat{u}/\overline{u}$ =10%, $\hat{u}/\overline{u}$ =30% and $\hat{u}/\overline{u}$ =55% respectively for the inlet acoustic modulation. The goal here is to perform three pulsed non reactive LES, one for each forcing level, and to assess the spatial decay of axial velocity perturbations β in each case. Since the effect of nonlinearities is more prominent around $f = 180$ Hz, this frequency is chosen for the three simulations. Note that in Sec. 3.5.2.2, decay rates β were found to be very close for both $f = 120$ Hz and $f = 180$ Hz for $\hat{u}/\overline{u} = 30\%$.

It is first checked that the three modulation amplitudes are indeed retrieved in the LES at the hot wire position, Fig. 3.43. After a short transient period, the forced signals indeed have the correct amplitude compared to the imposed value, which confirms that

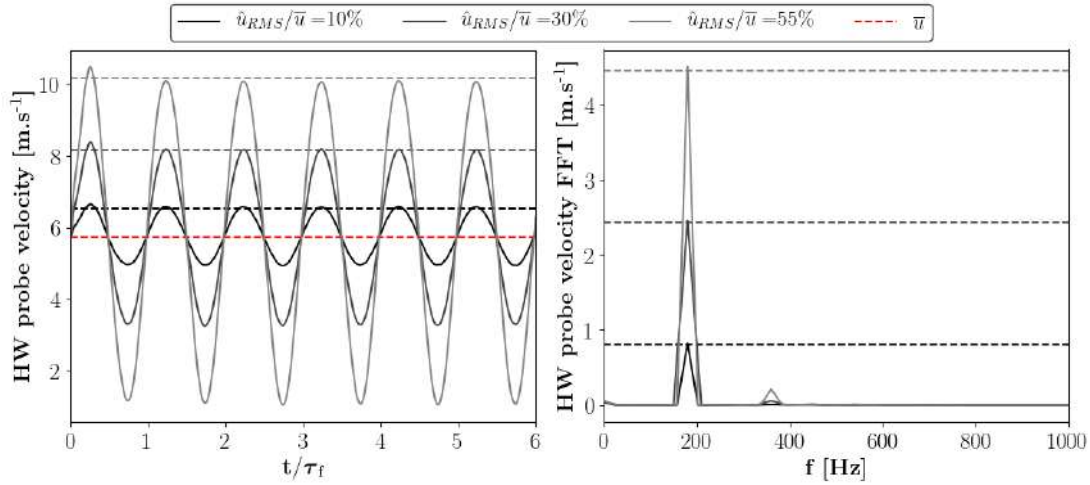


Figure 3.43: Axial velocity signals at the hot wire position for f = 180 Hz while applying forcing for amplitudes $\hat{u}/\overline{u}$ =10%, 30% and 55% respectively (left) and associated FFT (right). Dotted line show the target value for each amplitude.

no spurious reflections are generated at the inlet of the domain. Simulations are run for nine periods and the extraction procedure of sec. 3.5.2.2 for velocity disturbances amplitudes is applied: the latter are probed on a vertical line at $r/R_0 = 0.75$ which corresponds to the central line between the injector outer wall radius and the conical bluff body top radius. The obtained decaying curves are then fitted with and exponential function of the form $Ae^{-\gamma x}$ so that $\beta = \gamma\frac{U_{c-v}}{\omega}$ with $U_{c-v}|_{cold} = 3.83$ m.s^{-1}. Corresponding results are plotted in Fig. 3.44. The hierarchy is respected with higher

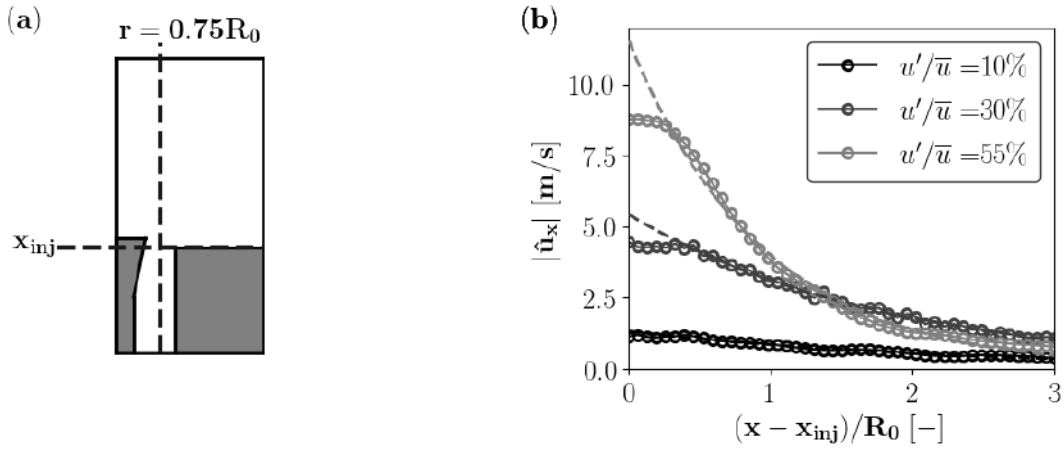


Figure 3.44: (a) Schematic of the central line located at r/R$_0$ = 0.75 used for the amplitude decay evaluation. (b) Acoustic velocity amplitudes on the same line, starting from the injector exit plane for $\hat{u}/\overline{u}$ =10%, 30% and 55% at f = 180 Hz. Dotted lines show the best fit for each amplitude in the form Ae$^{-\gamma x}$.

amplitudes at the injector exit for higher forcing levels. A good representation of the

decaying curve is obtained using an exponential function fit for all studied amplitudes. The three curves yield $\beta = 0.148$, $\beta = 0.188$ and $\beta = 0.37$ for amplitudes $u'/\overline{u}$ =10%, 30% and 55% respectively. Equivalently, the imaginary part of the correction factor $\Im(K) = U_0\beta/U_{c-v}$ is $\Im(K) = 0.20$, $\Im(K) = 0.25$ and $\Im(K) = 0.50$ for amplitudes $u'/\overline{u}$ =10%, 30% and 55% respectively.

The last remaining parameter that needs to be updated for each forcing amplitude is the swirl fluctuations intensity parameter χ. Following what was done in sec. 3.5 for $\hat{u}/\overline{u} = 30\%$, χ is obtained from an optimization process for $f = 120$ Hz using values of the FTF gain and phase as target values for all forcing levels. Here for $\hat{u}/\overline{u}$ =10% and 55% no LES simulation is performed but experimental values are used instead. This does not change anything about the procedure, and provided that the LES are accurate enough as they were for a 30% amplitude (Fig. 3.21), end results will be the same. The optimization yields $\chi = -0.365$, $\chi = -0.336$ and $\chi = 0.307$ for $\hat{u}/\overline{u}$ =10%, 30% and 55% respectively. When the forcing amplitude increases, so does β, and the optimization procedure at the minimum gain frequency needs to compensate by adjusting χ. The value of χ thus decreases with the forcing amplitude. All results are summarized in Tab. 3.7 for the sake of clarity.

Table 3.7: SFTF parameters as determined from SFTF3 procedure using spatial decays measured for f = 180 Hz and f = 120 Hz as a target for forcing levels $\hat{u}/\overline{u}$ =10%, 30% and 55%

Case	ω_*/ω [ms]	α [deg.]	K	χ	τ[ms]	ϕ_0[rad]
$\hat{u}/\overline{u} = 10\%$	2.43	34.8	$1.36 + 0.20i$	-0.365	5.55	-0.905
$\hat{u}/\overline{u} = 30\%$	2.43	34.8	$1.36 + 0.25i$	-0.336	5.55	-0.905
$\hat{u}/\overline{u} = 50\%$	2.43	34.8	$1.36 + 0.50i$	-0.307	5.55	-0.905

Finally, SFTF results are disclosed and compared to experimental FTF data in Fig. 3.45. Figure 3.45a confirms that the SFTF model fails at capturing the initial peak in the FTF gain for low frequencies, as a result of the strong unity gain constraint in the low frequency limit. This underlines the trade-off nature of this assumption which removes a degree of freedom but does not allow for an important first FTF gain peak as observed for such swirling V-shaped flames. Still, this assumption facilitates the flame response parametrization and thermoacoustic instabilities observed on similar NoiseDyn configurations are not encountered for such low frequencies [170]. SFTF modelled transfer functions for 10% and 30% amplitudes are almost identical, which was expected since experimental curves themselves are not very different. For both amplitudes, modelled and experimentally measured gains are in good agreement with reference data for $f \geq 120$ Hz but are underpredicted for lower frequencies as described earlier. Phase curves are essentially the same and are both in very good agreement

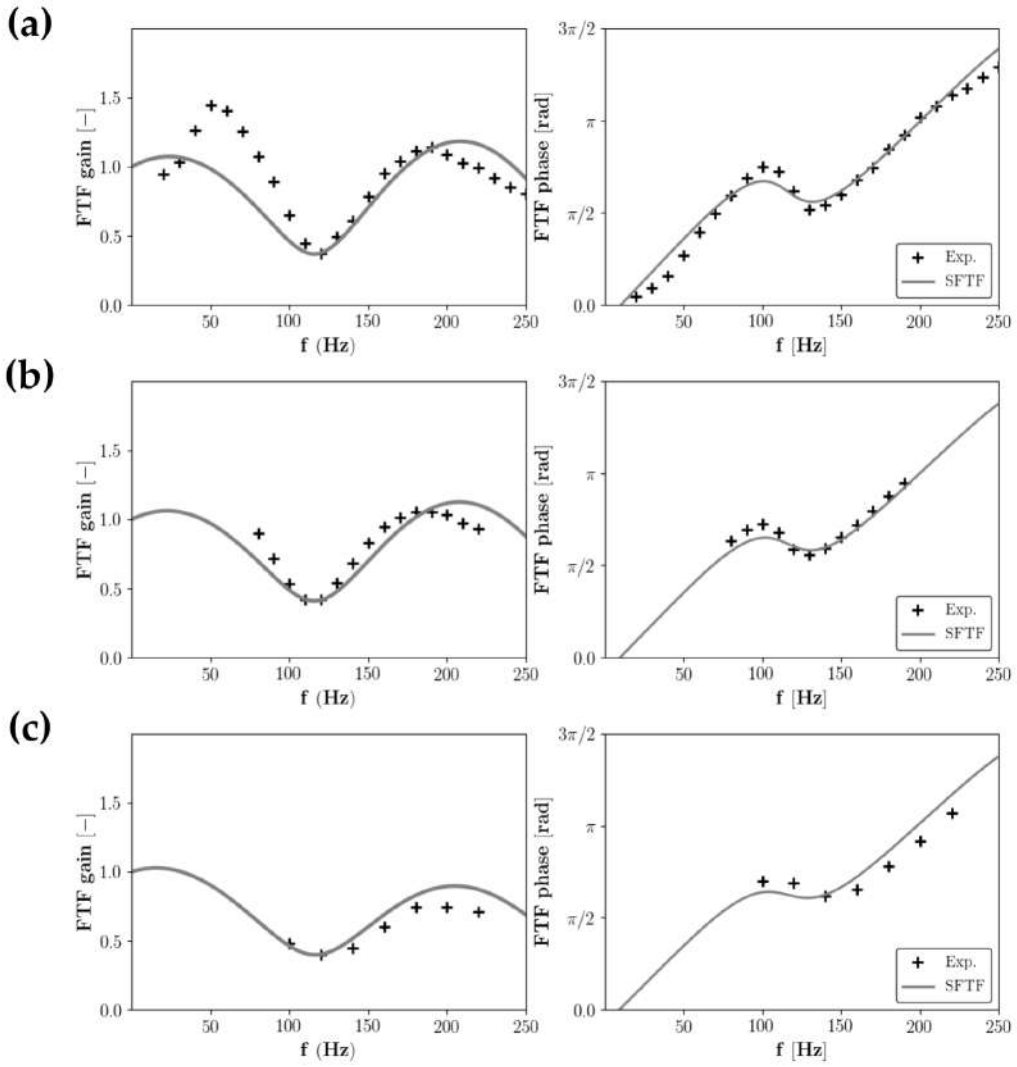


Figure 3.45: SFTF model results for (a) $\hat{u}/\overline{u} = 10\%$, (b) $\hat{u}/\overline{u} = 30\%$ and (c) $\hat{u}/\overline{u} = 55\%$ with corresponding parameters from 3.7 and reference experimental data for each case. β is obtained for f = 180 Hz and χ is optimized for f = 120 Hz.

with reference data. For the highest forcing level, few datapoints are available but the incorporation of a new value for β allows to retrieve the correct trend for the gain curve, while slightly overpredicting its value for the peak at $f = 180$ Hz. The overall agreement is still good, for both gain and phase.

One may note that the phase inflection is less strong for $\hat{u}/\overline{u} = 55\%$ compared to weaker forcing levels. This feature is partially retrieved when using the SFTF model and is a direct consequence of the lower value of χ obtained for this forcing amplitude. Still, the regular decrease for higher frequencies observed in experimental flame describing functions can be reproduced to a certain extent by the SFTF model by considering the

appropriate value of the decay rate parameter. For this reason, it is stated that the SFTF model works for any finite amplitude forcing and is not limited to vanishingly small perturbations unlike system identification based techniques.

3.6.2 Impact of minor geometrical modifications on the FTF

3.6.2.1 Shorter injection case overview and setup

In order to assess the SFTF model validity, and to fully characterize its possible range of applications, modified versions of the NoiseDyn configuration presented in Sec. 3.2 are submitted to the same parameter extraction procedure. Two configurations are hereafter explored:

- A variation of the reference configuration where the injector has been shortened down to $\delta = 40$ mm, compared to $\delta = 50$ mm in the previous study.
- A variation of the reference configuration without the central bluff-body piece, where the flame is aerodynamically stabilized.

Only the first configuration will be considered in this section for the sake of brevity. The reader is referred to Appendix. C for the study of the aerodynamically stabilized case, which yields a moderate agreement overall. The considered configuration is very similar to the one presented in Sec. 3.2. The only major difference lies in the distance δ_1 presented in Fig. 3.4a, which has been reduced to $\delta_1 = 6$ mm by removing two metallic spacers. As a consequence, the injection device is 10 mm shorter. Another minor difference is the modification of the bluff-body protruding distance δ_2 which is increased to $\delta_2 = 2.5$ mm up from 1.5 mm. This is achieved by elongating the central cylindrical piece while the conical bluff-body top remains unchanged. The latter change is only expected to have a marginal impact on the flame response. Figure 3.46 provides a direct comparison of these geometrical changes. Operating conditions remain the same as described in sec. 3.3 with a premixed methane/air mixture with equivalence ratio $\phi = 0.82$. In particular, the same thermal conditions at boundaries are kept. Experimental signals of OH* from a CCD camera for the original and modified setups indicate that the stationary flame shape is not altered by the modification of the injector length, Fig. 3.47. On the contrary, the FTF changes when varying δ since the time delay between acoustic axial and convective tangential velocity perturbations is directly affected by this length. Figure 3.48 presents experimental FTF measurements for the two aforementioned configurations and confirms this behaviour. The overall shape of gain and phase curves do not change when δ varies. The gain curve is shifted towards higher frequencies and the frequency of the first local minimum increases from 120 to 140 Hz. This frequency also corresponds to the inflexion point of the FTF phase curve.

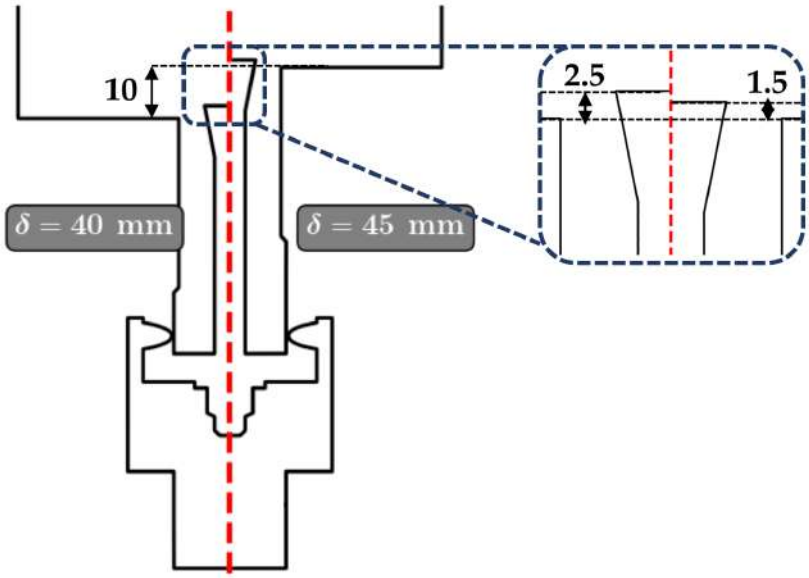


Figure 3.46: Comparison of the original ($\delta = 50$ mm) and modified NoiseDyn geometry ($\delta = 40$ mm). Dimensions are in mm.

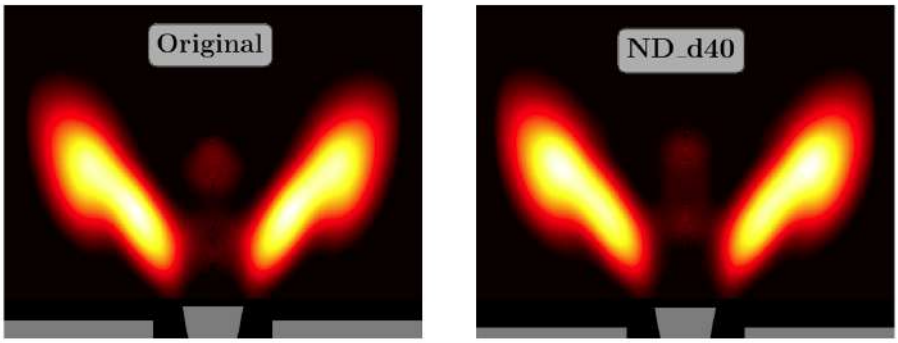


Figure 3.47: Mean flame visualization as obtained from an Abel transform of OH* signals from a CCD camera with a narrowband filter centered around 310 nm for injector lengths $\delta = 50$ mm (original) and $\delta = 40$ mm (modified). From [162].

For meshing, the methodology based on the LIKE criterion presented in sec. 3.3.2 is used to automatically refine the mesh twice in regions of interest. A baseline full tetrahedra mesh $Md1$ is generated with refined regions around the swirler, injector and supposed flame regions. After running a first cold flow stationary LES, $Md1$ is adapted near the injector exit yielding mesh $Md2$, then adapted a second time in the swirler zone, yielding $Md3$. For reacting numerical simulations, igniting the mixture and waiting long enough for the flow to reach thermal equilibrium everywhere in the chamber can necessitate numerous CPU hours. To save computational time, LES solutions of the

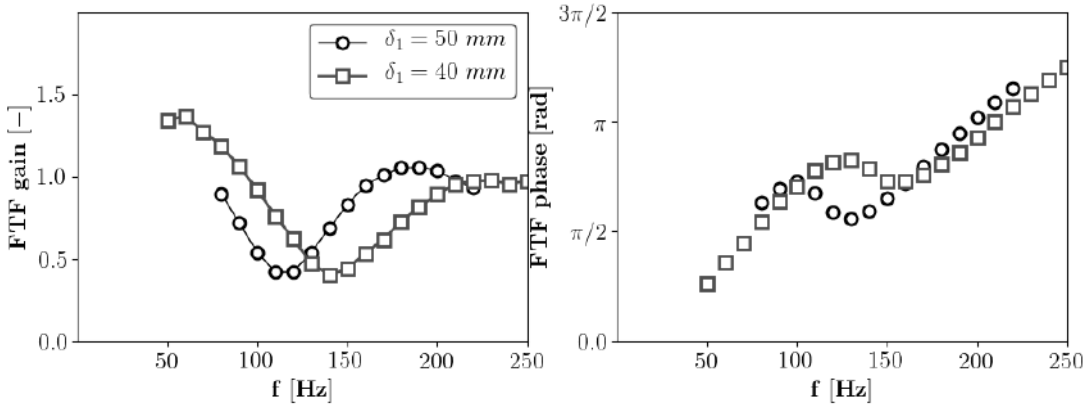


Figure 3.48: FTF of the Noisedyn burner for injector lengths $\delta_1 = 40$ mm and $\delta_1 = 50$ mm for a RMS forcing level $\hat{u}/\bar{u} = 30\%$, $\bar{u}$=5.44 m.s^{-1}. From [162].

case for which $\delta = 50$ mm can be interpolated onto the new mesh since only the injector has been modified. However, interpolations are known to create numerical errors that generate undesired spurious acoustic waves if donor and receiver meshes are different, or if the receiver mesh is not fine enough. This potential issue is minimized by applying a supplemental refinement based on reactive flow LES using $Md3$, this time using the mean normalized volumetric heat release rate as a metric, Fig. 3.49, yielding mesh $Md4$ where the flame region has been further refined. An overview of characteristic

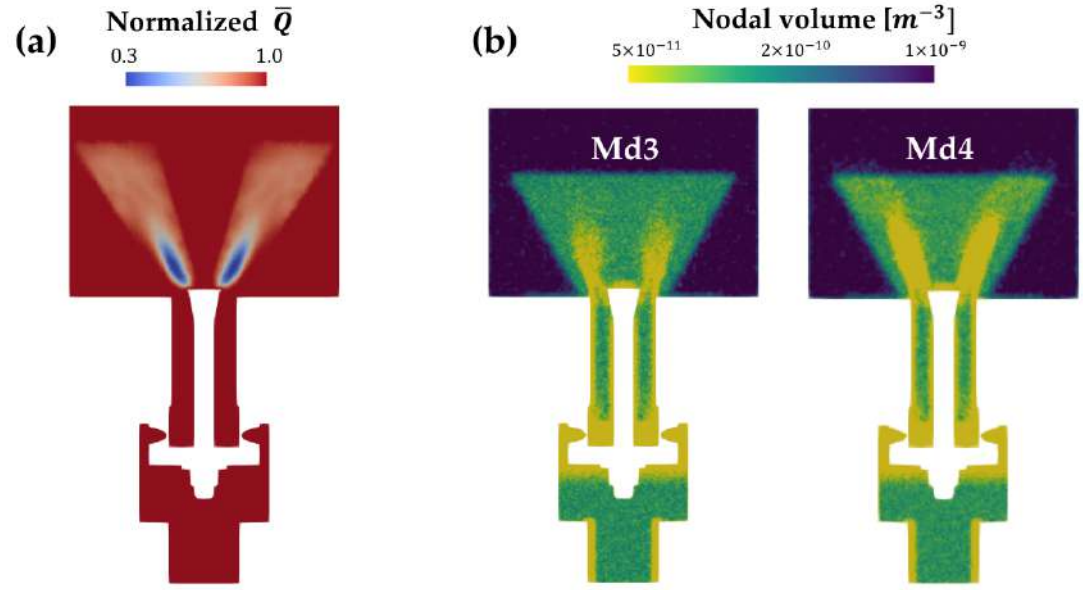
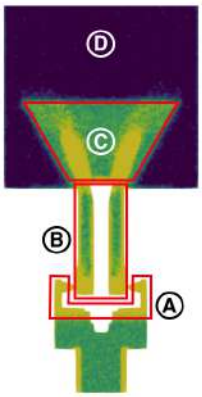


Figure 3.49: Cut view of the metric used for the automatic mesh adaptation of Md3 (a). Nodal volume for the original mesh Md3 and after refinement Md4.

dimensions for meshes $Md1$, $Md2$ and $Md3$ is available in Fig. 3.9 for the different mesh zones. All results presented in the following have been obtained using mesh $Md3$ when referring to cold flow simulations and with mesh $Md4$ for reactive conditions.



(a)

Mesh id.	Md1	Md2	Md3	Md4
N_{cells} (Millions)	15.1	15.8	17.9	25.0
Δ_x (A) (mm)	0.31	0.31	0.26	0.26
Δ_x (B) (mm)	0.31	0.25	0.23	0.23
Δ_x (C) (mm)	0.51	0.46	0.45	0.25
Δ_x (D) (mm)	1.0	1.0	1.0	1.0

(b)

Figure 3.50: Cut of mesh Md4 with main topological regions, and associated characteristic cell sizes in each zone for all meshes.

3.6.2.2 Stationary flame and FTF

The mean pressure drop observed with this new geometry is $\Delta P = 343$ Pa, which is approximately the same as the one $\Delta P = 341Pa$ obtained with $\delta = 50$ mm. This indicates that the major part of the pressure loss occurs when the flow goes through the swirler passage vanes. The steady flame shape obtained from LES is found to be very close to the one obtained with a longer injector as expected from experimental findings, Fig. 3.51. Both stationary flames are V-shaped with an intermittent apparition of secondary branches visible in the outer region of the injector exit. The latter seem to be more developed with the shorter injector, as a result of the modified flow interaction with the heat losing walls. In a second step, pulsed simulations were run for three frequencies corresponding to local FTF gain extrema $f_0 = 60$ Hz, $f_1 = 140$ Hz and $f_2 = 230$ Hz, see Fig. 3.48, with a pulsing amplitude $\hat{u}/\overline{u} = 30\%$ RMS. Temporal signals of the volume integrated heat release rate and velocity at the hot wire position were used to determine the FTF gain and phase for these frequencies. Once the initial transient period is finished, eight forcing periods were used in each case. LES results are compared to experiments in Fig. 3.52 and are overall in fair agreement. When it comes to the first local gain maximum at $f = 60$ Hz, the gain is slightly underestimated while the phase is in reasonable agreement with reference data. The second local gain maximum for $f = 230$ Hz is well predicted but the phase is overpredicted. The last frequency $f = 140$ Hz corresponds to the first local gain minimum and is not well predicted by the LES with a value 50% higher than the one obtained from experiments that cannot simply be attributed by uncertainties on both experiments and simulations. This result is quite unexpected since the methodology employed in Sec. 3.3.2 leads to fairly good results with a longer injection channel. One possible explanation lies in

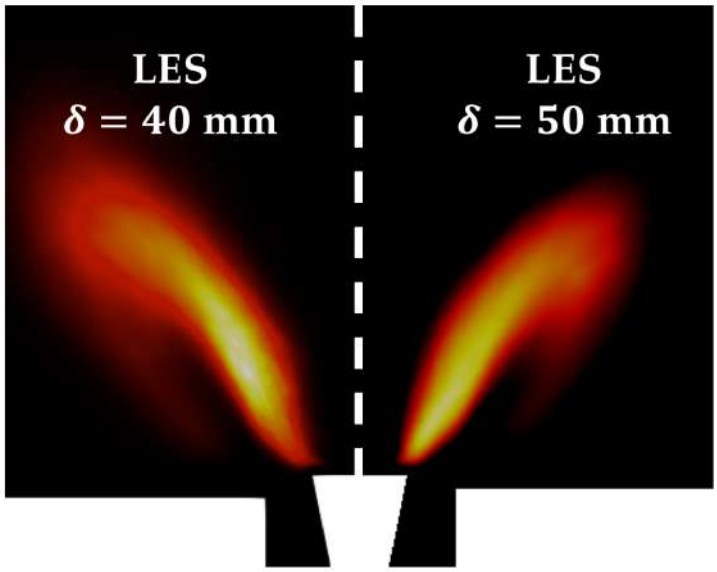


Figure 3.51: Comparison of steady flame shapes from LES for $\delta = 40$ mm and $\delta = 50$ mm using the normalized heat release rate.

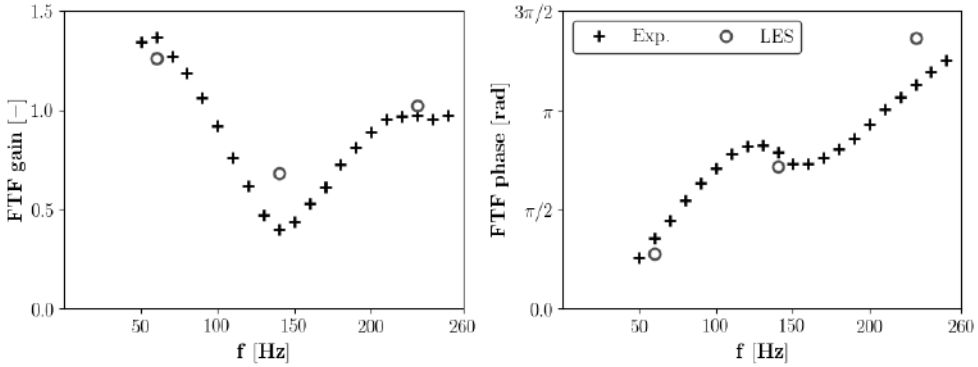


Figure 3.52: FTF of the Noisedyn configuration with $\delta_1 = 40$ mm as obtained from pulsed LES and experiments.

the fact that thermal conditions used for these calculations come from the case with $\delta_2 = 2.5$ mm whereas in the present case $\delta_2 = 1.5$ mm. The stabilization of intermittent secondary branches on the outer skirt of the flame is very much affected by thermal conditions on the chamber backplane, which may be different depending on δ_2 since the flame distance to the chamber backplane is directly linked to this quantity. Another possibility is that the mesh is not refined enough near the injector exit plane outer edge, so that in conjunction with a smaller distance, the computed flow cannot fully develop in the outer part of the channel and thus cannot accurately represent the vortical activity at the injector exit edges. The latter point is still under investigation.

3.6.2.3 SFTF model application

The SFTF methodology is applied following the same procedure that was used in Sec. 3.5 Firstly, parameters ω_*, α and K representative of the non-swirled flame response are extracted from the stationary reacting LES. The methodology described in Sec. 3.5.1 is applied once again to extract the main flame dimensions using the heat release rate center of mass. Normalized dimensions are found to be : $L_f/R_0 = 1.75$, $H_f/R_0 = 1.43$, $R_f/R_0 = 1.01$, while the mean half-flame angle is $\alpha = 35.1°$. Since the bluff-body has been slightly moved upwards in the chamber, the cross-section at the injector exit plane has been increased, yielding a bulk axial velocity $U_0 = 8.25$ m.s^{-1} compared to $U_0 = 8.78$ m.s^{-1} with the longer injector. Combining these quantities yields $\omega_*/\omega = 2.59$ ms. Similarly, the mean axial velocity U_{c-v} in the outer shear layer is probed from LES data using the procedure already presented in Sec. 3.5.1, yielding $U_{c-v} = 5.8$ m.s^{-1} and thus $K = U_0/U_{c-v} = 1.42$. The time delay $\tau = 4.73$ ms between bulk oscillations of acoustic and convective disturbances is computed from Eq. (3.9) with the new injector length $\delta = 40$ mm. As previously mentioned, this parameter is expected to be the main driver of the shift of the FTF gain extrema observed in the experiments when changing the injector length.

The next step consists in determining ϕ_0, the phase between bulk and edge velocities at the injector exit plane. The particular frequency $f = 140$ Hz corresponding to the first local FTF gain minimum is used. Using phase averaged data for $f = 140$ Hz, as presented in Fig. 3.53 yields $\phi_0 = -0.96$ rad. This corresponds to a 7% increase for

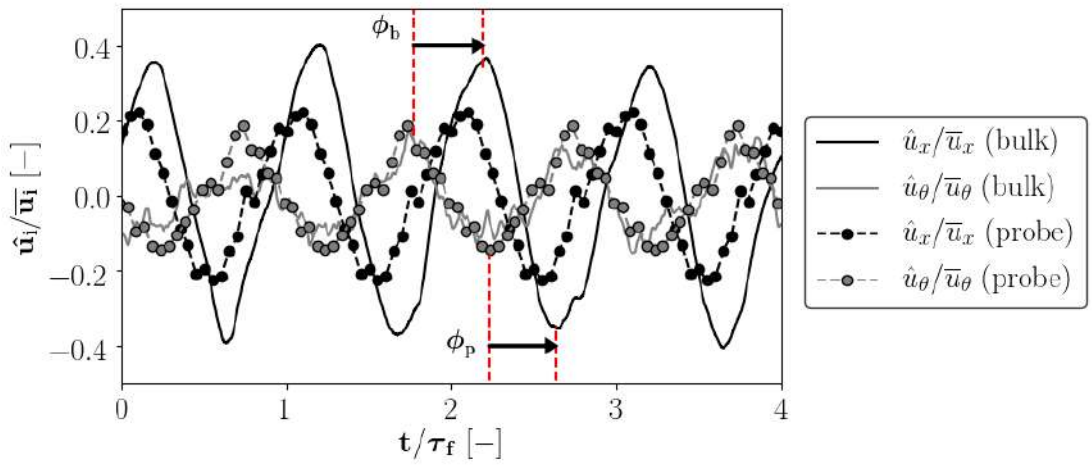


Figure 3.53: Normalized axial and tangential velocity signals on the injector exit plane (bulk, solid line) and a probe 0.5 mm away from the outer injector wall (dashed line with markers) for f = 140 Hz, $\phi_0 = -0.96$ rad. $\phi_0 = \phi_p - \phi_b$.

ϕ_0 compared to the value observed for $\delta = 50$ mm. Inserting back ϕ_0 in Eq. (3.14) for verification purposes yields a predicted minimum gain frequency $f_1 = 138$ Hz, which is

very close to the value observed in experiments. Note that if the frequency $f = 230$ Hz is used, one gets $\phi_0 = -1.13$ rad, yielding $f_1 = 144$ Hz, also in good agreement with the expected value.

Finally, a cold flow pulsed simulation for $f = 140$ Hz is performed in order to extract the decay rate of axial velocity disturbances β, Fig. 3.54. From the LES data, $\beta = 0.41$,

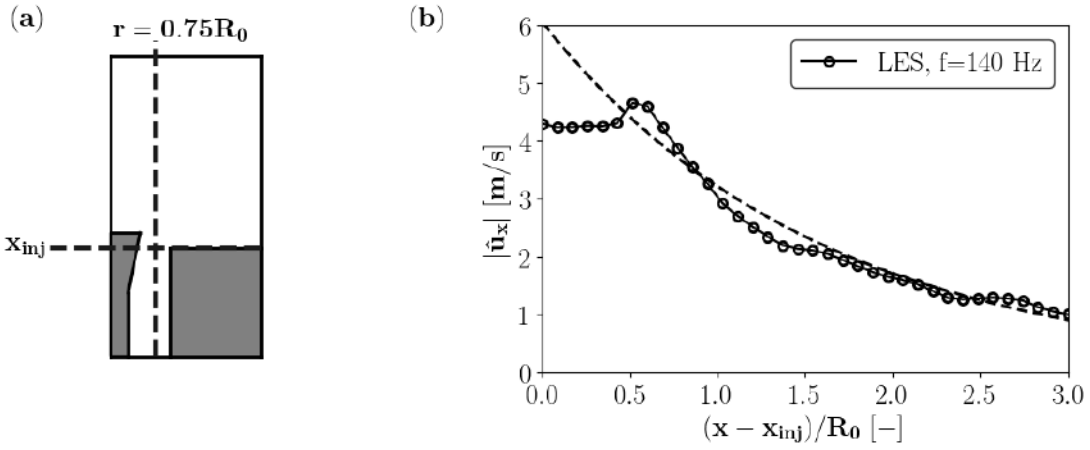


Figure 3.54: (a) Schematic of the central line located at $r/R_0 = 0.75$ used for the amplitude decay evaluation. (b) Acoustic velocity amplitudes for f = 140 Hz on the same line, starting from the injector exit plane. Dotted lines show the best fit for each frequency in the form $Ae^{-\gamma x}$.

which is similar to the value obtained for a 55% forcing amplitude in sec. 3.5.2.2 with a 25% longer injector. Such a high level was not expected. Using a simple optimization algorithm on both β and χ, the optimal decay rate value is found to be $\beta = 0.22$ which is closer to the value obtained in the case of the longer injector ($\beta = 0.18$). This may be explained by the fact that the exponential fitting presented in Fig. 3.54 does not fit very well the data for $0.5 \leq (x - x_{inj})/R_0 \leq 1.5$, and is quite sensitive to small variations. Another explanation may be that the LES is not precise enough to correctly capture this decay, but the simulation probed value is used anyway in order to verify the subsequent modelled FTF response. Since the FTF gain and phase estimated from LES for $f = 140$ Hz are not in good agreement with the experiment, the experimental values of gain and phase for this forcing frequency are used for the optimization procedure on χ instead of LES ones, which are not representative of real pulsed flame dynamics. Table 3.8 presents parameters as obtained from the three fidelity levels SFTF1, SFTF2 and SFTF3 for the current NoiseDyn configuration with $\delta = 40$ mm. The associated FTF predictions are shown in Fig. 3.55 for the three SFTF levels. With SFTF1, the alternating low and high gain regions are retrieved, as well as the phase curve inflection. However, the frequency of the phase inflection point, corresponding to the first FTF gain minimum is not well predicted.

Table 3.8: SFTF parameters for $\delta = 40$ mm as determined from accuracy levels SFTF1, SFTF2 and SFTF3. β is probed for f = 140 Hz. For SFTF2 and SFTF3, χ was determined from an optimization on the experimental FTF value.

Case	ω_*/ω[ms]	α [deg]	K	χ	τ [ms]	ϕ_0[rad]
(a) SFTF1	2.59	35.1	1.42	-0.33	4.73	0.0
(b) SFTF2	2.59	35.1	1.42	-0.39	4.73	-0.96
(c) SFTF3	2.59	35.1	$1.42 + 0.58i$	-0.30	4.73	-0.96

Going further with SFTF2, this frequency is matched, which greatly improves the agreement with the reference curves, especially for the phase. Still, the gain is largely overpredicted for $f \geq 160$ Hz. Introducing a spatial decay with SFTF3, the overall gain is reduced and high frequency FTF gains are much closer to the experimental reference. Doing so, the predicted gain for low frequencies is slightly deteriorated. Unlike what was observed for the longer injector in Sec 3.5.2, the phase is altered with a non null β value, leading to a smoother transition around $f = 140$ Hz which does not comply with the experimental observations. The limited improvement going from SFTF2 to SFTF3

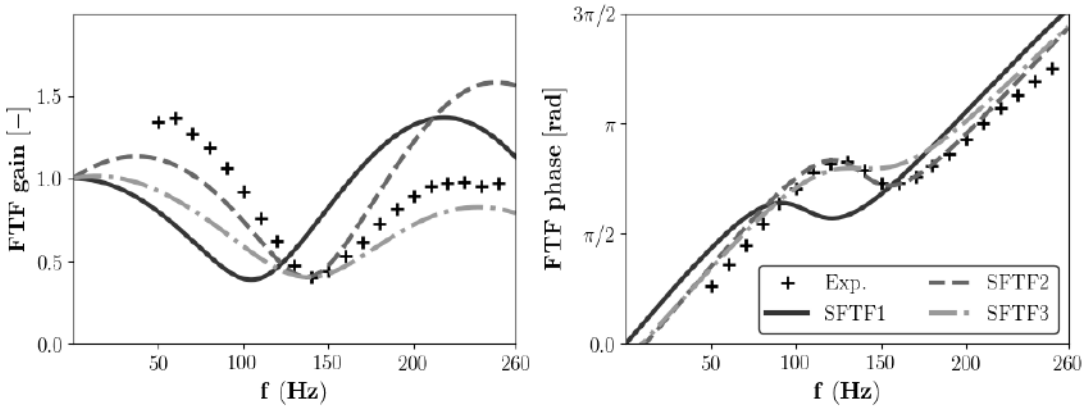


Figure 3.55: SFTF model results on the $\delta = 40$mm case with parameters presented in Tab. 3.8 for the three levels of accuracy SFTF1, SFTF2 and SFTF3.

can be explained by the large value of β measured for $f = 140$ Hz, which is not in line with values observed for a longer injector channel. Indeed, the decay rate of velocity disturbances measured for cold flow forcing in the chamber should be mainly dictated by the chamber geometry itself. Instead the value obtained for the same forcing RMS amplitude $\hat{u}/\overline{u} = 30\%$ for $\delta = 40$ mm is more than twice higher than for $\delta = 50$ mm. Still, the FTF phase is well predicted by the analytical model and thus, mode stability as predicted from low order codes or Helmholtz solvers should be correct.

3.6.3 Sensitivity of the SFTF model

The validation of the SFTF model on various geometrical variations of the NoiseDyn burner as done in previous sections is a good starting point for the assessment of the generality of the methodology. In the context of numerical simulation, another major aspect for further validation is to characterize how the model can be impacted by uncertainties on its input parameters. Indeed for turbulent complex flows, small modifications of the numerical setup or even user made choices (total average time, number of forcing periods for FTF data extraction, etc) are likely to affect the evaluation of the SFTF model parameters. The same comment also applies to experimental data for which measurements are always associated with an interval corresponding to uncertainties on the probed values.

In this section, the impact of uncertainties on model parameters is assessed on case with the longer injector ($\delta = 50$ mm) to illustrate the robustness of the methodology. The surface response method is used to explore the field of possibilities by assuming a maximum uncertainty ϵ. For each uncertain parameter $\mathcal{P}$, the continuous spectrum of possibilities is discretized using $n_t = 2 \times n_e + 1$ values so that the array of values effectively used $V_{\mathcal{P}}$ reads:

$$V_{\mathcal{P}} = \mathcal{P}\left(1 - \epsilon \times \frac{n_e - i}{n_e}\right)_{i=0,\dots,n_e} \cup \mathcal{P}\left(1 + \epsilon \times \frac{n_e - i}{n_e}\right)_{i=0,\dots,n_e-1}, \tag{3.15}$$

with $n_e \geq 1$. The modelled FTF response is then evaluated for each combination of arrays $V_{\mathcal{P}}$ for the chosen number of varying parameters n_p. Assuming that n_s levels of uncertainties ϵ are tested on n_p parameters, the total number of possible combinations N_c is :

$$N_c = n_s \times n_t^{n_p} \tag{3.16}$$

In a first attempt, uncertainties on all model parameters (ω_*, α, K, χ, τ, ϕ_0 and β) are considered. In the case of parameter χ which is obtained from a pointwise optimization on FTF gain and phase values, the uncertainty is directly applied to targeted gain and phase values. Note also that the value assigned to χ after optimization depends on other parameters such as K and β. Still, this study is representative of a worst case scenario. Four levels of maximum deviation ϵ are used : 1%, 3%, 5% and 10 %; while n_e is set to $n_e = 7$ to keep the computational cost within reasonable limits. The total number of explored combinations is $N_c = 3\ 294\ 172$.

For each uncertainty level ϵ, one can define an envelope marking the area between the minimum and maximum computed FTF values for each frequency. Figure 3.56 presents such uncertainty envelopes for the four studied deviations. Increasing the maximum uncertainty ϵ of course broadens the FTF gain and phase uncertainty envelopes. One

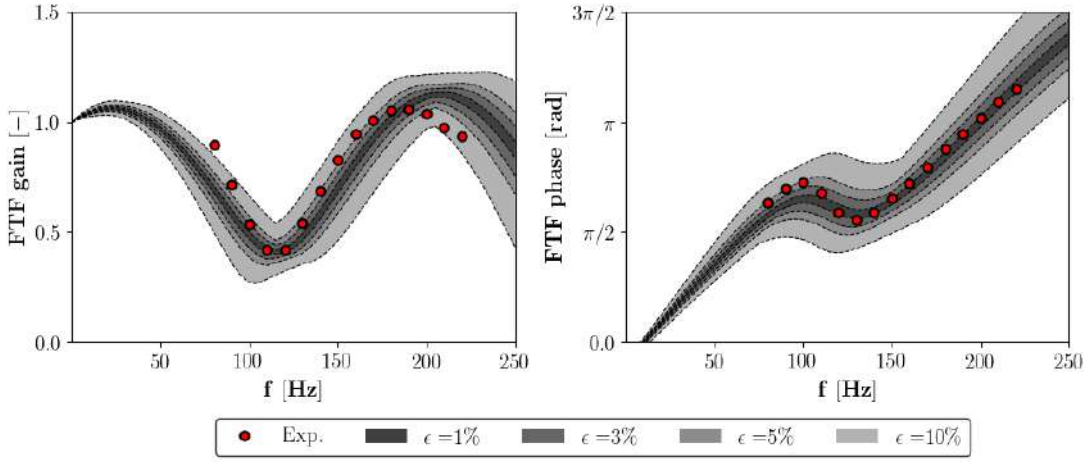


Figure 3.56: SFTF model results with uncertainties on all parameters (ω_*, α, K, χ, τ, ϕ_0 and β) for various maximum deviation levels ϵ.

observes that the combination of small uncertainties on all parameters can result in considerable variations of the predicted FTF gain and phase for frequencies $f \geq 60$ Hz. Minimum FTF gain deviations are observed in the low frequency limit because of the imposed unity gain condition, and around local extrema as a consequence of the optimization of χ for $f = 120$ Hz. For the maximum tested deviation $\epsilon = 10\%$, maximum variations of about 40% compared to the reference data are obtained in the frequency range 120 Hz$\leq f \leq$ 180 Hz. These area correspond to regions where the optimization of χ has the smaller influence. Regarding the phase curve, the relative variation for each level ϵ is almost the same for all frequencies and ranges from 2.5% for $\epsilon = 1\%$ to about 25% for $\epsilon = 10\%$. This data shows that even minimal errors on each parameter can have an impact on the FTF prediction when combined.

Parameters extracted from pulsed LES are more likely to be a subject to uncertainties during their determination. Indeed, even with a correct reproduction of the stationary flame, forced flame dynamics may not be well reproduced and variability is introduced when choosing the number of forcing periods for instance. In a second step, uncertainties are considered only for parameters χ, ϕ_0 and β probed from pulsed simulations. The following levels of maximum deviation ϵ are considered: 5%, 10%, 25% and 50,%. Each parametric array is discretized using $n_e = 21$ for a total of 43 values explored. The resulting total number of explored combinations is $N_c = 37\ 044$.

Figure. 3.57 presents the uncertainty envelopes obtained in this case. The FTF gain is directly affected by χ and β and as such, the FTF gain curve show increasing deviations to the reference for increasing uncertainty levels ϵ. Yet, for limited levels of uncertainty $\epsilon \leq 25\%$ the maximum observed deviation on gain remains under 15%. This time, the largest discrepancies compared to the reference values are obtained on local extrema frequencies. This is the result of the fixed time delay τ and variability

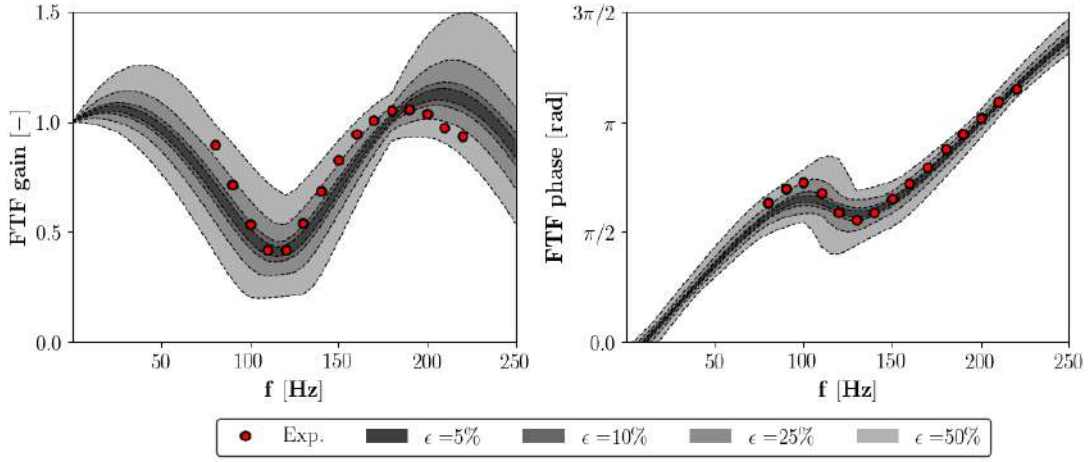


Figure 3.57: SFTF model results with uncertainties on parameters χ, ϕ_0 and β for various maximum deviation levels ϵ.

allowed on target FTF gain and phase used for the determination of χ. Compared to Fig 3.56, the phase curve general slope is almost unaffected when increasing ϵ, proving that parameters from stationary simulations (ω_*, α and K) are the ones governing this feature. One however notes that the FTF phase inflexion around $f = 120$ Hz increases with the uncertainty level ϵ, as a result of the variation of the swirl intensity parameter χ. A more thorough discussion on the deviations linked to each parameter is available in Appendix D.

Even with a high deviation $\epsilon = 50\%$, the maximum FTF phase deviation is limited to $\Delta\phi_{FTF} = 33\%$. In terms of thermoacoustic instability predictions, this means that the stability of modes will not be much affected by potential errors on pulsed simulations determined parameters, except in the FTF phase inflexion region. In contrast, FTF gains predicted by the analytical SFTF model can be considerably influenced by moderate mispredictions/miscalculations of few parameters. Among those, the parameter χ has been identified as the most important one. It is recalled that this quantity is obtained from an optimization on LES probed FTF gain and phase for a frequency corresponding to a minimum gain. Gain predictions capabilities are hence directly tied to the quality of the LES in the low gain region.

Since the prediction of thermoacoustic modes growth rates from low order codes relies on the FTF gain, discrepancies are to be expected even with minor changes in the simulation gauged parameters.

3.7 Concluding remarks

Numerical simulations of a premixed swirled V-shaped methane/air flame have been performed to validate an analytical model for the FTF of premixed swirling flames.

The numerical setup was handled with care to reproduce experimental data for the pressure drop, velocity profiles and flame response (FTF). An excellent agreement is obtained for all of these elements.

An analysis of the flow and flame dynamics at two frequencies corresponding to a minimum FTF gain and a maximum FTF gain respectively was carried out in Sec. 3.4.3. It is shown that the frequency dependent response of the flame is controlled by the preferential response of the injection channel, and more specifically by the repartition of momentum fluxes at its exit, in the vicinity of the flame anchoring position.

Then, the SFTF methodology introduced in Sec. 2.3.2 has been validated by determining model parameters using a robust process that could easily be transposed to other configurations/geometries. The model was applied in Sec. 3.5 and good agreement was obtained with reference experimental data, especially for the FTF phase lag which directly controls the stability of acoustic modes when introduced in a ROM. A distinction is made between three accuracy levels SFTF1, SFTF2, SFTF3, for which the total number of simulations is increased to yield a finer description of the swirling flame response.

Further studies conducted for various acoustic forcing amplitudes show that some of the characteristics of nonlinear swirling flames response can be reproduced using the SFTF methodology by accounting for the spatial decay of axial velocity disturbances, Sec 3.6.1. Compared to a reconstruction based on system identification techniques [112, 115], the method developed in this work is therefore not restricted to vanishingly small perturbation levels and can be used to determine the frequency response of premixed swirled flames submitted to flow rate modulations of any finite arbitrary amplitude.

In Sec. 3.6.2, a shorter injection channel was considered and SFTF was applied once again to validate the parameter extraction strategy, yielding good agreement with reference data. In particular, the FTF phase lag is well retrieved by the model. Finally, a qualitative sensitivity study was performed in Sec 3.6.3 to evidence which modelling parameters are likely to influence the FTF prediction. It is emphasized that the quality of the SFTF model is tied to the quality of the LES, and more specifically to an accurate representation of the swirling flame response for frequencies where the FTF gain is low.

These results obtained on an academic configuration are a first step towards the modelling of swirled flames as encountered in real aero-engines combustion chambers. In the following chapter, a joint numerical analysis relying on LES and Helmholtz computations is employed to characterize the stability of an industrial engine. At this occasion, the SFTF modelling strategy is also gauged.

Chapter 4

Thermoacoustic study of an industrial engine

Contents

4.1 Objectives 111
4.2 Description of the industrial combustor 112
4.2.1 Geometry 112
4.2.2 Combustion instability of interest 114
4.3 Numerical setup 114
4.3.1 Mesh and boundary conditions 114
4.3.2 Acoustic forcing and reference probes for FTF extraction . . 117
4.4 Determination of the real engine FTF 119
4.4.1 Stationary reactive flow and flame 119
4.4.2 Importance of the FTF reference location 121
4.4.3 Effect of the forcing amplitude on the FTF 127
4.4.4 Comparison of upstream and downstream forcing 137
4.5 Applicability of the SFTF model to a real combustor 145
4.5.1 Extracting SFTF model parameters 146
4.5.2 SFTF model application 149
4.6 Thermoacoustic stability analysis using a Helmholtz solver 151
4.6.1 Numerical setup 151
4.6.2 Helmholtz computations of the SAFRAN combustor 153
4.7 Conclusions 161

4.1 Objectives

This chapter focuses on the prediction of thermoacoustic instabilities in real engines or gas turbines. While few studies have been performed on industrial configurations using LES [31, 41, 199], most applications still rely on a reduced order modelling [83, 85, 200]. The FTF is the key element to predict the acoustic stability of a given combustor design with ROM codes. Yet, studies regarding the FTF of real industrial engines are scarce and often carried out with one particular type of acoustic excitation. Although the equivalence between an upstream and a downstream forcing has been

proven for academic burners when the reference location is close to the flame [39], there are presumptions that it may not hold for complex non-zero Mach numbers flows. In addition, in real combustors acoustics can interact with the mean flow through various mechanisms at different places: bypass channels, dilution holes, perforated liners, the high pressure distributor nozzle or swirling spray injection systems to name a few.

The objective of this chapter is to provide an extended analysis for the determination of a complex configuration FTF and to discuss the potential advantages and shortcomings of using a combination of LES and a Helmholtz solver to predict its acoustic stability for a given operating point. The applicability of the hybrid swirling flame FTF modelling strategy first presented in Chap. 2 is also discussed for the real engine considered.

The chapter is structured as follows. In Sec. 4.2 the geometry of the chosen combustor and the acoustic mode of interest are presented. Section 4.3 details the numerical setup as well as all the CFD diagnostics put in place for the determination of the flame response to acoustic modulations. In Section 4.4, numerical results for various forcing conditions are detailed and crucial modelling elements are identified in an effort to obtain a reliable flame transfer function. The applicability of the SFTF model for the considered industrial gas turbine is tested in Sec. 4.5. Finally, the acoustic stability of the combustor as predicted when using a 3D Helmholtz solver is examined in Sec. 4.6.

4.2 Description of the industrial combustor

4.2.1 Geometry

The industrial combustor considered in this study is an annular engine developed by SAFRAN Aircraft Engines and hereafter denoted as the SAFRAN combustor. Exact geometrical details as well as precise operating conditions will not be provided in this manuscript for confidentiality reasons. A global view of the full annular configuration is presented in Fig. 4.1. It is composed of N_{sec} identical sectors of angle $\alpha_{sec} = 360/N_{sec}$



Figure 4.1: SAFRAN annular combustor geometry, rear (left), side (middle) and front (right) views.

degrees, N_{sec} being a confidential integer number. Each sector features its own injection device and thus flame. The only periodicity breaking elements are the spark plugs placed unevenly around the chamber circumference. These are not considered in this study. The global design of a single sector is disclosed in Fig. 4.2.

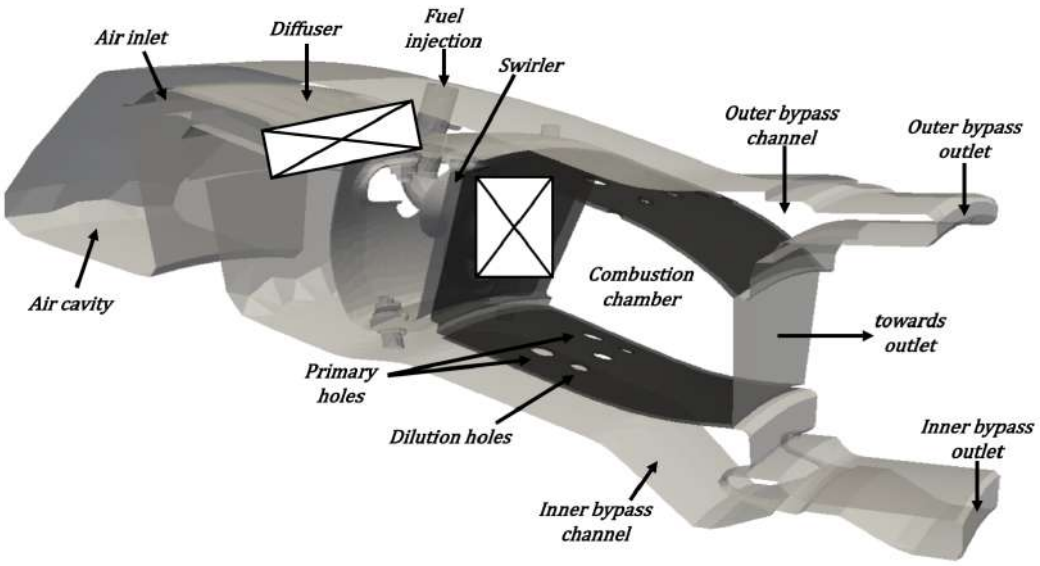


Figure 4.2: Single sector geometry of the SAFRAN combustor. Some geometrical details, including the outlet nozzle are hidden for confidentiality reasons, dimensions have been modified.

The high velocity discharge air coming from the compressor goes through a diffuser and is first slowed down. The flow is then split into a primary stream and a secondary stream. The primary stream goes through a two stage swirler unit and is injected in the combustion chamber where it mixes with kerosene injected in the form of a conical liquid spray. The fuel quickly evaporates and burns, forming a rich swirling flame attached in the vicinity of the injection device walls thanks to a strong hot gas central recirculation zone. Note that the chamber is inclined with an angle β_c with respect to the horizontal axis. At the same time, the secondary stream is guided through an inner and an outer bypass channels complex. A fraction of this air stream enters the chamber through the multi-perforated chamber enclosure as well as through a series of primary and dilution holes while the rest continues towards the later stages of the engine. Primary holes are used to quench the flame while dilution holes produce additional lean burning flames to consume the remaining unburnt fuel and reduce the overall temperature of the flow entering the turbine stages. This staged combustion technology is described as the Rich Quench Lean (RQL) method and has been increasingly used for its stability and low nitrogen oxides emission performances [8]. After combustion, these hot exhaust gases leave through a high pressure distributor leading to the turbine stages. For numerical simulations, the high pressure distributor is not modelled and the

outlet is either longitudinally extended, or simply cut at the chamber exit as presented in Fig. 4.2. The entire combustion chamber casing is composed of plates pierced by a multitude of holes allowing the creation of a cold air cooling film along the chamber walls, protecting the chamber integrity. Note that these multi-perforated plates also induce acoustic dissipation by converting part of the acoustic energy into vorticity [185, 201], as will be discussed in Sec. 4.6.

The SAFRAN combustor has some of the features already studied in the NoiseDyn configuration of Chap. 3: a swirl-attached flame in a closed chamber, an overall lean equivalence ratio, etc. However it also includes substantial differences: no bluff-body, secondary diffusion flames, a two stage swirler, liquid fuel injection, etc. It is therefore worth appraising what can be done and what is left to do compared to laboratory scale burners in the context of combustion instability prediction and control.

4.2.2 Combustion instability of interest

An instability at frequency $f_i = 500$ Hz was observed for the considered operating point when engine tests were carried out by SAFRAN Aircraft Engines. Pressure sensors signals from two diametrically opposed positions were measured as out of phase, indicating that the mode has an azimuthal component as frequently observed under various forms in annular combustors [202, 203, 204]. In regards to the data from previous experiments, the instability was identified as a combustion instability mode. Figure 4.3 shows the most energetic frequencies over time during one of the engine test sessions. A clear activity is observed around f_i for an extended period of time. The exact nature and spatial shape of the mode are not a priori known and need to be investigated using numerical simulations. Since the instability involves an azimuthal component, single sector LES will not be able to capture it. LES of the annular geometry would be a worthy option and has been done few times in the literature [199], but they remain computationally intensive. The flame response can however be computed for a single sector, and used in a full annular configuration for low order acoustic computations by applying the same FTF for all the flames. This strategy is valid when a given flame does not interact with the neighbouring ones, that is, if the flame dimensions are smaller than the distance between two consecutive burners. These interactions are neglected in this work.

4.3 Numerical setup

4.3.1 Mesh and boundary conditions

Reactive flow CFD simulations are carried out on the single sector configuration of Fig. 4.2 with axi-symmetric periodic boundary conditions and an artificially elongated

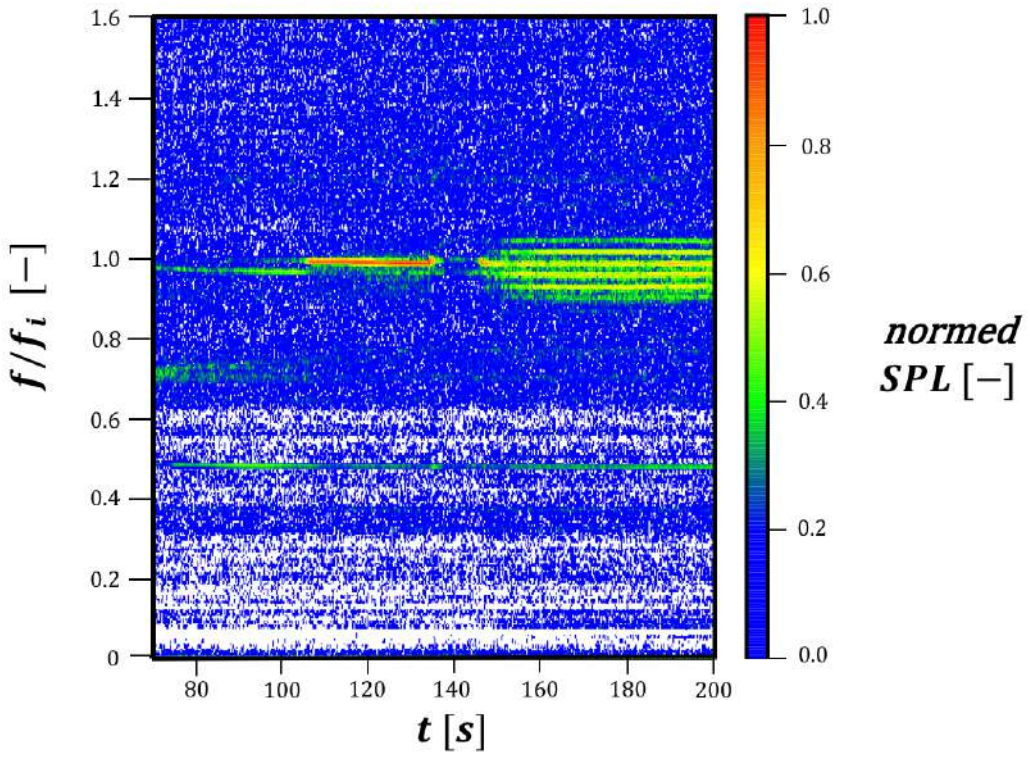


Figure 4.3: Frequency over time (FOTI) diagram, showing the most energetic frequencies during the engine testing session. The sound pressure level (SPL) is normalized for confidentiality reasons.

section towards the outlet to guide the hot exhaust gas. A view of a transverse cut of the mesh is presented in Fig. 4.4. The grid is refined near multi-perforated walls, as well

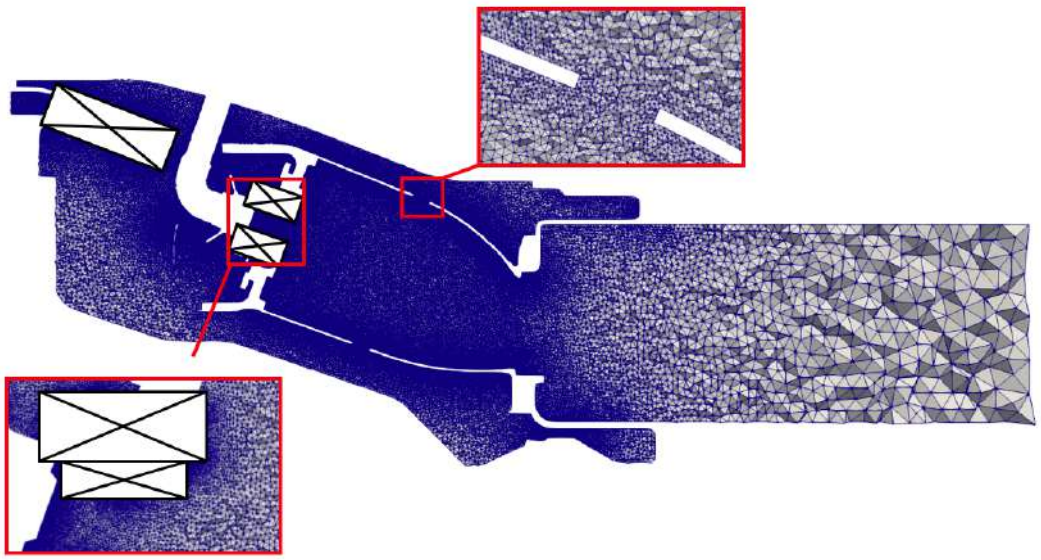


Figure 4.4: Transverse cut of the mesh used for the SAFRAN combustor simulations. Highlights on dilution holes and liquid injection regions.

as in the swirler and injection regions. It is composed of about 45 million tetrahedral cells with a minimum cell size $\Delta_x = 32$ μm. For all dilution and primary holes, it is ensured that at least 20 cells are used for one passage diameter. A gradual coarsening is applied towards the outlet of the domain to save computational time. Note that the mesh is obtained following the up to date meshing guidelines for SAFRAN real engine simulations. It does not allow for the resolution of all turbulent structures or to operate without any combustion model but constitutes a good trade-off between a good accuracy and a reasonable computational return time.

A characteristic inlet condition is used to inject air with a mass flow rate and a temperature set according to conditions where the instability described in Sec. 4.2.2 is occurring. Smaller streams of air also inject a small amount of mass through non-characteristic boundaries located on part of the swirler and on film inlets. The multi-perforated chamber casing is divided into six inner and six outer pairs of suction/injection surfaces using the homogeneous multiperforation model of [205] with the adequate porosity. The outlet is set to be characteristic, with an imposed mean pressure P_{out}. All remaining walls are treated as adiabatic and use a no slip velocity condition. Finally, the entire left and right surfaces of the single sector domain are set as a pair of axi-symmetric periodic boundary conditions where scalars are set to match from one side to another and vector quantities are rotated by the sector angle α_{sec} before being injected on the corresponding side.

Chemistry is handled with a reduced two-step *2S_KERO_BFER* mechanism for premixed kerosene/air mixtures validated for the range of fresh gas temperature, pressure and equivalence ratio considered in this study [206]. The global mechanism consists in a first oxidation reaction where the complex fuel is treated as a single specie, and a CO-CO_2 equilibrium reaction. The dynamic thickened flame DTFLES [178] combustion model is used to allow the flame front to adapt to the local mesh size with five imposed resolution points in the flame thickness. Since the flame does not only burn in a premixed regime, a look-up table is used to retrieve the local flame speed and its thickness based on the local equivalence ratio value. This specific reference information is obtained using one-dimensional premixed flames with the following discretization values:

- Equivalence ratio ϕ: 11 values ranging from 0.5 to 1.5,
- Fresh gas temperature T_f: 6 values ranging from 300 to 800 K,
- Pressure P: 8 values ranging from 1 to 30 atm,

for a total of 528 table entries. Local estimated flame properties are then used to apply the appropriate thickening to the flame front.

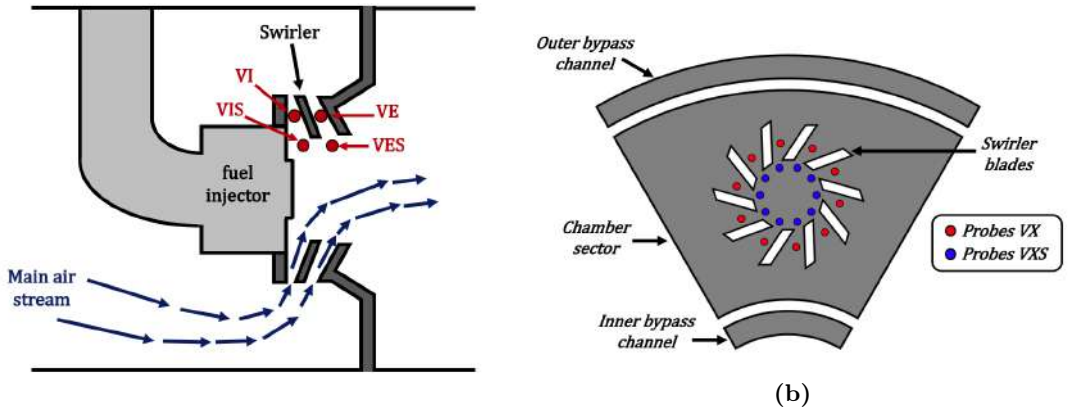
During the real engine operation, liquid fuel is injected through an orifice located just before the swirler channels exits in the form of a conical spray, producing droplets of Sauter mean diameter $d_{3,2}$ undisclosed here for confidentiality reasons. For the numerical simulations, the liquid phase is modelled as a dispersed continuous phase governed by a similar set of filtered Navier-Stokes equation as the gas phase [207]. This Eulerian-Eulerian approach is chosen over Lagrangian particle tracking as it is the standard procedure for SAFRAN engineers at the time. In this formalism, the gas and liquid phase equations are coupled using two source terms: an evaporation source term describing the conversion of mass from one phase to another, and a two-way drag force describing the kinetic energy transfer. Droplet evaporation is handled by a simplified Abramzon-Sirignano model [208]. The Stokes drag is approximated using a characteristic relaxation time computed thanks to an empirical correlation depending on the particle Reynolds number [209]. In the LES, the liquid fuel is injected as a hollow cone using an half spray angle α_{inj} and geometrical parameters following the approach of [210]. Boundary conditions for the dispersed phase are composed of characteristic inlets and slip walls. LES are performed using the AVBP solver with a two-step Taylor-Galerkin TTGC scheme [174] accurate to third order in time and space, and the SIGMA subgrid model [177].

4.3.2 Acoustic forcing and reference probes for FTF extraction

The flame transfer function formalism implies the choice of a reference location from which velocity fluctuations will be used to compute a gain and a time delay for the global heat release rate signal. For simple configurations this choice is both rather simple (the geometry itself is simpler) and not of crucial importance (the flow structure is often very directional). In the general case however, relying solely on a fluctuating velocity u' instead of considering both u' and p' for the FTF may not be sufficient if the probing location is located too far from the flame [122]. Four sets of probing positions have been defined in order to verify whether their placement is indeed of crucial importance or if it does not affect the FTF evaluation. Note that the two stage swirler features a periodic symmetry, allowing the use of multiple probes at once which should ideally be acoustically equivalent. The validity of this assumption will be assessed in the next sections. The four probing locations retained are :

- **VI** : halfway through the internal swirler stage channels,
- **VIS** : at the exit of the internal swirler stage channels,
- **VE** : halfway through the external swirler stage channels,
- **VES** : at the exit of the external swirler stage channels.

Probing locations VI and VIS are composed of N_i equally distributed probes in the first swirler stage while locations VE and VES are composed of N_e equally distributed probes in the second swirler stage. Figure 4.5 displays a schematic side and front visualization of the probe locations. The use of reference surfaces instead of pointwise



(a) (b)

Figure 4.5: (a) Schematic view of the two stage swirler and position of probe series VI, VIS, VE and VES. (b) Schematic view of a longitudinal cut in one of the swirler stages and position of probes in the swirler vanes, and at their exits. The number of swirler blades shown and geometrical details have been changed for confidentiality reasons.

locations has also been considered but was not retained in the present work as it presents several drawbacks: surfaces can be quite hazardous to define for complex geometries and evaluated gains may vary significantly depending on their location [211].

One should also note that the FTF methodology assumes the flame acoustic response to remain in the linear regime, which effectively translates into keeping the forcing amplitude low. Consequently, a legitimate question that arises is: how to define "low" ? Another concern lies in the location of the acoustic excitation source: the flow can be perturbed using an upstream or downstream forcing in regard to the flame. The equivalence of both forcing methods has been proven for academic geometries [39] but there is no data for complex cases. Three main acoustic forcing strategies are defined to tackle those issues, summarized in Tab. 4.1. The first two cases O08 and O25

Case	Type of forcing	Forcing amplitude
O08	outlet	0.83% P_{out}
O25	outlet	2.5% P_{out}
I10	inlet	10% $\overline{u}_{in}$

Table 4.1: Acoustic forcing conditions used for forced LES studies of the SAFRAN combustor.

correspond to an acoustic modulation of 0.83% and 2.5% of the imposed mean outlet

pressure respectively. For the latter case, the high modulation amplitude is likely to give rise to nonlinearities in the heat release signal. This aspect will be specifically discussed in Sec. 4.4.3. The remaining case I10 corresponds to a forcing of the main air inlet with a uniform velocity sine wave of amplitude $\hat{u}_{in}/\overline{u}_{in} = 10\%$ with $\overline{u}_{in}$ the bulk main inlet velocity. For all forcing cases, the goal is to capture the acoustic flame response in the absence of spurious acoustic reflections. Low relaxation coefficients are therefore applied in the LES on all inlets and outlets to avoid undesired reflections.

4.4 Determination of the real engine FTF

4.4.1 Stationary reactive flow and flame

The configuration is first studied for reacting conditions but in the absence of acoustic forcing. Figure 4.6 shows the mean velocity projected on the injection axis (inclined by an angle β_c from the horizontal axis) obtained after time averaging the LES fields over $t_{av} = 19$ ms, which corresponds to roughly five swirler exit to chamber exit plane convection times. The injected air stream splits between bypass channels and the swirler where it enters the combustion chamber with a high velocity. Several recirculation zones are observed in addition to the classical Inner recirculation zone (IRZ) and outter recirculation zones (ORZ) at the swirler exit. The largest one is observed in the air cavity located behind the injection device, while smaller ones establish downstream of the dilution holes. One can clearly identify the two central dilution holes high velocity

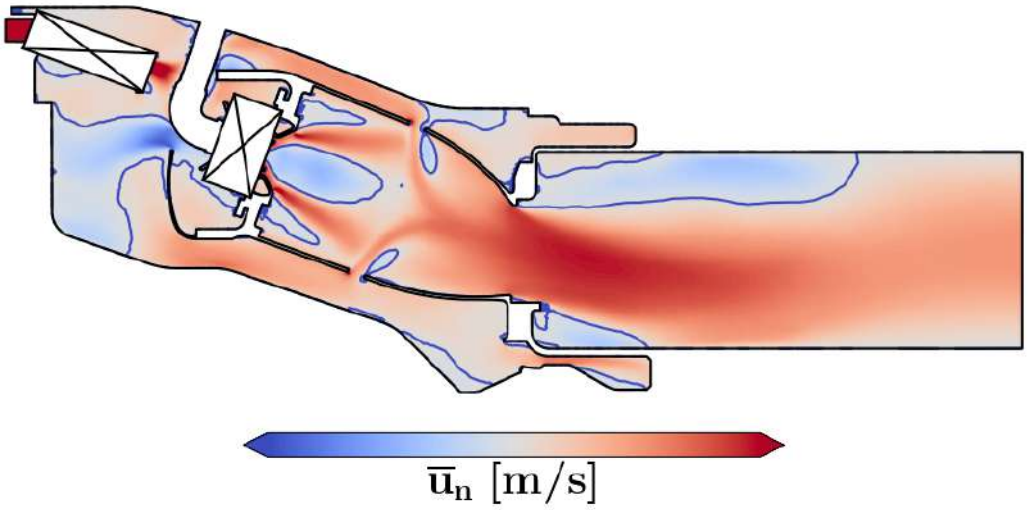


Figure 4.6: Mean velocity projected on the injection axis $\overline{u}_n$ on a transverse cut of the SAFRAN combustor. Recirculation zones can be identified from the $\overline{u}_n = 0$ isocontour in blue. The averaging time is $t_{av} = 19$ ms.

streams in Fig. 4.6 and the acceleration of the flow with the progressive reduction of

the chamber section towards its exit. The area surrounding the swirler exit is nearly azimuthally symmetric, allowing the investigation of velocities in a local reference frame tied to the injection axis. In that matter, Fig. 4.7 shows the three cylindrical velocity components for a temporally and azimuthally averaged cut in the injection reference frame. The kerosene/air mixture exits the swirler with a strong axial velocity component

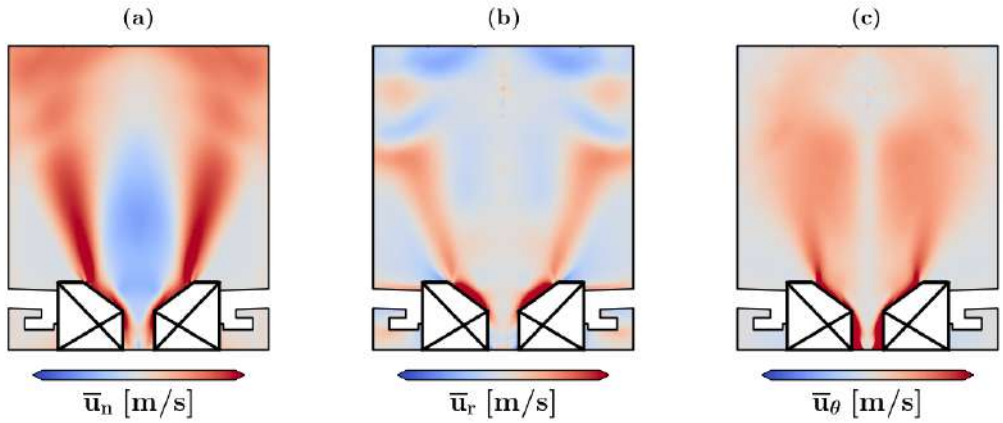
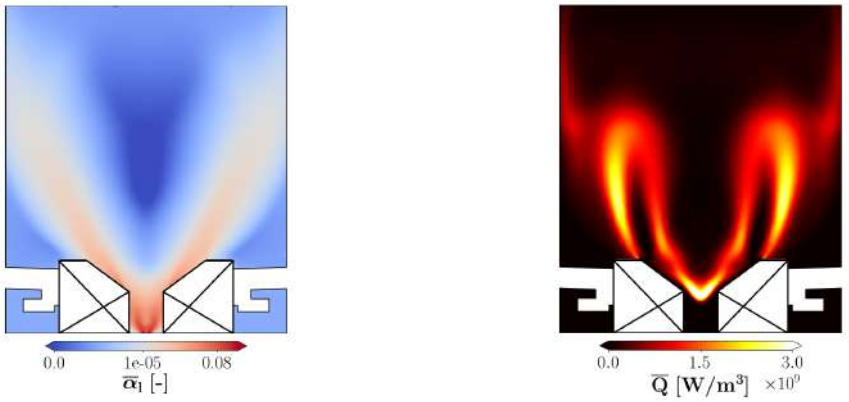


Figure 4.7: Mean axial (a), radial (b) and tangential (c) velocity components in the injector reference frame on an azimuthally and temporally averaged cut.

u_n forming a large IRZ as previously mentioned. Other velocity components are also strong, resulting in a swirl number $S = 0.67$ at the exit of the first swirler stage. Note also that further downstream, traces of the primary and dilution holes streams are visible on the radial velocity component even though an azimuthal average has been applied, Fig. 4.7b. The strong radial component at the exit of the first swirler stage is quickly mitigated when crossing the second swirler stage exit.

Regarding the combustion process, the high velocities and the temperature difference of few hundred degrees between the injected liquid fuel and the air stream result in a very quick evaporation of droplets. This is illustrated in Fig. 4.8a where the local liquid volume fraction $\alpha_l = V_l/V_g$, where V_l and V_g stand for the liquid and gaseous volumes, quickly drops when progressing towards the chamber main section. For this reason, the main rich flame burns almost fully in a gaseous regime and no thickening of the liquid phase is needed in the LES. The average flame is stabilized between the swirler exit and the IRZ, Fig. 4.8b. It has a classical M-shape, with core branches in the central region and secondary branches located in the outer part of the second swirler stage wake. The latter are attached to the swirler walls in the LES as a result of the adiabatic boundary conditions used. In reality, the main flame is very unlikely to be attached since the chamber back plane is cooled. From Fig. 4.8b one observes that the most reactive areas

are the central root of the flame and the inner zone of secondary branches. Note that the combustion process is weakened at the chamber backplane axial location for the central flame root. This is a result of the high velocity air stream exiting the second swirler stage. Besides, the trace of less energetic diffusion flames near multi-perforated walls can also be spotted on the azimuthal average.



(a) **(b)**

Figure 4.8: (a) Mean liquid volume fraction $\overline{\alpha_l}$ and (b) mean heat release rate $\overline{Q}$ in the injector reference frame on an azimuthally and temporally averaged cut. For α_l the scale is logarithmic.

4.4.2 Importance of the FTF reference location

In this section, the importance of the FTF reference location is specifically studied for the forcing case O08 for which an acoustic forcing of amplitude $\hat{p}/P_{out} = 0.83\%$ is applied at the outlet of the LES domain. The flame transfer function is then determined using probing locations VI, VIS, VE and VES as described in Sec.4.3.2 using at least six clean forcing periods for several frequencies f ranging from 300 to 700 Hz. For each forcing frequency, the global heat release signal is determined by integrating the heat release rate over the complete domain. This means that no distinction is made between the response of the main flame and the response of low power diffusion flames. Examples of raw heat release signals are shown in Fig. 4.9, with $\tau_f = 1/f$ the forcing period. The transient part of the signal is also removed. For example, for the signal at $f = 500$ Hz shown in Fig. 4.9b, the three first periods are not considered when performing the FTF gain and phase evaluation.

The reference velocity signal $u_{n,p}$ for each probe p is computed from the projection of the velocity components on the mean flow direction, that is:

$$u_{n,p} = u_p \frac{\overline{u_p}}{||V||} + v_p \frac{\overline{v_p}}{||V||} + w_p \frac{\overline{w_p}}{||V||} \tag{4.1}$$

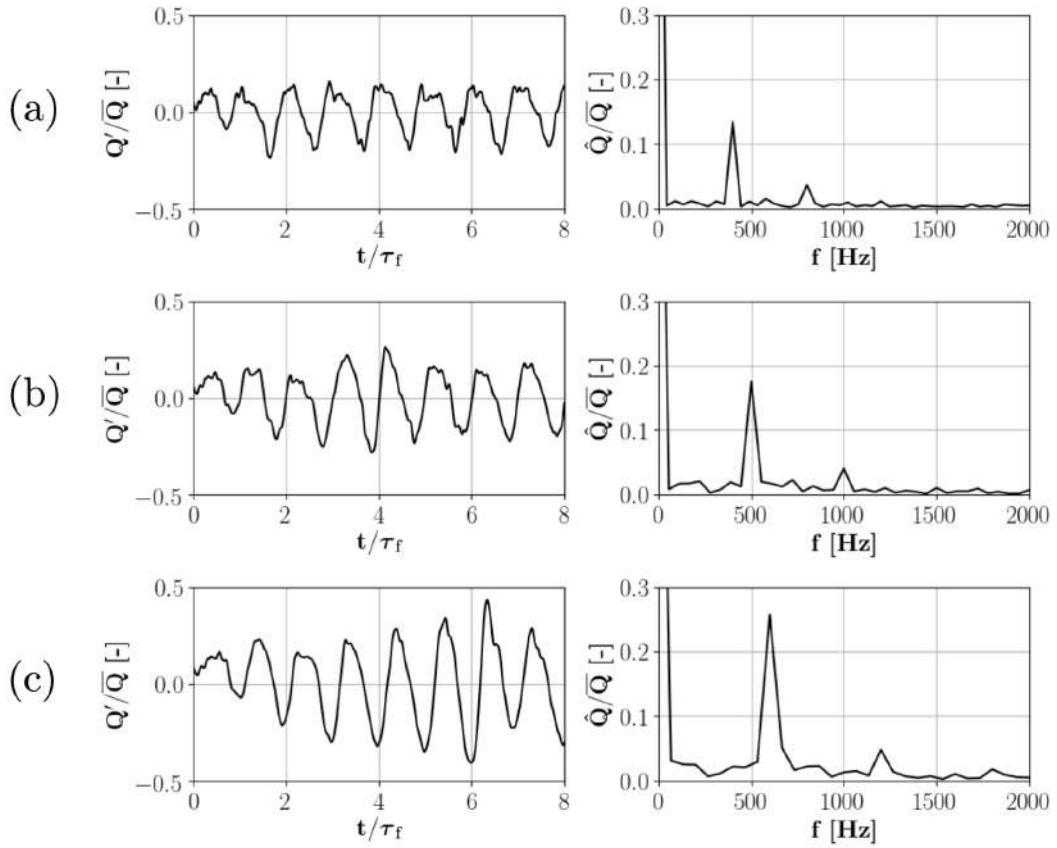


Figure 4.9: Global fluctuating heat release rate signals and associated FFT for (a) f = 400 Hz, (b) f = 500 Hz and (c) f = 600 Hz, for case O08 with an amplitude $\hat{p}/P_{out} = 0.83\%$. Note that all signals are normalized by the mean heat release rate.

with $||V|| = \left(\overline{u_p}^2 + \overline{v_p}^2 + \overline{w_p}^2\right)^{\frac{1}{2}}$ the mean velocity norm. For each probing location, a total of N_s probes is used where N_s is inferior or equal to the number of channels in the corresponding swirler stage: probes yielding erroneous data are discarded, that is probes with a high noise level or for which the forcing frequency is not visible enough. The final reference velocity signal u_n is then computed as:

$$u_n = \frac{1}{N_s} \sum_{k=1}^{N_s} u_{n,p} \tag{4.2}$$

Final reference velocity signals are presented in Fig. 4.10 for frequencies $f = 400$ Hz, $f = 500$ Hz and $f = 600$ Hz. Fourier transforms of these signals indicate that probing locations VI and VIS associated to the first swirler stage consistently provide data with more spectral content, and notably higher levels of harmonics. On the contrary, reference velocities from probing locations VE and VES provide normalized reference velocity signals closer to sine waves. For $f = 400$ Hz, the amplitude of normalized fluctuations is comparable for all probing locations. Moving to higher frequencies, and

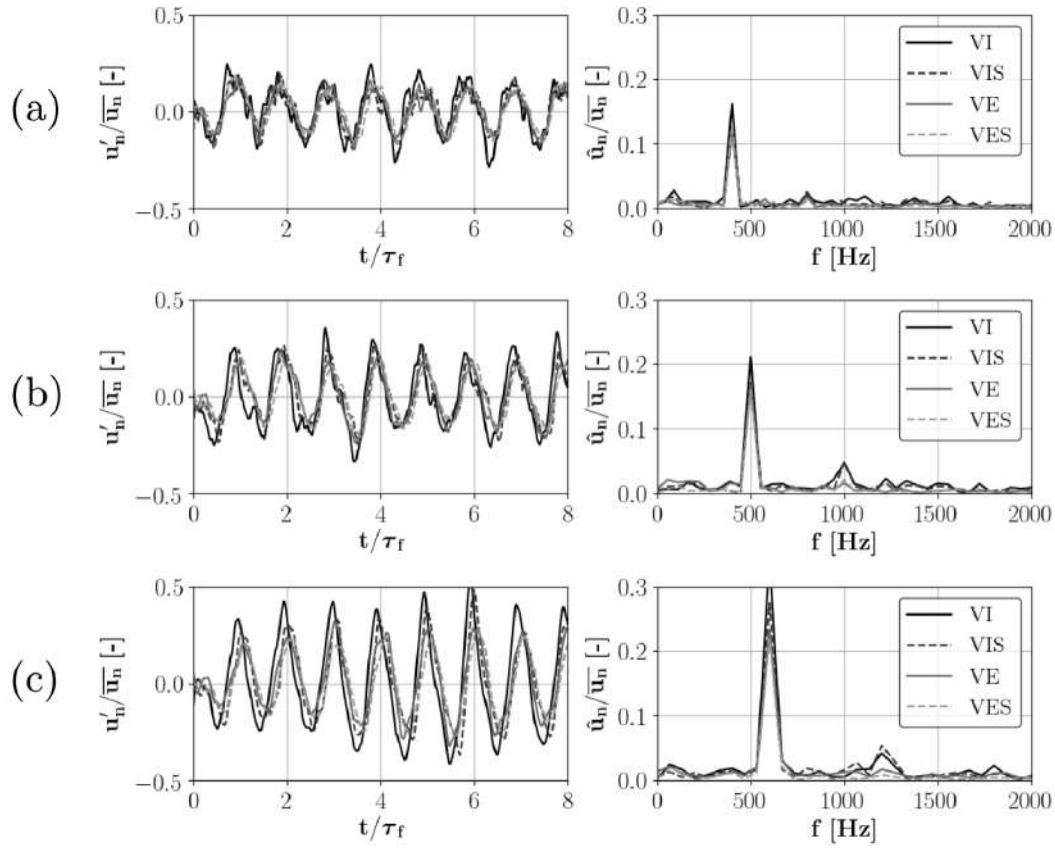


Figure 4.10: Normalized reference velocity signals and associated FFT for (a) f = 400 Hz, (b) f = 500Hz and (c) f = 600 Hz, for case O08 with an amplitude $\hat{p}/P_{out} = 0.83\%$.

especially for $f = 600$ Hz, the amplitude of $\hat{u}_n/\overline{u}_n$ remains comparable for VE and VES but differences are seen with VI and VIS. These observations tend to favour the use of probing locations VE and VES rather than VI and VIS. Note also that reference velocity fluctuations are overall slightly higher for $f = 600$ Hz. To complement the analysis, the modulus of characteristic acoustic impedances $Z(\omega) = \hat{p}/(\overline{\rho}\overline{c}\hat{u})$ measured at the exit of the swirler for probes of location VES is shown in Tab. 4.2 for the studied frequencies. Notably, a lower value is obtained for $f = 600$ Hz, which means that even though the same pressure modulation is used for all frequencies, the resulting reference velocity amplitude depends on the frequency response of the swirler itself, as seen in Fig. 4.10. This is not an issue as long as the flame response remains in the linear regime and as long as the reference points are chosen close enough to the flame base. The latter assumption may however not hold for probes VI and VIS from the first swirler stage and a double input FTF using both perturbed velocity and pressure may need to be used in such cases.

Another way to evaluate the quality of each probing location is to assess the Fourier

f [Hz]	|Z| [-]
300	0.31
400	0.31
500	0.29
550	0.28
600	0.26
700	0.30

Table 4.2: Modulus of the characteristic impedance obtained from probing location VES (exit of the second swirler stage) for a forcing amplitude $\hat{\mathbf{p}}/\mathbf{P_{out}} = 0.83\%$.

velocity component $\hat{u}_{n,p}$ at the forcing frequency f for each series of probes. Figure 4.11 discloses such Fourier coefficients $\hat{u}_{n,p}$ for each probe reference velocity, and all probing locations for $f = 500$ Hz. Reference velocity Fourier components are much more clustered in the complex plane for locations VE and VES than for VI and VIS, even though erroneous probes have been discarded. Worst results are obtained using location VIS, for which the values of Fourier coefficients are scattered around the mean due both amplitude and phase dispersion. On the contrary, results obtained from location VES are concentrated in a single region of the complex plane. Relative differences for the value of the FTF gain depending on the probing location can directly be guessed from Fig. 4.11 for $f = 500$ Hz. Indeed, the distance between the red dashed marked circle indicating the amplitude of $\hat{u}_n$ and the black square representing $\hat{Q}$ changes when using VI, VIS, VE or VES. As previously observed, amplitudes are similar for most locations except VI for which the resulting interaction index will be lower. Exploring the temporal data, it is interesting to evaluate the standard deviation $\sigma\left(\hat{u}_n/\overline{u}_n\right)$ with respect to the mean projected velocity for all probes u_n, that is:

$$\sigma\left(\hat{u}_n/\overline{u}_n\right) = \frac{1}{N_s}\sum_{p=0}^{N_s}\left(\frac{\hat{u}_n^2}{\overline{u}_n{}^2} - \frac{\hat{u}_{n,p}^2}{\overline{u}_{n,p}{}^2}\right)^{1/2}, \tag{4.3}$$

with N_s the number of probes retained for the analysis on a given location (VI, VIS, VE, or VES). Figure 4.12 shows the temporal evolution of the standard deviation $\sigma\left(\hat{u}_n/\overline{u}_n\right)$ obtained for $f = 500$ Hz. One observes that it is consistently lower when using probing location VES compared to VI. This once again confirms that data from probing location VES is more reliable than data from probing location VI.

In light of these observations, one needs to find a reason for the differences between results obtained using reference locations VI or VES for instance. A first potential explanation focuses on a difference in local mesh size in the first and second swirler stage channels that would yield a more resolved near-wall flow for one of the locations. This origin is however discarded since the local wall normalized distance y^+ is the

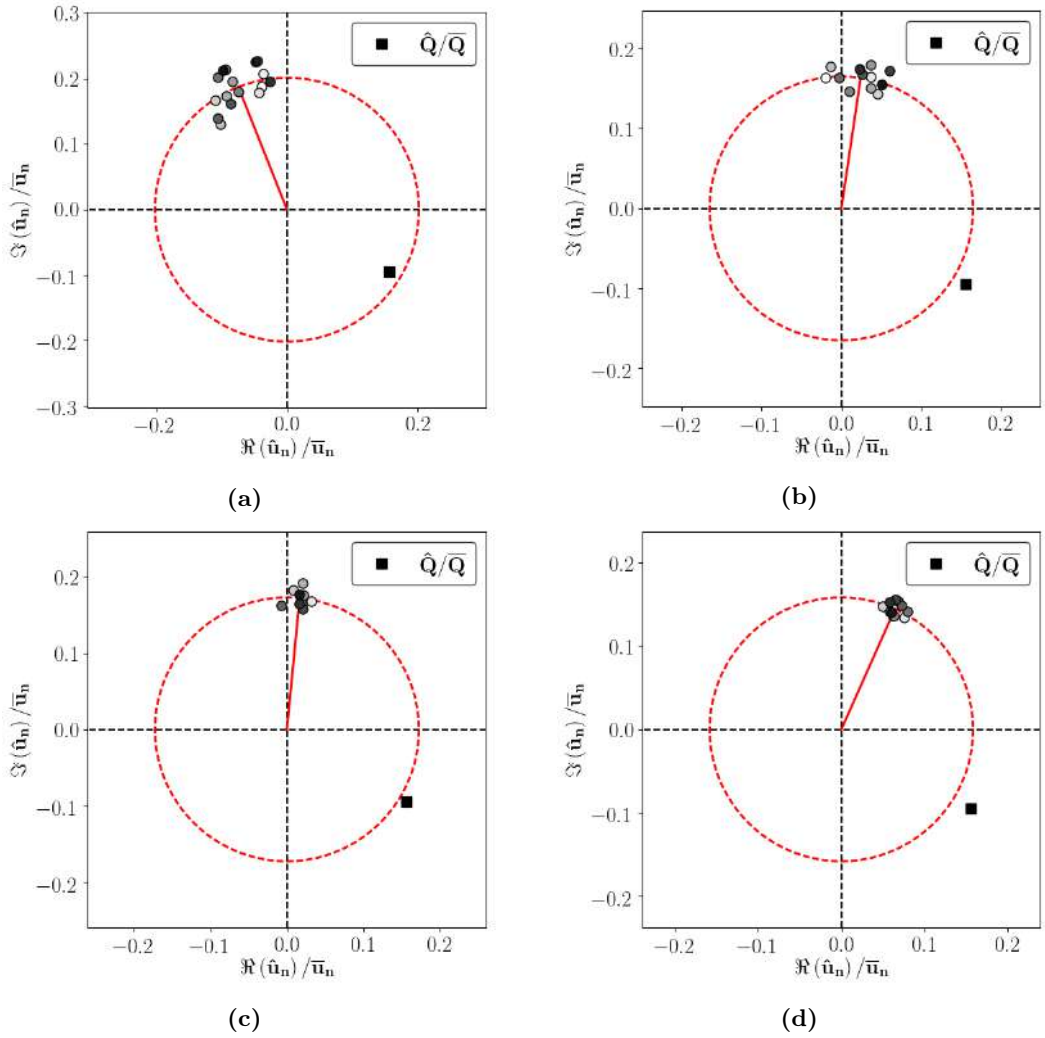


Figure 4.11: Fourier coefficients of normalized reference velocity signals $\hat{u}_{n,p}$ for probing location (a) VI, (b), VIS, (c) VE and (d) VES in the complex plane for f = 500 Hz and $\hat{p}/P_{out}$ = 0.83%. The black square indicates the Fourier coefficient of heat release $\hat{Q}$. The red dashed marked circle radius identifies the amplitude of the probe series mean velocity coefficient $\hat{u}_n$, while the red line indicates its phase angle.

same for both regions with the mesh used in this study (a few dozen units). Although each swirler stage presents a periodic symmetry, the main air stream entering the swirler channel does not since the injection fuel line lies in the wake of the diffuser (see Fig. 4.2). As a result, probes located directly in the wake of the injection line can be expected to be subject to stronger turbulent fluctuations. When progressing further towards the second swirler stage, the air stream establishes and local turbulence levels decrease. Hence, probes VE and VES should be less affected. One finally notes that the first swirler stage flow is affected by the liquid fuel injection crossing the stream exiting each channel.

To finish, the different FTF derived from each of the tested reference locations are

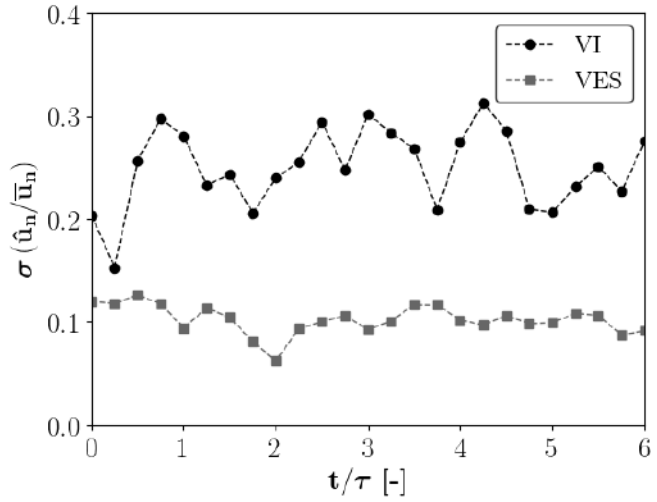


Figure 4.12: Standard deviation $\sigma\,(\hat{u}_n/\overline{u}_n)$ with respect to the mean projected velocity for all probes u_n for various points in a forcing cycle, f = 500 Hz and $\hat{p}/P_{out} = 0.83\%$.

shown in Fig. 4.13. FTF gain curves, Fig. 4.13a, produce different profiles depending on

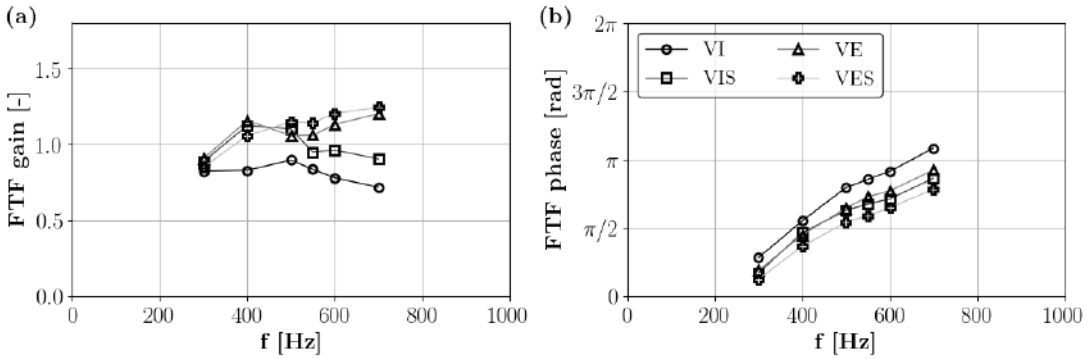


Figure 4.13: FTF gain (a) and phase (b) as obtained from forced LES for probing locations VI, VIS, VE and VES for forcing case O08 with amplitude $\hat{p}/P_{out} = 0.83\%$.

whether probes VI/VIS or VE/VES are considered. For the first swirler stage reference locations, a local gain maximum is observed while a monotonous increasing tendency is seen for second swirler stage reference locations. For the latter, the reliability behind the use of locations VE and VES is confirmed since corresponding curves are almost superimposed. On the contrary, using VI yields overall lower FTF gains. FTF phase curves, Fig. 4.13b, all share the same profile with a slight slope change depending on the reference location considered. This behaviour is expected since the FTF time delay τ_{FTF} is the sum of two components: an acoustic convection delay τ_c connecting the probing position to the flame and the intrinsic flame response delay τ_{fl}, $\tau_{FTF} = \tau_c + \tau_{fl}$. In the present case, LES obtained time delays range from $\tau_{FTF} = 0.2$ ms to $\tau_{FTF} = 0.8$

ms. The distance of probes located furthest from the flame base is few millimeters and the local sound speed is of the order of few hundreds meters per second. The acoustic convection time delay τ_c is therefore one order of magnitude lower than the flame time delay τ_{fl}. Simply put, τ_c is small but non negligible and since the FTF phase is computed as $\varphi_{FTF} = \omega\tau_{FTF}$, probes further away from the flame base should yield the highest FTF delays. The hierarchy is respected here since the probes further away from the flame (VI) show greater time delays and thus FTF phase, while probes closer to the flame (VES) have the smallest phase values.

In most cases, the stability of a mode is tied to the FTF time delay, or equivalently its phase. The only exception to this rule are the so called Intrinsic ThermoAcoustic (ITA) modes that have been recently observed in academic cases using anechoic chambers [198] as well as in DNS studies [53]. The stability of ITA modes indeed depends on both the FTF gain and phase. Such modes are not considered in the present study since the combustion chamber boundaries are far from anechoic. The previous observations made on FTF time delay thus indicate that predicted mode stability using ROM codes is likely to be the same regardless of the chosen velocity reference location. However, quantitative predictions of flame induced mode frequency shifts and associated growth rates will be affected since the input FTF gain varies with the reference choice. For this reason, only reference locations VE and VES will be considered in the rest of this study, as these were shown to be the most reliable ones.

4.4.3 Effect of the forcing amplitude on the FTF

4.4.3.1 Forced signals analysis

In this section, an investigation is carried out on the effects of the acoustic forcing amplitude for cases O08 and O25 from Tab. 4.1. These correspond to an outlet forcing with an amplitude $A_1 = \hat{p}/P_{out} = 0.83\%$ and $A_2 = \hat{p}/P_{out} = 2.5\%$ respectively ($A_2 = 3A_1$). The forcing methodology described in Sec. 4.4.2 is used for both cases, and comparisons are made using a reference signal computed from N_s probes distributed on a circle located at the second swirler stage exit (VES). For case O25, the high forcing amplitude results in a nonlinear flame response regime, the FTF formalism is therefore not particularly well adapted. Markers of nonlinearities are distinctly seen for low frequency forcing, as shown from the heat release signal in Fig. 4.14 for the specific case $f = 150$ Hz. Indeed, large overshoots of heat release are seen, making the signal far from the sine wave expected from the linear acoustics theory on which the standard FTF formalism relies. The associated FFT confirms the presence of several harmonics of the main forcing frequency in non negligible proportions. For instance, the amplitude

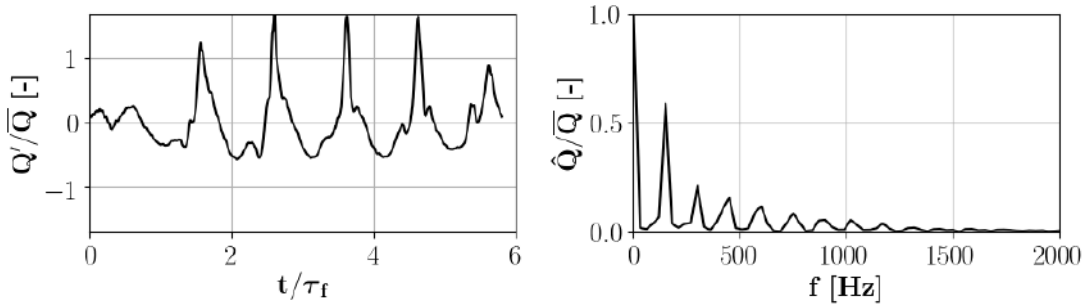


Figure 4.14: Integrated fluctuating heat release signal and associated FFT for $f = 150$ Hz, $\hat{p}/P_{out} = 2.5\%$ (O25). Several harmonics of the forcing frequency are visible.

of the first harmonic of heat release rate at $f = 150$ Hz reaches 35% of the amplitude of the fundamental forcing frequency.

As a first verification, reference velocity signals u_n at probing position VES are compared for the two considered cases, with examples illustrated for $f = 400$ Hz, $f = 500$ Hz and $f = 600$ Hz in Fig. 4.15. The ratio of reference velocity signals amplitudes A_{u_n} between case O08 and case O25 is computed from Fourier coefficients amplitude as $A_{u_n} = |\hat{u}_n|_{O25}/|\hat{u}_n|_{O08}$, yielding $A_{u_n} = 2.84$ for $f = 400$ Hz, $A_{u_n} = 3.0$ for $f = 500$ Hz and $A_{u_n} = 2.51$ for $f = 600$ Hz respectively. This data shows that controlling the fluctuation level at the outlet of the domain is not always sufficient to retrieve the exact expected ratio $A_{u_n} = 3$ at VES probes. Still, the imposed forcing amplitude difference is reasonably respected and comparisons are made on this basis. A second verification then consists in evaluating the ratio between heat release rate amplitudes for the two considered forcing amplitudes $A_Q = |\hat{Q}|_{O25}/|\hat{Q}|_{O08}$. Corresponding heat release signals are disclosed in Fig. 4.16 for frequencies $f = 400$ Hz, $f = 500$ Hz and $f = 600$ Hz. For the higher amplitude forcing, O25, temporal evolution of heat release varies from one frequency to another. For $f = 400$ Hz, an overshoot is first observed, followed by an undershoot, finally ending in a stabilized amplitude fluctuation. Note that only this last phase is used when evaluating FTF gains and phases. For $f = 500$ Hz and $f = 600$ Hz, a period of growth is first observed before reaching a stabilized amplitude. Amplitude ratios are then evaluated as $A_Q = 3.32$ for $f = 400$ Hz, $A_Q = 3.53$ for $f = 500$ Hz and $A_Q = 2.12$ for $f = 600$ Hz. If both forcing amplitudes were to remain in the linear flame response regime, the same scaling $A_Q = A_{u_n} = 3$ should be expected. This assumption is invalidated by LES data, thus indicating the nonlinear characteristics of at least one of the two forcing levels.

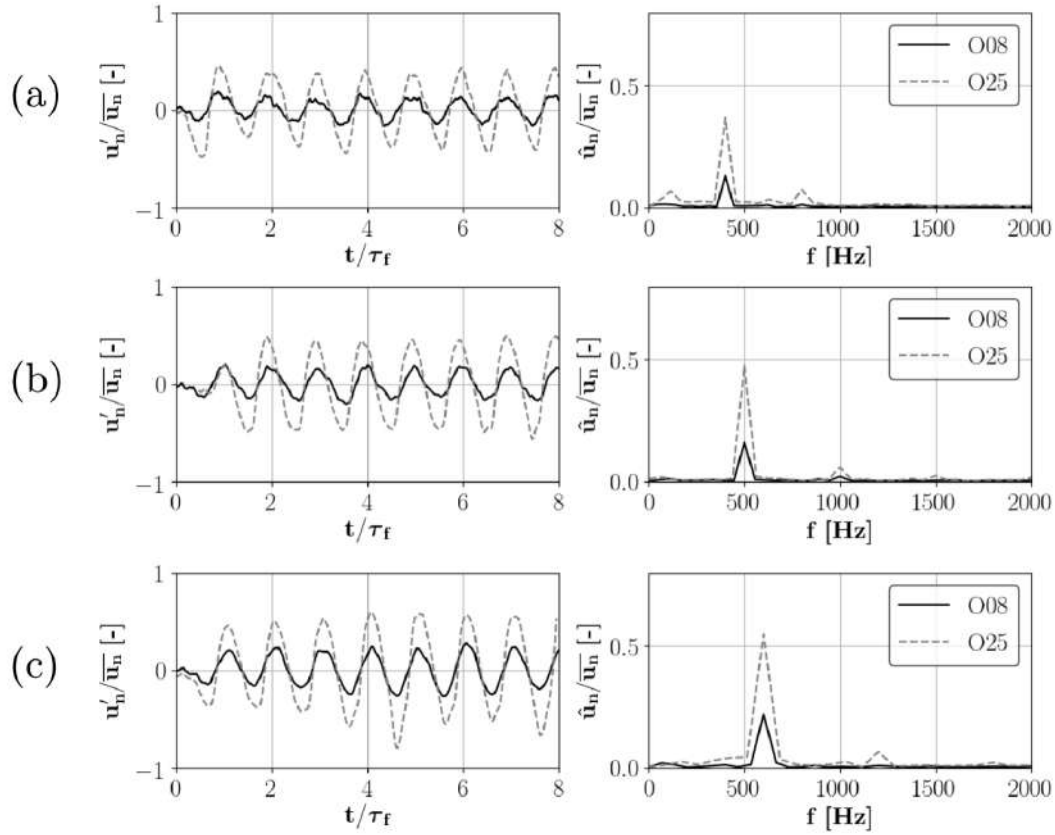


Figure 4.15: Normalized reference velocity signals and associated FFT for (a) f = 400 Hz, (b) f = 500 Hz and (c) f = 600 Hz for forcing amplitudes $\hat{p}/P_{out}$ = 0.83% (O08) and $\hat{p}/P_{out}$ = 2.5% (O25).

4.4.3.2 Forcing amplitude and flame dynamics

Up to this point, all observations regarding nonlinearities have been made from global data, it is thus interesting to get a deeper insight on the underlying physical mechanisms responsible for these different flame responses. For that purpose, phase averaged fields of volumetric heat release rate Q and fuel mass fraction Y_{kero} for a forcing frequency f = 500 Hz are compared for cases O08 and O25. This frequency was chosen as it provides the most enhanced differences but the general conclusion applies to all frequencies. Figures 4.17 and 4.18 provide a visualization of the heat release rate field for four different phases of the forcing cycle for cases O08 and 025 respectively. The phase ϕ_c is here defined with respect to the pressure signal in the chamber, so that $\phi_c = \pi/2$ corresponds to a maximal chamber pressure while $\phi_c = 3\pi/2$ corresponds to a minimal chamber pressure. For both forcing amplitudes, the flame has an oscillating motion along the injection axis (tilted by an angle β_c with respect to the horizontal axis). When the chamber pressure is high, $\phi_c = \pi/2$, the flame is pushed towards the injector as

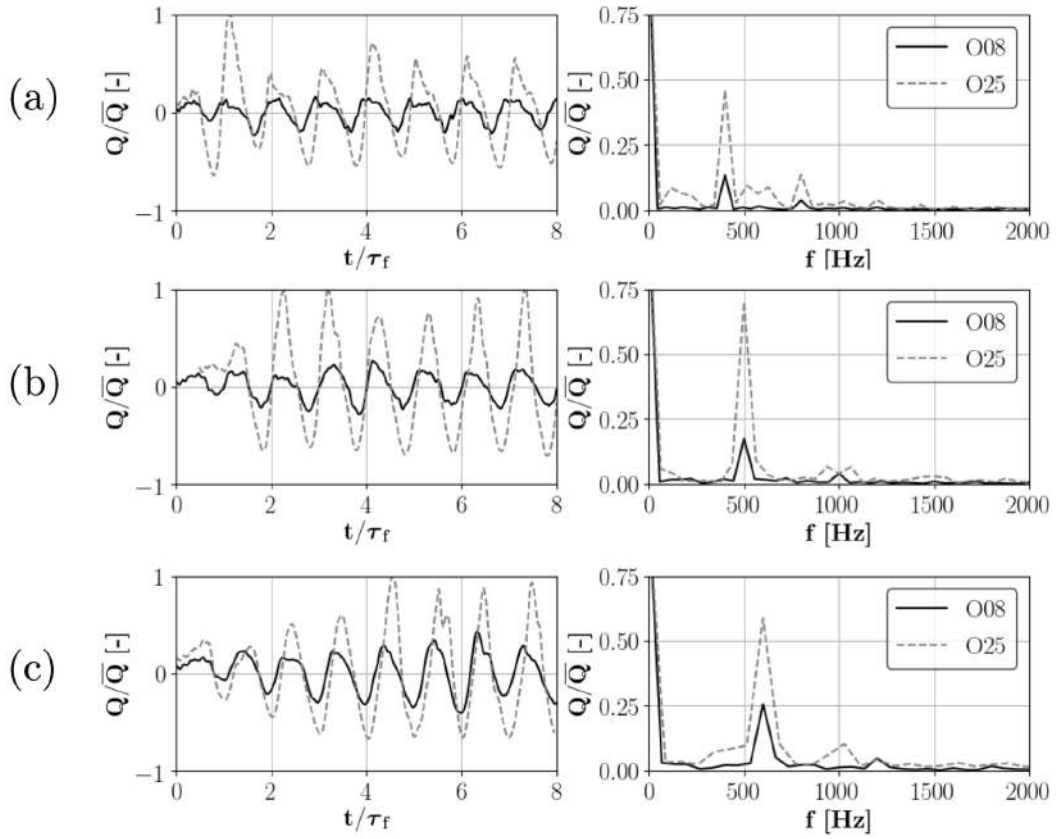


Figure 4.16: Integrated fluctuating heat release signals and associated FFT for (a) f = 400 Hz, (b) f = 500 Hz and (c) f = 600 Hz for forcing amplitudes $\hat{p}/P_{out} = 0.83\%$ (O08) and $\hat{p}/P_{out} = 2.5\%$ (O25). All signals are normalized by the mean heat release $\overline{Q}$.

indicated by the narrow angle high energetic region in the near swirler exit zone. On the contrary, when the chamber pressure drops, $\phi_c = 3\pi/2$, the flame moves downstream, and the flame root is pushed towards the middle of the chamber. Global forced flame dynamics are very different depending on the forcing amplitude. In the low forcing amplitude case O08, the flame motion is essentially one-dimensional and the regions of maximum flame wrinkling identified by high local heat release rate levels roll from the flame root towards the end of the flame branches. Diffusion flames are always present during the forcing cycle near the dilution holes. The flame dynamics for the high amplitude forcing case O25 do not exhibit the same behaviour. The strong oscillating motion almost extinguishes the flame as seen in Fig. 4.18 for $\phi_c = 3\pi/2$. It is yet able to sustain itself and to fully redevelop later in the cycle by further expanding and recreating secondary flame branches.

Phase averaged fuel mass fraction fields for both forcing cases are shown in Figs. 4.19 and 4.20. When the chamber pressure increases, liquid fuel droplets are maintained in

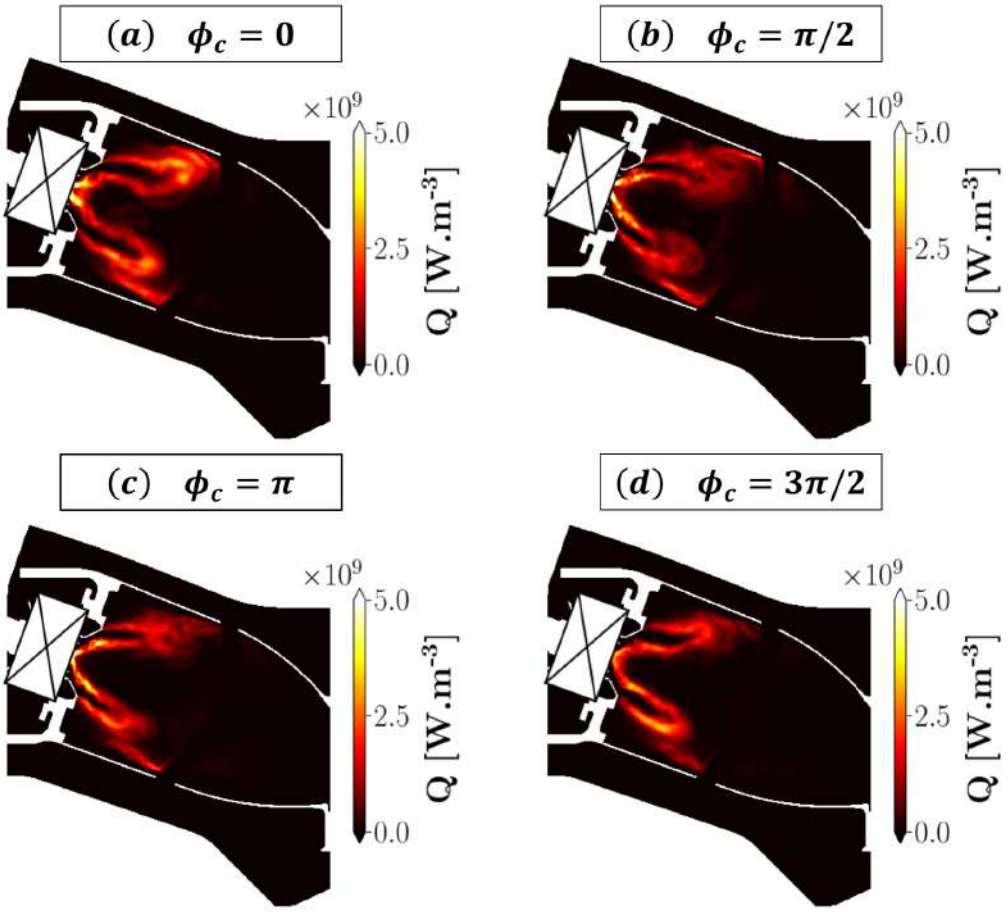


Figure 4.17: Phase averaged field of volumetric heat release rate Q for different phases ϕ_c of the forcing cycle at f = 500 Hz for case O08, 8 forcing periods are used. The phase is here defined with respect to the pressure signal in the chamber: $\phi_c = \pi/2$ corresponds to a maximal chamber pressure while $\phi_c = 3\pi/2$ corresponds to a minimal chamber pressure.

the swirler exit/injection area where they are trapped in a recirculation zone and are not able to burn ($\phi_c = \pi/2$). Later in the cycle, the chamber pressure drops and pockets of droplets are released into the burning area ($\phi_c = \pi$ and $\phi_c = 3\pi/2$). In the low forcing amplitude case, O08, these liquid pockets are small and penetrate the chamber when the chamber pressure is minimal, $\phi_c = 3\pi/2$. They quickly evaporate and burn so that the majority of the unsteady heat release occurs at $\phi_c = 0$ and is localized at the flame branches tips. On the contrary for case 025, the pockets of liquid droplets are large enough so that only their outer surface is able to directly burn at phase $\phi_c = 0$, generating intense rich burning regions at the flame tips. The gaseous remainder of these pockets is later partially trapped in the IRZ and burns while the rest of these burns in a lean diffusion regime in the wake of the dilution holes at phase $\phi_c = \pi/2$.

From a flame transfer function perspective, this indicates that computing a single

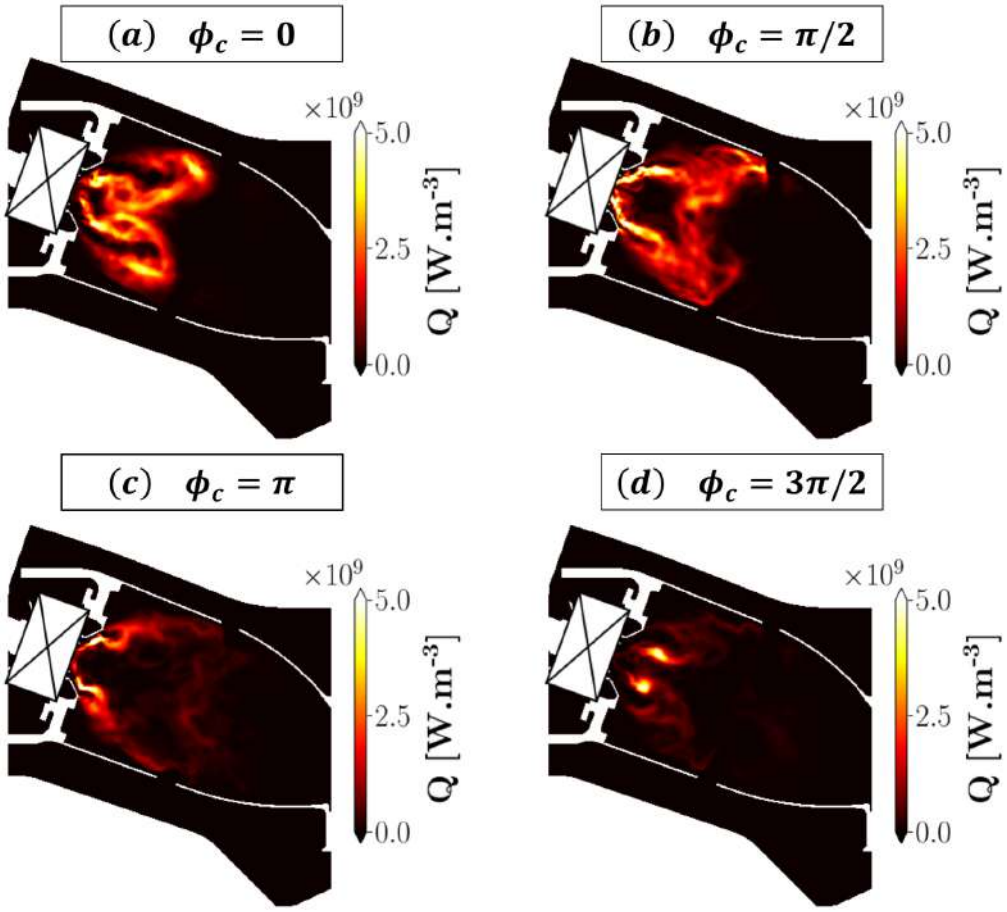


Figure 4.18: Phase averaged field of volumetric heat release rate Q for different phases ϕ_c of the forcing cycle at f = 500 Hz for case O25, 8 forcing periods are used. The phase is here defined with respect to the pressure signal in the chamber: $\phi_c = \pi/2$ corresponds to a maximal chamber pressure while $\phi_c = 3\pi/2$ corresponds to a minimal chamber pressure.

valued global FTF is not fully correct [212]: the main rich flame may not be the main driver of the acoustic response. Transfer functions are still computed using the global heat release Q for both forcing levels in an effort to demonstrate final differences, with results presented in Fig. 4.21. Major differences are observed for the FTF gain, with higher predicted gains for forcing case O25 for $f \leq 600$ Hz and lower predicted gain for higher frequencies. The highest FTF gain is obtained for $f = 500$ Hz, which is the frequency of the combustion instability mode observed during engine test sessions. FTF phase curves share the same tendency for both cases, with a mean additional flame response time delay $\tau_{fl} = 0.12$ ms for the higher forcing amplitude. This supplementary time delay may induce changes on predicted modes stability obtained from acoustic solvers.

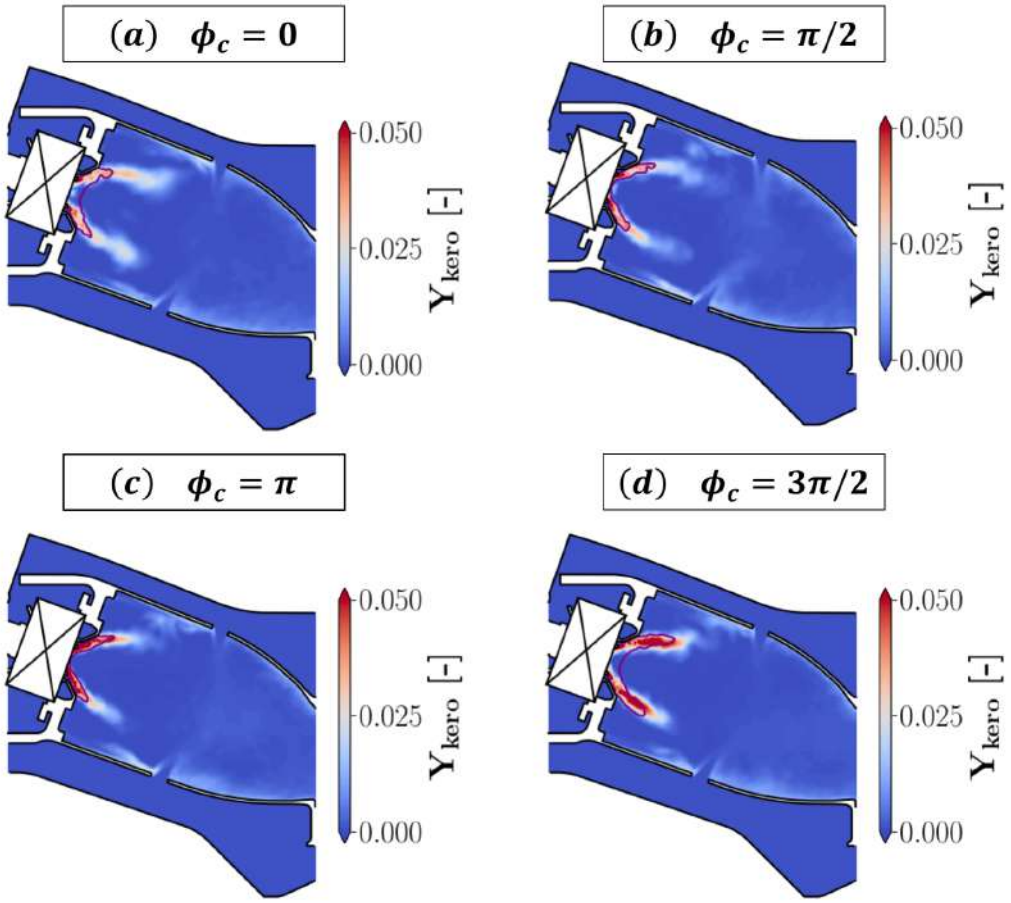


Figure 4.19: Phase averaged field of kerosene mass fraction Y_{kero} for different phases ϕ_c of the forcing cycle at f = 500 Hz for case O08, 8 forcing periods are used. The phase is here defined with respect to the pressure signal in the chamber: $\phi_c = \pi/2$ corresponds to a maximal chamber pressure while $\phi_c = 3\pi/2$ corresponds to a minimal chamber pressure. The brown liquid volume fraction isocontour $\alpha_l = 6 \times 10^{-5}$ identifies the liquid core region.

4.4.3.3 FTF/FDF

Finally, it is worth noticing that an accurate numerical estimation of the FTF necessitates two contradictory conditions:

- **C1**: the forcing amplitude should be low enough to guarantee that the flame response remains in the linear regime.
- **C2**: the forcing amplitude should be high enough so that the signal to noise ratio is sufficient for a good spectral analysis of reference signals. In addition, only the limit cycle of the instability is looked for here.

The ideal forcing level is therefore a trade-off between the two conditions. It was previously shown that the high amplitude forcing case O25 interferes with the first

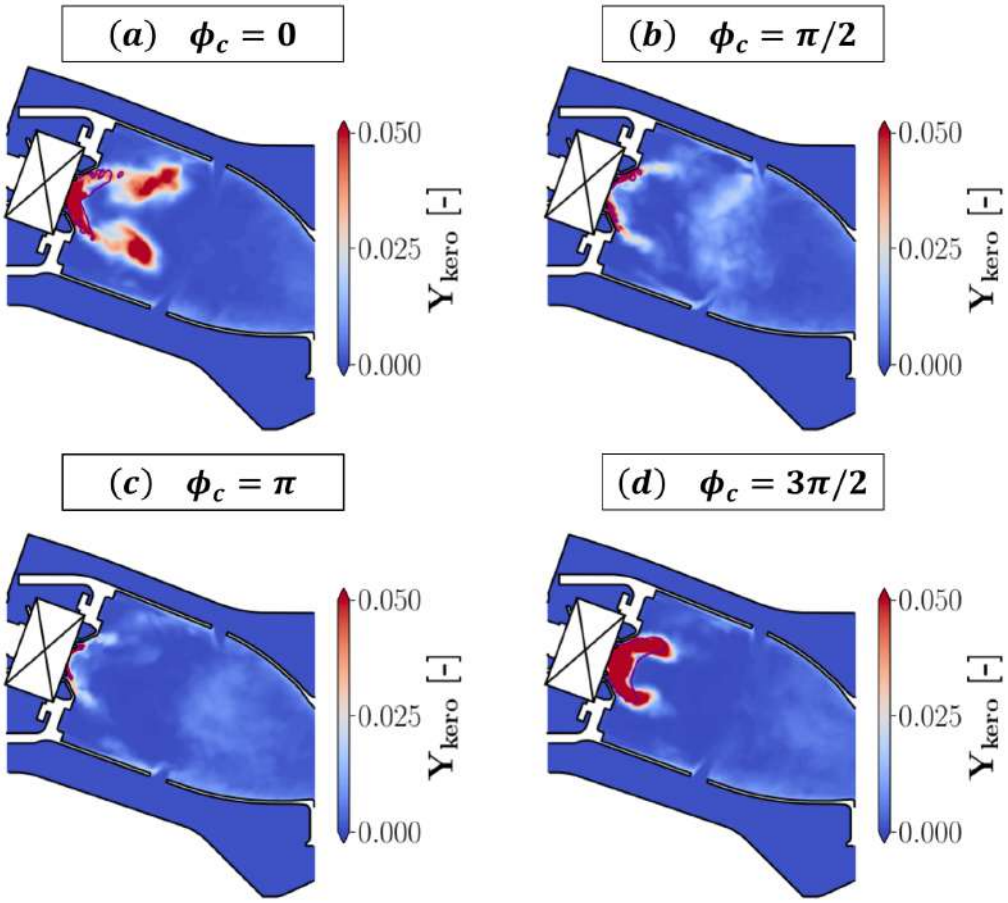


Figure 4.20: Phase averaged field of kerosene mass fraction Y_{kero} for different phases ϕ of the forcing cycle at f = 500 Hz for case O08, 8 forcing periods are used. The phase is here defined by the pressure signal in the chamber: $\phi_c = \pi/2$ corresponds to a maximal chamber pressure while $\phi_c = 3\pi/2$ corresponds to a minimal chamber pressure. The brown isocontour identifies $\alpha_l = 6 \times 10^{-5}$ identifies the liquid core region

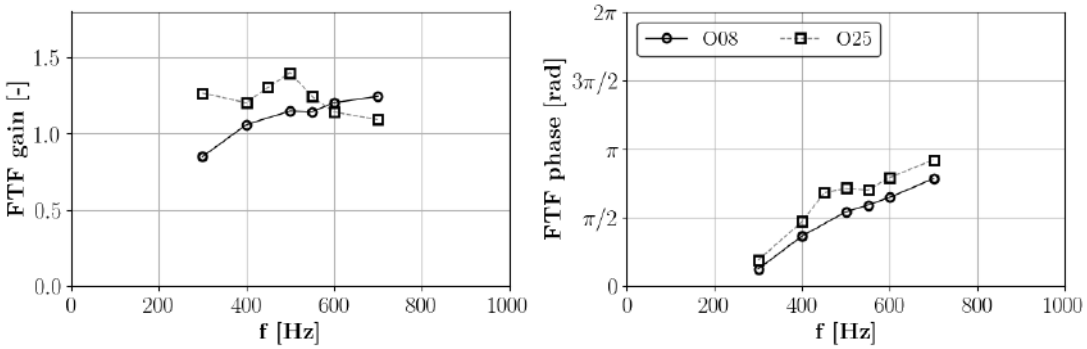


Figure 4.21: FTF gain and phase curves as obtained from forced LES for acoustic forcing levels $\hat{p}/P_{out} = 0.83\%$ (O08) and $\hat{p}/P_{out} = 2.5\%$ (O25).

condition. An investigation is therefore pursued for frequencies $f = 400$ Hz and $f = 500$ Hz using a collection of forcing amplitudes in an effort to determine the amplitude corresponding to the "sweet spot". The chosen forcing amplitudes are 0.5%, 0.83%, 1.25%, 1.67% and 2.5% of the mean imposed outlet pressure. In every case, LES are performed and the FTF is evaluated from a Fourier analysis of heat release and reference velocity signals after removing the initial transient, and for a minimum of six clean forcing periods.

First, the power spectral density (PSD) distribution of heat release is assessed for all cases, Tab 4.3. For comprehension purposes, this data is also plotted in Fig. 4.22.

$\hat{p}/P_{out}$ [%]	PSD $f = f_0$ [%]	PSD $f = 2f_0$ [%]	PSD $f = 3f_0$ [%]	remainder [%]
0.50	76.5	1.3	0.3	21.9
0.83	86.1	8.1	0.5	5.3
1.25	82.7	11.0	0.4	5.9
1.67	80.3	14.7	1.4	3.7
2.50	85.5	8.4	0.8	5.2

$\hat{p}/P_{out}$ [%]	PSD $f = f_0$ [%]	PSD $f = 2f_0$ [%]	PSD $f = 3f_0$ [%]	remainder [%]
0.50	83.4	2.6	0.3	13.6
0.83	92.9	3.7	0.1	3.2
1.25	91.7	5.4	1.0	1.8
1.67	88.2	6.7	1.0	4.1
2.50	95.5	0.5	0.5	3.6

Table 4.3: Power spectral density distribution of heat release rate for frequencies f = 400 Hz (top) and f = 500 Hz (bottom) for several downstream forcing amplitudes.

Distinction is made between the fundamental frequency, its first two harmonics and the remaining spectral content. When using a low forcing level such as $\hat{p}/P_{out} = 0.5\%$, the heat release signal features high noise levels, with respectively 21.9% ($f = 400$ Hz) and 13.6% ($f = 500$ Hz) of the total PSD energy contained in this background signal. This data therefore underlines the fact that both simulations do not comply with condition C2. When gradually increasing the forcing amplitude from 0.83% to 1.67%, the proportion of the PSD energy tied to the first two harmonics increases, indicating a progressive rise of nonlinear effects. It is also worth noting that for the highest forcing amplitude $\hat{p}/P_{out} = 2.5\%$, the proportion of PSD energy linked to the harmonics diminishes, and is even the lowest for $f = 500$ Hz. However, as previously demonstrated, such a high forcing level drastically modifies both the main flame and secondary diffusion flames dynamics, which may require further modelling for the Helmholtz solver. In future works,

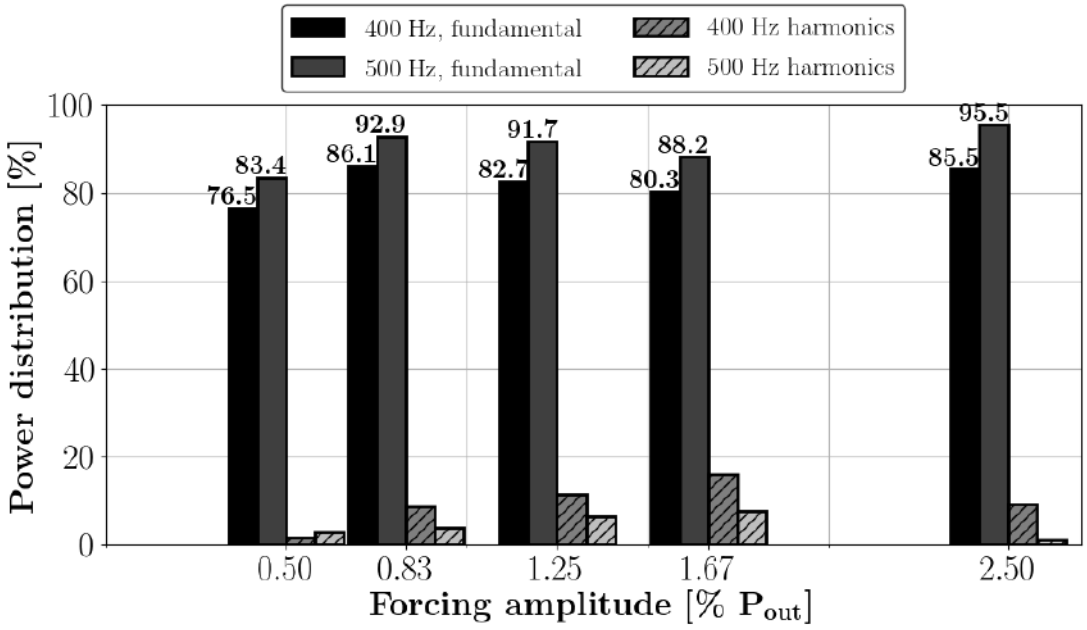


Figure 4.22: Power spectral density distribution of heat release rate for frequencies f = 400 Hz and f = 500 Hz for various downstream acoustic forcing amplitudes. The fundamental frequency and its first two harmonics are considered in each case.

it would be valuable to assess the contribution of each type of flames on the global FTF for the various forcing amplitudes. Likewise, the evaluation of the FTF corresponding to each flame region could be valuable.

From Tab. 4.3, the C1 and C2 requirements indicate that the forcing level $\hat{p}/P_{out} = 0.83\%$ is the most suitable candidate for a reliable determination of the FTF for this SAFRAN combustor. FTF gain and time delays can nonetheless be extracted for all simulations, Fig. 4.23. Comparing the results for the gain, Fig. 4.23a,c and phase Fig. 4.23b,d, clear tendencies are visible for both $f = 400$ Hz and $f = 500$ Hz. FTF gain and phase both increase when increasing the forcing amplitude. The only notable exception to this rule is the gain obtained for $f = 500$ Hz and $\hat{p}/P_{out} = 1.67\%$. This may be explained by the occurrence of several undershoots in the heat release signal peaks. This underlines the limitations of the current FTF formalism and the need for a more complete descriptions such as the one proposed with the FDF formalism [119]. For a classical acoustic solver relying solely on a FTF input and as shown above, the quality and accuracy of stability predictions depend on the amplitude for which the FTF is obtained. Contrarily to academic configurations, real combustors rely on complex subsystems and a highly turbulent flow, for which defining a "linear regime" can be quite arduous. For these reasons and considering the computational power needed, investigating forced flame dynamics and FTF by means of numerical simulations should

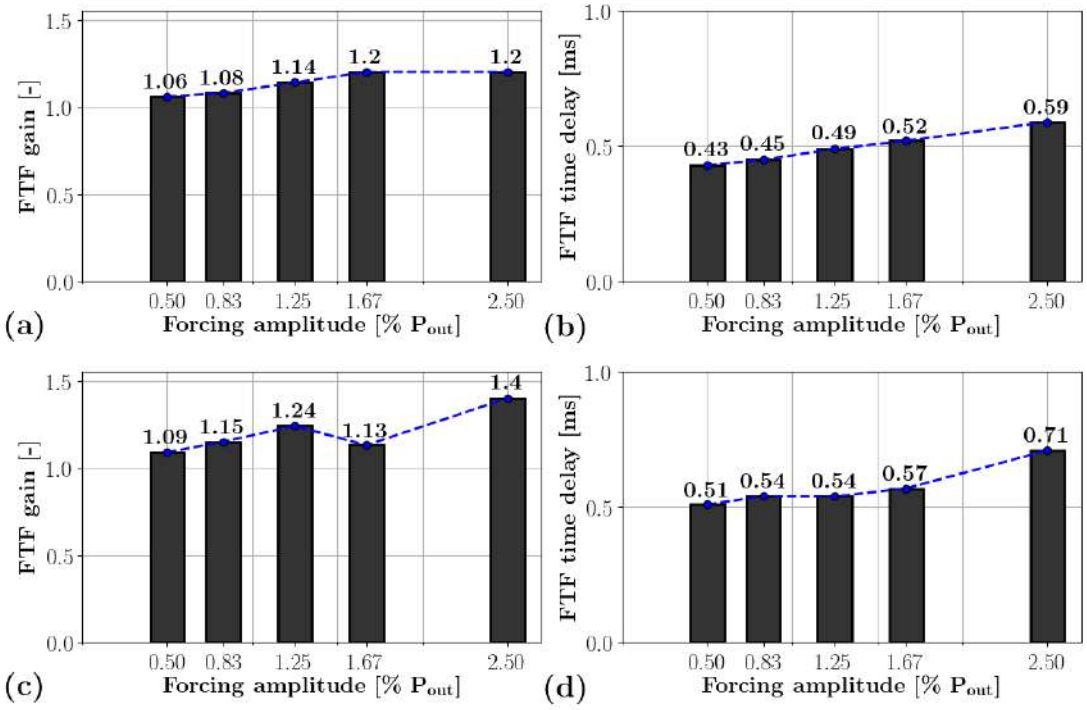


Figure 4.23: FTF gain and time delays obtained for several downstream forcing amplitudes for f = 400 Hz (a,b) and f = 500 Hz (c,d).

be done with conditions C1 and C2 in mind. Note furthermore that damping effects also need to be precisely measured for ROM to provide a reliable prediction.

4.4.4 Comparison of upstream and downstream forcing

4.4.4.1 Forced signals analysis

In this section the differences between upstream and downstream forcing on the SAFRAN combustor are investigated. Several studies in the literature make use of either upstream forcing [213, 214], downstream forcing [215] or more scarcely both [39, 216] for academic configurations. In [39], Gaudron *et al.* show that for a swirled academic flame, upstream and downstream acoustic forcing are equivalent as long as the reference point is close enough to the flame. They also show that conversely, using reference locations upstream of the swirler or further in the combustion chamber does not yield the same transfer functions for a given forcing level depending on the forcing type. This behaviour is attributed to the fact that the upstream and downstream acoustic boundary conditions differ depending on the type of forcing leading in turn to differences in the acoustic pressure drop across the swirler. While for simple one-dimensional geometries one can directly quantify the equivalence between upstream and downstream forcing by use of tranfer matrices, such a thing cannot be done easily for three-dimensional cases [211].

Another major difference between the present configuration and the case of [39] lies

in the fact that academic swirlers are often fully transmitting when considering acoustic waves [129]. In the present case, the swirler has two stages and the frequency range of interest is larger than for typical laboratory flames since the combustion chamber features a large variety of characteristic dimensions. In [158], Wang *et al.* show that the admittance (defined as the inverse of the impedance Z) of a two stage swirler submitted to an upstream acoustic modulation depends on the forcing frequency, in agreement with results obtained for the downstream forcing of Tab.4.2. In this work, reference locations have been chosen to be close to the flame, but the equivalence or non equivalence in regard to the forcing type needs to be assessed. In the eventuality of a frequency dependent swirler impedance Z, matching reference signals for a particular frequency f for both upstream and downstream forcing does not guarantee equivalent reference velocity amplitudes at other frequencies.

In the context of numerical simulations, several strategies can therefore be defined to match reference signals for both forcing types. Since focus is made on $f = 500$ Hz, it is chosen in the following to modify the inlet forcing amplitude until the reference velocity signal u_n at probing location VES matches its downstream forced counterpart of case O08 at this frequency. A trial and error process is therefore performed until a reasonable difference is obtained on the reference velocity signal amplitude. Note that only the main air inlet is subject to an acoustic modulation, the fuel injection is kept unchanged. The amplitude ratio of the obtained reference velocity signals for upstream and downstream forcing simulations is then investigated and noted $A_{u_n} = |\hat{u}_n|_{I10}/|\hat{u}_n|_{O08}$. It is found that for $f = 500$ Hz, downstream forcing with amplitude $\hat{p}/P_{out} = 0.83\%$ (case O08) is almost equivalent to upstream forcing with amplitude $\hat{u}_{in}/\overline{u}_{in} = 10\%$ (case I10) where $\overline{u}_{in}$ is the main inlet bulk velocity. Corresponding data is shown in Fig. 4.24, with $A_{u_n} = 0.96$. With the same upstream forcing conditions, $A_{u_n} = 0.7$ for $f = 400$ Hz and $A_{u_n} = 1.14$ for $f = 600$ Hz.

Specific impedances Z are probed using average data of probes from reference location VES at the exit of the swirler. With the limited number of periods available, one obtains $|Z| = 0.113$ for $f = 400$ Hz, $|Z| = 0.116$, for $f = 500$ Hz and $|Z| = 0.119$ for $f = 600$ Hz. These values are clearly lower than their downstream forced counterparts (see Tab. 4.2). This phenomenon is expected: for the same level of acoustic velocity at the second swirler stage exit $\hat{u}_n$, acoustic pressure levels $\hat{p}_n$ are lower with upstream forcing, due to the acoustic pressure drop across the swirler. These results confirm the analysis of [39] stating that the two types of forcing are not symmetrical because of the swirler pressure drop. One should also note that the frequency dependency of the swirler specific impedance obtained when applying an upstream forcing is very limited in the studied frequency range. This was not the case when applying downstream forcing, which explains the difference in the velocity signals amplitude from Fig. 4.24. Another

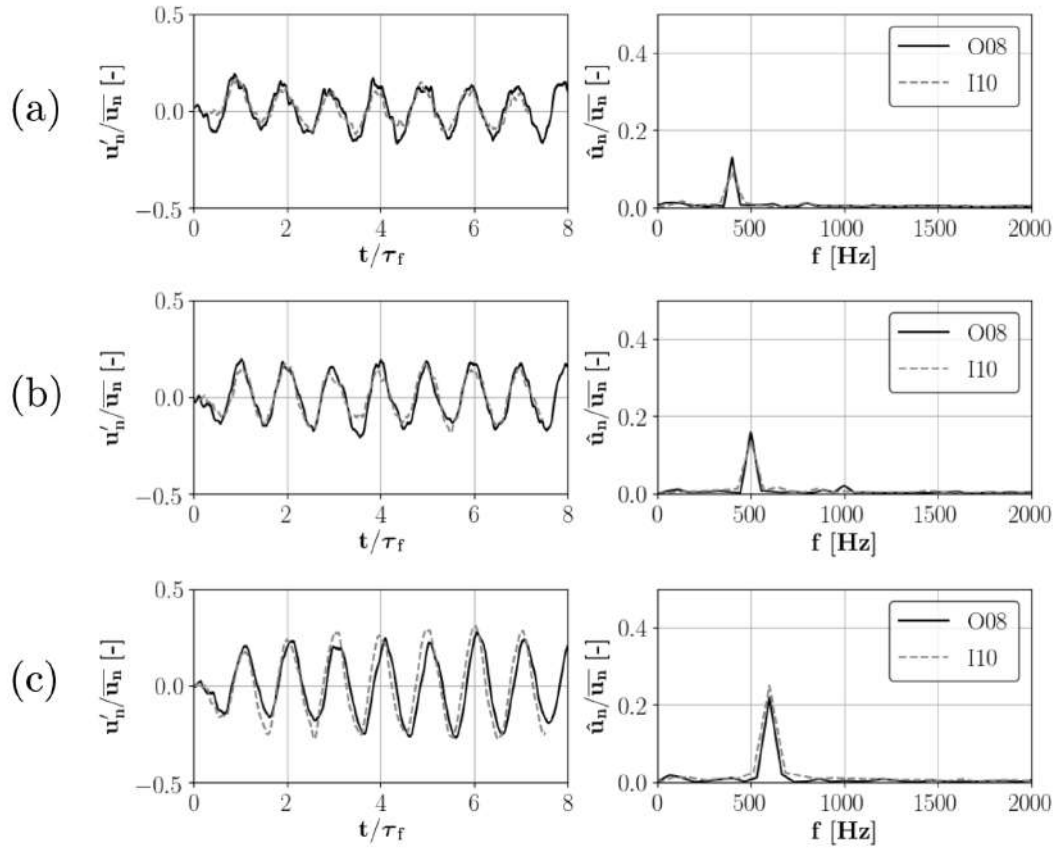


Figure 4.24: Normalized reference velocity signals and associated FFT for (a) f = 400 Hz, (b) f = 500 Hz and (c) f = 600 Hz cases O08 and I10.

difference between upstream and downstream forcing is the response of the first swirler stage. When applying an upstream modulation, the acoustic pressure drop between the inlet acoustic pressure $\hat{p}_{in}$ and the first swirler stage exit $\hat{p}_{VIS}$ is $\hat{p}_{in} - \hat{p}_{VIS} = 0.01 P_{out}$. In contrast, when applying a downstream forcing, the acoustic pressure drop $\hat{p}_{in} - \hat{p}_{VIS}$ is close to zero. As a result, pressure oscillations near the liquid-fuel injection are not the same depending on the forcing type.

Corresponding heat release signals are plotted in Fig. 4.25. For $f = 400$ Hz, data shows that upstream forcing yields much lower heat release oscillation levels, $A_Q = 0.3$, an observation that is not simply explained by the difference in reference signal amplitude. The same behaviour applies to the data obtained for $f = 500$ Hz, *i.e.* $A_Q = 0.55$ although the reference velocity signals share the same amplitude whenever produced from a downstream or upstream forcing. Even more surprising, a similar heat release rate oscillation amplitude is obtained regardless of the forcing type for $f = 600$ Hz. One should however take into account the fact that heat release signals obtained using an upstream modulation are quite noisy and further from the expected sine wave. These observations translate into different measured levels of FTF gain as

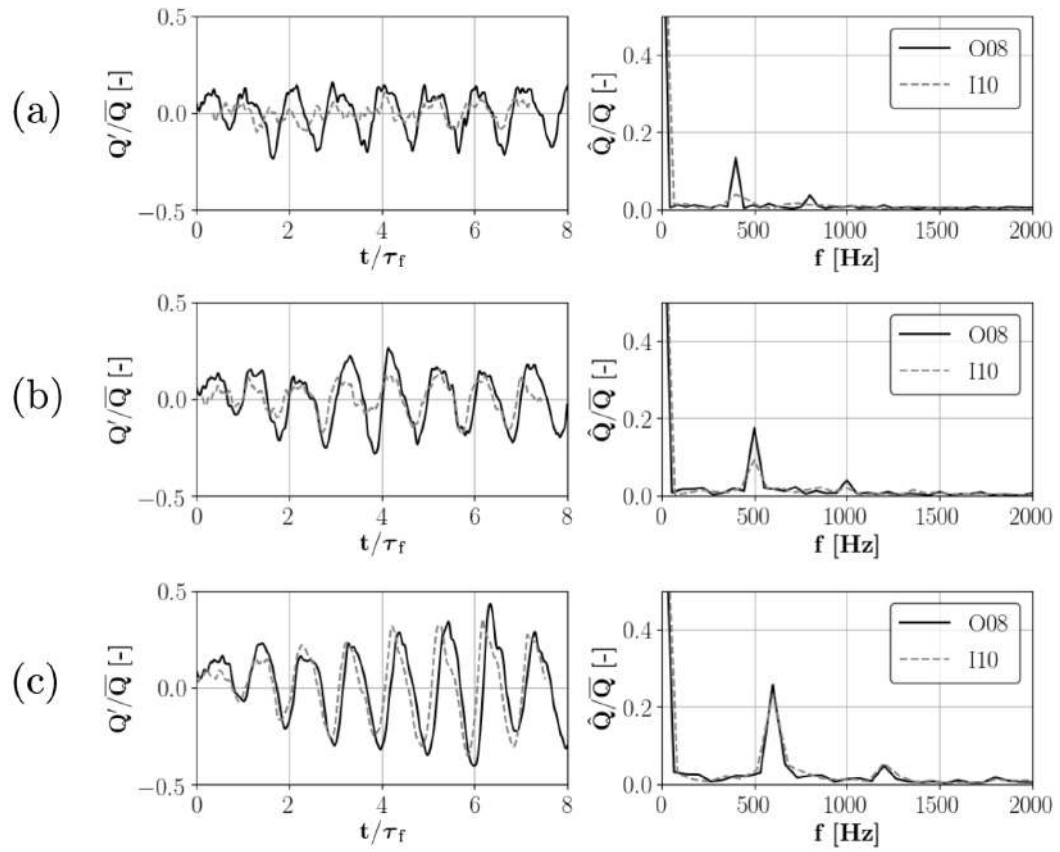


Figure 4.25: Normalized reference heat release signals and associated FFT for (a) f = 400 Hz, (b) f = 500 Hz and (c) f = 600 Hz for cases O08 and I10.

shown by Fig. 4.26 where gains from upstream forcing are consistently lower than for a downstream forcing. The FTF phases are also slightly lower when measured with I10 forcing, with a mean time delay advance of 0.1 ms. These results prove that the

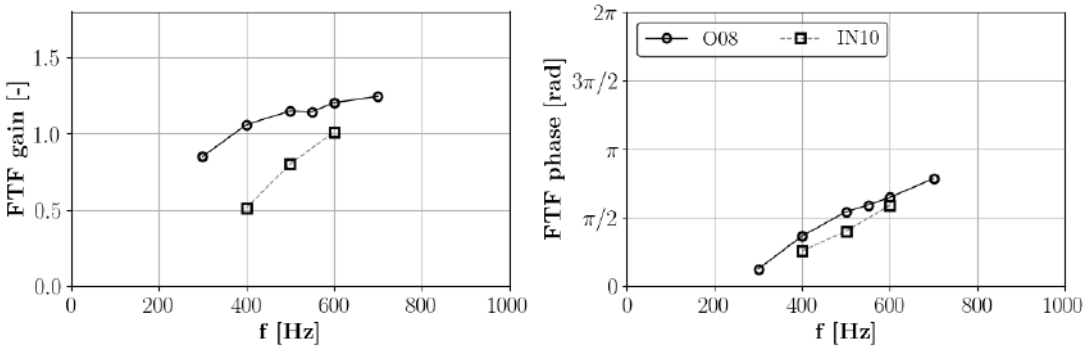


Figure 4.26: FTF gain and phase curves as obtained from forced LES for acoustic forcing levels O08 ($\hat{p}/P_{out} = 0.83\%$) and I10 ($\hat{u}/\overline{U}_{in} = 10\%$).

equivalence between upstream and downstream forcing does not hold for the considered operating point of the SAFRAN combustor.

4.4.4.2 Forced flame dynamics

The equivalence of forcing techniques was proven for fully premixed gaseous flames whereas the current study focuses on a two-phase flow non premixed case. Studies in the literature report a higher sensibility of the latter to acoustic pressure through the response of droplets dynamics for instance [217]. This effect is not considered in the FTF formulation of the current work. The combustion chamber is furthermore more complex and has several dilution holes, a multi-perforated enclosure and it is surrounded by two bypass channels. The role of the latter component is investigated by gauging the fluctuating pressure in both bypass channels over several oscillation cycles at $f = 500$ Hz for cases O08 and I10. Results disclosed in Fig. 4.27 show two majors differences when forcing from one end of the combustor or the other. First, the amplitude of pressure

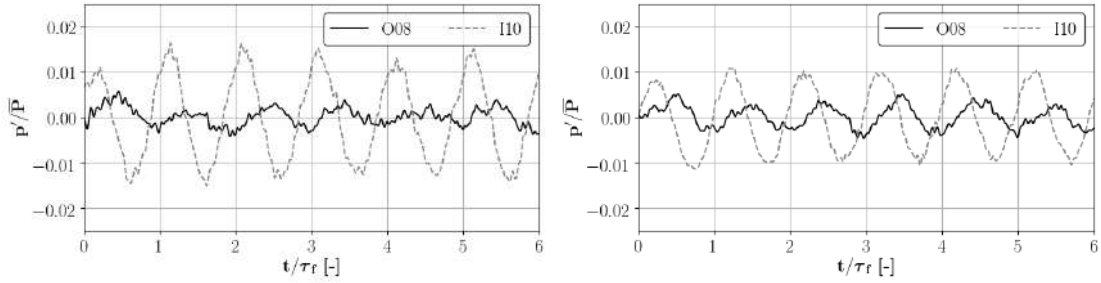


Figure 4.27: Fluctuating pressure in the upper (a) and lower (b) bypass channels for upstream forcing I10 and downstream forcing O08 for a forcing frequency f = 500 Hz. Measurements are taken from a collection of probes located in between two dilution holes rows.

fluctuations in both channels is much more important when imposing an upstream modulation. One can also note that while fluctuations are similar in amplitude for case O08 in both the upper and the lower bypass channels, for case I10, they are 1.5 times higher in the upper part compared to the lower part. This phenomenon is due to the position of the main air inlet which is closer to the upper channel so that the only obstacle for the flow to reach this position is the fuel injection line. In the case of the lower bypass channel, the flow has to recirculate for a longer time in the back chamber cavity (see Fig. 4.2) before reaching the annular passage. When the acoustic modulation is imposed from the chamber outlet, acoustic waves travel mainly in one direction opposite to the flow direction in the combustor and then perpendicularly to the flow direction in the bypass channels. These cavities are hence only marginally affected by acoustic waves. On the contrary when the modulation is imposed from the main air inlet, the acoustic perturbation direction is only marginally different from the bypass channel flow directions. Second, the phase of bypass channels pressure fluctuations

differs depending on the type of forcing. This means that the contribution of secondary diffusion flames to the global FTF may differ depending on the type of forcing used since the Rayleigh criterion defined by the pressure/heat release rate product integral will be different. Pressure signals alone are however not sufficient to predict the response of secondary flames. Indeed, another criteria of primary importance is the forced dynamics of the main upstream located flame which will discharge different quantities of fuel during a cycle.

In that respect, it is worth investigating whether flame dynamics are the same when upstream or downstream forcing are applied. To do so, phase averaged images of the heat release rate are compared for cases I10 and O08 for $f = 500$ Hz. In that case, the flame is identified as the isosurface $Q = 10^9$ W.m^{-3} for different phases of the cycle in Fig. 4.28. Comparisons of the two cases show that the main swirl attached

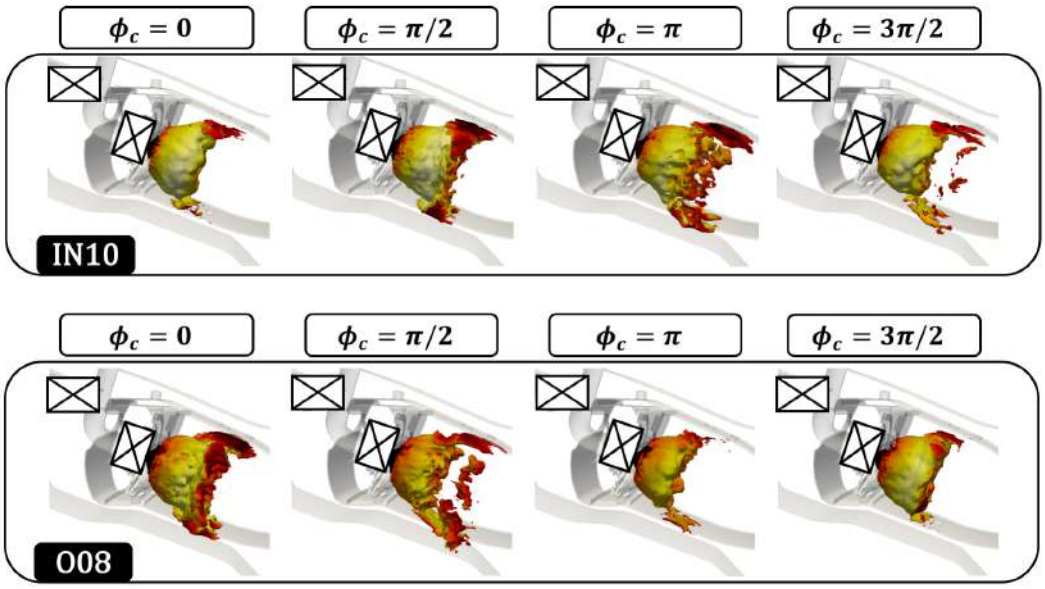


Figure 4.28: Flame surface as identified by the volumetric heat release rate isocontour Q = 10^9 W.m^{-3} obtained from phase averaging over 6 periods, and coloured by temperature for different phases of a forcing cycle at f = 500 Hz for upstream and downstream forcing. The phase is here defined by the pressure signal in the chamber: $\phi_c = \pi/2$ corresponds to a maximal chamber pressure while $\phi_c = 3\pi/2$ corresponds to a minimal chamber pressure.

flame dynamics do not appear to change and consist in an alternation between flame elongation and flame contraction depending on the phase. A first rough visual analysis of the main flame extremal positions does not allow to identify whether one of the forcing type yields stronger unsteady motions. However, the primary flame surface appears to be the largest for $\phi_c = \pi/2$ when upstream forcing is applied, while the same occurs for $\phi_c = 0$ when downstream forcing is considered.

The global heat release being the sum of two contributions: from the main flame and from secondary diffusion flames, these contributions may interact in a positive or negative manner depending on their relative phase. To better understand these interactions, a decomposition of the heat release is performed based on the geometrical regions identified from the mean primary and secondary flame positions for $f = 500$ Hz. On this basis, corresponding signals are shown in Fig. 4.29. Two observations can be

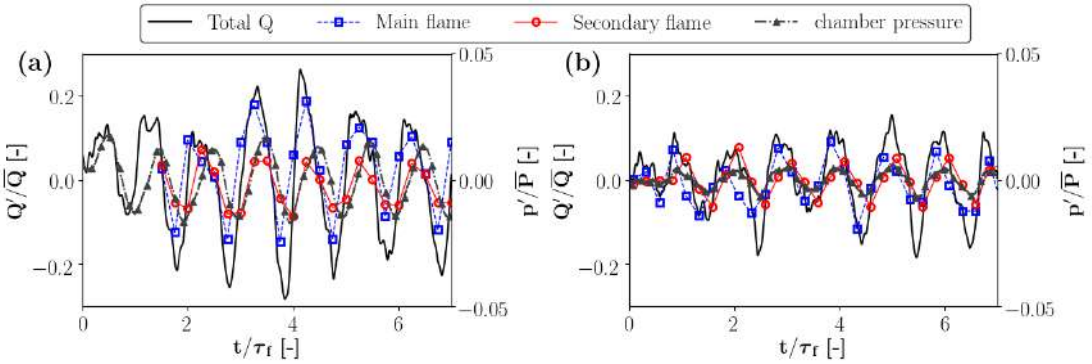


Figure 4.29: Normalized unsteady heat release contribution of each flame for downstream forcing O08 (a) and upstream forcing I10 (b), f = 500 Hz. The normalization factor is the mean global heat release $\overline{Q}$. Chamber pressure is also plotted on a secondary axis.

drawn from this decomposition. First, the main and secondary heat release signals are in phase for case O08 while they are in phase quadrature for case I10. The global unsteady heat release Q is hence enhanced in the first case while it is not in the latter, confirming previous observations. However, while the amplitude of secondary flame heat release is about the same for both investigated cases, the main flame unsteady heat release is much lower when applying an upstream acoustic modulation. The diffusion flames are therefore not the only factor responsible for the diminished fluctuations of global heat release when forcing the flow using an inlet modulation. In fact, the phase between the chamber pressure and the total heat release varies from one forcing type to another: signals are in phase for case I10 and in phase quadrature for case O08. Fig. 4.30 indicates that for the I10 case, liquid fuel pockets enter the chamber at an early phase of the pressure cycle compared to O08 (Fig. 4.19), but that this state corresponds to approximately the same phase of reference velocity signals, Fig. 4.24c. The differences observed in the levels of primary heat release are thus not attributed to a different response of the liquid spray but solely to differences in the chamber pressure. This consideration is further emphasized when comparing chamber pressures for $f = 500$ Hz and $f = 600$ Hz as done in Fig. 4.31. Indeed, for the latter frequency, pressure signals are in phase for both forcing locations and yield much closer FTF gains (see the FTF gain and phase curves of Fig. 4.26).

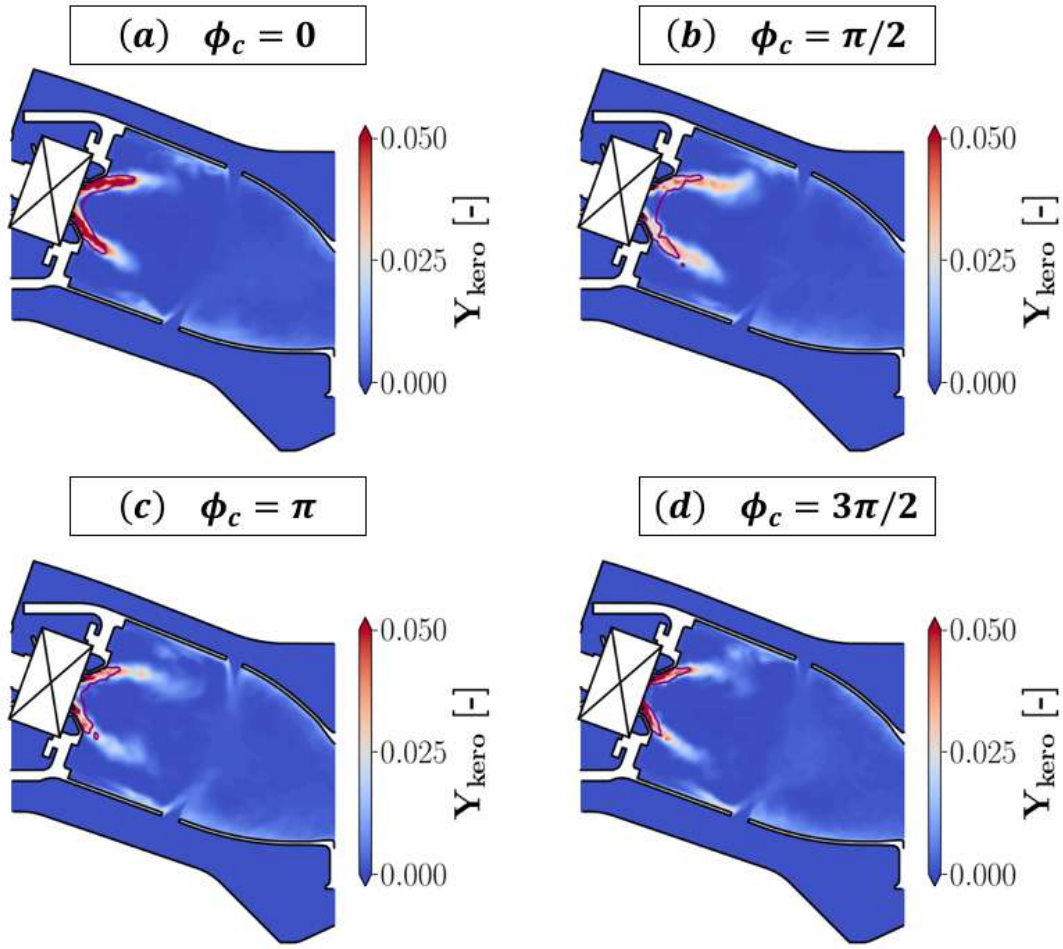


Figure 4.30: Phase averaged field of kerosene mass fraction Y_{kero} for different phases ϕ_c of the forcing cycle at f = 500 Hz for case O08. The phase is here defined with respect to the pressure signal in the chamber: $\phi_c = \pi/2$ corresponds to a maximal chamber pressure while $\phi_c = 3\pi/2$ corresponds to a minimal chamber pressure. The brown liquid volume fraction isocontour $\alpha_l = 6 \times 10^{-5}$ identifies the liquid core region.

It is concluded that the acoustic response of complex real engine swirled flames depends on the choice of the forcing source location. In particular, the FTF gain may largely differ for certain frequencies due to the directionality of the swirler unit or equivalently the difference of pressure fluctuations in the chamber. This will affect acoustic modes growth rates predicted from reduced order codes. A solution to overcome this issue would be to consider a FTF accounting for both velocity and pressure fluctuations at a reference position. This method however presents a serious drawback in terms of computational power needed: it necessitates two independent LES for the system to be fully characterized [122], either with different amplitudes in the linear regime, or relying on both downstream and upstream forcing. Moreover, ROM codes need to be adapted to handle this double input formalism. This was not done in the present study and

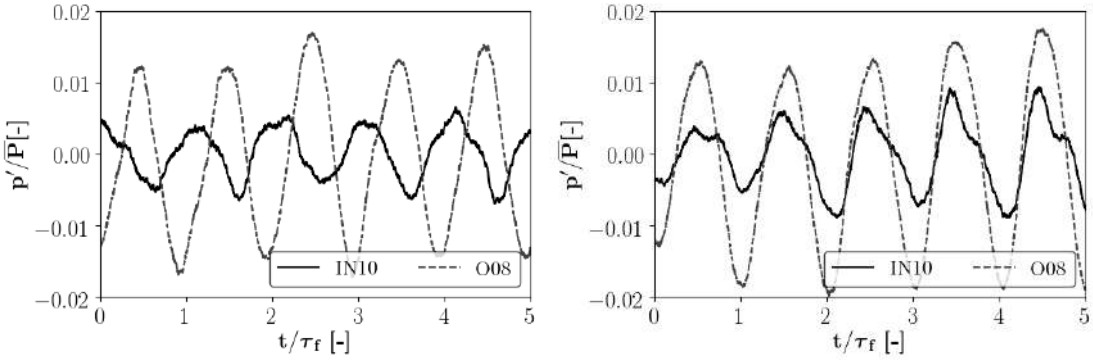


Figure 4.31: Chamber pressure from a series of probes in the middle of the combustion chamber for upstream forcing (I10) and downstream forcing (O08), f = 500 Hz (left) and f = 600 Hz (right).

may be investigated in the future. Another possibility would be to choose a reference position "very close to the flame base", which is impossible in practice for industrial swirling flames that undergo large oscillations during a forcing cycle. In this work reference locations were chosen at the swirler channels exit, very close to the flame, but not sufficiently according to the reported differences in predicted FTF. While acoustic fluctuations are imposed in numerical simulations, in reality they can originate from either the upstream main air feed, the fuel supply line (leading to differences in droplet radii which was not investigated here) or from elements downstream of the combustion chamber such as turbine stages. In most cases, the identification of the exact perturbation source remains difficult if not impossible. For lack of a better strategy, the worse case scenario should be considered from a numerical simulation standpoint of view. As a consequence, the FTF obtained from downstream forcing will be considered in the present case as it presents the highest levels of gain for the studied frequency range and due to the limited differences observed on time delays if compared to do the upstream forcing (see Fig. 4.26). Also and in future studies, the exact contribution of each flame should be characterized with a single FTF for each flame. In the case of the SAFRAN combustor, this would mean additional FTF for each of the upper and lower diffusion flames in the wake of dilution holes. The difficulty would then be linked to the choice of the technique or algorithm used to precisely identify each flame zone.

4.5 Applicability of the SFTF model to a real combustor

The objective of this section is to assess the analytical FTF model for swirling V-shaped premixed flames (SFTF) proposed in Sec. 2.3 whenever applied to the SAFRAN combustor. The primary reason behind such an evaluation is to qualify this computationally

efficient approach to evaluate the flame response. Note however that several assumptions and flow characteristics are not verified for this case. Typically:

- The fuel is not injected in a gaseous state, and is not fully premixed,
- Several flame zones are present, and the global flame may not be reduced to a single V-shaped flame. Indeed, the mean primary flame appears to be closer to an M-shape,
- The chamber walls are multi-perforated,
- The swirler includes two stages that will generate different vorticity perturbations.

Although there is a priori little chance to achieve an excellent match with the reference data, it is still worth investigating what is missing in terms of physics in an effort to further improve or adapt the analytical model for future studies.

4.5.1 Extracting SFTF model parameters

The methodology to obtain the SFTF model parameters first presented for the NoiseDyn swirl burner in Chap. 3 is again used here. First, a time and azimuthally averaged mean flow solution is used to identify the flame dimensions from the heat release rate center of mass with coordinates (x_c, y_c) as defined by Eq. (3.6). In this case, the mean flame opening angle is not constant along the direction of the injector axis. As shown in Fig. 4.32, the Q centroid is located in the outer branches of the main flame, the anchoring point of the flame being identified as the lowest point along the axial direction and for which Q is at least 1% of its maximum value. It is located in between the first and second swirler stage channel exits. For practical purposes, all geometric quantities will be expressed as a fraction of the radius R_0 corresponding to the cross section starting 6.5 mm away from the fuel injector tip and undisclosed here for confidentiality reasons. Using the LES data, one gets the following flame dimensions: $R_f/R_0 = 3.97$, $L_f/R_0 = 7.03$, $H_f/R_0 = 5.8$, resulting in a flame opening angle $\alpha = 34.4°$. The reduced frequency ratio $\omega_*/\omega = \omega L_f^2/(U_0 H_f)$ is consequently computed as $\omega_*/\omega = 8.84 \times 10^{-1}$ ms with $U_0 = 41$ m.s^{-1} the bulk velocity at the base of the flame.

The second step consists in the determination of the axial convection velocity U_{c-v} of vortical disturbances along the shear layer of the swirling jet. Contrary to the NoiseDyn case, the definition of this shear layer is subject to interpretation since the two stage swirler produces two shear layers. The first one denoted Inner Shear Layer (ISL), is located on the outskirts of the swirling core and impacts inner flame branches. The second one, denoted Outer Shear Layer (OSL), lies in the wake of the second swirler stage and impacts the inner part of the secondary flame branches. For the downstream

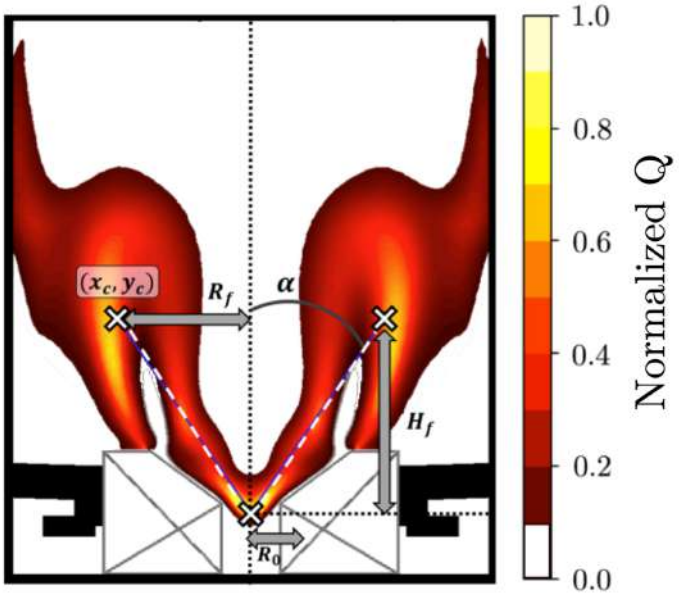


Figure 4.32: Schematic of the SAFRAN combustor mean flame volumetric heat release rate field and associated flame dimensions. The position of the heat release rate center of mass coordinates $(\mathbf{x_c}, \mathbf{y_c})$ is shown.

modulation case O08, phase images of the heat release rate, Fig. 4.17, show that the roll-up motion is mostly located around the flame inner branches. For this reason, the ISL is chosen for the evaluation of U_{c-v}. Since the swirl number of the configuration is high, $S = 0.67$, the I_2 criterion defined by Eq. 3.7 is used to mark the ISL, Fig. 4.33, before computing U_{c-v} following Eq. 3.8. Finally, one obtains $U_{c-v} = 25.2$ m/s, leading to a real valued correction factor $K = 1.63$ for the SFTF model. This value is comparable to the one obtained for the NoiseDyn configuration ($K = 1.41$).

The third and fourth estimated parameters of the SFTF model correspond to the delay τ between the axial acoustic and the azimuthal vortical perturbations complemented by the associated phase at the origin ϕ_0. In the following, the axial velocity perturbation $\hat{u}_x$ and the azimuthal velocity perturbation $\hat{u}_\theta$ are defined in the cylindrical frame with the injector axis as the main axis and are obtained by projecting the cartesian grid aligned velocity components on the new frame. For simple geometries, one can easily derive an approximation for parameter τ based on the difference between acoustic and convective propagation speeds, Eq. (3.9). In the present case, the flow cannot be considered as one-dimensional and the sound speed field varies considerably near the injection point due to the temperature difference between the cold fuel and the mildly hot surrounding air stream. Since the focus is only on the assessment of the SFTF capabilities for an industrial burner, it is chosen here to directly evaluate τ and ϕ_0 from the forced LES data of case O08 corresponding to a downstream modulation

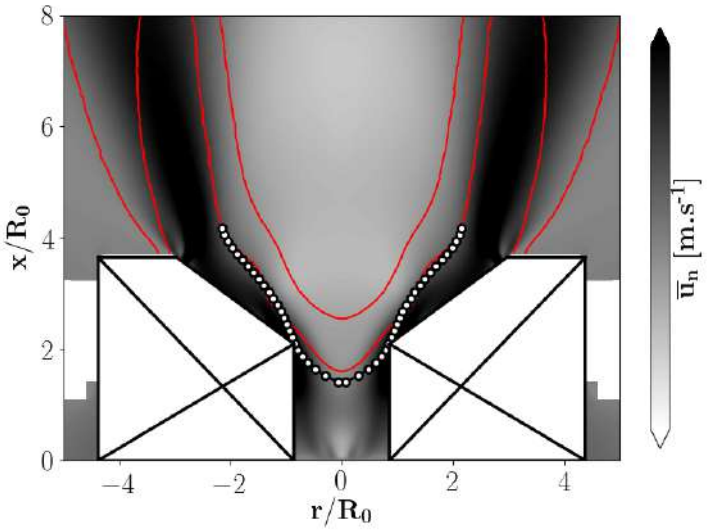


Figure 4.33: Identification of the shear layer of interest for the SAFRAN combustor using the I_2 criterion. Each white dot represents the local maximum at a given height x/R_0. The red isocontour $Q = 10^9$ W.m^{-3} is used to identify the mean flame position.

with amplitude $\hat{p}/P_{out} = 0.83\%$. To do so, velocity signals from six probes equally distributed on a circle of radius $R_p = 3$ mm located 1 mm below the flame root position in the axial direction are averaged. This position is chosen as it is very close to the flame, yet it is outside of the recirculation zone generated at the fuel injector tip by the conical liquid injection, Fig. 4.34a. It also corresponds to one of the first radial location of the shear layer identified using the I_2 criterion, so that the phase at origin ϕ_0 can be directly assessed. A linear regression of the data obtained for forcing frequencies rang-

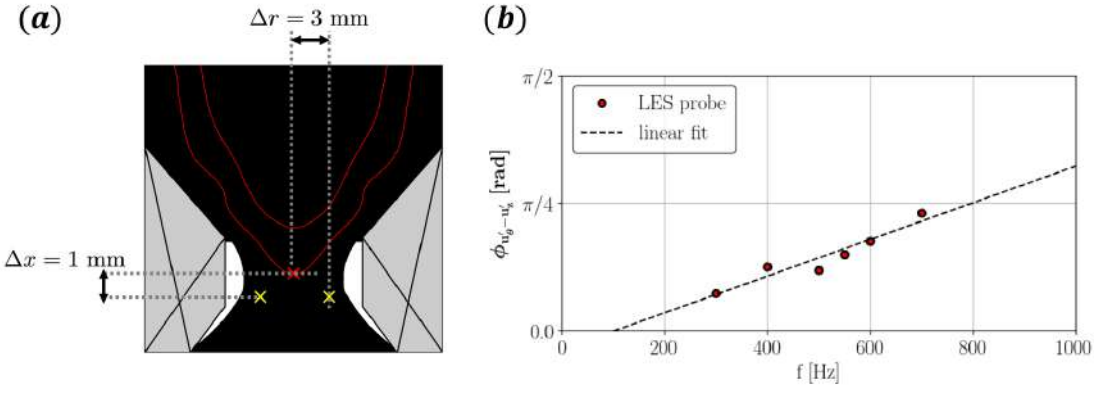


Figure 4.34: (a) Probing locations used for the evaluation of τ and ϕ_0 (yellow crosses) and distance to the mean flame base. Dimensions have been tweaked for confidentiality reasons. (b) Phase between axial and azimuthal velocity perturbations gauged from probes for several frequencies when applying a downstream modulation with amplitude $\hat{p}/P_{out} = 0.83\%$.

ing from 300 to 700 Hz is then performed, yielding $\tau = 0.18$ ms and $\phi_0 = -0.12$ rad, Fig. 4.34b. Considering the axial distance from the injector tip to the probing plane Δx_c, and assuming a mean sound speed $c_0 = 420$ m.s^{-1}, Eq. (3.9) yields $\tau = 0.147$ ms, which is of the correct order of magnitude. This rough estimation will nonetheless not be considered and the LES probed value will be used instead.

The estimation of the axial velocity disturbance decay rate parameter β on a series of lines starting from the plane at the flame base does not show the expected exponential decay and will not be considered for the current validation process. Finally, the last remaining model parameter is the swirling flow strength parameter χ. In this study the reference FTF is looked for. For this reason, instead of doing a single frequency optimization as done in Sec. 3.5.2, χ is optimized using the entire set of frequencies for which the FTF gain and phase were obtained for the O08 forced LES case. With this approach, the obtained value is $\chi = 0.78$, which is positive unlike all values obtained for the NoiseDyn configuration. Table 4.4 summarizes all the SFTF model parameters obtained from numerical simulations.

ω_*/ω [ms]	α [deg.]	K	χ	τ [ms]	ϕ_0 [rad]
$8.84e^{-1}$	34.4	1.63	0.78	0.18	-0.12

Table 4.4: SFTF model parameters as determined from LES for the SAFRAN combustor.

4.5.2 SFTF model application

The resulting SFTF model FTF prediction is compared to the reference LES data of the downstream forcing case O08 in Fig. 4.35. Large discrepancies are obtained between

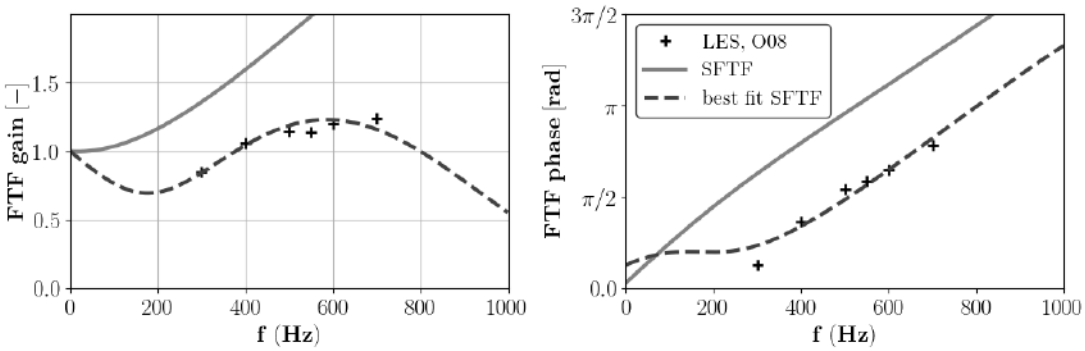


Figure 4.35: FTF gain and phase as obtained from single frequency downstream forcing with amplitude $\hat{p}/P_{out} = 0.83\%$, using the analytical SFTF model with parameters of Tab. 4.4, and with optimized parameters.

the FTF obtained from LES and the SFTF model results. Indeed, the SFTF predicted gain rapidly increases to large values resulting in a clear overestimation. While both

FTF phase curves show a linear tendency for the studied range of frequencies, the SFTF phase is shifted upwards compared to the LES data and its phase at origin is close to null when a linear regression of LES points yields a phase close to $-\pi/2$ instead.

A complementary study was also performed by using a bayesian optimization algorithm [218] to obtain the best set of parameters for the SFTF model to match FTF gain and phase as obtained from LES. The only imposed constraint is in this case $\tau \leq 5$ ms to avoid erroneous matching results due to aliasing. This assumption is very reasonable in regard to the combustion chamber dimensions and high flow velocity encountered in the flame area. The obtained best fit parameters are presented in Tab. 4.5.

ω_*/ω [ms]	α [deg.]	K	χ	τ [ms]	ϕ_0 [rad]
$8.46e^{-1}$	81.9	1.53	0.46	0.94	-1.01

Table 4.5: SFTF model parameters as determined from an optimization procedure to match the LES gauged FTF for the SAFRAN combustor.

From these results, one observes that parameters ω_* and K do not differ very much from the LES values. This brute-force optimization however ends up providing an extremely large value of the flame angle α that will be qualified as non-physical. Likewise, the time delay τ obtained is five times larger than the LES obtained value which means that either the LES probing method is incorrect or more likely that something is missing in the analytical model description. The associated best fit FTF is plotted in Fig. 4.35. Although the optimization provides a good match with the few reference data points, the steep decrease of the FTF gain in the low frequency range is unlikely and has not been observed in the literature to the author's knowledge.

These results confirm that the analytical model in its current state cannot be used to produce the transfer function of the present industrial engine flame. As previously stated, such a result could be expected since the model derivation is done with much simpler cases as a target. Some limitations may however potentially be removed, for instance a double G-equation could be used when building the base laminar FTF $\mathcal{F}_v$ to track both sides of the M-shaped flame. Still, the role of other phenomena such as the fuel droplets evaporation or the heat release repartition between the main rich flame and secondary diffusion flames needs to be incorporated if one wants to achieve a proper modelling. Few attempts have been made in the literature to include two-phase flow features for RQL combustors FTF [219] (droplet dispersion, spray flame transfer function, etc) but they do no allow for quantitative results. Arguably, one critical missing feature may not lie in the model itself but rather in the decomposition of the heat release into a flame transfer function for each identified flame in the present combustor. In any case, this study underlines the need for further analytical developments under assumptions that could better cope with real high power non-premixed flames. It should

therefore be seen as first rough attempt providing some insight on additional physics to consider and/or assumptions to relax to reproduce real engine FTF.

4.6 Thermoacoustic stability analysis using a Helmholtz solver

Following the determination of the SAFRAN combustor FTF from the previous sections, the AVSP Helmholtz solver is used in the following to determine the acoustic modes of the configuration as well as their linear stability. Starting from the cavity modes, the complexity of the acoustic modeling is increased step by step by adding active flames and multi-perforations. The stated goal is to verify the linear stability of the unstable mode at $f = 500$ Hz observed during the real engine test session. The stability of all obtained acoustic modes is assessed and conclusions are drawn on the prediction capabilities of the FTF extraction and Helmholtz solver modelling chain.

4.6.1 Numerical setup

The AVSP Helmholtz solver developped at CERFACS [43] is used to compute the acoustic modes of the SAFRAN combustor. The code solves the Helmholtz equation on three-dimensional unstructured grids and can account for active flames [44], acoustic damping through multiperforations [78, 220] and complex impedances [79, 221].

The geometry considered for Helmholtz computations is presented in Fig. 4.2 with the air cavity behind the air inlet (which was removed for LES) and the exit of the combustion chamber as the main outlet. Acoustic modes encountered in annular chambers often present an azimuthal component that compels the use of the full annular geometry or special treatments using Bloch waves for acoustic studies [200]. In the present case the chamber characteristic length is a few dozen centimetres, which allows to use large mesh cells for acoustic calculations so that the needed computational power remains very reasonable. A single sector mesh is first conceived, with much fewer cells that its counterpart used in the previous section for LES computations. This mesh is then duplicated $N_{sec} - 1$ times (N_{sec} being the total number of sectors) to produce the full annular geometry. The final grid comprises 9 million tetrahedral cells with a maximum cell size $\Delta_x = 10$ mm guaranteeing a sufficient wavelength resolution for the frequency range of interest.

Classical acoustic boundary conditions are first considered by applying a null normal acoustic velocity on all boundaries, $\hat{\mathbf{u}}.\mathbf{n} = 0$. Apart from walls, this includes the main air inlet and the chamber outlet. Regarding the inlet, a very stiff high velocity profile is imposed for the considered operating point, thus assuming $\hat{\mathbf{u}}.\mathbf{n} = 0$ on the corresponding surface is justified. For the outlet, the discussion is more open. Ideally one should use

the appropriate impedance representing the reflection of acoustic waves on the turbine stages. Such data is however not available in the present case. For the real industrial geometry, the hot gas flow exits through a converging nozzle on the high pressure turbine which can be considered as a wall to first order, thus legitimating a zero normal velocity. Note that results obtained with a zero pressure fluctuation boundary condition at the outlet are available in Appendix E for completeness.

Helmholtz solvers use mean fields of heat capacity ratio $\overline{\gamma}$, density $\overline{\rho}$ and sound speed $\overline{c}$ as inputs. In the present case, these mean fields are directly provided by a 20 ms average solution of the unforced single sector LES interpolated on the AVSP mesh and replicated to cover the 360° geometry. Baseline mean fields are shown in Fig.4.36. The maximum Mach number is $M = 0.28$ and is reached in local regions

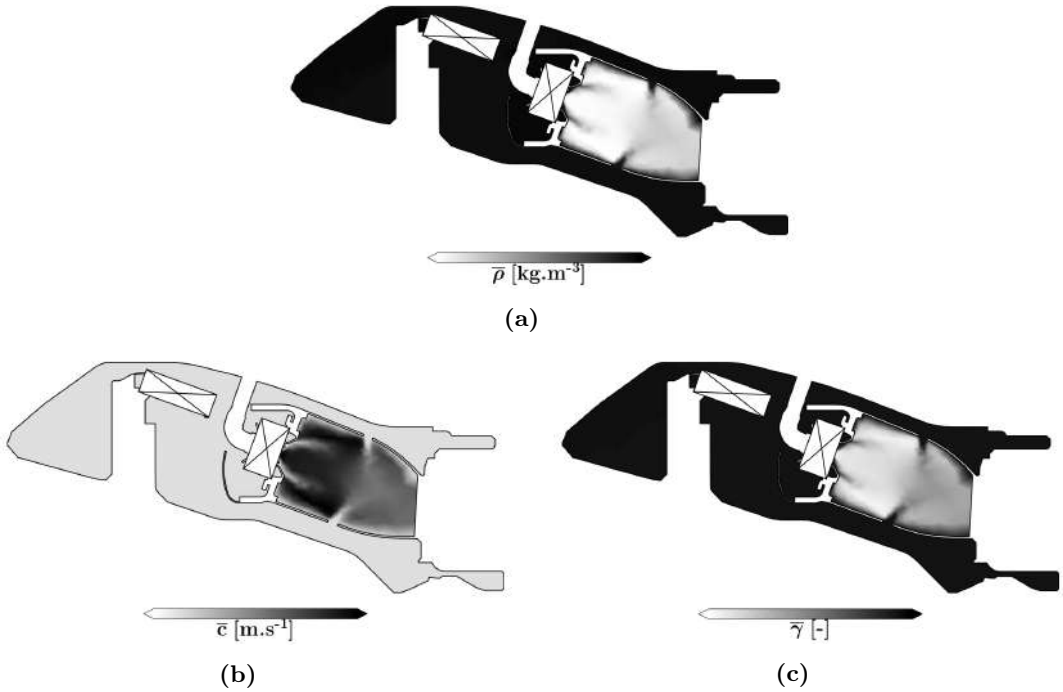


Figure 4.36: Mean flow quantities used for Helmholtz computations of the SAFRAN combustor: (a) density, (b) sound speed, (c) heat capacity ratio.

around the swirler channels exits or near dilution holes. Non zero Mach number effects are not accounted for in AVSP unless specific impedance boundary conditions are used [79]. These effects should nonetheless remain minor and standard acoustic boundary conditions are kept.

For the analysis and clearer understanding, complex elements are progressively included in the computations so that three distinct cases are identified, Tab. 4.6. In case R1, only density and sound speed non uniformities are considered, yielding the so called passive modes of the configuration. Case R2 adds the modelling of the flame response or FTF, and finally, case R3 features a more accurate representation of the

Case	Sound speed field	Flame model	Multi-perforated plates
R1	non uniform	no unsteady flame	zero normal velocity
R2	non uniform	active flame, FTF from LES	zero normal velocity
R3	non uniform	active flame, FTF from LES	Howe uniform model

Table 4.6: Summary of Helmholtz computations cases performed.

multi-perforated chamber liners. The two latter cases result in a nonlinear eigenvalue problem which is solved using a fixed point algorithm with a relaxation method [43] for one frequency at a time, using an initial guess for a given complex frequency.

4.6.2 Helmholtz computations of the SAFRAN combustor

4.6.2.1 Passive modes

As a first step, a baseline computation of the linear eigenvalue problem of case R1 is performed with the input mean flow fields of Fig. 4.36. A list of the first 10 eigenmode frequencies obtained is provided in Tab. 4.7. Since only null velocity boundary

Mode	Re(f)	Im(f)	Mode structure
M0	0.04	9.7×10^{-1}	NA
M1	308.0	-1.0×10^{-6}	1A
M2	308.0	9.5×10^{-8}	1A
M3	389.3	6.6×10^{-6}	1L
M4	497.5	1.8×10^{-7}	1A1L
M5	497.5	1.9×10^{-6}	1A1L
M6	550.5	-1.6×10^{-7}	2A
M7	550.5	-9.2×10^{-7}	2A
M8	661.7	1.8×10^{-5}	2L
M9	714.7	2.8×10^{-5}	2A1L

Table 4.7: List of the first 10 eigenmode frequencies Re(f) and growth rates Im(f) obtained for case R1 (passive flame and null normal velocity on all boundaries). The mode structure is also specified: for instance mode 1A corresponds to the first azimuthal mode and mode 1A1L corresponds to a first mixed azimuthal/longitudinal mode.

conditions are used, the 0 frequency mode is a trivial solution of the problem (mode M0). All modes featuring an azimuthal component (mode structure denoted with "A" in Tab. 4.7) are found as a pair of degenerate eigenvalues. For each pair, the two modes share the same azimuthal mode shape but are orthogonal: one can be reconstructed from the other by applying a rotation of angle $\theta = \pi/2^m$ where m is the azimuthal wavenumber. Also, note that in the absence of complex boundary condition or active

acoustic element, all modes have an almost zero growth rate, in agreement with theory. Modes M4 and M5 with a frequency $f = 497.5$ Hz are very close to the potential thermoacoustic instability frequency ($f_1 = 500$ Hz) observed during engine test sessions. The structure of these modes is one longitudinal and one azimuthal (1A1L), as displayed in Fig. 4.37. The pressure mode shape features a phase which is constant by

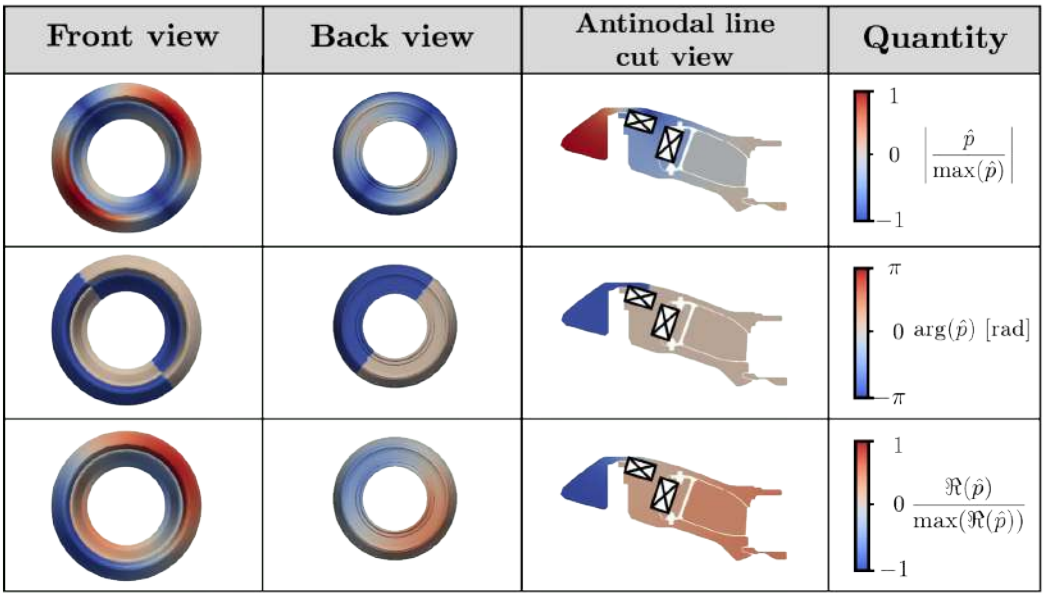


Figure 4.37: Structure of modes M4/M5 for case R1. The front view faces the compressor stages, the back view faces the combustion chamber outlet. The transverse cut is extracted on the antinodal line for which $|\hat{\mathbf{p}}|$ is maximum.

part in the azimuthal direction, indicating the standing nature of the mode.

4.6.2.2 Active flame modes

In a second step, active flames are incorporated in the R2 Helmholtz computations. The flame shape is identified using the mean LES fields by isovolumes of volumetric heat release rate using a threshold value $\overline{Q} = 10^9$ W.m^{-3}, Fig. 4.38. The flame is of course replicated $N_s - 1$ times to cope with the annular geometry. The flame acoustic response is modelled in the frequency domain with a FTF, here chosen as the one obtained with LES for downstream forcing with an amplitude $\hat{p}/P_{out} = 0.83\%$ and reference locations VE and VES (see Fig. 4.13). Uniform gain and time delays are used for the FTF determination, and the same is done in the Helmholtz solver. The adimensionalized FTF gain N_3 obtained from LES using Eq. (3.5) is converted to its dimensional counterpart $N_2 = N_3\overline{u}/\overline{Q}$. Finally the volumetric gain n is equally distributed within the identified flame volume V_f, so that:

$$N_2 = \int_{V_f} n dV \tag{4.4}$$

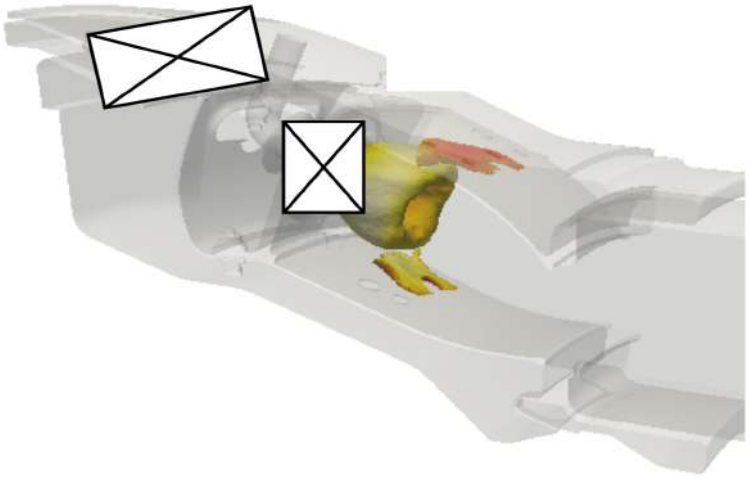


Figure 4.38: Flame zone identified by the isocontour $\overline{Q} = 10^9$ W.m^{-3} and used for Helmholtz computations. Dimensions have been modified.

Similarly, a constant time delay is applied on all flame points. Note that the Helmholtz solver representation of the FTF relies on a single reference point per injector while collections of probes were used in the LES. In that respect, a study is performed in Appendix F by using diametrically opposed probes of a given probing location. Computations yield less than 0.5% difference on the predicted mode frequencies and less than 10% difference for the growth rates, thus proving their acoustic equivalence for the Helmholtz solver. In the following, all computations are performed using a single reference point located in the upper part of the swirler exit.

For this new series of computations, acoustic eigenmodes M3, M4, M6 and M8 of Tab. 4.7 are used as initial guess one at a time for the resolution of the nonlinear active flame eigenvalue problem. Eigenfrequencies obtained for the present case (R2) are presented in Tab. 4.8 for the FTF obtained using reference probes VE and VES. Similar trends are seen between the two tested reference locations for modes M3, M4 and M6, but higher growth rates and deviations compared to the initial guessed frequencies are seen when using VE probes. Such discrepancies cannot be explained by the limited differences in FTF gain between VE and VES. This difference is instead related to the difference in the reference velocity fluctuation amplitudes computed by the Helmholtz solver which are higher for all modes in the swirler channels (corresponding to probe VE). The notable exception is mode M8 which is predicted as stable using reference probe VE and unstable using reference probe VES. The exact reason of this difference is not yet fully understood. Note that when starting from the passive flame mode structure using VES as a reference, for this mode, the computation converged on mode M9 with a 2A1L structure and a frequency $f = 722$ Hz. A new input frequency was therefore chosen: $f = 661.7 + 20i$ Hz to retrieve the 2L mode. Such a behaviour is a

Mode	Passive mode frequency (R1) [Hz]	Active mode frequency (R2) [Hz]	growth rate [s^{-1}]	Frequency shift [%]	Linear stability
M3	389.3	430.5	39.4	10.6	unstable
M4	497.5	514.1	27.3	3.3	unstable
M6	550.5	563.1	-25.7	2.3	stable
M8	661.7	675.7	-75.9	2.1	stable

Mode	Passive mode frequency (R1) [Hz]	Active mode frequency (R2) [Hz]	growth rate [s^{-1}]	Frequency shift [%]	Linear stability
M3	389.3	407.2	20.3	4.7	unstable
M4	497.5	500.1	13.2	0.7	unstable
M6	550.5	553.1	-8.7	0.5	stable
M8	661.7	631.4	48.8	4.6	unstable

Table 4.8: Non exhaustive list of eigenmodes of the SAFRAN combustor obtained using AVSP with an active flame (case R2) and FTF parameters of case O08 derived with reference probes VE (top) and VES (bottom). The linear stability criterion is simply derived from the sign of the growth rate: a positive value corresponds to a linearly stable mode.

known drawback of fixed point methods, especially for complex valued problems: the evaluated function may not be locally contracting so that the converged value may heavily depend on the initial guess. One possibility to achieve a full coverage of the frequency spectrum is to perform several computations using initial guesses distributed along the real and imaginary axes. All the analyses presented in the remainder of this document will refer to results obtained using the VES reference location.

For all modes, the frequency shift, defined as the relative difference between frequencies of the active case R2 with frequencies of the passive case remains under 5%. The pressure mode shape of the specific mode of interest, M4 for case R2, is displayed in Fig. 4.39. The addition of active flames does not modify the mode structure but it is found to be of spinning nature whereas it was found to be standing in the passive flame case: the pressure modulus is constant for a given axial plane but its phase varies linearly with the azimuthal angle θ. The exact reason of this change of the mode nature is yet to be determined. One explanation could be the fact that the flames introduced in R2 computations are not perfectly symmetric , which may influence convergence towards a spinning state. While the frequency of mode M4 is only marginally modified, adding an active flame yields a positive growth rate $\sigma_4 = 13.2\ s^{-1}$ indicative of an unstable mode. Ideally, this mode should be identified as the only one unstable since it is the only one observed during experiments. However, the linear stability of a mode may not be sufficient as nonlinear effects and sources of acoustic damping are neglected. In the present study, the mode M3 is also identified as unstable with a growth rate $\sigma_3 = 20.3 s^{-1}$ $\geq \sigma_4$. This latter was however not reported experimentally.

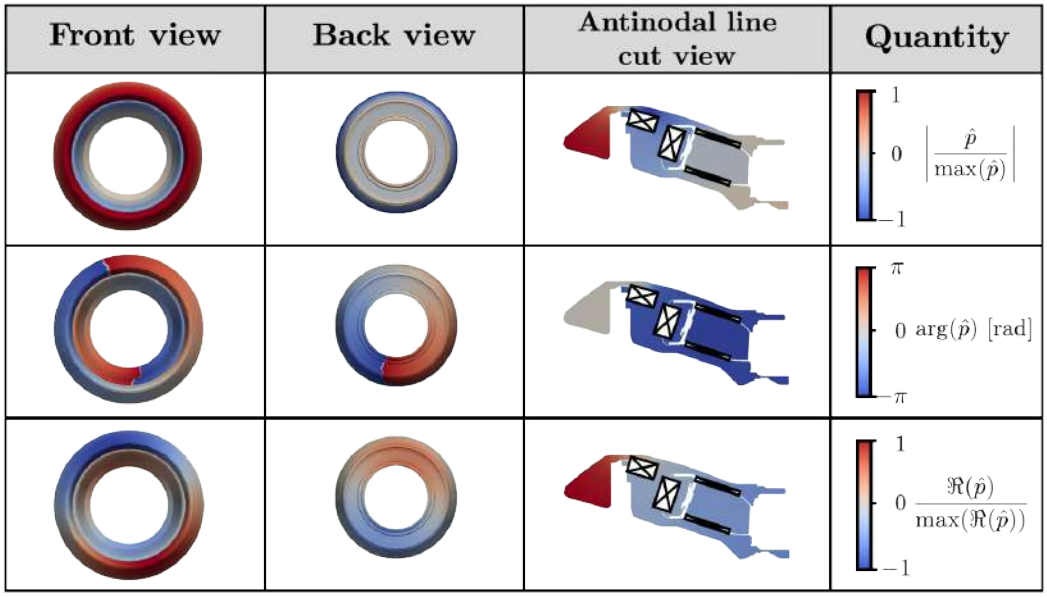


Figure 4.39: Structure of mode M4 for case R2. Front view faces the compressor stages, back view faces the combustion chamber outlet. The transverse cut is extracted on the antinodal line for which $|\hat{\mathbf{p}}|$ is maximum.

4.6.2.3 Active flame and multi-perforations

Before drawing any conclusion, a last case R3 is studied. For this case, acoustic damping introduced by the multi-perforated liners is added to the modelling. As already mentioned, such devices were originally introduced to cool the combustion chamber walls, but were also observed to introduce acoustic dissipation by introducing a pressure discontuity. They have been subject to numerous experimental [185, 222, 223, 224] as well numerical studies of various types [205, 225]. Notably, it was shown that acoustic energy is converted into vorticity in the unstable shear layer at the edge of a hole through viscous effects. Meshing the tiny holes of each liner is already a challenge in itself for standard CFD, but it is even more prohibitive in the context of low order models and Helmholtz solvers which have been specifically designed to cope with coarse meshes. For this reason, homogeneous boundary conditions based on Howe's model [185] have been developed and used in acoustic solvers [78] like the present one. Howe's model provides a convenient approximation for the Rayleigh conductivity K_R characterizing the pressure discontinuity through an orifice [201], so that:

$$K_R = \frac{i\overline{\rho}\omega d_h^2 \hat{\mathbf{u}}.\mathbf{n}}{|\hat{p}^+ - \hat{p}^-|} \tag{4.5}$$

where $\hat{u}$ is the acoustic velocity on both sides of the plate and d_h is the distance between the center of two orifices as presented in Fig. 4.40. The model assumes uniformly distributed orifices with a circular cross section and a flow-through direction normal to

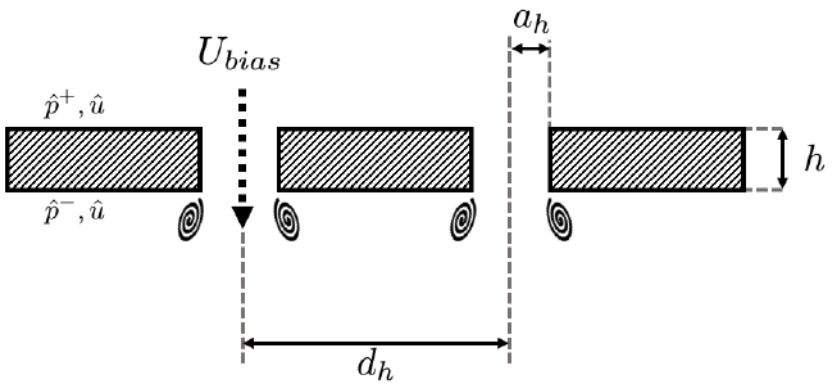


Figure 4.40: Schematic representation of uniformly distributed multi-perforations on a plate as considered in Howe's model.

the plate surface. Using notations of the figure, the Rayleigh conductivity is expressed as:

$$K_R = 2a_h \left(\Gamma_{St} - i\Delta_{St}\right) \tag{4.6}$$

where Γ_{St} and Δ_{St} are two real valued functions of the Strouhal number $St = \omega a_h / U_{bias}$. These are defined by:

$$\Gamma_{St} - i\Delta_{St} = 1 + \frac{\frac{\pi}{2} I_1(St) e^{-St} - iK_1(St)\sinh(St)}{St\left(\frac{\pi}{2} I_1(St) e^{-St} + iK_1(St)\cosh(St)\right)} \tag{4.7}$$

where I_1 and K_1 are modified Bessel functions of the first and second kind respectively. The evolution of these functions with increasing Strouhal number is plotted in Fig 4.41. In the low Strouhal number limit, liners behave like rigid walls, while in the

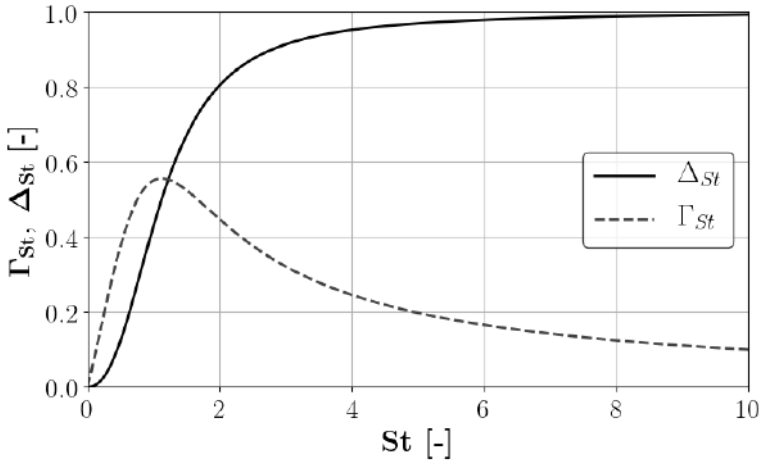


Figure 4.41: Evolution of the real part Δ_{St} and imaginary part Γ_{St} of the Rayleigh conductivity lK_R using the definition of Eq. (4.7)**.**

high Strouhal number limit the model yields the theoretical value first proposed by Rayleigh: $K_R = 2a_h$.

The boundary condition implemented in the AVSP version is a modified version of the model by Jing and Sun [226] which also takes into account the thickness of the multi-perforated plate h:

$$K_R = 2a_h \left(\frac{1}{\Gamma_R - i\Delta_R} + \frac{2h}{\pi a_h} \right)^{-1} \tag{4.8}$$

As a result, multi-perforations are modelled using four quantities:

- a_h: the radius of holes.
- d_h: the average distance between holes.
- U_{bias}: the mean bias flow speed through each aperture.
- h: the plate thickness.

In the case of the SAFRAN combustor, multi-perforations have a radius r_{pf} and are not straight but tilted by an angle α_{pf} undisclosed here for confidentiality reasons. The parameter h therefore does not correspond to the plate thickness but rather to the distance between the center of a hole on one side of the plate to the other so that, if e is the thickness of the plate (including thermal coating layers):

$$h = \frac{e}{\cos \alpha_{pf}}. \tag{4.9}$$

If one notes S_{pf} the surface of multi-perforations, and S_p the surface of the full plate, the associated porosity reads $\epsilon = S_{pf}/S_p$. The bias flow is thus computed as:

$$U_{bias} = \frac{\dot{m} \cos \alpha}{\rho S_{pf}} = \frac{\dot{m} \cos \alpha}{\rho \epsilon S_p}, \tag{4.10}$$

where $\dot{m}$ corresponds to the mass flow rate used in LES computations and the mean density ρ is taken from an LES average solution upstream of holes, in the bypass channel. Finally, the average distance between holes d_h is calculated as:

$$d_h = \left(\frac{\pi a_h^2 \cos \alpha}{\epsilon} \right)^{\frac{1}{2}} \tag{4.11}$$

These properties are not uniform along the length of both inner and outer liners. Each liner is hence subdivided into 6 zones with constant properties as shown in Fig. 4.42. The mean resulting Strouhal number for all multi-perforated plate is $St = 0.02$, which means that they should behave almost like rigid walls according to Fig. 4.41. Accordingly, the expected changes with case R3 will be small and only a small decrease of the eigenmodes growth rates is expected. Results of case R3 presented in Tab. 4.9 indeed confirm this behaviour when compared to results of case R2 shown in Tab. 4.8. For all studied modes, a small reduction of the growth rate is observed, with

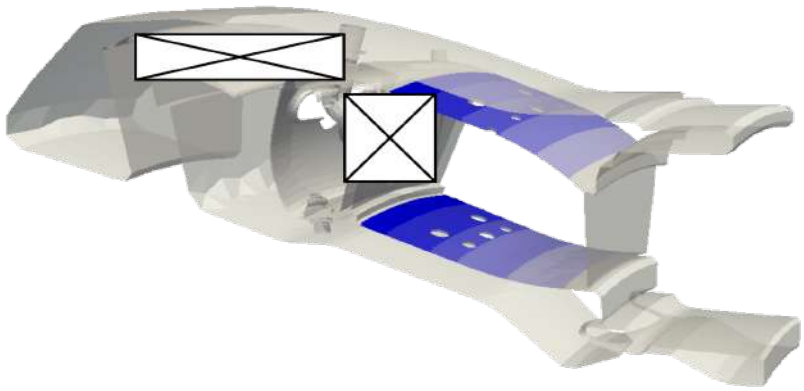


Figure 4.42: Visualization of the perforated plate patches used for Helmholtz computations. Each coloured patch has different properties. Dimensions have been modified.

Mode	Passive mode frequency (R1) [Hz]	Active mode frequency (R2) [Hz]	growth rate [s^{-1}]	Frequency shift [%]	Linear stability
M3	389.3	406.7	20.0	4.5	unstable
M4	497.5	500.0	13.1	0.5	unstable
M6	550.5	553.6	-10.0	0.6	stable
M8	661.7	631.2	47.9	4.6	unstable

Table 4.9: Non exhaustive list of eigenmodes of the SAFRAN combustor obtained using AVSP with an active flame and multi-perforations modelling (case R3). FTF parameters of case O08 derived with reference probes VES are used.

higher decrease for higher frequencies linked to a higher Strouhal number. Pressure mode shapes are only marginally modified and are thus not shown here. This means that the mode of interest at $f = 500$ Hz is still not the only one predicted as unstable by the Helmholtz solver results. Indeed modes M3, M4 and M8 have a positive growth rate even when the damping from multi-perforations is taken into account.

Finally a study is performed to assess the evolution of predicted mode frequencies and growth rates when increasing the level of the forcing perturbation. This effectively comes down to providing a different FTF as an input. To do so, additional Helmholtz computations are performed on the base of case R2, that is with an active flame, but with a FTF obtained with case O25, corresponding to a forcing amplitude $\hat{p}/P_{out} = 2.5\%$. Multi-perforations are not modelled since their effect is minor and does not change final conclusions. Figure 4.43 shows the evolution of modes frequencies and growth rates with increasing forcing amplitudes. The stability of considered modes is not altered when increasing the forcing level. With the higher forcing level FTF, a larger frequency shift with respect to the passive mode frequency is obtained for the first three modes, since the FTF gain and phase are higher for case O25 than for case O08 for $f \leq 550$ Hz (Fig. 4.21). On the contrary, the FTF gain is decreased around $f = 660$ Hz when

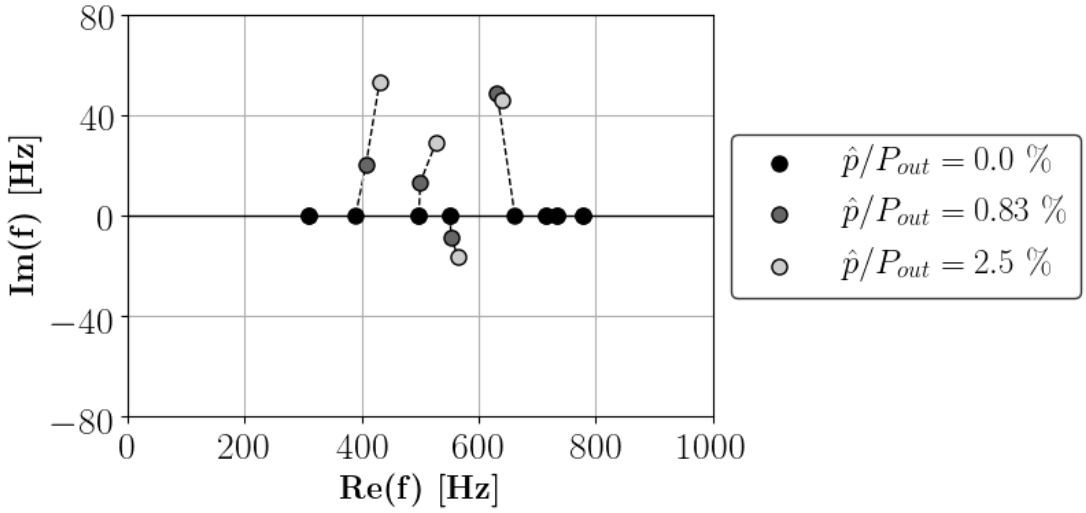


Figure 4.43: Evolution of modes frequencies and growth rates with increasing acoustic perturbation amplitude for downstream forcing p'/P_{out}. Acoustic liners are not modelled here

increasing the perturbation level, yielding a slightly lower frequency shift.

From this analysis, one concludes that an unstable thermoacoustic mode at $f = 500$ Hz is indeed found for the SAFRAN combustor at the particular studied operating point. However the low order analysis predicts several modes to be unstable and therefore does not permit to conclude on the dominance of the mode observed during test sessions. This result underlines the need for adequate boundary conditions at the domain outlet [80], as well as for a precise characterization of damping mechanisms in the chamber that will affect the final limit cycle observed in the engine. Indeed, the modal stability of a given combustor is governed by an energy balance between acoustic energy generated by the flame and acoustic damping across the chamber. A corollary to this is the need for a flame acoustic modelling taking into account the excitation amplitude such as the FDF formalism, which was already used with success in Helmholtz solvers [44] while only two excitation amplitudes have been considered in the present work.

4.7 Conclusions

The response of a high power swirling flame to an acoustic modulation has been investigated on a real engine configuration by means of a joint two-phase flow LES - Helmholtz solver analysis. The steady reacting regime has first been briefly analysed to identify the characteristic features of the flow, and the unperturbed flame structure. The swirling flow produces typical inner and outer recirculation zones that help anchoring the M-shaped flame in the vicinity of the liquid fuel injection feed. A comprehensive analysis of the pulsed flow dynamics has then be conducted. The specific roles of the reference

position for the FTF evaluation, the forcing amplitude, and the location of the forcing source have been studied using LES.

Regarding the reference position, four sets of probes equally distributed around the burner axis have been used, located directly in the first and second swirler stages, as well as at their respective exits. The comparison shows that the FTF time delay is correctly captured regardless of the probing location, since differences in final values are simply linked to the distance from the probing location to the flame base. It is also shown that FTF gains assessed from reference probes in the second swirler stage are comparable, while discrepancies appear when considering the first swirler stage references.

A second investigation focused on forced flames dynamics when submitted to various acoustic modulation amplitudes. Numerical simulations reveal that in the case of high amplitude forcing, the flame response is governed by the intermittent release of large pockets of liquid fuel in the chamber, which alter the flame surface in a major way during a forcing cycle. The FTF gain and time delays are shown to increase with the forcing amplitude for the two tested frequencies, a feature that is not observed for academic swirled flames such as the one presented in Fig. 3.42.

The non equivalence of upstream and downstream forcing for this industrial configuration was demonstrated. Such a study had never been done thoroughly on a complex industrial geometry. The contribution of diffusion flames was shown to remain similar regardless of the forcing type. On the contrary, the primary flame heat release differed depending on whether upstream or downstream forcing was applied. The origin of such differences was found to be the phase of the chamber pressure with respect to the reference velocity signal. This result suggests that a FTF accounting for both pressure and velocity fluctuations close to the flame may be necessary to fully characterize the flame response.

When combined, all these analyses underline the difficulty to evaluate the transfer function of swirling flames as encountered in real gas turbines, as well as the multitude of factors affecting their response. This work however provides insights and guidelines for the numerical evaluation of the FTF using LES.

In another section, the SFTF methodology was applied on the complex two phase flow configuration. Model parameters were extracted thanks to the methodology defined for the academic NoiseDyn burner. The model was derived under assumptions that are inherently false for such a complex case, and the predicted FTF does therefore not match the reference LES data. It is concluded that further modelling is needed, and in light of LES findings, it is underlined that separating the response from the primary flame and the one from lean diffusion flames could be a determining limit.

Finally, Helmholtz computations were performed using the FTF obtained from forced LES. The damping associated to multi-perforated liners is shown to be negli-

gible in the frequency range of interest. An unstable mode with structure 1A1L is identified from the analysis, with a frequency close to the one observed during engine test sessions. The analysis however also predicts other modes to be unstable while these were not observed during experiments.

Chapter 5

General conclusions

Over the last two decades, aircraft engines manufacturers have focused their efforts on lean combustion technologies to reduce pollutant emissions and meet the increasingly stringent targets imposed by international regulation agencies. However, improvements on emission levels cannot be met without issues, and such engines are prone to the development of unwanted oscillations known as combustion instabilities. These instabilities result from a coupling between flames and acoustics in confined environments and are still a very active field of research for both academics and aeronautical gas turbines manufacturers. As of today, and even considering recent advancements in computing hardware, the only viable solution to predict the stability map of a given engine relies on the joint use of reduced order models and flame response models such as the flame transfer function.

In this thesis, numerical simulations are used to provide insights on forced swirling flame dynamics and a procedure is proposed to characterize the response of premixed swirling flames, with the intent of investigating combustion instabilities prediction and control. Typically, a hybrid model was developed based on previous works on laminar V-shaped Flame Transfer Functions and building upon the work of Palies *et al.* on the modeling of swirling flames. At the same time, the predictive capabilities of Large Eddy Simulations in the context of thermoacoustics were demonstrated, and several aspects were investigated. In the following, general conclusions are drawn and perspectives for improvements are discussed.

- *About the modelling of swirling flame transfer functions:*
  A novel approach was proposed for the determination of the transfer function of premixed V-shaped swirling flames with a reduced number of high fidelity simulations. The methodology, denoted as SFTF is qualified as "hybrid" in the sense that it combines a simple analytical formulation and the extraction of key parameters using high fidelity numerical simulations. The main objective is to provide a reliable evaluation of the FTF, which also decreases the total computational time necessary to characterize the flame response to acoustics. Six parameters are identified from the analytical derivation, three of which describe the laminar flame response while the remaining ones account for the effects of swirl. A robust step by step methodology is proposed to extract these parameters from a reduced set of LES, depending on the available computational resources. The procedure proved

satisfactory in retrieving the FTF of an academic premixed swirling flame at a reduced computational cost compared to standard methods. A complementary study on a configuration featuring a shorter injector also yielded good agreement with experimental data. Moreover, the model was shown to be able to handle non vanishingly small perturbation amplitudes through one of the SFTF model parameter accounting for the decay rate of axial velocity disturbances. Applied to an industrial two-phase flow swirling flame, the model was however not able to deliver satisfactory results, as a result of flow characteristics in contradiction with the original scope of the SFTF derivation. Although the present work focuses on premixed V-shaped flames, it would valuable to extend the formulation to comply with other standard swirling flames shapes, notably M-shaped ones. This could be achieved using a double G-equation with matching conditions at the flame tips.

- *Regarding the characteristics of forced premixed swirling flames:*
  LES have been employed to analyse the dynamics of an academic turbulent V-shaped swirling flame submitted to an acoustic modulation in Chap. 3. The numerical simulations were shown to remarkably reproduce the reference experimental data under non reacting, reacting, and pulsed flow conditions. In particular the local high and low gain regions of the FTF were correctly captured, and the inflexion of the phase curve at the minimum gain frequency was reproduced. The analysis was then pursued by considering the phenomena occurring in the vicinity of the injector exit rim. Notably, it was shown that the flame response is bound to the preferential frequency response of the injector, generating vortical structures that can be affected by the inner recirculation zone. When these structures are able to roll up along the flame, they wrinkle its surface and thus, a high FTF gain is obtained. Conversely, when weak vortices are released, they are torn apart by the inner recirculation zone movement and can only marginally affect the flame surface, leading to a low FTF gain. These mechanisms were also observed in the absence of combustion, indicating that this behaviour is not linked to flame/vortex interactions. As for perspectives, this work mainly focused on bluff-body stabilized swirling flames. The case of fully aerodynamically stabilized flame, that do not present local low and high FTF gain regions, was only partially studied, Appendix C. Making use of LES to identify the different injector flow properties leading to a different forced response would surely be of interest.

- *On the flame transfer function of an industrial combustor*
  A series of forced LES of an industrial combustor from SAFRAN featuring a two-phase flow swirling flame has been conducted in Chap. 4. Particular attention was drawn to the effects of various parameters on the FTF evaluation: the position of

the reference velocity probes, the amplitude of the forcing signal, and the effect of downstream/upstream forcing. From a signal processing standpoint, probes located at the exit of the swirler channels are found to be the most reliable for the FTF assessment. The preponderant role of liquid droplet clusters formation in the increase of FTF gain with increasing forcing levels was demonstrated, albeit only for a narrow frequency range. The non equivalence of upstream and downstream forcing on this industrial case was shown to originate from the difference of the fluctuating pressure state within the combustor. In this matter, it is concluded that it would be of great interest to compute a transfer function relying on both fluctuating pressure and velocity at a reference location. In this work, an Eulerian-Eulerian approach was adopted. Another compelling study would be to quantify the benefits of using a Lagrangian formulation for the liquid phase, if they exist. A final study was dedicated to the joint use of LES to determine the FTF of the industrial combustor swirling flame, and of a Helmholtz solver to predict unstable thermoacoustic eigenmodes. While an unstable mode was identified at a frequency close to the one observed during the engine test session, the analysis also determined other modes to be unstable. In Helmholtz computations the only sources of acoustic dissipation that have been accounted for were the perforated liners, that were shown to have a negligible impact in the frequency range of interest. Swirlers, and large orifices such as dilution holes are known to introduce acoustic damping and could be included in Helmholtz computations.

Bibliography

[1] "World energy balances 2019." `https://www.https://www.iea.org/data-and-statistics`. Last accessed: 2020-03-12. 2

[2] A. G. Rao, F. Yin, J. P. van Buijtenen, and A. Isikveren, "A hybrid engine concept for multi-fuel blended wing body," *Aircraft Engineering and Aerospace Technology*, vol. 86, no. 6, pp. 483–493, 2014. 4

[3] B. C. Bobusch, P. Berndt, C. O. Paschereit, and R. Klein, "Shockless explosion combustion: An innovative way of efficient constant volume combustion in gas turbines," *Combustion Science and Technology*, vol. 186, no. 10-11, pp. 1680–1689, 2014. 4

[4] F. A. Bykovskii, S. A. Zhdan, and E. F. Vedernikov, "Continuous spin detonations," *Journal of Propulsion and Power*, vol. 22, no. 6, pp. 1204–1216, 2006. 4

[5] A. H. Lefebvre and D. R. Ballal, *Gas turbine combustion: alternative fuels and emissions*. CRC press, 2010. 6

[6] N. Patel and S. Menon, "Simulation of spray–turbulence–flame interactions in a lean direct injection combustor," *Combustion and Flame*, vol. 153, no. 1-2, pp. 228–257, 2008. 6

[7] A. H. Lefebvre, "Lean premixed/prevaporized combustion," *NASA Lewis Research Center technical reports*, 1977. 6

[8] A. S. Feitelberg and M. A. Lacey, "The GE rich-quench-lean gas turbine combustor," *Journal of Engineering for Gas Turbines and Power*, vol. 120, no. 3, pp. 502–508, 1998. 6, 113

[9] F. Boudy, D. Durox, T. Schuller, and S. Candel, "Nonlinear mode triggering in a multiple flame combustor," *Proceedings of the Combustion Institute*, vol. 33, no. 1, pp. 1121–1128, 2011. 6

[10] S. M. Correa, "Power generation and aeropropulsion gas turbines: From combustion science to combustion technology," in *Symposium (International) on Combustion*, vol. 27, pp. 1793–1807, Elsevier, 1998. 6

[11] Y. Huang and V. Yang, "Dynamics and stability of lean-premixed swirl-stabilized combustion," *Progress in Energy and Combustion Science*, vol. 35, no. 4, pp. 293–364, 2009. 6, 41

[12] T. Poinsot, "Prediction and control of combustion instabilities in real engines," *Proceedings of the Combustion Institute*, vol. 36, no. 1, pp. 1–28, 2017. 6, 9, 10, 13

[13] T. Poinsot and D. Veynante, *Theoretical and Numerical Combustion.* Third Edition (www.cerfacs.fr/elearning), 2011. 7, 8, 12, 14, 15, 20, 194

[14] P. L. Rijke, "Notice of a new method of causing a vibration of the air contained in a tube open at both ends," *The London, Edinburgh, and Dublin Philosophical Magazine and Journal of Science*, vol. 17, no. 116, pp. 419–422, 1859. 7

[15] L. Rayleigh, "The explanation of certain acoustic phenomena," *Nature*, vol. 18, pp. 319–321, 1878. 7

[16] F. Nicoud and T. Poinsot, "Thermoacoustic instabilities: Should the rayleigh criterion be extended to include entropy changes ?," *Combustion and Flame*, vol. 142, no. 1-2, pp. 153–159, 2005. 8

[17] S. Ducruix, T. Schuller, D. Durox, and S. Candel, "Combustion dynamics and instabilities: Elementary coupling and driving mechanisms," *Journal of Propulsion and Power*, vol. 19, no. 5, pp. 722–734, 2003. 8, 23

[18] C. J. Goy, S. R. James, S. Rea, T. Lieuwen, and V. Yang, "Monitoring combustion instabilities: E. ON UK's experience," *Combustion Instabilities in Gas Turbine Engines: Operational Experience, Fundamental Mechanisms, and Modeling*, vol. 210, pp. 163–175, 2005. 9

[19] L. Crocco, "Aspects of combustion instability in liquid propellant rocket motors. Part I.," *Journal of the American Rocket Society*, vol. 21, pp. 163–178, 1951. 9

[20] L. Crocco, "Aspects of combustion instability in liquid propellant rocket motors. part II.," *Journal of the American Rocket Society*, vol. 22, pp. 7–16, 1952. 9

[21] F. E. C. Culick and P. Kuentzmann, *Unsteady Motions in Combustion Chambers for Propulsion Systems.* NATO Research and Technology Organization, 2006. 9, 10, 21

[22] A. A. Putnam, *Combustion driven oscillations in industry.* American Elsevier, J.M. Beer editor, Fuel and Energy Science Series, 1971. 9

[23] T. C. Lieuwen and V. Yang, *Combustion instabilities in gas turbine engines: operational experience, fundamental mechanisms, and modeling.* American Institute of Aeronautics and Astronautics, 2005. 9

[24] R. C. Steele, L. H. Cowell, S. M. Cannon, and C. E. Smith, "Passive control of combustion instability in lean premixed combustors," *Journal of Engineering and Gas Turbines Power*, vol. 122, no. 3, pp. 412–419, 2000. 9

[25] G. A. Richards, D. L. Straub, and E. H. Robey, "Passive control of combustion dynamics in stationary gas turbines," *Journal of Propulsion and Power*, vol. 19, no. 5, pp. 795–810, 2003. 9

[26] N. Tran, S. Ducruix, and T. Schuller, "Damping combustion instabilities with perforates at the premixer inlet of a swirled burner," *Proceedings of the Combustion Institute*, vol. 32, no. 2, pp. 2917–2924, 2009. 9

[27] M. Bauerheim, P. Salas, F. Nicoud, and T. Poinsot, "Symmetry breaking of azimuthal thermo-acoustic modes in annular cavities: a theoretical study," *Journal of Fluid Mechanics*, vol. 760, pp. 431–465, 2014. 10, 20

[28] D. Kim, J. Park, D. Han, and K. T. Kim, "Symmetry-breaking for the control of combustion instabilities of two interacting swirl-stabilized flames," *Combustion and Flame*, vol. 194, pp. 180–194, 2018. 10

[29] A. P. Dowling and A. S. Morgans, "Feedback control of combustion oscillations," *Annual Review of Fluid Mechanics*, vol. 37, pp. 151–182, 2005. 10

[30] S. Candel, "Combustion dynamics and control: Progress and challenges," *Proceedings of the Combustion Institute*, vol. 29, no. 1, pp. 1–28, 2002. 10

[31] P. Wolf, G. Staffelbach, A. Roux, L. Gicquel, T. Poinsot, and V. Moureau, "Massively parallel LES of azimuthal thermo-acoustic instabilities in annular gas turbines," *Comptes Rendus Mecanique*, vol. 337, no. 6-7, pp. 385–394, 2009. 10, 111

[32] A. Kaufmann, F. Nicoud, and T. Poinsot, "Flow forcing techniques for numerical simulation of combustion instabilities," *Combustion and Flame*, vol. 131, no. 4, pp. 371–385, 2002. 10, 11

[33] T. Sattelmayer and W. Polifke, "Assessment of methods for the computation of linear stability of combustors," *Combustion Science and Technology*, vol. 175, no. 3, pp. 453–476, 2003. 10

[34] M. Bauerheim, G. Staffelbach, N. A. Worth, J. Dawson, L. Y. Gicquel, and T. Poinsot, "Sensitivity of LES-based harmonic flame response model for turbulent swirled flames and impact on the stability of azimuthal modes," *Proceedings of the Combustion Institute*, vol. 35, no. 3, pp. 3355–3363, 2015. 10, 11, 15

[35] F. Nicoud and K. Wieczorek, "About the zero mach number assumption in the calculation of thermoacoustic instabilities," *International Journal of Spray and Combustion Dynamics*, vol. 1, no. 1, pp. 67–111, 2009. 10, 16, 17

[36] W. Na, G. Efraimsson, and S. Boij, "Prediction of thermoacoustic instabilities in combustors using linearized Navier-Stokes equations in frequency domain," in *22nd International Congress on Sound and Vibration, ICSV 2015*, vol. 2, pp. 2011–2018, International Institute of Acoustics and Vibrations, 2015. 10, 17

[37] L. Crocco and S. I. Cheng, *Theory of combustion instability in liquid propellant rocket motors*, vol. Agardograph No 8. Butterworths Science, 1956. 10, 22, 30

[38] M. P. Juniper and R. Sujith, "Sensitivity and nonlinearity of thermoacoustic oscillations," *Annual Review of Fluid Mechanics*, vol. 50, pp. 661–689, 2018. 11, 20

[39] R. Gaudron, M. Gatti, C. Mirat, and T. Schuller, "Flame describing functions of a confined premixed swirled combustor with upstream and downstream forcing," *Journal of Engineering for Gas Turbines and Power*, vol. 141, no. 05, p. 051016, 2019. 11, 52, 112, 118, 137, 138

[40] K. Wieczorek, *Numerical study of mach number effects on combustion instability.* PhD thesis, Université Montpellier II, 2010. 11, 17

[41] P. Wolf, R. Balakrishnan, G. Staffelbach, L. Y. Gicquel, and T. Poinsot, "Using LES to study reacting flows and instabilities in annular combustion chambers," *Flow, Turbulence and Combustion*, vol. 88, no. 1-2, pp. 191–206, 2012. 11, 13, 19, 111

[42] C. Pankiewitz and T. Sattelmayer, "Time domain simulation of combustion instabilities in annular combustors," *Journal of Engineering for Gas Turbines and Power*, vol. 125, no. 3, pp. 677–685, 2003. 11

[43] F. Nicoud, L. Benoit, C. Sensiau, and T. Poinsot, "Acoustic modes in combustors with complex impedances and multidimensional active flames," *AIAA journal*, vol. 45, no. 2, pp. 426–441, 2007. 11, 19, 151, 153

[44] C. F. Silva, F. Nicoud, T. Schuller, D. Durox, and S. Candel, "Combining a helmholtz solver with the flame describing function to assess combustion instability in a premixed swirled combustor," *Combustion and Flame*, vol. 160, no. 9, pp. 1743–1754, 2013. 12, 19, 24, 151, 161

[45] D. Laera, G. Campa, and S. Camporeale, "A finite element method for a weakly nonlinear dynamic analysis and bifurcation tracking of thermo-acoustic instability in longitudinal and annular combustors," *Applied Energy*, vol. 187, pp. 216–227, 2017. 12, 19

[46] D. Laera, T. Schuller, K. Prieur, D. Durox, S. M. Camporeale, and S. Candel, "Flame describing function analysis of spinning and standing modes in an annular combustor and comparison with experiments," *Combustion and Flame*, vol. 184, pp. 136–152, 2017. 12, 19, 24

[47] P. Moin and K. Mahesh, "Direct numerical simulation: a tool in turbulence research," *Annual Review of Fluid Mechanics*, vol. 30, no. 1, pp. 539–578, 1998. 12

[48] S. B. Pope, *Turbulent flows*. Cambridge University Press, 2000. 12, 15

[49] P. Sagaut, *Large Eddy Simulation for incompressible flows*. Scientific computation series, Springer-Verlag, 2000. 12

[50] H. Pitsch, "Large-eddy simulation of turbulent combustion," *Annual Review of Fluid Mechanics*, vol. 38, pp. 453–482, 2006. 12

[51] T. Komarek and W. Polifke, "Impact of swirl fluctuations on the flame response of a perfectly premixed swirl burner," *Journal of Engineering for Gas Turbines and Power*, vol. 132, no. 06, p. 061503, 2010. 13, 27, 43, 44, 83

[52] F. Duchaine, F. Boudy, D. Durox, and T. Poinsot, "Sensitivity analysis of transfer functions of laminar flames," *Combustion and Flame*, vol. 158, no. 12, pp. 2384–2394, 2011. 13, 29

[53] E. Courtine, L. Selle, and T. Poinsot, "DNS of intrinsic thermoacoustic modes in laminar premixed flames," *Combustion and Flame*, vol. 162, no. 11, pp. 4331–4341, 2015. 13, 127

[54] Y. Huang, H.-G. Sung, S.-Y. Hsieh, and V. Yang, "Large-eddy simulation of combustion dynamics of lean-premixed swirl-stabilized combustor," *Journal of Propulsion and Power*, vol. 19, no. 5, pp. 782–794, 2003. 13

[55] P. Schmitt, T. Poinsot, B. Schuermans, and K. Geigle, "Large-eddy simulation and experimental study of heat transfer, nitric oxide emissions and combustion instability in a swirled turbulent high-pressure burner," *Journal of Fluid Mechanics*, vol. 570, pp. 17–46, 2007. 13

[56] L. Selle, L. Benoit, T. Poinsot, F. Nicoud, and W. Krebs, "Joint use of compressible large-eddy simulation and helmholtz solvers for the analysis of rotating modes in an industrial swirled burner," *Combustion and Flame*, vol. 145, no. 1-2, pp. 194–205, 2006. 13

[57] A. Ghani, T. Poinsot, L. Gicquel, and G. Staffelbach, "LES of longitudinal and transverse self-excited combustion instabilities in a bluff-body stabilized turbulent premixed flame," *Combustion and Flame*, vol. 162, no. 11, pp. 4075–4083, 2015. 13

[58] A. Urbano, L. Selle, G. Staffelbach, B. Cuenot, T. Schmitt, S. Ducruix, and S. Candel, "Exploration of combustion instability triggering using large eddy simulation of a multiple injector liquid rocket engine," *Combustion and Flame*, vol. 169, pp. 129–140, 2016. 13

[59] L. Y. Gicquel, G. Staffelbach, and T. Poinsot, "Large eddy simulations of gaseous flames in gas turbine combustion chambers," *Progress in Energy and Combustion Science*, vol. 38, no. 6, pp. 782–817, 2012. 13, 61

[60] S. Hermeth, G. Staffelbach, L. Y. Gicquel, and T. Poinsot, "LES evaluation of the effects of equivalence ratio fluctuations on the dynamic flame response in a real gas turbine combustion chamber," *Proceedings of the Combustion Institute*, vol. 34, no. 2, pp. 3165–3173, 2013. 13

[61] R. Mercier, T. Guiberti, A. Chatelier, D. Durox, O. Gicquel, N. Darabiha, T. Schuller, and B. Fiorina, "Experimental and numerical investigation of the influence of thermal boundary conditions on premixed swirling flame stabilization," *Combustion and Flame*, vol. 171, pp. 42–58, 2016. 13, 199

[62] M. Miguel-Brebion, D. Mejia, F. Xavier, Pradip and, B. Bédat, L. Selle, and T. Poinsot, "Joint experimental and numerical study of the influence of flame holder temperature on the stabilization of a laminar methane flame on a cylinder," *Combustion and Flame*, vol. 172, pp. 153–161, 2016. 13

[63] S. Ghosal and P. Moin, "The basic equations for the large eddy simulation of turbulent flows in complex geometry," *Journal of Computational Physics*, vol. 118, no. 1, pp. 24–37, 1995. 14

[64] P. Auzillon, B. Fiorina, R. Vicquelin, N. Darabiha, O. Gicquel, and D. Veynante, "Modeling chemical flame structure and combustion dynamics in les," *Proceedings of the Combustion Institute*, vol. 33, no. 1, pp. 1331–1338, 2011. 15

[65] F. Marble and S. Candel, "Acoustic disturbance from gas non-uniformities convected through a nozzle," *Journal of Sound and Vibration*, vol. 55, no. 2, pp. 225–243, 1977. 17

[66] A. Powell, "Theory of vortex sound," *The Journal of the Acoustical Society of America*, vol. 36, no. 1, pp. 177–195, 1964. 17

[67] A. K. M. F. Hussain and W. C. Reynolds, "The mechanics of an organized wave in turbulent shear flow," *Journal of Fluid Mechanics*, vol. 41, no. 2, pp. 241–258, 1970. 17

[68] J. Gikadi, S. Föller, and T. Sattelmayer, "Impact of turbulence on the prediction of linear aeroacoustic interactions: Acoustic response of a turbulent shear layer," *Journal of Sound and Vibration*, vol. 333, no. 24, pp. 6548–6559, 2014. 17

[69] A. Holmberg, A. Kierkegaard, and C. Weng, "A frequency domain linearized Navier–Stokes method including acoustic damping by eddy viscosity using RANS," *Journal of Sound and Vibration*, vol. 346, pp. 229–247, 2015. 17

[70] J. Gikadi, *Prediction of Acoustic Modes in Combustors using Linearized Navier-Stokes Equations in Frequency Space.* PhD thesis, Technische Universität München, 2014. 17

[71] M. Blanchard, T. Schuller, D. Sipp, and P. Schmid, "Response analysis of a laminar premixed M-flame to flow perturbations using a linearized compressible Navier-Stokes solver," *Physics of Fluids*, vol. 27, no. 4, p. 043602, 2015. 17, 24

[72] K. Wieczorek, C. Sensiau, W. Polifke, and F. Nicoud, "Assessing non-normal effects in thermoacoustic systems with mean flow," *Physics of Fluids*, vol. 23, no. 10, p. 107103, 2011. 17

[73] G. L. Sleijpen and H. A. Van der Vorst, "A Jacobi–Davidson iteration method for linear eigenvalue problems," *SIAM review*, vol. 42, no. 2, pp. 267–293, 2000. 19

[74] R. B. Lehoucq and D. C. Sorensen, "Deflation techniques for an implicitly restarted Arnoldi iteration," *SIAM Journal on Matrix Analysis and Applications*, vol. 17, no. 4, pp. 789–821, 1996. 19

[75] G. W. Stewart, "A Krylov–Schur algorithm for large eigenproblems," *SIAM Journal on Matrix Analysis and Applications*, vol. 23, no. 3, pp. 601–614, 2002. 19

[76] L. Benoit and F. Nicoud, "Numerical assessment of thermo-acoustic instabilities in gas turbines," *International Journal for Numerical Methods in Fluids*, vol. 47, no. 8-9, pp. 849–855, 2005. 19

[77] S. Camporeale, B. Fortunato, and G. Campa, "A finite element method for three-dimensional analysis of thermo-acoustic combustion instability," *Journal of Engineering for Gas Turbines and Power*, vol. 133, no. 01, p. 011506, 2011. 19

[78] E. Gullaud and F. Nicoud, "Effect of perforated plates on the acoustics of annular combustors," *AIAA journal*, vol. 50, no. 12, pp. 2629–2642, 2012. 19, 151, 157

[79] E. Motheau, L. Selle, and F. Nicoud, "Accounting for convective effects in zero-mach-number thermoacoustic models," *Journal of Sound and Vibration*, vol. 333, no. 1, pp. 246–262, 2014. 19, 151, 152

[80] E. Motheau, F. Nicoud, and T. Poinsot, "Mixed acoustic–entropy combustion instabilities in gas turbines," *Journal of Fluid Mechanics*, vol. 749, pp. 542–576, 2014. 19, 161

[81] C. F. Silva, L. Magri, T. Runte, and W. Polifke, "Uncertainty quantification of growth rates of thermoacoustic instability by an adjoint helmholtz solver," *Journal of Engineering for Gas Turbines and Power*, vol. 139, no. 01, p. 011901, 2017. 20

[82] J. G. Aguilar and M. P. Juniper, "Adjoint methods for elimination of thermoacoustic oscillations in a model annular combustor via small geometry modifications," in *ASME Turbo Expo 2018: Turbomachinery Technical Conference and Exposition*, pp. GT2018–75692, V04AT04A054, American Society of Mechanical Engineers Digital Collection, 2018. 20

[83] U. Krüger, J. Hüren, S. Hoffmann, W. Krebs, and D. Bohn, "Prediction of thermoacoustic instabilities with focus on the dynamic flame behavior for the 3A-series gas turbine of siemens KWU," in *ASME 1999 International Gas Turbine and Aeroengine Congress and Exhibition*, no. 99-GT-111, V002T02A016, 1999. 20, 111

[84] A. P. Dowling and S. R. Stow, "Acoustic analysis of gas turbine combustors," *Journal of Propulsion and Power*, vol. 19, no. 5, pp. 751–764, 2003. 20

[85] M. Bauerheim, J.-F. Parmentier, P. Salas, F. Nicoud, and T. Poinsot, "An analytical model for azimuthal thermoacoustic modes in an annular chamber fed by an annular plenum," *Combustion and Flame*, vol. 161, no. 5, pp. 1374–1389, 2014. 20, 111

[86] N. Noiray, M. Bothien, and B. Schuermans, "Investigation of azimuthal staging concepts in annular gas turbines," *Combustion Theory and Modelling*, vol. 15, no. 5, pp. 585–606, 2011. 20, 21

[87] X. Han, J. Li, and A. S. Morgans, "Prediction of combustion instability limit cycle oscillations by combining flame describing function simulations with a thermoacoustic network model," *Combustion and Flame*, vol. 162, no. 10, pp. 3632–3647, 2015. 20

[88] J. Li and A. S. Morgans, "Time domain simulations of nonlinear thermoacoustic behaviour in a simple combustor using a wave-based approach," *Journal of Sound and Vibration*, vol. 346, pp. 345–360, 2015. 20

[89] P. Palies, D. Durox, T. Schuller, and S. Candel, "Nonlinear combustion instability analysis based on the flame describing function applied to turbulent premixed swirling flames," *Combustion and Flame*, vol. 158, no. 10, pp. 1980–1991, 2011. 20, 26

[90] J. Li, D. Yang, C. Luzzato, and A. Morgans, "OSCILOS: the open source combustion instability low order simulator," in *Technical Report*, Imperial College London, 2014. 20

[91] M. Bauerheim, M. Cazalens, and T. Poinsot, "A theoretical study of mean azimuthal flow and asymmetry effects on thermo-acoustic modes in annular combustors," *Proceedings of the Combustion Institute*, vol. 35, no. 3, pp. 3219–3227, 2015. 20

[92] C. Laurent, M. Bauerheim, T. Poinsot, and F. Nicoud, "A novel modal expansion method for low-order modeling of thermoacoustic instabilities in complex geometries," *Combustion and Flame*, vol. 206, pp. 334–348, 2019. 21

[93] B. T. Zinn and M. E. Lores, "Application of the galerkin method in the solution of non-linear axial combustion instability problems in liquid rockets," *Combustion Science and Technology*, vol. 4, no. 1, pp. 269–278, 1971. 21

[94] F. Culick, "Nonlinear behavior of acoustic waves in combustion chambers—ii," *Acta Astronautica*, vol. 3, no. 9-10, pp. 735–757, 1976. 21

[95] K. Balasubramanian and R. Sujith, "Non-normality and nonlinearity in combustion–acoustic interaction in diffusion flames," *Journal of Fluid Mechanics*, vol. 594, pp. 29–57, 2008. 21

[96] M. P. Juniper, "Triggering in the horizontal rijke tube: non-normality, transient growth and bypass transition," *Journal of Fluid Mechanics*, vol. 667, pp. 272–308, 2011. 21

[97] G. Ghirardo, M. Juniper, and J. P. Moeck, "Weakly nonlinear analysis of thermoacoustic instabilities in annular combustors," *Journal of Fluid Mechanics*, vol. 805, pp. 52–87, 2016. 21

[98] V. Bellucci, B. Schuermans, D. Nowak, P. Flohr, and C. O. Paschereit, "Thermoacoustic modeling of a gas turbine combustor equipped with acoustic dampers," *Journal of Turbomachinery*, vol. 127, no. 2, pp. 372–379, 2005. 21

[99] S. R. Stow and A. P. Dowling, "A time-domain network model for nonlinear thermoacoustic oscillations," *Journal of Engineering for Gas Turbines and Power*, vol. 131, no. 03, p. 031502, 2009. 21

[100] J.-F. Bourgouin, D. Durox, J. P. Moeck, T. Schuller, and S. Candel, "Characterization and modeling of a spinning thermoacoustic instability in an annular combustor equipped with multiple matrix injectors," *Journal of Engineering for Gas Turbines and Power*, vol. 137, no. 02, p. 021503, 2015. 21, 23

[101] S. Evesque and W. Polifke, "Low-order acoustic modelling for annular combustors: Validation and inclusion of modal coupling," in *ASME Turbo Expo 2002: Power for Land, Sea, and Air*, no. GT2002-30064, pp. 321–331, American Society of Mechanical Engineers Digital Collection. 22

[102] D. Yang and A. S. Morgans, "Low-order network modeling for annular combustors exhibiting longitudinal and circumferential modes," in *ASME Turbo Expo 2018: Turbomachinery Technical Conference and Exposition*, no. GT2018-76506, V04BT04A026, American Society of Mechanical Engineers Digital Collection, 2018. 22

[103] A. Orchini, G. A. Mensah, and J. P. Moeck, "Effects of nonlinear modal interactions on the thermoacoustic stability of annular combustors," *Journal of Engineering for Gas Turbines and Power*, vol. 141, no. 02, p. 021002, 2019. 22

[104] S. Ducruix, D. Durox, and S. Candel, "Theoretical and experimental determinations of the transfer function of a laminar premixed flame," *Proceedings of the combustion institute*, vol. 28, no. 1, pp. 765–773, 2000. 23, 30, 35, 40

[105] K. Kim, J. Lee, H. Lee, B. Quay, and D. Santavicca, "Characterization of forced flame response of swirl-stabilized turbulent lean-premixed flames in a gas turbine combustor," *Journal of Engineering for Gas Turbines and Power*, vol. 132, no. 04, p. 041502, 2010. 23, 27, 208

[106] P. Palies, D. Durox, T. Schuller, and S. Candel, "The combined dynamics of swirler and turbulent premixed swirling flames," *Combustion and Flame*, vol. 157, no. 9, pp. 1698–1717, 2010. 23, 26, 27, 42, 43, 47, 48, 72, 74

[107] B. Cosic, S. Terhaar, J. Moeck, and C. Paschereit, "Response of a swirl-stabilized flame to simultaneous perturbations in equivalence ratio and velocity at high oscillation amplitudes," *Combustion and Flame*, vol. 162, pp. 1046–1062, 2015. 23, 27

[108] M. Gatti, R. Gaudron, C. Mirat, L. Zimmer, and T. Schuller, "Impact of swirl and bluff-body on the transfer function of premixed flames," *Proceedings of the Combustion Institute*, vol. 37, pp. 5197–5204, 2019. 23, 52, 199, 200, 202, 205

[109] C. Armitage, R. Balachandran, E. Mastorakos, and R. Cant, "Investigation of the nonlinear response of turbulent premixed flames to imposed inlet velocity oscillations," *Combustion and Flame*, vol. 146, no. 3, pp. 419–436, 2006. 23

[110] L. Tay-Wo-Chong, S. Bomberg, A. Ulhaq, T. Komarek, and W. Polifke, "Comparative validation study on identification of premixed flame transfer function," *Journal of Engineering for Gas Turbines and Power*, vol. 134, no. 02, p. 021502, 2012. 23

[111] A. Giauque, L. Selle, L. Gicquel, T. Poinsot, H. Buechner, P. Kaufmann, and W. Krebs, "System identification of a large-scale swirled partially premixed combustor using LES and measurements," *Journal of Turbulence*, no. 6, p. N21, 2005. 23

[112] L. T. W. Chong, T. Komarek, R. Kaess, S. Foller, and W. Polifke, "Identification of flame transfer functions from LES of a premixed swirl burner," in *ASME Turbo expo 2010*, no. GT2010-22769, pp. 623–635, American Society of Mechanical Engineers, 2010. 23, 27, 85, 109

[113] D. Pampaloni, A. Andreini, B. Facchini, and C. Paschereit, "Large-eddy-simulation modeling of the flame describing function of a lean-premixed swirl-stabilized flame," *Journal of Propulsion and Power*, vol. 35, no. 5, pp. 994–1004, 2019. 23, 27

[114] A. Chatelier, T. Guiberti, R. Mercier, N. Bertier, B. Fiorina, and T. Schuller, "Experimental and numerical investigation of the response of a swirled flame to flow modulations in a non-adiabatic combustor," *Flow, Turbulence and Combustion*, vol. 102, no. 4, pp. 995–1023, 2019. 23, 27, 85

[115] W. Polifke, "Black-box system identification for reduced order model construction," *Annals of Nuclear Energy*, vol. 67, pp. 109–128, 2014. 23, 85, 109

[116] T. Schuller, S. Ducruix, D. Durox, and S. Candel, "Modeling tools for the prediction of premixed flame transfer functions," *Proceedings of the Combustion Institute*, vol. 29, no. 1, pp. 107–113, 2002. 24, 39

[117] S. H. Preetham and T. C. Lieuwen, "Response of turbulent premixed flames to harmonic acoustic forcing," *Proceedings of the Combustion Institute*, vol. 31, no. 1, pp. 1427–1434, 2007. 24

[118] A. Orchini and M. P. Juniper, "Linear stability and adjoint sensitivity analysis of thermoacoustic networks with premixed flames," *Combustion and Flame*, vol. 165, pp. 97–108, 2016. 24

[119] N. Noiray, D. Durox, T. Schuller, and S. Candel, "A unified framework for nonlinear combustion instability analysis based on the flame describing function," *Journal of Fluid Mechanics*, vol. 615, pp. 139–167, 2008. 24, 93, 136

[120] B. Ćosić, J. P. Moeck, and C. O. Paschereit, "Nonlinear instability analysis for partially premixed swirl flames," *Combustion Science and Technology*, vol. 186, no. 6, pp. 713–736, 2014. 24

[121] B. Schuermans, W. Polifke, and C. Paschereit, "Modeling transfer matrices of premixed flames and comparison with experimental results," *ASME, International Gas Turbine and Aeroengine Congress and Exhibition, Indianapolis*, no. 99-GT-132, V002T02A024, 1999. 24

[122] K. Truffin and T. Poinsot, "Comparison and extension of methods for acoustic identification of burners," *Combustion and Flame*, vol. 142, no. 4, pp. 388–400, 2005. 24, 117, 144

[123] R. Gaudron, M. Gatti, C. Mirat, and T. Schuller, "Impact of the acoustic forcing level on the transfer matrix of a turbulent swirling combustor with and without flame," *Flow, Turbulence and Combustion*, vol. 103, no. 3, pp. 751–771, 2019. 24

[124] C. J. Lapeyre, A. Misdariis, N. Cazard, D. Veynante, and T. Poinsot, "Training convolutional neural networks to estimate turbulent sub-grid scale reaction rates," *Combustion and Flame*, vol. 203, pp. 255–264, 2019. 24

[125] Y. Huang and V. Yang, "Effect of swirl on combustion dynamics in a lean-premixed swirl-stabilized combustor," *Proceedings of the Combustion Institute*, vol. 30, no. 2, pp. 1775–1782, 2005. 25

[126] S. Candel, D. Durox, T. Schuller, J.-F. Bourgouin, and J. P. Moeck, "Dynamics of swirling flames," *Annual Review of Fluid Mechanics*, vol. 46, pp. 147–173, 2014. 25, 27, 41, 42

[127] D. Durox, T. Schuller, and S. Candel, "Combustion dynamics of inverted conical flames," *Proceedings of the combustion Institute*, vol. 30, no. 2, pp. 1717–1724, 2005. 26, 31, 37, 81

[128] P. Palies, T. Schuller, D. Durox, and S. Candel, "Modeling of premixed swirling flames transfer functions," *Proceedings of the combustion institute*, vol. 33, no. 2, pp. 2967–2974, 2011. 26, 28, 45, 46, 47, 48, 83, 86, 87

[129] P. Palies, D. Durox, T. Schuller, and S. Candel, "Acoustic–convective mode conversion in an aerofoil cascade," *Journal of Fluid Mechanics*, vol. 672, pp. 545–569, 2011. 27, 41, 43, 61, 83, 138

[130] S. Wysocki, G. Di-Chiaro, and F. Biagioli, "Effect of fuel mixture fraction and velocity perturbations on the flame transfer function of swirl stabilized flames," *Combustion Theory and Modelling*, vol. 19, no. 6, pp. 714–743, 2015. 27

[131] X. Han and A. S. Morgans, "Simulation of the flame describing function of a turbulent premixed flame using an open-source LES solver," *Combustion and Flame*, vol. 162, no. 5, pp. 1778–1792, 2015. 27, 85

[132] R. Gaudron, M. Gatti, C. Mirat, and T. Schuller, "Impact of the injector size on the transfer functions of premixed laminar conical flames," *Combustion and Flame*, vol. 179, pp. 138–153, 2017. 29

[133] P. G. Mehta, M. Soteriou, and A. Banaszuk, "Impact of exothermicity on steady and linearized response of a premixed ducted flame," *Combustion and Flame*, vol. 141, no. 4, pp. 392–405, 2005. 29

[134] D. Durox, T. Schuller, N. Noiray, and S. Candel, "Experimental analysis of nonlinear flame transfer functions for different flame geometries," *Proceedings of the Combustion Institute*, vol. 32, no. 1, pp. 1391–1398, 2009. 29, 37, 39, 48

[135] A. P. Dowling, "Nonlinear self-excited oscillations of a ducted flame," *Journal of Fluid Mechanics*, vol. 346, pp. 271–290, 1997. 29, 31

[136] H. Tsien, "Servo-stabilization of combustion in rocket motors," *Journal of the American Rocket Society*, vol. 22, no. 5, pp. 256–262, 1952. 30

[137] H. Merk, "An analysis of unstable combustion of premixed gases," in *Symposium (International) on Combustion*, vol. 6, pp. 500–512, Elsevier, 1957. 30

[138] T. Sugimoto and Y. Matsui, "An experimental study on the dynamic behavior of premixed laminar flames," in *Symposium (International) on Combustion*, vol. 19, pp. 245–250, Elsevier, 1982. 30

[139] F. E. Marble and S. M. Candel, "An analytical study of the non-steady behavior of large combustors," in *Symposium (International) on Combustion*, vol. 17, pp. 761–769, Elsevier, 1979. 30

[140] L. Boyer and J. Quinard, "On the dynamics of anchored flames," *Combustion and Flame*, vol. 82, no. 1, pp. 51–65, 1990. 31, 33

[141] M. V. Subbaiah, "Nonsteady flame spreading in two-dimensional ducts," *AIAA Journal*, vol. 21, no. 11, pp. 1557–1564, 1983. 30

[142] G. Bloxsidge, A. Dowling, and P. Langhorne, "Reheat buzz: an acoustically coupled combustion instability. part 2. theory," *Journal of Fluid mechanics*, vol. 193, pp. 445–473, 1988. 30

[143] T. Schuller, D. Durox, and S. Candel, "A unified model for the prediction of laminar flame transfer functions: comparisons between conical and V-flame dynamics," *Combustion and Flame*, vol. 134, no. 1, pp. 21–34, 2003. 32, 35, 36, 38, 40, 48, 72

[144] R. Balachandran, B. Ayoola, C. Kaminski, A. Dowling, and E. Mastorakos, "Experimental investigation of the nonlinear response of turbulent premixed flames to imposed inlet velocity oscillations," *Combustion and Flame*, vol. 143, no. 1-2, pp. 37–55, 2005. 32, 81

[145] G. H. Markstein, *Nonsteady flame propagation: AGARDograph.* Elsevier, 1964. 32

[146] F. A. Williams, *Combustion Theory.* Benjamin Cummings, 1985. 32

[147] M. Fleifil, A. M. Annaswamy, Z. Ghoneim, and A. F. Ghoniem, "Response of a laminar premixed flame to flow oscillations: A kinematic model and thermoacoustic instability results," *Combustion and Flame*, vol. 106, no. 4, pp. 487–510, 1996. 34

[148] A. Dowling, "A kinematic model of a ducted flame," *Journal of Fluid Mechanics*, vol. 394, pp. 51–72, 1999. 34, 35, 36

[149] F. Baillot, D. Durox, and R. Prud'Homme, "Experimental and theoretical study of a premixed vibrating flame," *Combustion and Flame*, vol. 88, no. 2, pp. 149–168, 1992. 35

[150] F. Baillot, A. Bourehla, and D. Durox, "The characteristics method and cusped flame fronts," *Combustion Science and Technology*, vol. 112, no. 1, pp. 327–350, 1996. 35

[151] D. You, Y. Huang, and V. Yang, "A generalized model of acoustic response of turbulent premixed flame and its application to gas-turbine combustion instability analysis," *Combustion Science and Technology*, vol. 177, no. 5-6, pp. 1109–1150, 2005. 37

[152] H. Preetham, Santosh and T. Lieuwen, "Dynamics of laminar premixed flames forced by harmonic velocity disturbances," *Journal of Propulsion and Power*, vol. 24, no. 6, pp. 1390–1402, 2008. 37, 38, 40, 48

[153] A.-L. Birbaud, D. Durox, and S. Candel, "Upstream flow dynamics of a laminar premixed conical flame submitted to acoustic modulations," *Combustion and Flame*, vol. 146, no. 3, pp. 541–552, 2006. 39

[154] A. Cuquel, *Dynamics and nonlinear thermo-acoustic stability analysis of premixed conical flames*. PhD thesis, Châtenay-Malabry, Ecole centrale de Paris, 2013. 39, 48

[155] R. S. Blumenthal, P. Subramanian, R. Sujith, and W. Polifke, "Novel perspectives on the dynamics of premixed flames," *Combustion and Flame*, vol. 160, no. 7, pp. 1215–1224, 2013. 39, 40

[156] T. Steinbacher, A. Albayrak, A. Ghani, and W. Polifke, "Consequences of flame geometry for the acoustic response of premixed flames," *Combustion and Flame*, vol. 199, pp. 411–428, 2019. 40

[157] E. Æsøy, J. G. Aguilar, S. Wiseman, M. R. Bothien, N. A. Worth, and J. R. Dawson, "Scaling and prediction of transfer functions in lean premixed H2/CH4-flames," *Combustion and Flame*, vol. 215, pp. 269–282, 2020. 40

[158] S. Wang and V. Yang, "Unsteady flow evolution in swirl injectors with radial entry. II. external excitations," *Physics of Fluids*, vol. 17, no. 4, p. 045107, 2005. 41, 138

[159] N. Syred, "A review of oscillation mechanisms and the role of the precessing vortex core (PVC) in swirl combustion systems," *Progress in Energy and Combustion Science*, vol. 32, no. 2, pp. 93–161, 2006. 41, 201

[160] J. P. Moeck, J.-F. Bourgouin, D. Durox, T. Schuller, and S. Candel, "Nonlinear interaction between a precessing vortex core and acoustic oscillations in a turbulent swirling flame," *Combustion and Flame*, vol. 159, no. 8, pp. 2650–2668, 2012. 41

[161] N. Cumpsty and F. Marble, "The interaction of entropy fluctuations with turbine blade rows; a mechanism of turbojet engine noise," *Proceedings of the Royal Society of London. A. Mathematical and Physical Sciences*, vol. 357, no. 1690, pp. 323–344, 1977. 41

[162] M. Gatti, *Combustion dynamics of premixed swirling flames with different injectors*. PhD thesis, Université Paris-Saclay; Technische Universität Darmstadt (Allemagne), 2019. 43, 52, 55, 56, 72, 79, 83, 93, 94, 99, 100, 204

[163] P. Palies, T. Schuller, D. Durox, L. Gicquel, and S. Candel, "Acoustically perturbed turbulent premixed swirling flames," *Physics of Fluids*, vol. 23, no. 3, p. 037101, 2011. 44, 45, 72, 79

[164] N. A. Bunce, B. D. Quay, and D. A. Santavicca, "Interaction between swirl number fluctuations and vortex shedding in a single-nozzle turbulent swirling fully-premixed combustor," *Journal of Engineering for Gas Turbines and Power*, vol. 136, no. 02, p. 021503, 2014. 44, 45, 72

[165] S. Ishizuka, "Flame propagation along a vortex axis," *Progress in Energy and Combustion Science*, vol. 28, no. 6, pp. 477–542, 2002. 45

[166] Z. Han and S. Hochgreb, "The response of stratified swirling flames to acoustic forcing: Experiments and comparison to model," *Proceedings of the Combustion Institute*, vol. 35, no. 3, pp. 3309–3315, 2015. 46, 83

[167] W. Polifke and C. Lawn, "On the low-frequency limit of flame transfer functions," *Combustion and Flame*, vol. 151, no. 3, pp. 437–451, 2007. 47

[168] R. Gaudron, M. Gatti, C. Mirat, and T. Schuller, "Impact of the injector size on the transfer functions of premixed laminar conical flames," *Combustion and Flame*, vol. 179, pp. 138–153, 2017. 52

[169] M. Gatti, R. Gaudron, C. Mirat, L. Zimmer, and T. Schuller, "A comparison of the transfer functions and flow fields of flames with increasing swirl number," in *ASME Turbo Expo 2018*, no. GT2018-76105, V04BT04A003, American Society of Mechanical Engineers Digital Collection, 2018. 52, 55, 72

[170] M. Merk, R. Gaudron, M. Gatti, C. Mirat, W. Polifke, and T. Schuller, "Quantitative comparisons between LES predictions and experimental measurements of sound pressure spectra in a confined swirl combustor," in *53rd AIAA/SAE/ASEE Joint Propulsion Conference*, p. 4687, 2017. 52, 96

[171] M. Merk, W. Polifke, R. Gaudron, M. Gatti, C. Mirat, and T. Schuller, "Measurement and simulation of combustion noise and dynamics of a confined swirl flame," *AIAA Journal*, vol. 56, pp. 1930–1942, 2018. 52

[172] R. Gaudron, *Réponse acoustique de flammes prémélangées soumises à des ondes sonores harmoniques*. PhD thesis, Université Paris-Saclay, 2018. 52

[173] T. Schonfeld and M. Rudgyard, "Steady and unsteady flow simulations using the hybrid flow solver AVBP," *AIAA journal*, vol. 37, no. 11, pp. 1378–1385, 1999. 57

[174] O. Colin and M. Rudgyard, "Development of high-order taylor–galerkin schemes for LES," *Journal of Computational Physics*, vol. 162, no. 2, pp. 338–371, 2000. 57, 117

[175] T. J. Poinsot and S. Lele, "Boundary conditions for direct simulations of compressible viscous flows," *Journal of Computational Physics*, vol. 101, no. 1, pp. 104–129, 1992. 57

[176] E. N. Sieder and G. E. Tate, "Heat transfer and pressure drop of liquids in tubes," *Industrial & Engineering Chemistry*, vol. 28, no. 12, pp. 1429–1435, 1936. 58

[177] F. Nicoud, H. B. Toda, O. Cabrit, S. Bose, and J. Lee, "Using singular values to build a subgrid-scale model for large eddy simulations," *Physics of Fluids*, vol. 23, no. 8, p. 085106, 2011. 59, 117

[178] O. Colin, F. Ducros, D. Veynante, and T. Poinsot, "A thickened flame model for large eddy simulations of turbulent premixed combustion," *Physics of fluids*, vol. 12, no. 7, pp. 1843–1863, 2000. 59, 116

[179] B. Franzelli, E. Riber, L. Y. Gicquel, and T. Poinsot, "Large eddy simulation of combustion instabilities in a lean partially premixed swirled flame," *Combustion and Flame*, vol. 159, no. 2, pp. 621–637, 2012. 59

[180] F. Charlette, C. Meneveau, and D. Veynante, "A power-law flame wrinkling model for LES of premixed turbulent combustion part I: non-dynamic formulation and initial tests," *Combustion and Flame*, vol. 131, no. 1-2, pp. 159–180, 2002. 59

[181] G. Daviller, M. Brebion, P. Xavier, G. Staffelbach, J.-D. Müller, and T. Poinsot, "A mesh adaptation strategy to predict pressure losses in les of swirled flows," *Flow, Turbulence and Combustion*, vol. 99, no. 1, pp. 93–118, 2017. 59

[182] M. Brebion, *Joint numerical and experimental study of thermoacoustic instabilities*. PhD thesis, Institut National Polytechnique de Toulouse, 2017. 59

[183] C. Dobrzynski and P. Frey, "Anisotropic delaunay mesh adaptation for unsteady simulations," in *Proceedings of the 17th international Meshing Roundtable*, pp. 177–194, Springer, 2008. 59

[184] C. Dapogny, C. Dobrzynski, and P. Frey, "Three-dimensional adaptive domain remeshing, implicit domain meshing, and applications to free and moving boundary problems," *Journal of Computational Physics*, vol. 262, pp. 358–378, 2014. 59

[185] M. Howe, "On the theory of unsteady high reynolds number flow through a circular aperture," *Proceedings of the Royal Society of London. A. Mathematical and Physical Sciences*, vol. 366, no. 1725, pp. 205–223, 1979. 61, 114, 157

[186] M. Zahn, M. Schulze, C. Hirsch, M. Betz, and T. Sattelmayer, "Frequency domain predictions of acoustic wave propagation and losses in a swirl burner with linearized Navier-Stokes equations," in *ASME Turbo Expo 2015*, no. GT2015-42723, V04AT04A05, American Society of Mechanical Engineers Digital Collection, 2015. 61

[187] D. Bechert, "Sound absorption caused by vorticity shedding, demonstrated with a jet flow," *Journal of Sound and Vibration*, vol. 70, no. 3, pp. 389–405, 1980. 61

[188] M. S. Howe, *Acoustics of fluid-structure interactions*. Cambridge University Press, 1998. 61

[189] J. Herrin and J. Dutton, "An investigation of ldv velocity bias correction techniques for high-speed separated flows," *Experiments in Fluids*, vol. 15, no. 4-5, pp. 354–363, 1993. 64

[190] H. Najm, O. Knio, P. Paul, and P. Wyckoff, "A study of flame observables in premixed methane-air flames," *Combustion Science and Technology*, vol. 140, no. 1-6, pp. 369–403, 1998. 66

[191] L. Selle, F. Nicoud, and T. Poinsot, "Actual impedance of nonreflecting boundary conditions: Implications for computation of resonators," *AIAA journal*, vol. 42, no. 5, pp. 958–964, 2004. 70

[192] J. Jeong and F. Hussain, "On the identification of a vortex," *Journal of Fluid Mechanics*, vol. 285, pp. 69–94, 1995. 75

[193] D. Kim, J. G. Lee, B. D. Quay, D. Santavicca, K. Kim, and S. Srinivasan, "Effect of flame structure on the flame transfer function in a premixed gas turbine combustor," *Journal of Engineering for Gas Turbines and Power*, vol. 132, no. 02, p. 021502, 2010. 80

[194] T. Günther and H. Theisel, "The state of the art in vortex extraction," in *Computer Graphics Forum*, vol. 37, pp. 149–173, Wiley Online Library, 2018. 81

[195] U. Rist, "Visualization and tracking of vortices and shear layers in the late stages of boundary-layer laminar-turbulent transition," in *50th AIAA Aerospace Sciences Meeting including the New Horizons Forum and Aerospace Exposition*, p. 84, 2012. 81

[196] P. Palies, D. Durox, T. Schuller, and S. Candel, "Experimental study on the effect of swirler geometry and swirl number on flame describing functions," *Combustion Science and Technology*, vol. 183, no. 7, pp. 704–717, 2011. 83, 208

[197] A. Albayrak, M. P. Juniper, and W. Polifke, "Propagation speed of inertial waves in cylindrical swirling flows," *Journal of Fluid Mechanics*, vol. 879, pp. 85–120, 2019. 83, 208

[198] M. Hoeijmakers, V. Kornilov, I. L. Arteaga, P. de Goey, and H. Nijmeijer, "Intrinsic instability of flame–acoustic coupling," *Combustion and Flame*, vol. 161, no. 11, pp. 2860–2867, 2014. 88, 127

[199] G. Staffelbach, L. Gicquel, G. Boudier, and T. Poinsot, "Large eddy simulation of self excited azimuthal modes in annular combustors," *Proceedings of the Combustion Institute*, vol. 32, no. 2, pp. 2909–2916, 2009. 111, 114

[200] G. A. Mensah, G. Campa, and J. P. Moeck, "Efficient computation of thermoacoustic modes in industrial annular combustion chambers based on bloch-wave theory," *Journal of Engineering for Gas Turbines and Power*, vol. 138, no. 08, p. 081502, 2016. 111, 151

[201] L. Rayleigh, "XXXVII. on the passage of waves through apertures in plane screens, and allied problems," *The London, Edinburgh, and Dublin Philosophical Magazine and Journal of Science*, vol. 43, no. 263, pp. 259–272, 1897. 114, 157

[202] J. Kopitz, A. Huber, T. Sattelmayer, and W. Polifke, "Thermoacoustic stability analysis of an annular combustion chamber with acoustic low order modeling and validation against experiment," in *ASME Turbo Expo 2005*, no. GT2005-68797, pp. 583–593, American Society of Mechanical Engineers Digital Collection, 2005. 114

[203] N. A. Worth and J. R. Dawson, "Self-excited circumferential instabilities in a model annular gas turbine combustor: Global flame dynamics," *Proceedings of the Combustion Institute*, vol. 34, no. 2, pp. 3127–3134, 2013. 114

[204] J.-F. Bourgouin, D. Durox, J. Moeck, T. Schuller, and S. Candel, "A new pattern of instability observed in an annular combustor: The slanted mode," *Proceedings of the Combustion Institute*, vol. 35, no. 3, pp. 3237–3244, 2015. 114

[205] S. Mendez and F. Nicoud, "Adiabatic homogeneous model for flow around a multiperforated plate," *AIAA journal*, vol. 46, no. 10, pp. 2623–2633, 2008. 116, 157

[206] B. Franzelli, E. Riber, M. Sanjosé, and T. Poinsot, "A two-step chemical scheme for kerosene–air premixed flames," *Combustion and Flame*, vol. 157, no. 7, pp. 1364–1373, 2010. 116

[207] M. Boileau, S. Pascaud, E. Riber, B. Cuenot, L. Gicquel, T. Poinsot, and M. Cazalens, "Investigation of two-fluid methods for large eddy simulation of spray combustion in gas turbines," *Flow, Turbulence and Combustion*, vol. 80, no. 3, pp. 291–321, 2008. 117

[208] B. Abramzon and W. Sirignano, "Droplet vaporization model for spray combustion calculations," *International Journal of Heat and Mass Transfer*, vol. 32, no. 9, pp. 1605–1618, 1989. 117

[209] C. T. Crowe, J. D. Schwarzkopf, M. Sommerfeld, and Y. Tsuji, *Multiphase flows with droplets and particles*. CRC press, 2011. 117

[210] M. Sanjosé, J. Senoner, F. Jaegle, B. Cuenot, S. Moreau, and T. Poinsot, "Fuel injection model for euler–euler and euler–lagrange large-eddy simulations of an evaporating spray inside an aeronautical combustor," *International Journal of Multiphase Flow*, vol. 37, no. 5, pp. 514–529, 2011. 117

[211] F. Ni, *Accounting for complex flow-acoustic interactions in a 3D thermo-acoustic Helmholtz solver*. PhD thesis, Institut National Polytechnique de Toulouse, 2017. 118, 137, 215

[212] F. Lacombe and Y. Méry, "Mixed acoustic-entropy combustion instabilities in a model aeronautical combustor: Large eddy simulation and reduced order modeling," *Journal of Engineering for Gas Turbines and Power*, vol. 140, no. 3, p. 031506, 2018. 132

[213] F. Boudy, D. Durox, T. Schuller, G. Jomaas, and S. Candel, "Describing function analysis of limit cycles in a multiple flame combustor," *Journal of Engineering for Gas Turbines and Power*, vol. 133, no. 06, p. 061502, 2011. 137

[214] C. Mirat, D. Durox, and T. Schuller, "Stability analysis of a swirl spray combustor based on flame describing function," *Proceedings of the Combustion Institute*, vol. 35, no. 3, pp. 3291–3298, 2015. 137

[215] S. Hochgreb, D. Dennis, I. Ayranci, W. Bainbridge, and S. Cant, "Forced and self-excited instabilities from lean premixed, liquid-fuelled aeroengine injectors at high pressures and temperatures," in *ASME Turbo Expo 2013*, no. GT2013-95311, V01BT04A023, American Society of Mechanical Engineers Digital Collection, 2013. 137

[216] C. Paschereit, B. Schuermans, W. Polifke, and O. Mattson, "Measurement of transfer matrices and source terms of premixed flames," *Journal of Engineering and Gas Turbines Power*, vol. 124, no. 2, pp. 239–247, 2002. 137

[217] C. Sohn, S. Chung, J. Kim, and F. Williams, "Acoustic response of droplet flames to pressure oscillations," *AIAA journal*, vol. 34, no. 9, pp. 1847–1854, 1996. 141

[218] J. Ching and Y.-C. Chen, "Transitional Markov chain Monte Carlo method for Bayesian model updating, model class selection, and model averaging," *Journal of Engineering Mechanics*, vol. 133, no. 7, pp. 816–832, 2007. 150

[219] J. Eckstein and T. Sattelmayer, "Low-order modeling of low-frequency combustion instabilities in aeroengines," *Journal of Propulsion and Power*, vol. 22, no. 2, pp. 425–432, 2006. 150

[220] F. Ni, M. Miguel-Brebion, F. Nicoud, and T. Poinsot, "Accounting for acoustic damping in a Helmholtz solver," *AIAA Journal*, pp. 1205–1220, 2016. 151

[221] N. Lamarque and T. Poinsot, "Boundary conditions for acoustic eigenmodes computation in gas turbine combustion chambers," *AIAA journal*, vol. 46, no. 9, pp. 2282–2292, 2008. 151

[222] U. Ingard and H. Ising, "Acoustic nonlinearity of an orifice," *The Journal of the Acoustical Society of America*, vol. 42, no. 1, pp. 6–17, 1967. 157

[223] T. H. Melling, "The acoustic impendance of perforates at medium and high sound pressure levels," *Journal of Sound and Vibration*, vol. 29, no. 1, pp. 1–65, 1973. 157

[224] X. Jing and X. Sun, "Effect of plate thickness on impedance of perforated plates with bias flow," *AIAA journal*, vol. 38, no. 9, pp. 1573–1578, 2000. 157

[225] C. Ji and D. Zhao, "Lattice Boltzmann investigation of acoustic damping mechanism and performance of an in-duct circular orifice," *The Journal of the Acoustical Society of America*, vol. 135, no. 6, pp. 3243–3251, 2014. 157

[226] X. Jing, X. Sun, J. Wu, and K. Meng, "Effect of grazing flow on the acoustic impedance of an orifice," *AIAA journal*, vol. 39, no. 8, pp. 1478–1484, 2001. 159

[227] T. Lu and C. K. Law, "Toward accommodating realistic fuel chemistry in large-scale computations," *Progress in Energy and Combustion Science*, vol. 35, no. 2, pp. 192–215, 2009. 194

[228] B. Rochette, F. Collin-Bastiani, L. Gicquel, O. Vermorel, D. Veynante, and T. Poinsot, "Influence of chemical schemes, numerical method and dynamic turbulent combustion modeling on LES of premixed turbulent flames," *Combustion and Flame*, vol. 191, pp. 417–430, 2018. 201

Appendices

Appendix A

Navier-Stokes equations for reacting flows

Navier-Stokes equations for multi-species reacting flows are here recalled. The index notation and Einstein's rule of summation are used. Indices i and j are reserved for spatial variables while index k is reserved for species. Equations are presented for an ideal gas mixture composed of $k = 1, ..., N$ species.

Conservation of mass

The global mass balance is:

$$\frac{\partial \rho}{\partial t} + \frac{\partial}{\partial x_i}\rho u_i = 0 \tag{A.1}$$

with ρ the density and u_i the i$^{\text{th}}$ velocity component. It is obtained by summation of mass conservation equations for each species k:

$$\frac{\partial}{\partial t}\rho Y_k + \frac{\partial}{\partial x_i}\rho Y_k u_i = -\frac{\partial}{\partial x_i}J_{ik} + \dot{\omega}_k \tag{A.2}$$

with Y_k the mass fraction of species k, J_{ik} the species diffusive flux and $\dot{\omega}_k$ the source term for species k. The species diffusion flux J_{ik} is modelled with the Hirschfelder Curtis approximation:

$$J_{ik} = -\rho\left(D_k\frac{W_k}{W}\frac{\partial X_k}{\partial x_i} - Y_k V_i^c\right) \tag{A.3}$$

where D_k is the diffusivity of species k, W_k its molecular weight, and $X_k = Y_k W/W_k$ its molar fraction. The mean molecular weight is W defined by:

$$\frac{1}{W} = \sum_{k=1}^{N}\frac{Y_k}{W_k} \tag{A.4}$$

The correction velocity V_i^c ensures mass conservation:

$$V_i^c = \sum_{k=1}^{n} D_k\frac{W_k}{W}\frac{\partial X_k}{\partial x_i} \tag{A.5}$$

Species source terms $\dot{\omega}_k$ appearing in the RHS of Eq. (A.2) need to be modelled. In CFD simulations, these source terms are provided by chemical schemes made of series of elementary (or global) reactions, calibrated with appropriate reaction rates depending

on temperature and/or pressure using standard Arrhenius laws. Further details regarding chemistry modelling can be found in [13]. One may use either detailed chemistry, globally reduced chemistry or analytically reduced chemistry depending on the accuracy sought and the available computational resources. A review of chemical schemes is available in [227].

Conservation of momentum

The momentum conservation equation reads:

$$\frac{\partial}{\partial t}\rho u_j + \frac{\partial}{\partial x_i}\rho u_i u_j = -\frac{\partial p}{\partial x_j} + \frac{\partial \tau_{ij}}{\partial x_i} + \rho f_j \tag{A.6}$$

with p the pressure, f_j the volume force acting in direction j and τ_{ij} the viscous stress tensor defined for a newtonian fluid using Stokes' hypothesis by:

$$\tau_{ij} = -\frac{2}{3}\mu\frac{\partial u_l}{\partial x_l}\delta_{i,j} + \mu\left(\frac{\partial u_i}{\partial x_j} + \frac{\partial u_j}{\partial x_i}\right) \tag{A.7}$$

where μ is the dynamic viscosity and δ_{ij} is the Kronecker symbol: $\delta_{ij} = 1$ if $i = j$, 0 otherwise.

Conservation of energy

Multiple forms of energy equations can be written from different quantities. Here the total non chemical energy E, defined as the sum of sensible and kinetic energy is used, with volume forces neglected:

$$\frac{\partial}{\partial t}\rho E + \frac{\partial}{\partial x_i}\rho u_i E = \dot{\omega}_T - \frac{\partial q_i}{\partial x_i} - \frac{\partial}{\partial x_j}u_i\left(p\delta_{ij} - \tau_{ij}\right) + \dot{\mathrm{Q}} \tag{A.8}$$

with $\dot{\mathrm{Q}}$ the external heat source term (energy provided by an electric spark, a laser or a radiative flux for example) and q_i the energy flux defined by:

$$q_i = -\lambda\frac{\partial}{\partial x_T}x_i + \rho\sum_{k=1}^{N} J_{i,k}h_{s,k} \tag{A.9}$$

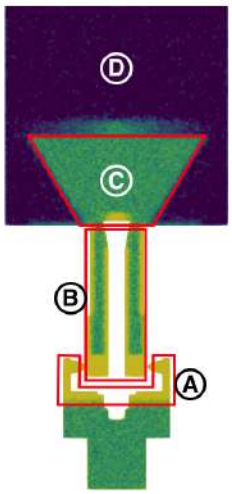
For a given species k, the associated specific enthalpy is noted h_k, its specific sensible enthalpy is noted $h_{s,k}$ and its formation enthalpy is noted $\Delta h^0_{f,k}$. The energy flux is the sum of a heat diffusion term modelled by Fourier's law and a diffusion term for species. Finally, $\dot{\omega}_T$ is the heat release source term generated by combustion defined as the sum of chemical mass reaction rates $\dot{\omega}_k$:

$$\dot{\omega}_T = -\sum_{k=1}^{N}\Delta h^0_{f,k}\dot{\omega}_k \tag{A.10}$$

Appendix B

NoiseDyn configuration mesh convergence study

A study was performed to assess mesh invariance based on meshes $M3$ and $M4$ presented in section 3.3 in the core manuscript. Main geometric dimensions of the two meshes are reminded in Fig. B.1.



(a)

Mesh id.	**M3**	**M4**
N_{cells} (Millions)	19.1	55.8
Δ_x (A) (mm)	0.25	0.16
Δ_x (B) (mm)	0.29	0.2
Δ_x (C) (mm)	0.48	0.26
Δ_x (D) (mm)	1.0	1.0

(b)

Figure B.1: Main topologic regions, and associated characteristic cell sizes in each zone meshes M3 and M4.

The goal here was to compare the automatic mesh refinement process used to obtain $M3$ to what a more traditional "human made" refinement of the original mesh $M1$ would provide. Characteristic cell sizes in the swirler, injector and flames regions were therefore divided by 2 compared to the baseline mesh $M1$. Compared to $M3$, $M4$ is overall more refined in the swirler, injector, and especially flame regions, Fig. B.2. However, it is worth noting that the automatic refinement yielded comparable or smaller cell sizes in specific regions of the mesh like around the injector exit edges or in the swirler passage vanes. A total of 80 ms and 54 ms have been simulated for M3 and M4 respectively. Small improvements regarding dimensionless wall distances y^+ are observed, Fig. B.3 which could potentially yield different flow fields and need investigation. The probed pressure drop is $\Delta P = 367.3$ Pa, which yields a 9.6% error compared to the experiment, a higher value than when using $M3$ (2%). This puts emphasis on how the pressure drop

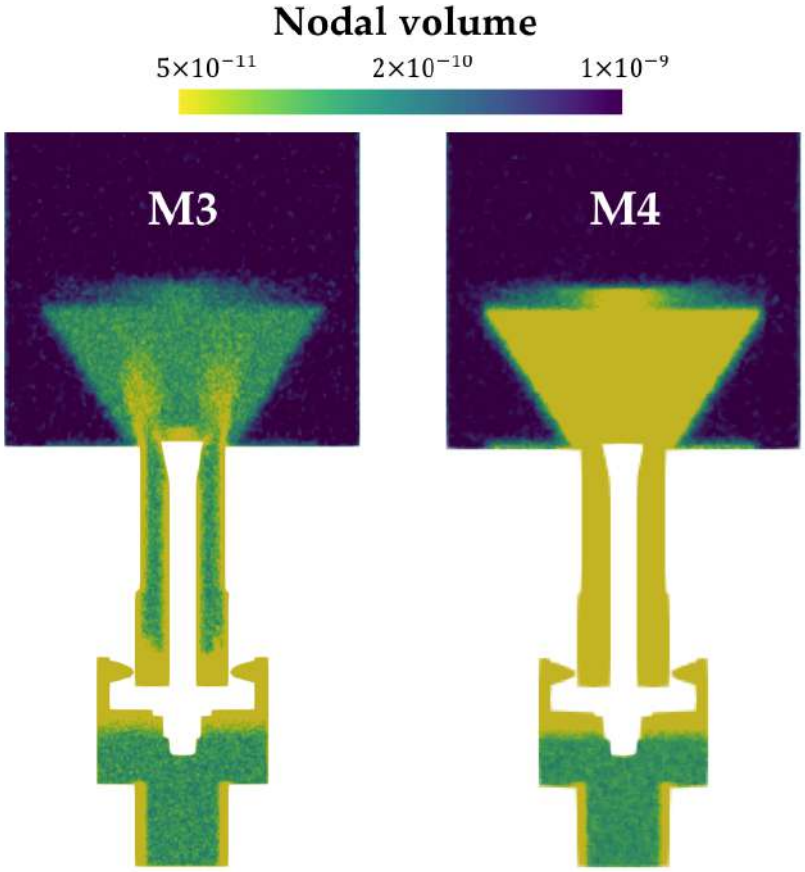


Figure B.2: Comparison of meshes M3 and M4 nodal volumes

across the swirler is conditioned by local small zones like the swirler passage vanes, which have been identified as critical and refined when creating mesh $M3$. Velocity

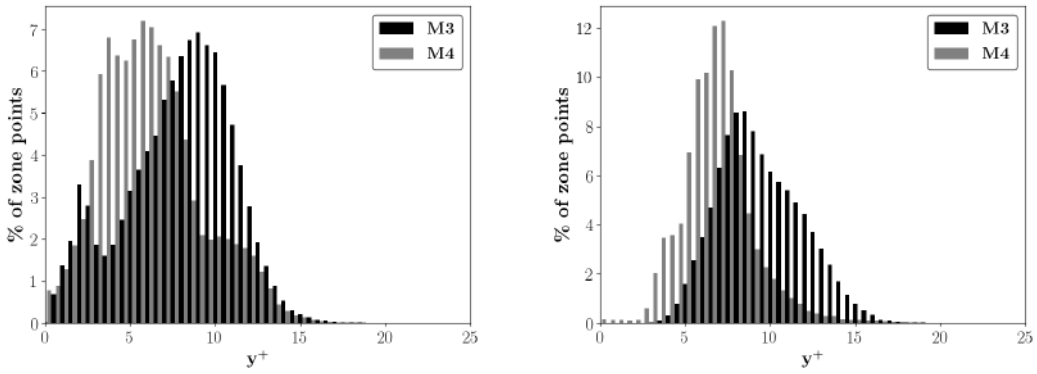


Figure B.3: Repartition of dimensionless distance y^+ for zones A (left) and B (right) as presented in B.1.

profiles for meshes $M3$ and $M4$ are compared to PIV data for various axial positions in Fig. B.4. There is almost no distinguishable difference between the two meshes for

mean axial and radial velocities close to the injector. For higher axial positions, only minor differences are observed around $r/R_0 = 2$, with higher velocities for $M4$. For RMS velocities, $M3$ yields higher local peaks compared to $M4$ but the overall profiles remain very similar.

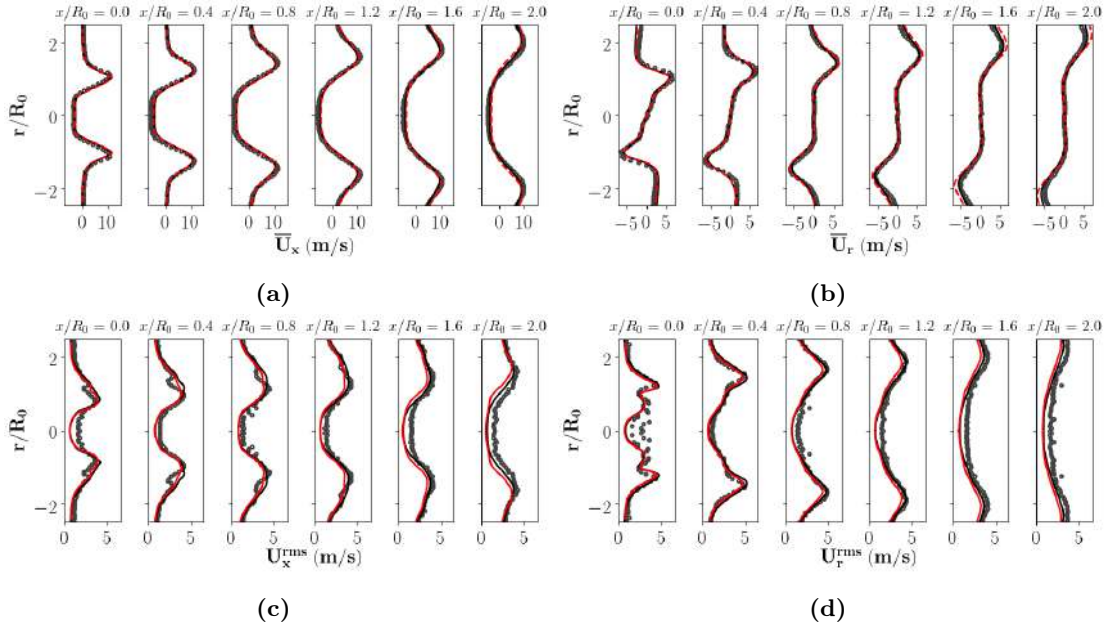


Figure B.4: Comparison of reactive flow mean axial (a), mean radial (b), RMS axial (c) and RMS radial (d) velocity profiles for various axial locations ((o) is Exp., — M3, —is M4). $x/R_0 = 0$ corresponds to the bottom of PIV data, that is 3.5 mm above the combustion chamber backplane.

These minor differences can also be seen on the flame position (Fig. B.5). The repartition of the volumetric heat release rate obtained on the refined mesh is more homogeneous. Still, flame shapes and the opening angle are similar. Secondary branches are present in both cases. These observations are a result of the change in the flame thickening that is directly linked to the reduction of the characteristic cell size Δ_x in the flame zone. Dividing Δ_x by two results in half of the thickening obtained on $M3$. As a result, the flame brush differs between the two meshes since thickened flames are less sensitive to local wrinkling phenomena. This is further emphasized by looking at heat release rate profiles for various axial locations B.6. While the flame brush at the base of the flame is larger for $M4$, it becomes thinner than $M3$ for higher axial positions. The mean flame barycenter has been slightly moved upwards, but not in a meaningful manner. This could be expected when using DTFLES and overall, profiles for $M3$ and $M4$ are once again very similar. Finally, when compared to $M3$, the computational time needed to achieve the same simulated physical time on $M4$ is multiplied by 2.5, while the flow field and the flame do not differ significantly. From all these observations, is it

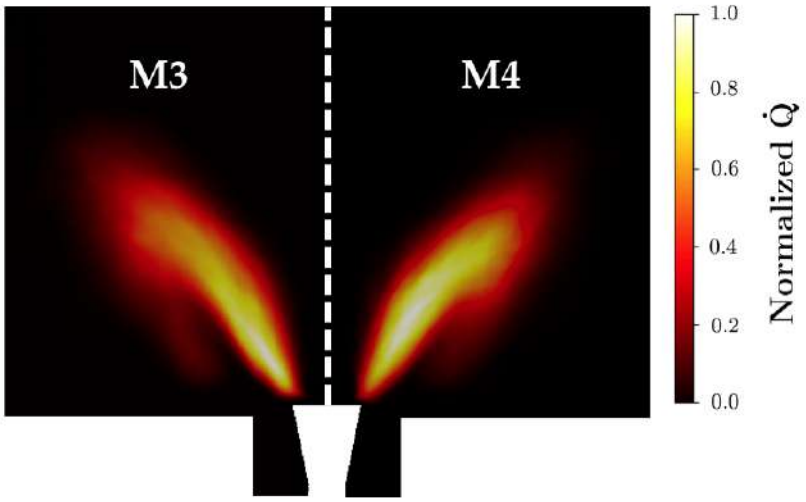


Figure B.5: Visualization of the mean flame for meshes M3 and M4 from an azimuthal average of the normalized volumetric heat release rate. Normalization is performed using the maximum obtained on mesh M4.

s

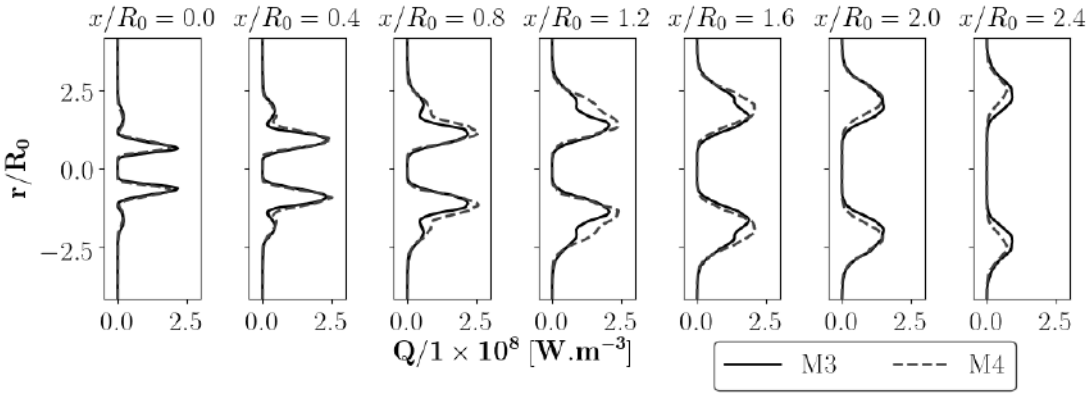


Figure B.6: Comparison of heat release rate profiles for various axial locations ((o) is Exp., — is M3, —is M4). $x/R_0 = 0$ corresponds to the bottom of PIV data, that is 3.5 mm above the combustion chamber backplane.

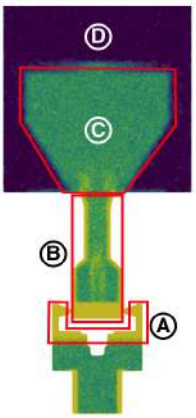
is concluded that mesh convergence had not been fully reached but that the remaining possible differences are too minor to be meaningful.

Appendix C

Study of the Noisedyn aerodynamically swirled stabilized flame

Following studies made on bluff-body stabilized flames for the Noisedyn injector, an additional study is performed on a configuration where the bluff-body has been removed so that the flame is aerodynamically stabilized, Fig. 3.4b. This configuration was investigated by Gatti *et al.* in [108] All metallic spacers are used so that $\delta_1 = 16$ mm. for a total injector length $\delta = 50$ mm. Without the stabilizing rod, the flame is harder to stabilize and more prone to flame flashback for high acoustic forcing as its vertical motion is more pronounced during a forcing cycle. The injector diameter is dropped down to 12 mm, with a 15° opening angle at the injector exit edges to facilitate the anchoring process. Doing so, the flame is anchored few millimeters above the chamber backplane and still has a classical V shape as illustrated in Fig. C.2a with an Abel transform of OH^* signals from a photomultiplier applied on the left and right sides of flame images.

The geometrical changes led to the conception of a new mesh $ML1$ refined in the swirler and injector regions, and with a wider refined flame zone compared to the previous cases since the flame is expected to be higher/larger according to Fig. C.2a. This mesh was subjected to an automatic mesh refinement using the LIKE criterion of Eq. (3.3), which ended up refining the shear layer in the wake of the injector exit walls, Fig. C.1. The final mesh $ML2$ is used for all results presented in the following section. The numerical setup is almost identical to the ones described in Sec.3.3.1 . In particular, temperature profiles have not been altered although they may be different due to the new flame dimensions. Wall temperatures are extremely important when it comes to the flame stabilization mechanisms as stated in [61] for a similar confined swirl burner. A brief study of the impact of the chamber wall heat resistance R_{cw} and chamber backplane heat resistance R_{cb} was performed, by allowing a variation to the real value denoted as R_x^{ref}. Resulting flame shapes shown in Fig. C.2 indicate that the flame stabilization position is indeed very dependent on the imposed thermal conditions. When high thermal resistances are applied to the chamber walls, the flame is not able to exchange a lot of heat with its surrounding so that even regions close to the cold



(a)

Mesh id.	ML1	ML2
N_{cells} (Millions)	18.0	19.8
Δ_x (A) (mm)	0.31	0.30
Δ_x (B) (mm)	0.40	0.33
Δ_x (C) (mm)	0.52	0.51
Δ_x (D) (mm)	1.0	1.0

(b)

Figure C.1: Cut of mesh ML1 with main topological regions, and associated characteristic cell sizes in each zone for all meshes.

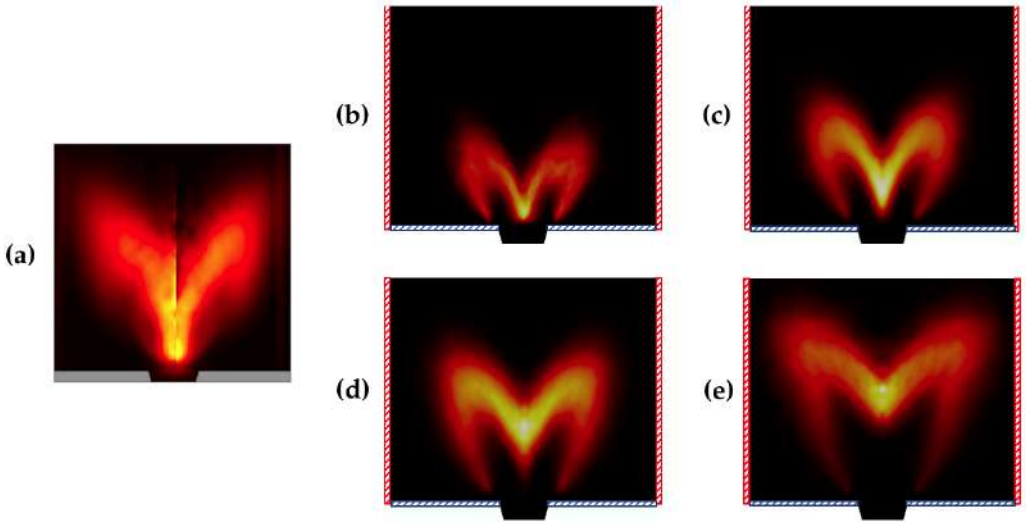
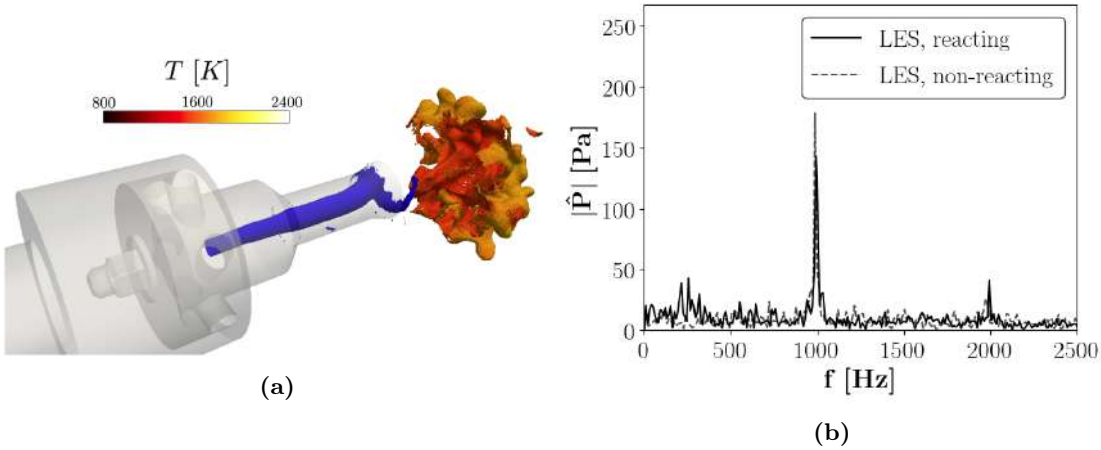


Figure C.2: (a) Flame visualization as obtained from an Abel transform of OH* signals from a CCD camera with a narrowband filter centered around 310 nm for the aerodynamically stabilized case [108]. LES stabilized flame heat release rate obtained from time and azimuthal average for $\mathbf{R_{cw}/R_{cw}^{ref} = 10}$, $\mathbf{R_{cb}/R_{cb}^{ref} = 10}$ (b), $\mathbf{R_{cw}/R_{cw}^{ref} = 5}$, $\mathbf{R_{cb}/R_{cb}^{ref} = 5}$ (c), $\mathbf{R_{cw}/R_{cw}^{ref} = 10}$, $\mathbf{R_5/R_{cb}^{ref} = 1}$ (d) and $\mathbf{R_{cw}/R_{cw}^{ref} = 1}$, $\mathbf{R_{cb}/R_{cb}^{ref} = 1}$ (e).

injection feed are quickly heated up by the burnt gas. As a result the flame stabilizes close to the chamber backplane. If perfectly adiabatic walls were used, the flame would be attached to the chamber backplane wall. Reducing these resistances, the flame loses more heat and gradually elevates in the axial direction, while the flame angle α diminishes. When using the real values, Fig. C.2 (e), the mean flame is stabilized high in the chamber. Noting $R_0 = 7.6$ mm the injector radius at its exit plane, the distance



(a) **(b)**

Figure C.3: (a) Visualization of the PVC at f = 1000 Hz using an isocontour of pressure at P = 0.95P_{atm} in blue, along with an isocontour of heat release rate Q = 10^8 W.m^{-3} coloured by temperature. (b) FFT of pressure for a probe in the middle of the injector exit plane for both non-reacting/reacting cases.

from the core heat release location to the chamber backplane is $\delta_{lift} = 4.26R_0$. Note that lowering only R_{cw} from $5 \times R_{cw}^{ref}$ to R_{cw}^{ref} has the most notable influence on the flame stabilization region because the outer recirculation zones are heavily affected by the burnt gas ability to cool the quartz enclosing walls. In all considered numerical simulations, the stable flame has non negligible secondary branches, making it M-shaped instead of the expected V-shape. This may be explained by the lack of verified temperature data on the wall. Also, the two-step chemistry used here may not be able to accurately represent the response of the flame to high strain rates and force secondary branches to appear in the low strain region [228]. Considering the mean experimental flame position, it was decided to stick with $R_{cw}/R_{cw}^{ref} = 5$ and $R_{cb}/R_{cb}^{ref} = 5$ since these conditions led to the flame stabilization region closest to the experiment.

Under cold flow conditions, the measured pressure drop is $\Delta P = 742$ Pa, a value very close to the 720 Pa measured in the experiments. The swirler still is the radial one presented in Fig. 3.3, and hence, the LES measured swirl number remains unchanged: $S = 0.73$. Compared to previous geometries, the removal of the bluff-body is responsible for the apparition of a strong Precessing Vortex Core (PVC) with a frequency $f_{PVC} = 1000$ Hz, as often observed for such swirling flows [159]. This robust helical structure is observed for both non-reacting and reacting flows. Its frequency is only marginally affected by the presence of the flame, while its strength is reduced under reacting conditions as indicated by the pressure FFT on a probe in the middle of the injection exit plane, Fig. C.3b. A dynamic mode decomposition analysis on the 3D pressure field also confirms that $f_{PVC} = 1000$ Hz and identifies the hydrodynamic helical mode's origin as the last quarter part of the injection channel.

Reacting pulsed simulations are run for frequencies $f_1 = 120$ Hz and $f_2 = 180$ Hz corresponding to local FTF gain minima for the bluff-body stabilized flame presented in sec. 3.4.3. Once again the goal here is to validate the LES capability to represent pulsed flame dynamics and to extract parameters used as inputs for the SFTF model. After eight forcing periods, the gain and phase are evaluated for the two frequencies, yielding results presented in Fig. C.4. The experimental FTF reveals that the forced

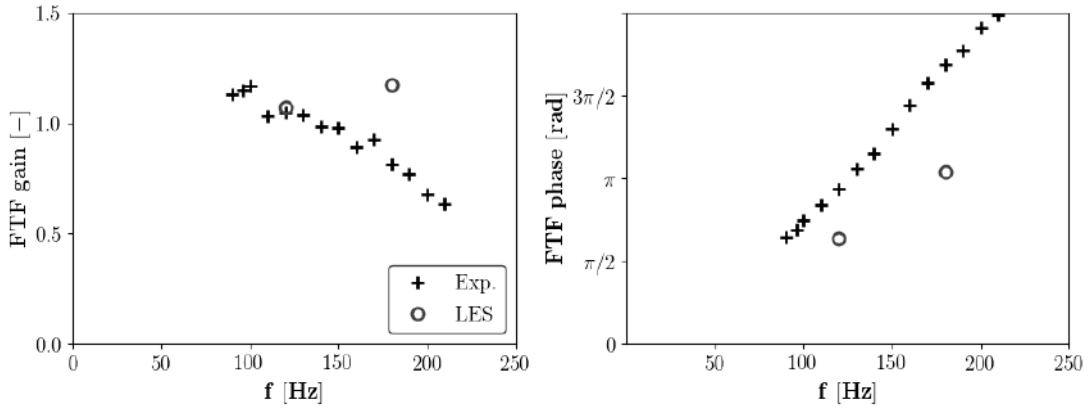


Figure C.4: FTF of the Noisedyn configuration without bluff-body as obtained from pulsed LES and experiments.

flame response is very different from the ones presented in Fig 3.48 for which the flame is stabilized on a metallic rod. When removing this central piece, the classical gain curve of a laminar V-shaped flame is retrieved with an initial increase of the gain followed by a gradual decay for high frequencies. There are no alternating regions of low and high FTF gain. Besides, the FTF phase is fully linear for the studied frequency range, with no inflection as seen previously. The agreement between experiments and LES data is moderate at best for the two studied frequencies. In particular, the gain obtained from LES for $f = 180$ Hz largely overestimates the real value. The phase slope predicted from the two evaluated phase is also off from the expected value. This can be attributed to the uncertainties on thermal boundary conditions and as such on the flame stabilization mechanism.

Still, LES are used to extract SFTF model parameters in an attempt to judge how simulation results translate for the semi-analytical model when predictions are not in full agreement with reality (experiments here). Note also that as pointed out in [108], the flame leading edge point undergoes a large axial movement during a forcing cycle and is not fixed as it was assumed for the SFTF model derivation.

LES of the unforced flame are ran for a total of 90 ms which corresponds to approximately 10.5 inlet to injector backplane flow through times. Flame dimensions are then determined from temporal and azimuthally averaged fields using Eq. (3.6) and the

lowest point in the axial direction where the heat release rate Q is superior to at least 1% of its maximum value.

For the specific configuration of this section, one gets : $R_f/R_0 = 2.02$, $L_f/R_0 = 3.69$, $H_f/R_0 = 3.09$ with $R_0 = 7.6$ mm the radius of the injection exit plane cross-section. The resulting half flame angle is $\alpha = 33.2°$. The mean axial velocity at the injector exit plane $U_0 = 11.4$ m.s^{-1} is measured from the stationary unperturbed LES to complete the analysis and corresponds to the expected bulk velocity from mass conservation. Combining the obtained flame dimensions and bulk velocity yields the reduced frequency $\omega_*/\omega = 2.94$ ms.

The velocity of vortical disturbances is evaluated using the I_2 criterion from Eq .(3.7) and probed as $U_{c-v} = 3.63$ m.s^{-1} which is much lower than the value obtained when a bluff-body is used to stabilize the flame ($U_{c-v} = 6.46$). This yields $K = U_0/U_{c-v} = 3.14$. The time delay between acoustic and convective perturbations is computed from Eq. (3.9) as $\tau = 4.24$ ms.

The SFTF methodology is applied once again to determine ϕ_0, the phase between bulk and edge velocities at the injector exit plane. Using phase averaged data for $f = 180$ Hz and Eq. (3.13) yields $\phi_0 = -0.11$ rad. The corresponding signals are plotted in Fig. 3.53. Note that the level of noise for the probe signals are quite high in this aerodynamically stabilized simulation so that the uncertainties on this parameter may be high. Finally, a cold flow pulsed simulation for $f = 180$ Hz is performed in order to

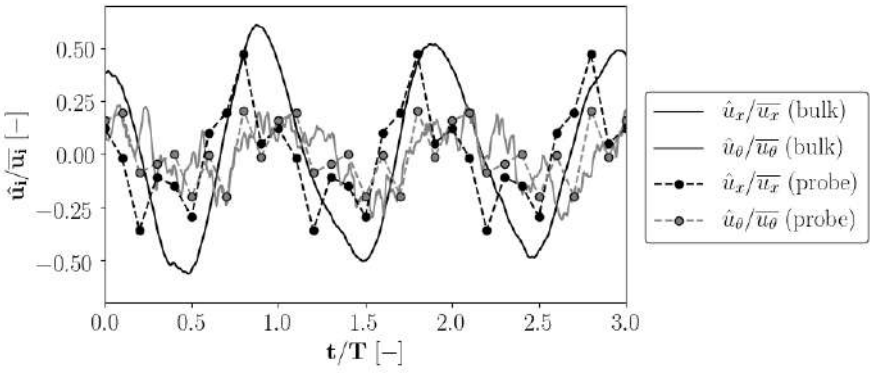


Figure C.5: Normalized axial and tangential velocity signals on the injector exit plane (bulk, solid line) and a probe 0.5 mm away from the outer injector wall (dashed line with markers) for f = 180 Hz, $\phi_0 = -0.11$ rad.

extract the decay rate of axial velocity disturbances β. Results from Fig. C.6 provide a decay rate parameter $\beta = 0.161$. This value is of the same order of magnitude as the one found for the bluff-body stabilized configuration with a 50 mm long injector ($\beta = 0.184$), which was expected since the chamber geometry itself has not been changed.

Table C.1 presents parameters as obtained from the three fidelity levels SFTF1, SFTF2 and SFTF3 for the current NoiseDyn configuration where the flame is aerody-

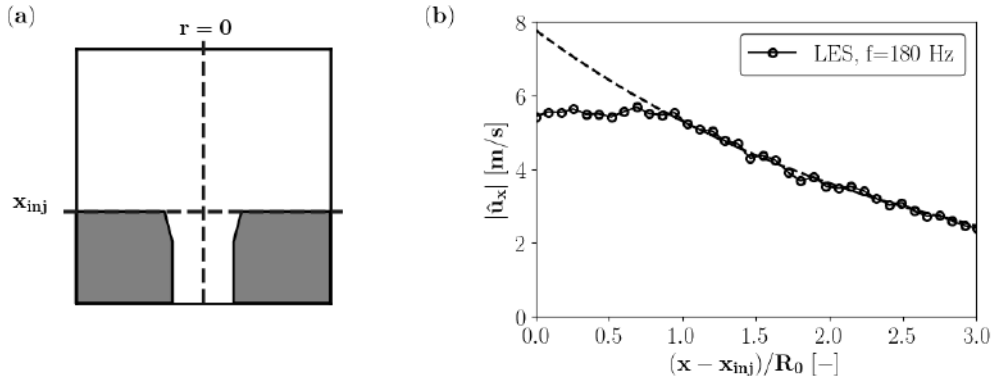


Figure C.6: (a) Schematic of the central line located at $r/R_0 = 0$ used for the amplitude decay evaluation. (b) Acoustic velocity amplitudes for f = 180 Hz on the same line, starting from the injector exit plane. Dotted lines show the best fit for each frequency in the form $Ae^{-\gamma x}$.

namically stabilized. When only a stationary flame LES is used, SFTF1, χ is chosen as null since various publications have shown that swirled FTF only show alternating low and high gain region only if a flame is swirling and attached on a bluff body [162].

Table C.1: SFTF parameters for the aerodynamically stabilized case as determined from accuracy levels SFTF1, SFTF2 and SFTF3. For SFTF2 and SFTF3, χ was determined from an optimization on the experimental FTF value for f = 180 Hz.

Case	ω_*/ω [ms]	α [deg]	K	χ	τ [ms]	ϕ_0 [rad]
(a) SFTF1	15.3	33.2	3.14	−0.0	4.24	0.0
(b) SFTF2	15.3	33.2	3.14	−0.23	4.24	−0.11
(c) SFTF3	15.3	33.2	$3.14 + 0.51i$	0.18	4.24	−0.11

The associated FTF predictions are shown in Fig. C.7 for the three SFTF levels.

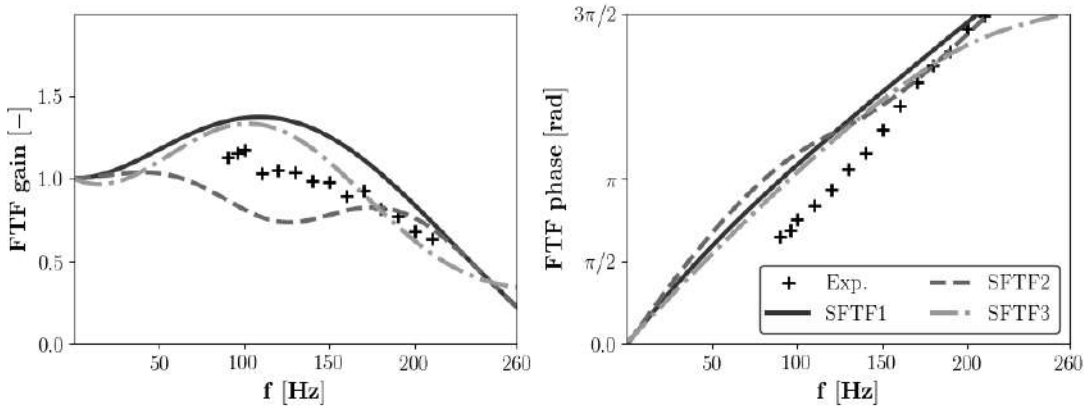


Figure C.7: SFTF model results with parameters presented in Tab. C.1 for the three levels of accuracy SFTF1, SFTF2 and SFTF3.

The FTF obtained from SFTF1 shows an initial increase in the gain response as expected from experimental data but overpredicts the local maximum value. The introduction of a non null phase ϕ_0 for SFTF2 has almost no impact on the FTF shape. On the contrary, optimizing χ using experimental gain and phase for $f = 180$ Hz greatly affects the gain curve. Here the optimization strategy tends to show its limits since the overall gain and phase curves agreement with the experiment is not improved compared to SFTF1. Including the velocity disturbances spatial decay with SFTF3, the agreement improves for the FTF gain where the correct decrease with frequency is retrieved.

Overall, the SFTF model does not provide a good agreement with reference data for this configuration featuring a swirling aerodynamically stabilized flame. Regardless of the SFTF model accuracy level, a mismatch is seen between modelled and experimentally measured phase curves. For the SFTF model, the slope of the phase curve is controlled by parameters ω_* and α that depend on the flame length and flame radius. Due to the lack of thermal data in this case, the LES predicts an M-shaped flame and thus, flame dimensions may be very different from the intended values. In addition, a linear fit of the experimental FTF phase value yield a phase $\phi = -\pi/2$ in the low frequency limit. Such value cannot be obtained considering the low phase lag $\phi_0 = -0.11$ that was probed on noisy LES data. Another important point lies in the fact that the SFTF model is not designed to cope with large variations of the flame leading edge point, which is the case for the present configuration [108].

Further studies or experimental data are therefore needed to achieve a finer representation of the flame anchoring and acoustic response.

Appendix D

Extended SFTF model sensitivity analysis

The sensitivity analysis carried out in Sec. 3.6.3 details the combined effect of allowing a deviation ϵ on all or a set of three SFTF model parameters for the Noisedyn bluff-body stabilized flame. Here the focus is made on assessing the effect of uncertainties of each individual parameter independently to emphasize its main effect on the predicted flame acoustic response.

The notations of Sec. 3.6.3 are used. For each model parameter $\mathcal{P}$, the interval $[\mathcal{P} \times (1-\epsilon), \mathcal{P} \times (1+\epsilon)]$ is discretized using $n_t = 501$ values for four deviation values ϵ : 5%, 10%, 25% and 50%. Figures D.1 to D.7 present obtained uncertainty envelopes for each model parameter. The particular influence of uncertainties on the evaluation of each parameter is discussed hereafter :

- $\boldsymbol{\omega_*}$, (Fig. D.1): Increasing the deviation ϵ only affects the FTF gain near the first local minimum at $f = 120$ Hz while other frequencies remain very close to the reference case. Large variations of the phase are observed when modifying this parameter.

- $\boldsymbol{\alpha}$, (Fig. D.2): In the present case deviations of this parameter do not induce large variations of FTF gain and phase. However the determination of this parameter is tied to flame dimensions as is the determination of ω_*. For this reason, larger discrepancies on the final FTF are to be expected when modifying LES probed flame dimensions.

- $\mathbf{K}$, (Fig. D.3): The effect of this parameter is the same as the one of α. Its evaluation requires the identification of a shear layer, which may introduce difficulties for strongly turbulent configurations.

- $\boldsymbol{\tau}$, (Fig. D.4): Uncertainties on this parameter need to be mastered as it controls the position of local gain extrema. Hence even with an uncertainty $\epsilon = 10\%$, very different results could be obtained.

- $\boldsymbol{\chi}$, (Fig. D.5): It is recalled that uncertainties on this parameter are considered to be uncertainties on LES obtained values of FTF gain and phase at a particular frequency corresponding to a minimum FTF gain (this frequency can be devised

using Eq. (3.14)). The corresponding figure shows that model results are tied to the LES capabilities. If LES fails at predicting the flame response at frequency f, the model itself cannot provide a good estimation of the FTF gain, and will not accurately predict the FTF phase curve inflexion.

- $\boldsymbol{\phi_0}$, (Fig. D.6) : Variations of this parameter act similarly to those of the time delay τ.

- $\boldsymbol{\beta}$, (Fig. D.7): This parameter aims at retrieving appropriate high frequency FTF gain levels and does not affect the FTF phase to a significant extent. Thus, errors on its estimation will lead to an over or under-prediction of the high frequency FTF gain.

From these observations, one identifies three particularly sensitive parameters, for which a small offset will modify the predicted FTF, are ω_*, τ and χ.

The reduced frequency ω_* is assessed from a reacting stationary flame LES through an estimation of flame dimensions based on the heat release rate center of mass. The prediction of this quantity requires a correct prediction of the flame position and thus an adequate representation of thermal conditions in the case of numerical simulations. Such a thing can only be achieved by providing precise reference temperature measurements or by using a coupled fluid/solid heat transfer approach.

The time delay τ is derived in this work assuming a 1D propagation of acoustic and convective waves, Eq. (3.9). The determining factor in its correct prediction relies on the correct prediction of the convective velocity u_c which was taken here as the bulk velocity. Some authors [105, 196] showed that experiments and model predict a convective velocity 40 to 50% superior to the bulk velocity. Recently, Albayrak *et al.* [197] suggested that inertial waves should be considered instead of a simple convection model. These authors proposed an analytical formulation for u_c that was shown not to agree with LES findings of Sec. 3.5.2.1. In the absence of a definitive answer, one should pay close attention to the value of u_c and check that its consistency by measuring the time delay τ from bulk velocity signals stemming from a pulsed reactive simulation.

Finally, parameter χ depends on the target FTF gain and phase value used for its optimization. Hence, simulations need to be accurate enough to capture the pulsed flame dynamics and correctly predict the FTF gain and time delay at the target frequency. Doing so necessitates several conjugate factors: an adequate mesh, precise thermal conditions, non dissipative numerical schemes, *etc.*

Unsurprisingly, it is therefore concluded that the quality of modelled FTF predictions directly depends on the quality of numerical simulations used for the parameters estimation.

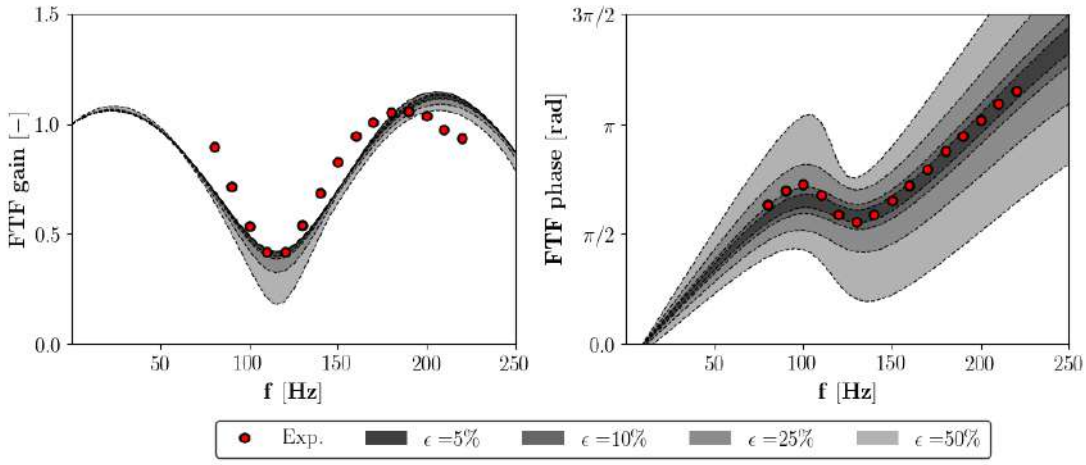


Figure D.1: SFTF model results for the bluff-body stabilized Noisedyn flame with baseline parameters from Tab. 3.5 and various maximum deviations levels ϵ on parameter ω_* only.

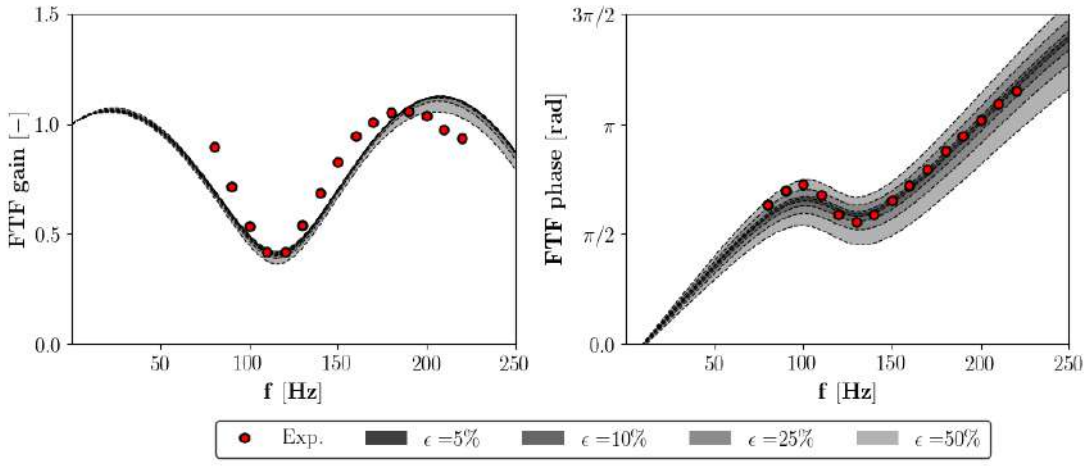


Figure D.2: SFTF model results for the bluff-body stabilized Noisedyn flame with baseline parameters from Tab. 3.5 and various maximum deviations levels ϵ on parameter α only.

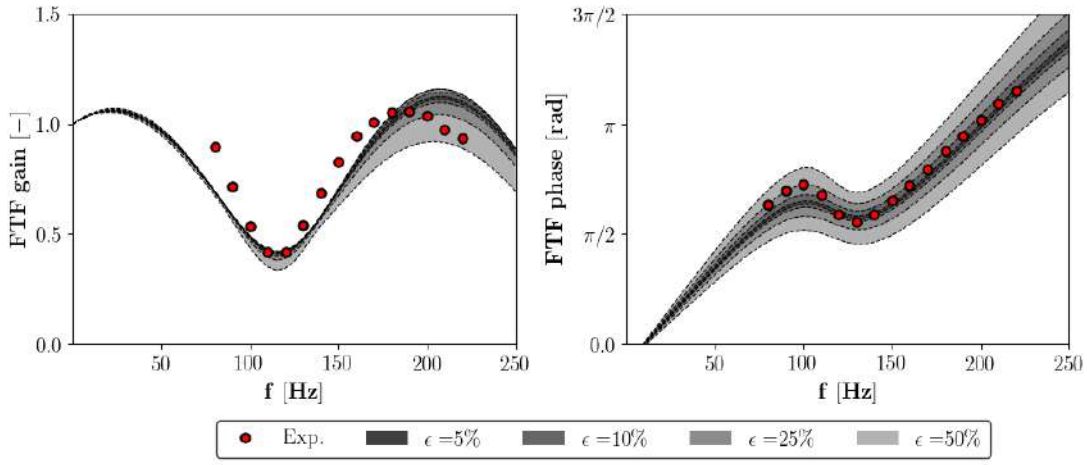


Figure D.3: SFTF model results for the bluff-body stabilized Noisedyn flame with baseline parameters from Tab. 3.5 and various maximum deviations levels ϵ on parameter K only.

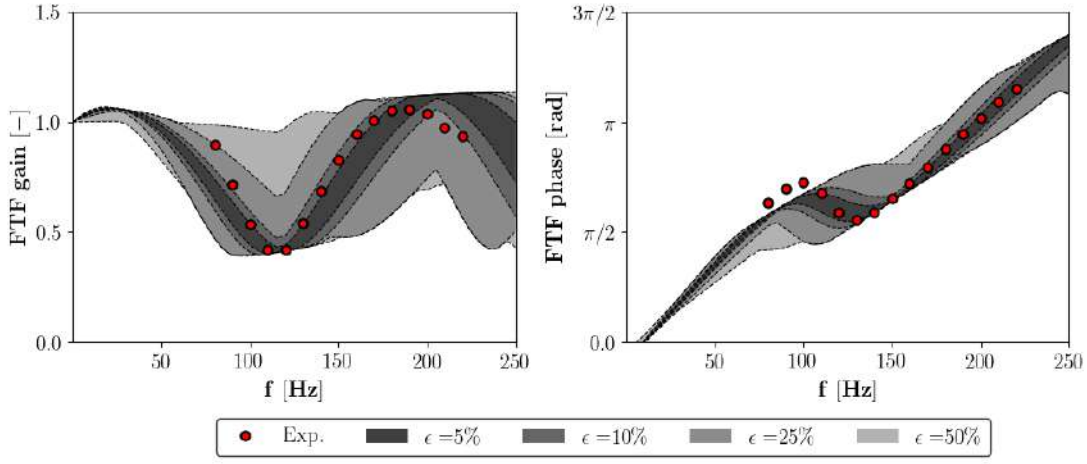


Figure D.4: SFTF model results for the bluff-body stabilized Noisedyn flame with baseline parameters from Tab. 3.5 and various maximum deviations levels ϵ on parameter τ only.

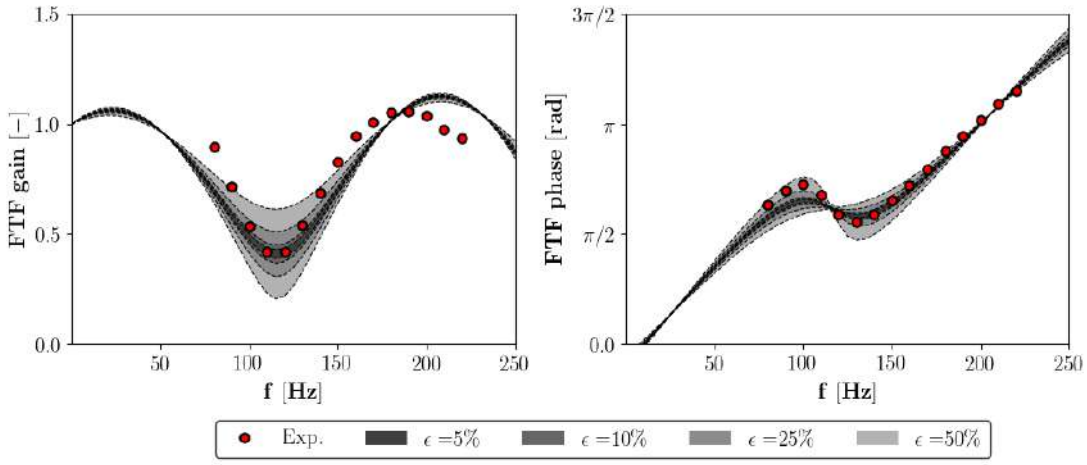


Figure D.5: SFTF model results for the bluff-body stabilized Noisedyn flame with baseline parameters from Tab. 3.5 and various maximum deviations levels ϵ on parameter χ only.

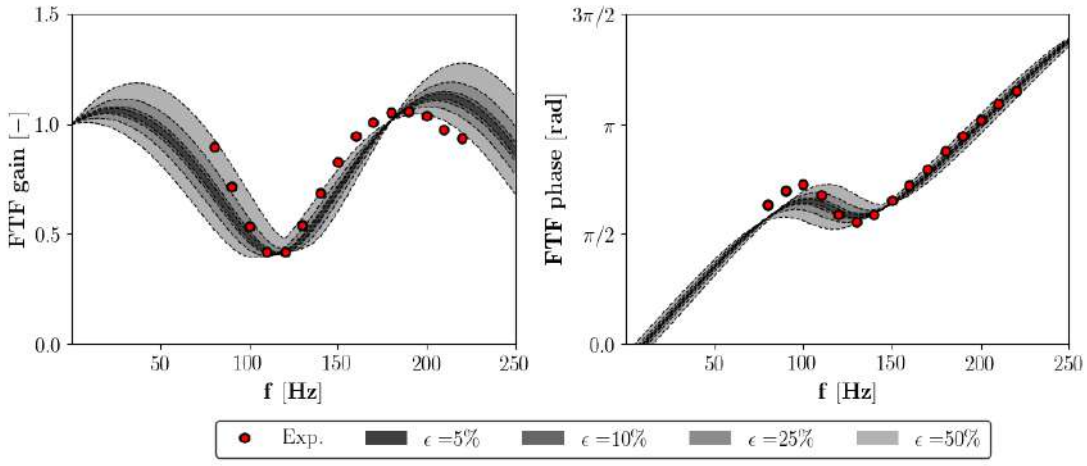


Figure D.6: SFTF model results for the bluff-body stabilized Noisedyn flame with baseline parameters from Tab. 3.5 and various maximum deviations levels ϵ on parameter ϕ_0 only.

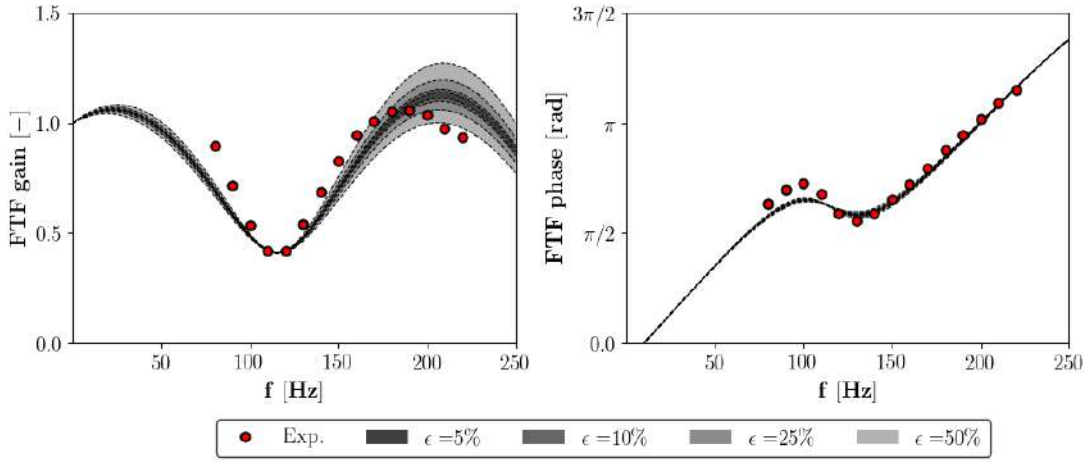


Figure D.7: SFTF model results for the bluff-body stabilized Noisedyn flame with baseline parameters from Tab. 3.5 and various maximum deviations levels ϵ on parameter β only.

Appendix E

Helmholtz computations of the SAFRAN combustor with a null acoustic pressure outlet boundary condition

In Sec. 4.6.2, Helmholtz computations of the SAFRAN combustor are performed considering a null normal acoustic velocity $\hat{\mathbf{u}}.\mathbf{n} = 0$ on all boundaries. In this appendix, the boundary condition on the main outlet of the domain is changed to null pressure $\hat{p} = 0$. The geometry and numerical setup remain the same and correspond to the case R1 of Tab. 4.6, for which neither active flames nor multi-perforated plate are considered. Obtained eigenfrequencies and mode shapes are summarized in Tab. E.1.

Mode	Re(f)	Im(f)	Mode structure
M0	278.3	-3.2×10^{-9}	1L
M1	370.7	5.3×10^{-9}	1A
M2	370.7	-1.9×10^{-8}	1A
M3	553.4	3.5×10^{-8}	2L
M4	562.5	7.9×10^{-8}	2A
M5	562.5	1.1×10^{-7}	2A
M6	608.9	-1.5×10^{-6}	1A1L
M7	608.9	1.1×10^{-6}	1A1L
M8	749.6	-1.7×10^{-7}	2A1L
M9	749.6	1.8×10^{-6}	2A1L

Table E.1: List of the first 10 eigenmodes frequencies Re(f) and growth rates Im(f) obtained for case R1 modified with zero pressure outlets. The mode structure is also specified: for instance mode 1A corresponds to the first azimuthal mode and mode 1A1L corresponds to a first mixed azimuthal/longitudinal mode.

The azimuthal component of concerned modes is mainly located in the cavity located upstream of the combustion chamber and air inlet as a result of the null acoustic pressure boundary condition. This is exemplified for modes M4/M5 in Fig. E.1 with frequency $f = 562.5$ Hz. In regard to the combustion instability observed during engine test

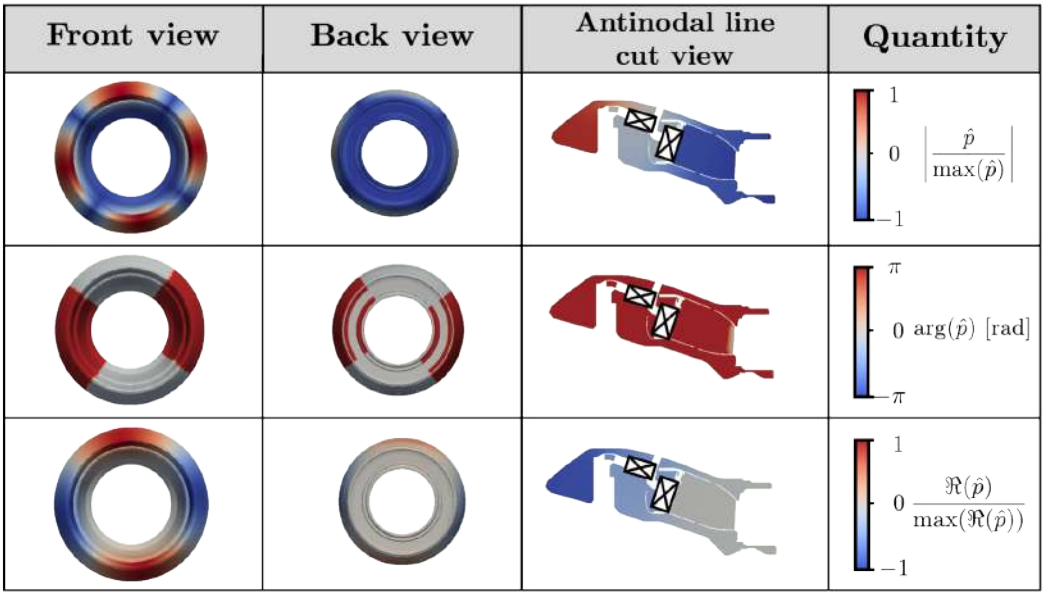


Figure E.1: Structure of mode M4/M5 for case R1 with null acoustic pressure outlets. Front view faces the compressor stages, back view faces the combustion chamber outlet. The transverse cut is extracted on the antinodal line for which $|\hat{\mathbf{p}}|$ is maximal.

session at $f_1 = 500$ Hz, these two modes are the most likely candidates since they have an azimuthal component and the closest frequency.

There is no definitive conclusion on the exact boundary condition to use at the configuration outlet for a good representation of the experiments where the combustion instability was identified. The assumption is made that the frequency shift generated by adding active flame elements in the Helmholtz computations is low. In that view, null acoustic velocity acoustic simulations are preferred since they provide the passive mode with the closest frequency $f = 497$ Hz (see Sec. 4.6.2.3).

Appendix F

Acoustic equivalence of reference points in Helmholtz computations

Helmholtz computations including active flame elements necessitate a description of the flame response. In most Helmholtz solver this is achieved thanks to a flame transfer function which relates unsteady heat release fluctuations to a reference velocity on a given point, and sometimes a reference surface [211]. In this work FTF are extracted from LES using a collection of equally distributed points that should in theory be acoustically equivalent. Not only does one need to make sure that the evaluation of the FTF from LES is performed in a correct manner, but also one needs to be assured that probing locations are equivalent for the acoustic solver.

A study is performed using two diametrically opposed probes of location VE and VES defined in Sec. 4.3.2, corresponding to the second swirler stage. The reader is referred to Fig. 4.5b for a visualization of these probing locations. The two probes are denoted as Pb_1 and Pb_2. Here only active flame are considered and all acoustic boundary conditions are set to a zero normal velocity (case R2 as defined in Tab. 4.6). Results are presented in Tab. F.1 for probing location VE and in Tab. F.2 for probing location VES. Errors on the predicted frequency remain extremely limited for a given

Mode	**Passive frequency [Hz]**	$\mathbf{f_{Pb_1}}$ **[Hz]**	$\mathbf{f_{Pb_2}}$ **[Hz]**	$\mathbf{\Delta Re\,(f)}$ **[%]**	$\mathbf{\Delta Im\,(f)}$ **[%]**
M3	389.3	$430.5 + 39.4i$	$430.6 + 37.5i$	0.02	5.07
M4	497.5	$514.1 + 27.3i$	$513.2 + 25.1i$	0.16	8.76
M6	550.5	$563.1 - 25.7i$	$563.3 - 25.3i$	0.05	1.58
M8	661.7	$675.7 - 75.8i$	$672.5 - 74.4i$	0.47	2.02

Table F.1: Acoustic modes of the SAFRAN combustors with active flames (case R2) for probes $\mathbf{Pb_1}$ and $\mathbf{Pb_2}$ from probing location VE.

set of probes with less than 0.5% for both probing locations. The maximum error on growth rates for two diametrically opposed reference points is also reasonable with less than 10% for VE and less than 5% for VES. These small errors are attributed to differences in the local mesh topology.

Mode	Passive frequency [Hz]	$\mathbf{f_{Pb_1}}$ [Hz]	$\mathbf{f_{Pb_2}}$ [Hz]	$\mathbf{\Delta Re\,(f)}$ [%]	$\mathbf{\Delta Im\,(f)}$ [%]
M3	389.3	$407.2 + 20.3i$	$406.5 + 19.7i$	0.17	3.05
M4	497.5	$500.1 + 13.1i$	$499.8 + 12.6i$	0.06	3.97
M6	550.5	$553.1 - 8.74i$	$553.1 - 8.37i$	0.00	4.42
M8	661.7	$631.4 + 48.8i$	$631.1 + 48.1i$	0.05	1.46

Table F.2: Acoustic modes of the SAFRAN combustors with active flames (case R2) for probes Pb_1 and Pb_2 from probing location VES.